UNIVERSITÀ
DEGLI STUDI
DI PADOVA

Sede Amministrativa: Università degli Studi di Padova

Dipartimento di Scienze Chimiche

Scuola di Dottorato di Ricerca in Scienza e Ingegneria dei Materiali

XXIII ciclo

Doctor Europaeus

Metal Nanoparticles on TiO_x/Pt(111) Ultrathin Films with Different Structures and Stoichiometries: a Study of their Properties and Reactivity

Direttore della Scuola: Ch.mo Prof. Gaetano Granozzi

Supervisore: Ch.mo Prof. Gaetano Granozzi

Dottorando: Luca Artiglia

Index

Chapter I
Introduction

Heterogeneous catalysis plays a central role in many emerging fields such as energy storage and conversion, reduction of pollutants, production of chemicals, conversion of hydrocarbons and fuels, gas sensing etc… The term catalysis was first introduced in 1835 by J. J. Berzelius to describe an enhancement of a chemical reaction rate obtained through the use of a substance (or a mix of substances), called catalyst, which is not consumed during the reaction. Nowadays catalysts are commonly used in many important industrial processes (e.g. oil refinery, organic synthesis and many other fields). They are generally composed of several components combined in a precise proportion and optimised in order to provide the highest reaction rate and selectivity on the basis of an empirical *trial and error procedure*, i.e. a simple test of different formulations and the selection of the most active between them by simply evaluating the reaction rate and the overall chemical yield (hereafter called as *real catalysts*). Commonly, the main *building blocks* of a *real catalyst* are known through the chemical preparative process but it is hard to associate a well-defined role to each component in such a multi-component system. Moreover, a complete understanding of the elementary steps underlying the catalytic processes at the atomic level is really difficult to be achieved studying *real catalysts* because of the intrinsic complexity of most of them, and because of the chemical complexity of the steps involved in the whole process.

It is well known that no real improvement in science can be achieved without a knowledge-based approach. Focusing on catalysis a typical surface process, in order to avoid a mere trial-and-error approach and the role of the different parameters affecting the catalytic performance, should be analyzed in details using a rigorous approach based on the concepts and tools developed by Surface Science (SS) applied

to well-defined systems. In other words, a multidisciplinary reductionist approach is really needed in order to ascertain the role of the several different factors, e.g. the electronic and structural effects (e.g. morphological changes, role of defects…).

Real catalysts are usually composed by metal particles of nanometric size (hereafter, nanoparticles, NPs) dispersed on a high surface area inert material used as a substrate (usually an oxide). The use of metallic NPs arises from their unique physical properties associated with their spatial confinement. As a result, the properties of these species are neither those of the bulk material nor those of molecular compounds, and are strongly dependent on particle size, surface structure and composition of the particle itself. This has generated a new area, called Nanocatalysis,[1, 2, 3] where in recent years much efforts have focused to understand what governs the behaviour of matter within the 1-10 nm range. In this field, the results obtained with nano-sized gold are promising, especially because these kind of NPs are able to activate the oxygen molecule, making Au based catalyst suitable for selective oxidation reactions.[4]

However, many open questions concerning nanocatalysis are still pending: what is the role of the catalyst particle size, shape and structure? What is the role of the substrate, i.e. of the particle support, in terms of structure, morphology, crystallinity? What is the role of the substrate-particle interface, and what is the role of phenomena like charge exchange?

To overcome many of the experimental difficulties in applying SS to catalysis and to answer the above questions, an approach based on the so-called *model catalysts* has been developed. At the beginning (late 1960s), following the development of Ultra-High-Vacuum (UHV) equipments, *model catalysts* were obtained creating well ordered extended surfaces of catalytic metals. Hence, their electronic behaviour and, above all, their chemical properties (through chemisorption properties) were successfully investigated using the common SS techniques.[5] Using this approach, the mechanism of some important reactions like the CO oxidation[6] and the ammonia or methanol synthesis[7, 8] has been described. However, a metal single crystal surface is not a good model to reproduce a *real catalyst*, since two important features are not taken into account: the finite size of the metal particles, affecting both the catalyst reactivity and selectivity[9] and the presence of the substrate, that is used as a mechanical support but in many cases can modify the electronic properties of the NPs[10,11,12] or migrate over them as a consequence of the Strong Metal Support

Interaction effect (SMSI).[13] The use of *supported model catalysts* helped the scientists to overcome these limitations, usually referenced as *material gap*.[14] The *supported model catalysts* are obtained depositing, under UHV, metal NPs on a clean planar oxidic surface used as a substrate. Metal NPs can be nucleated and grown on such samples using several deposition methods: UHV evaporation, Chemical Vapor Deposition (*in situ* decomposition of a metal precursor), wet impregnation etc.. In a further improvement of the *supported model catalyst,* the oxidic substrate has been implemented as an ultrathin film on a metal single crystal substrate, so avoiding any charging of the substrate itself under the conditions of a typical SS experiment.[15]

Another important limitation to the use of *model catalyst* regards the *pressure gap*. In fact these model systems are usually prepared *in situ* in UHV (common pressures in the 10^{-10} mbar range) and it is not clear whether they can survive after exposure to ambient conditions, maintaining their morphology and allowing us to extend the validity of studies performed in UHV to real conditions. As a consequence of this, High Pressure (HP) cells, directly connected to UHV chambers where the sample preparation is carried on, have been developed so that the sample can be characterized with SS techniques before and after the HP treatment.[16] Moreover, in many systems the reactions taking place during the HP exposure can be monitored using infrared spectroscopy coupled with a Quadrupole Mass Spectrometer (QMS) for residual gas analysis.[17]

Based on the experience built up in the research group, where such thesis has been developed, in the field of TiO_x ultrathin films grown on Pt(111) (and widely described in chapter 3),[18] a method to prepare $M/TiO_x/Pt(111)$ (where M stands for a generic metal) *model catalysts* in UHV following reproducible preparative strategies has been developed in the present thesis work. Metal NPs show different behaviour depending on the TiO_x phase where they are deposited. Hence, through Low Energy Electron Diffraction (LEED), X Ray Photoelectron Spectroscopy and Diffraction (XPS-XPD), Scanning Tunneling Microscopy (STM) and Thermal Programmed Desorption (TPD) it was possible to establish a connection between the NPs morphology, their interaction with the substrate and the overall system reactivity, that was investigated using probe molecules (commonly CO and O_2). The thermal evolution of the systems was also considered, and a complete study regarding the HP evolution of $Au/TiO_x/Pt(111)$ using Fourier Transform-InfraRed Absorption

Reflection Spectroscopy (FT-IRAS) will be presented in section 6.4 in order to fill the *pressure gap*.

In this thesis I will present the results of a three years long PhD research project on *model catalysts*. It will be divided in four different sections. In the first section I will present the SS experimental techniques and setups that have been used to characterize our samples (**chapter II).** In section two (**chapter III**) I will briefly focus on the state of the art regarding the TiO_x/Pt(111) ultrathin films so far characterized in the group and I will present an update on the stoichiometric *rect* and *rect'*-TiO_2 ultrathin films (**chapter IV**). In the third section, Au based model catalysts will be considered: in **chapter V** I will first summarize the state of the art on Au at the nanoscale and in **chapter VI** I will present the results obtained on the Au/TiO_x/Pt(111) *model catalysts*, describing their electronic properties on different TiO_x substrates, their morphology and reactivity. In the last section I will present the results obtained on Fe based model catalysts: in **chapter VII** I will briefly describe the literature data on the *model catalysts* based on Fe NPs, and discuss the current status of understanding of the SMSI effect. Then, in **chapter VIII,** I will focus on the Fe/TiO_x/Pt(111) *model systems*, reporting the analysis of the morphology, the electronic properties and the thermal evolution in order to show the differences occurring between a reactive metal like Fe, showing SMSI effect, and a noble metal like Au. Finally, I will present the conclusion and perspectives in **chapter IX**.

When the results have been already published, the corresponding papers have been adopted as part of this thesis. On the contrary, the arguments not yet published have been reported in details.

References

[1] A. T. Bell, *Science* 2003, **299**, 1688.

[2] R. Schlogl, H. Abd, *Angew. Chemie Int. Ed.*, 2004, **43**, 1628.

[3] T. E. Madey, K. Pelhos, Q. Wu, R. Barnes, I. Ermanoski, W. Chen, J.J. Kolodziej, J. E. Rowe, *PNAS* 2002, **99**, 6503.

[4] M. Haruta, *Nature*, 2005, **347**, 1098.

[5] G. A. Somorjai, *Introduction to Surface Chemistry and Catalysis*, Wiley, New York, 1994.

[6] T. Engel, G. Ertl, *Adv. Catal.* 1978, **28**, 1.

[7] G. Ertl, in: J.R. Anderson, M. Boudart (Eds.), *Catalysis, Science and Technology, vol. 4*, Springer, Berlin, 1983, p. 209.

[8] T.S. Askgaard, J.K. Norskov, C.V. Ovesen, P.J. Stoltze, *J. Catal.* 1995, **156**, 229.

[9] M. Che, C.O. Bennett, *Adv. Catal.* 1989, **36**, 55.

[10] C.C. Kao, S.C. Tsai, M.K. Bahl, Y.W. Chung, W.J. Lo, *Surf. Sci.* 1980, **95**, 1.

[11] S. Ogawa, S. Ichikawa, *Phys. Rev. B* 1995, **51**, 17231.

[12] G. Pacchioni, N. Rorsch, *Surf. Sci.* 1994, **306**, 169.

[13] Q. Fu, T. Wagner, *Surf. Sci. Rep.* 2007, **62**, 431–498.

[14] D.W. Goodman, *Surf. Rev. Lett.* 1995, **2**, 9.

[15] Q. H. Wu , A. Fortunelli, G. Granozzi, *Int. Rev. Phys. Chem.* 2009, **28**, 517-576.

[16] J. A. Rodriguez, D.W. Goodman, *Surf. Sci. Rep.* 1991, **14**, 1.

[17] Z. Zhao, T. Diemant, T. Haring, H. Rauscher, R. J. Behm, *Rev. Sci. Instrum.* 2005, **76**, 123903.

[18] F. Sedona, G.A. Rizzi, S. Agnoli, F. X. Llabrés i Xamena, A. Papageorgiou, D. Ostermann, M. Sambi, P. Finetti, K. Schierbaum and G. Granozzi, *J. Phys. Chem. B*, 2005, **109**, 24411.

Section 1

Methods

Chapter II
Experimental setup and equipments

In this chapter I will briefly mention the very basic principles of the experimental techniques used for the sample characterization during this PhD thesis, i.e. TPD, XPS, XPD, STM, LEED and IRAS. For more detailed information regarding both the experimental set-up and the rigorous interpretative principles the reader is redirected to the Surface Science textbooks.[1, 2, 3] In the second part of this chapter, I will focus on the experimental setup (UHV chambers and HP cell) used during the experiments.

II.1 Experimental setup

II.1.1 Thermal Programmed Desorption (TPD) [4]

The Thermal Programmed Desorption (TPD) represents an important method for the study and determination of thermodynamic and kinetic parameters describing the desorption processes. Commonly, the sample is heated following a temperature ramp ($\beta(t) = dT/dt$) where the temperature (T) vary linearly with the time. The partial pressures corresponding to the atoms or molecules desorbing from the sample surface are detected by a Quadrupole Mass Spectrometer (QMS) so that the final output of the experiment provides a spectrum reporting the partial pressures intensities as a function of the temperature.

The experimental method used in this thesis for all the TPD experiments is the following:

_ sample exposure to a precise amount (expressed in Langmuirs [L]) of a *probe* molecule/s (usually CO) at room temperature (RT) or low temperature (LT)
_ sample heating (applying a linear temperature ramp by 1 or 2 K/s) up to a top temperature while the QMS monitor the *probe* molecule/s partial pressure intensities
_ sample cool-down after the top temperature is reached.

The adsorption process takes place when the interaction energy between an adsorbate (probe molecule) in the gas phase and the surface is high enough to exceed the thermal disorder due to the temperature. Depending on the strength of such interaction both fisisorption (typically Van der Waals interactions, with a $\Delta H_{ads} < 50$ kJ/mol) or chemisorption (when the interaction strength is comparable to a chemical bond and $\Delta H_{ads} > 50$ kJ/mol) are observed. While the former, being a low energy interaction, is favoured by low temperatures and is non-specific (each kind of molecule can be adsorbed under appropriate experimental conditions), the latter leads to the formation of a chemical bond, thus to a specific orientation of the molecules. Moreover, the chemisorption interaction can weaken the intra-molecular bonds and in some cases leads to a dissociation of the molecule (dissociative chemisorption). The kinetic aspects regarding the adsorption/desorption processes are well described by the Langmuir isotherm, that relates the surface coverage to the gas pressure on the surface. The main assumptions to obtain this equation are the following:
_ the adsorption process is localized;
_ the sample surface is saturated so that the degree of coverage is $\Theta = 1$ ML when all the active sites are occupied;
_ the interactions between the adsorbed molecules are negligible.
It is then possible to obtain the rate (r) both for the adsorption and the desorption processes:

$$r_{ad} = A_n \cdot p(1-\Theta)^n$$

$$r_{des} = B_n \cdot \Theta^n \qquad (A_n, B_n = \cos t., n = 1,2)$$

When the equilibrium is reached $r_{ad} = r_{des}$ and then:

$$\Theta = \frac{(b_n p)^{1/n}}{1+(b_n p)^{1/n}} \qquad (b_n = A_n / B_n = \cos t., n = 1,2)$$

For n = 1, the adsorption/desorption kinetic is first order, for n = 2 second order and so on.

The microscopic reversibility principle applied to the adsorption/desorption processes states that both the processes can be described by the same kinetic equations. Hence the reaction rate for a n order process can be written as:

$$r_{des} = -\frac{d\Theta}{dt} = k_n \cdot \Theta^n$$

where k is the rate constant that can be described using an Arrhenius equation:

$$k_n = \nu_n(\Theta) \cdot \exp\left(-\frac{\Delta E_{des}(\Theta)}{RT}\right)$$

Combining the two it is possible to obtain the Polanyi-Wigner equation:

$$r_{des} = -\frac{d\Theta}{dt} = \nu_n(\Theta) \cdot \exp\left(-\frac{\Delta E_{des}(\Theta)}{RT}\right) \cdot \Theta^n$$

where $\nu_n(\Theta)$ is a pre-exponential frequency factor, Θ is the degree of coverage, n is the kinetic order of the process (in this case the desorption) and $\Delta E_{des}(\Theta)$ is the activation energy for the same process. It is possible to apply the Polanyi-Wigner equation to our experimental technique (TPD), reminding that $dt = (1/\beta) \cdot dT$ so that:

$$-\frac{d\Theta}{dT} = \frac{1}{\beta}\nu_n(\Theta_n) \cdot \exp\left(-\frac{\Delta E_{des}(\Theta_n)}{RT}\right) \cdot \Theta^n$$

This last equation shows that:

_ the desorption temperature (T) depends on ΔE_{des}, β, Θ_n;

_ the desorption peaks shape depends on ν_n, β, n;

_ the peaks area depends on Θ_n.

If a sequence of desorption spectra is recorded keeping the coverage (Θ_n) constant (both ν_n and ΔE_{des} become independent from it) and using different heating rate (β), it is possible to obtain the desorption temperature corresponding to the peak maximum for each β. Then, it is possible to get a plot reporting the $\ln(T_{max}^2/\beta)$ vs $(1/T_{max})$ allowing us to calculate the ΔE_{des} value.

II.1.2 X-Ray Photoelectron Spectroscopy (XPS) [5]

The X-Ray Photoelectron Spectroscopy (XPS) is based on the photoelectric effect: a solid surface is exposed to an X ray radiation ($10^{-12} \le \lambda \le 10^{-8} m$) that cause the emission of photoelectrons. The most simple configuration for an XPS setup is reported in figure II.1 a and is composed by an X ray primary source, a sample holder and an electron analyzer.

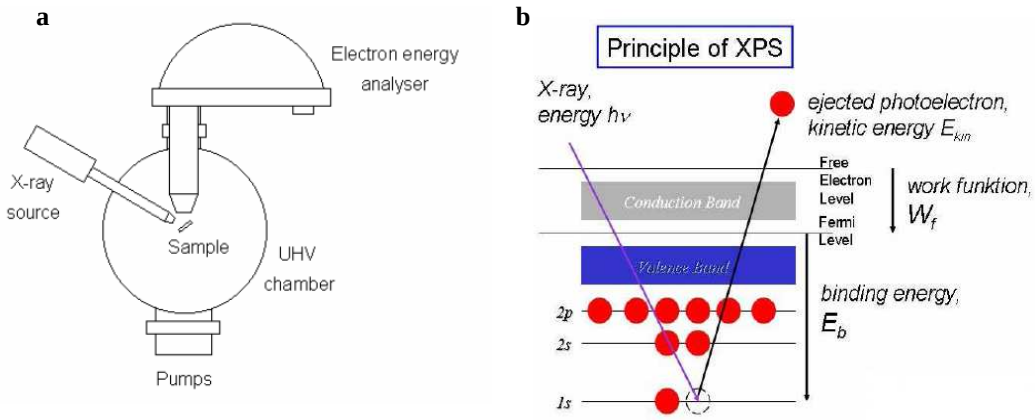

Figure II.1. (a) Schematic representation of an XPS setup; (b) The photoemission process (in the case of a 1s photoelectron emission).

The X-rays photon flux, generated by the source (usually through electron bombardment of a metal anode, Mg or Al), is directed on the sample and generate a flux of photoelectrons, emitted both from the core and the valence shells (figure II.1 b). The photoelectrons emitted after the interaction between the X-ray photons and the sample can have different fates: they can either be excited and emitted without any energy loss, giving the characteristic elastic peaks, or some of them can undergo

anelastic diffusion releasing part of their energy as heat and contributing to the spectrum baseline. The analyzer can discriminate the kinetic energy associated to the photoelectrons, providing an output spectrum where the signal intensity (counts per second) is reported as a function of the kinetic energy. The kinetic energy depends on the incident photons energy (primary radiation $E = h\nu$) and on the electron binding energy to the atom (BE) through the equation:

$$E_k = h\nu - BE - \Phi$$

where Φ is the analyzer work-function. The BE is strongly influenced by the oxidation state of the analyzed element: it is more difficult to extract a photoelectron from an oxidized element with respect to its reduced counterpart. Therefore, an XPS spectrum can provide important information about the electronic structure of a solid sample, through the analysis of its output core and valence peaks (figure II.2).

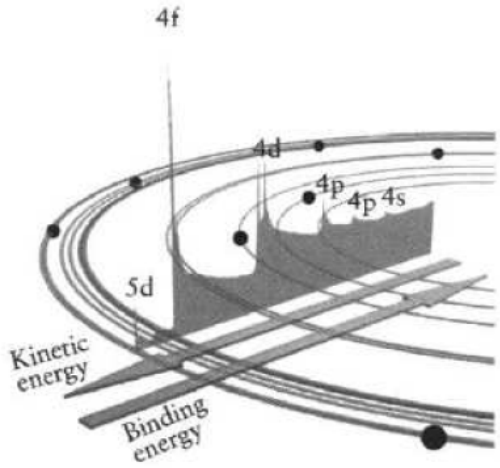

Figure II.2 Example of an XPS spectrum.

Another important parameter in XPS is the sampling depth, that depends on the emitted electrons kinetic energies. Moreover, the electrons kinetic energy affect the anelastic attenuation length (Λ_e), that is directly related to the electron mean free path. Since the variation in the XPS signal intensity is expressed by the following:

$$I = I_0 \cdot \exp\left(\frac{-z}{\Lambda_e sen\theta}\right)$$

where $-z/sen\theta$ is the length covered by the electron, it is possible to demonstrate that the 65% signal intensity comes from a $< \Lambda_e$ distance, the 85% comes from a $< 2\ \Lambda_e$ distance and the 95% comes from a $< 3\ \Lambda_e$ distance. Hence, it is easy to understand why this technique is considered "surface sensitive", being limited to a few nm sample thickness. As a direct consequence of this, if the angle between the sample surface and the analyzer (θ) is 90° (normal revelation with respect to the surface) the sampled thickness is $3\ \Lambda_e$. When the angle θ is reduced ($\theta < 90°$) then the sampled thickness becomes $3\Lambda_e \cdot sen\theta$, and the analysis results to be more surface sensitive.

The conventional notation used in this thesis to indicate the XPS peaks refers to the quantum numbers related to the orbital where the photoelectron comes from. It is indicated as nl_j, where n indicates the principal quantum number representing the orbital energy level and l indicates the azimuthal quantum number representing the orbital geometry. When $l \neq 0$ the XPS peaks are generally present as doublets because the magnetic moment (m) associated to the angular one interacts with the spin magnetic moment (m_s) associated to the electron. The sum vector of these two creates a vector (j), indicated as a subscript in the notation, whose magnitude is given by $j = l + s$. Therefore a p peak can originate 2 values of j: 1/2 (which originates from $l - s$) and 3/2 (which originates from $l + s$). The peak corresponding to it will be a doublet, whose components will be separated by an energy difference corresponding to the spin-orbit coupling and an intensity ratio given by ($2j + 1$).

During my PhD research experience, I also worked at the Elettra synchrotron facility, in Basovizza, Trieste. Through the use of synchrotron radiation it is possible to set, by mean of monochromators, a precise photon wavelength to use during High Resolution (HR)-XPS experiments. Since the selected radiation derive from a storage ring where electrons are accelerated in a magnetic field up to 2.0 GeV energy, the photon fluxes are extremely high compared to that produced by a common X-Ray source. Therefore, the use of an intense and tunable photon energy allows a maximization of the photoionization cross sections of the elements that are useful for the analysis. At the same time, it is possible to minimize some contributions coming, for example, from the bulk substrates, basing on the photoionization cross sections

Cooper's minimum energy position. The latter procedure is particularly useful in the valence band studies, where the presence of a bulk signal affect the overall spectrum appearance.

II.1.3 Photoelectron Diffraction (PD)[6]

Electrons emitted from the core levels of a photon-irradiated crystalline sample (either photoelectron or Auger electrons) undergo scattering by atoms close to the emitting species. Subsequent interference between the primary electron wave**,** which propagates to the detector without undergoing any elastic scattering, and the secondary or scattered electron waves, which are caused by the scattering of the primary wavefront at atoms surrounding the emitter, produces strong intensity modulations as a function of either the direction of detection or the kinetic energy of the emitted electron. PD is a surface structural probe sensitive to short range order, with atomic, chemical state and site specificity. The short range order surface sensitivity is due to the lack of coherence between photoelectron waves emitted at different atomic sites because of the random nature of the emission process, coupled with the l/r decay of the outgoing core photoelectron wave and with the relatively short electron inelastic mean free paths at the energies typical for a PD experiment. On the other hand, to obtain a PD pattern, a long-range ordered sample is needed so as to sum up the contributions from many equivalent emitters.

The experimental procedure in PD implies to select one emission line in the XPS spectrum and to measure its integrated intensity either as a function of the emission angle (Angle Scanned PD, AS-PD) or as a function of the photon energy, then changing the kinetic energy of the outgoing photoelectrons (Energy Scanned PD, ES-PD, only possible at Synchrotron facilities).

A typical AS-PD experimental setup is reported in figure II.3 a. The polar angle θ is individuated by the surface normal and the direction of the wave vector $\boldsymbol{k}$, while the azimuthal angle φ is defined arbitrarily within the surface plan. By varying θ and φ it is possible to acquire the whole photoemission hemisphere above the sample surface (the so called 2π plot reported in figure II.3 c).

PD data are then usually reported as χ value, where χ is defined by:

$$\chi = \frac{I - I_{min}}{I_{max}}$$

where I is the photoemission intensity in a selected angular direction (or energy value), I_{max} and I_{min} are the maximum and minimum intensities values over the entire measured range.

When doing AS-PD, Azimuthal (APD) and Polar (PPD) scans of the photoemission signal (in an energy range above ca. 400 eV) provide a direct information about the directions of the atomic rows. In particular it has been demonstrated both by experimental evidences and theoretically that the scattering factor for an electron wave presents a maximum along the axis joining the scatterer and the emitter; this phenomenon is known as forward scattering (FS) and represents the first order approximation of diffracted intensity. When the kinetic energy decreases and is lower than a few hundredths eV the scattering amplitude becomes relevant for each value of θ. Moreover the scattering probability increases and also multiple scattering events are possible.

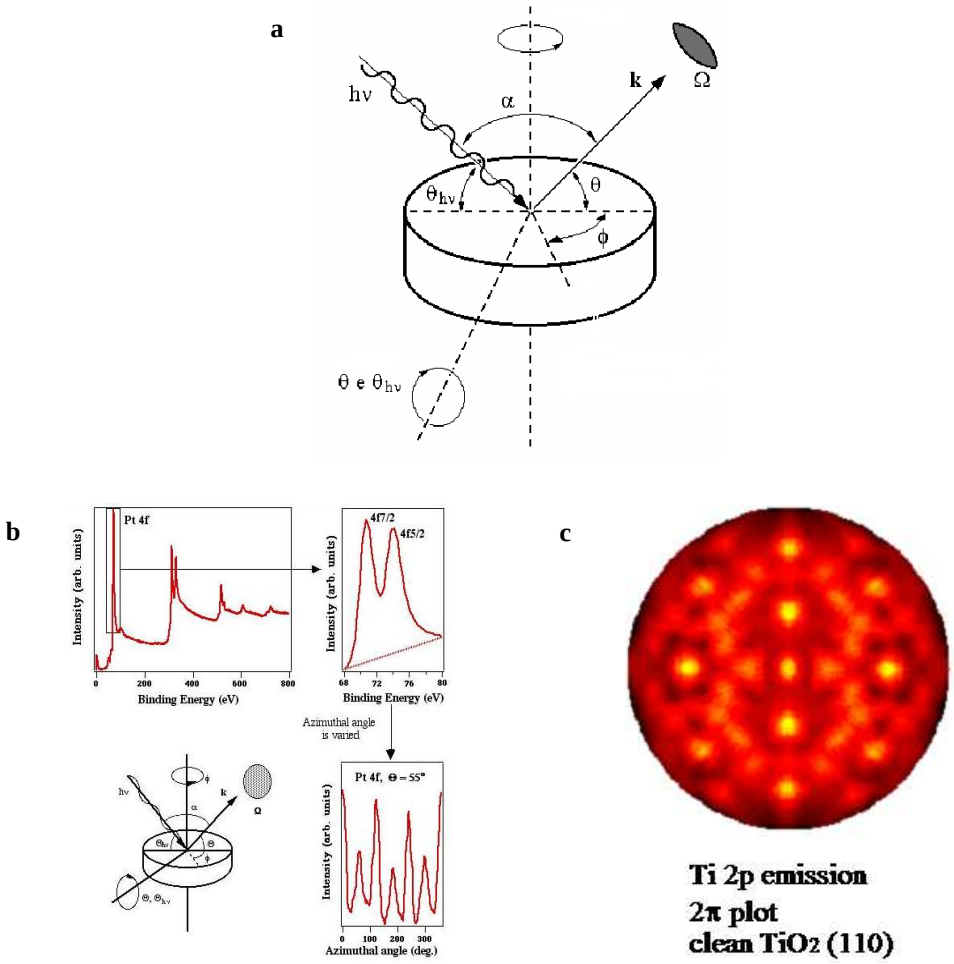

Figure II.3 (a) Schematic AR-PD setup; (b) Schematic example representing the sample-holder geometry and how an azimuthal scan can be achieved; (c) Example of a 2π plot, obtained collecting the Ti 2p peak both in azimuthal and polar directions

II.1.4 Low Energy Electron Diffraction (LEED)

The Low Energy Electron Diffraction is based on the oscillation behaviour of a primary electron beam at low energy (20-500 eV), whose corresponding wavelengths variation is between 0.5 and 2.0 Å.[7] If this beam interacts with a crystal lattice having comparable inter-atomic distances, then the electrons are diffracted and the images obtained are diffraction spots matching the reciprocal lattice ones. Analyzing these spots it is possible to trace back to the real lattice and then to the surface geometry. The electrons mean escape depth values are low (as reported previously for XPS), usually less than 10 Å, so that electrons are used to analyze the surface atoms layers.

In the usual experimental setup (figure II.4) the sample is illuminated with an electron beam, produced through thermoionic effect from a filament placed in the back screen side (electron gun). The electrons are then accelerated up to the desired energy through a potential gap and collide on the sample.

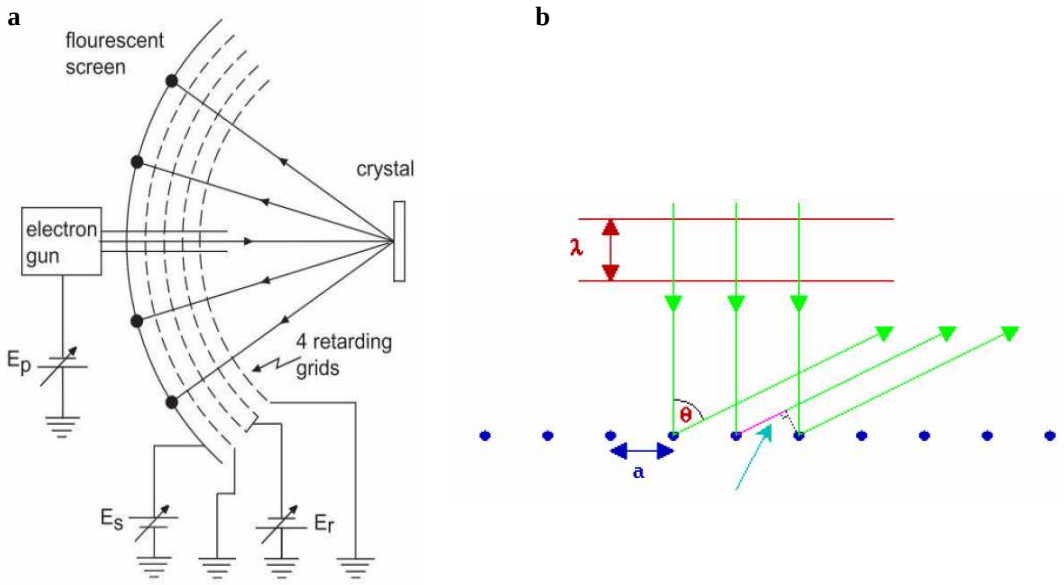

Figure II.4 (a)Example of a rear-view LEED configuration; (b) Schematic representation of the diffraction process from atoms separated by a periodic distance a

The diffracted electrons are emitted back in precise directions (with respect to the primary beam), until they collide with a suppressor made by a series of grids kept at a variable potential, in order to select their energy. The selected electrons, emerging from the last grid, are then able to hit the hemispheric fluorescent screen where the diffraction spots are revealed.

The diffraction spots are typical of the sample crystal lattice and are also used to obtain important information on the degree of surface order. If they are small, intense and well defined (with respect to the screen background), they indicate large and ordered domains. On the contrary, an high spots background indicates an electron diffusion in many directions and then the presence of a disordered lattice. The diffraction spots correspond to the positive interference of the waves. If we consider the example reported in figure II.4 b, where an electron beam with λ wavelength colliding with a mono-dimensional chain of atoms separated by a distance (a) is reported, the positive interference condition is given by the Bragg's law:

$$n\lambda = a sen\theta$$

where $n\lambda$ is an entire number of waves (n is the diffraction order) and $asen\theta$ is the inter-atomic distance projection along the propagation direction. The first diffraction order is then obtained when $sen\theta = \lambda a^{-1}$. Hence, if the value of θ is known, it's easy to get the inter-atomic distance a. The simplest way to measure θ is to put the sample at the centre of the LEED screen, so that the distance between the zero order spot (covered by the electron gun) and the first diffraction order a can be easily measured. Therefore, knowing the values of both the distance between the screen and the sample (R) and the one between the zero and first order diffraction spots (a^*) the following relation can be obtained: $sen\theta = a^*/R$, thus allowing us the calculation the a value:

$$a = \frac{R \cdot \lambda}{a^*}$$

II.1.5 Infrared Reflection Absorption Spectroscopy (IRAS)

Infrared Reflection Absorption Spectroscopy (IRAS) is an established analytical technique for the characterization of adsorbed matter and thin layers on metal surfaces. In IRAS experiments, the sample is investigated in reflection geometry under grazing incidence (typically 80°). The vibrations are generated by the interaction between the electric field held by the IR radiation and the molecules dipole moment and are allowed by a selection rule implying that the molecule dipole moment must be perpendicular to the sample surface. The IR radiation absorption by an adsorbate on a metal surface is also influenced by the metal dielectric behaviour. The sensitivity of this method can be significantly enhanced by employing the Polarization Modulation technique (PM). PM-IRAS uses the PM of the incident infrared light and is based on the predominance of p- over s-polarized light at a metal surface. Accordingly, the differential reflectance $\Delta R/R$ that is measured with PM-IRAS provides the surface vibrational spectrum while no bulk (gas phase) species are detected.

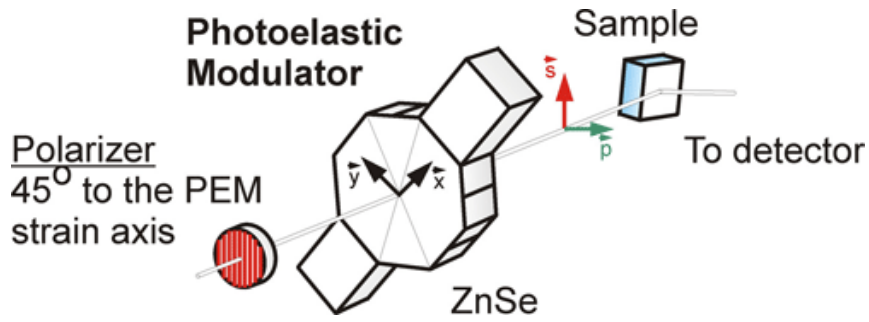

Figure II.4 A typical geometry for a PM-IRAS instrument

II.1.6 Scanning Tunneling Microscopy (STM)

Scanning Tunneling Microscopy (STM) is a powerful technique for imaging surfaces at an atomic level. This technique is based on the concept of quantum tunnelling: a conductive tip is brought close to the sample surface (ca. 1 nm) and a voltage difference (called Bias) is applied between the two, allowing electrons to tunnel through the vacuum.

The measured electron current (tunneling current) is a function of the bias, the tip position and the local density of states (LDOS) of the sample.[8] The tunnelling current is a quantum mechanical effect, with two major properties for STM: it flows between two electrodes, and even through a thin insulator or a vacuum gap and it decays on the length scale of one atomic radius. Acquiring the measured current as a function of the tip scan position it is possible to display a surface image plot. When the tip is close to the sample its movements in the three dimensions are controlled by piezoelectric devices, maintaining a tip-sample separation that is typically in equilibrium between attractive and repulsive interactions. When the tip is moved across the sample (in the x-y planes) the changes in the surface morphology and LDOS cause changes in the current that is mapped in images. There are two main way to operate with STM: either mapping the above mentioned changes in the tunneling current (constant height mode) or in the tip height (z) maintaining a constant current (constant current mode), then calibrating the z position by applying a voltage to the piezoelectric height control mechanism. In the latter operating mode variations in the images contrast are due to variations in the sample charge density.

Figure II.5 Resulution limits in a conventional STM instrument. Images of step walls and holes are distorted when their size is comparable to that of the tip apex

As already reported above, the basic physical principle of the STM method is the interaction between the scanning probe and the sample. If this interaction has a near field character, it is possible to overcome the resolution limits of far-fields techniques like microscopies (optical and SEM), which are generally in the order of half a wavelength of the photons or the electrons. However, the resolution in STM is limited by the geometrical shape of the tip. The lateral resolution thus depends on the vertical amplitude of the structures on the surface. We can imagine the probing tip as a cone with an opening angle and a finite radius at the apex. Hence, images of the surface steps with walls steeper than the tip opening angle will be distorted due to the convolution of the tip shape with the surface structure. All the holes with a diameter smaller than the tip radius will not be imaged at all or with a reduced corrugation, as it is possible to observe in figure II.5. On atomically flat surfaces or molecular layers the resolution is determined by the atomic structure of the tip apex.

The most powerful near-field interaction is the tunnelling current across a vacuum gap for two main reasons:

- the decay length is as smaller as an atomic diameter
- there are no other electrical currents, which could obscure the measurements, flowing through the vacuum.

II.2 Equipments

The experiments presented in this thesis were performed on three different UHV chambers: two are located at the University of Padova, Surface Science Laboratories, and one in Ulm, at the Institute of Surface Chemistry and Catalysis (Prof. Dr. R. J. Behm).

In Padova, the TPD experiments were performed in a multi technique UHV chamber (figure II.5 a), equipped with a 4 degree of freedom (x, y, z and polar angle θ) manipulator and the possibility to heat the sample up to 1000 K and down to 110 K, an high sensibility QMS, a four grid rear-view LEED, a double anode (Mg/Al) X ray source interfaced with a single channeltron electron hemispherical analyzer (CLAM 2), two e-beam water cooled evaporators and a cold cathode ion gun. The sample is mounted on 2 0.30 mm thick Ta wires and the temperature is measured through a welded K type thermocouple. Moreover, the QMS is covered by a glass cylinder with a small aperture facing the sample at ca. 2 mm. This setup is necessary to focus the analysis on the desorption from the sample surface, avoiding any other contribution.

The High Resolution XPS and AR-XPD experiments were performed in a multi technique UHV chamber (figure II.5 b) equipped with a 5 degree of freedom (x, y, z, polar angle θ and azimuthal angle φ) manipulator and the possibility to heat the sample up to 1000 K, a four grid rear-LEED, a double anode (Mg/Al) X ray source interfaced with a 5 channeltrons electron hemispherical analyzer, an UV radiation source (used for UPS, HeI and HeII photon excitation energies), two e-beam water cooled evaporators, a QMS for the residual gas analysis and a filament ion gun.

In Ulm, the Polarization Modulation (PM) FT-IRAS experiments were performed in a multi technique UHV chamber equipped with a 4 degree of freedom (x, y, z and polar angle θ) manipulator and the possibility to heat the sample up to 1200 K and down to 80 K, an high sensibility QMS, a 4 grid rear-LEED, a double anode (Mg/Al) X ray source interfaced with a single channeltron hemispherical electron analyzer (CLAM 2), an ion gun and two e-beam water cooled evaporators. Moreover, two IRAS cells were alternatively connected to the main UHV chamber: one UHV IRAS cell, where probe molecules adsorption was monitored in UHV keeping the sample at low temperature and an high pressure (HP) IRAS cell, where HP dosing of probe

molecules were possible thanks to the presence of O-rings and differential pumping separating the cell from the UHV apparatus.

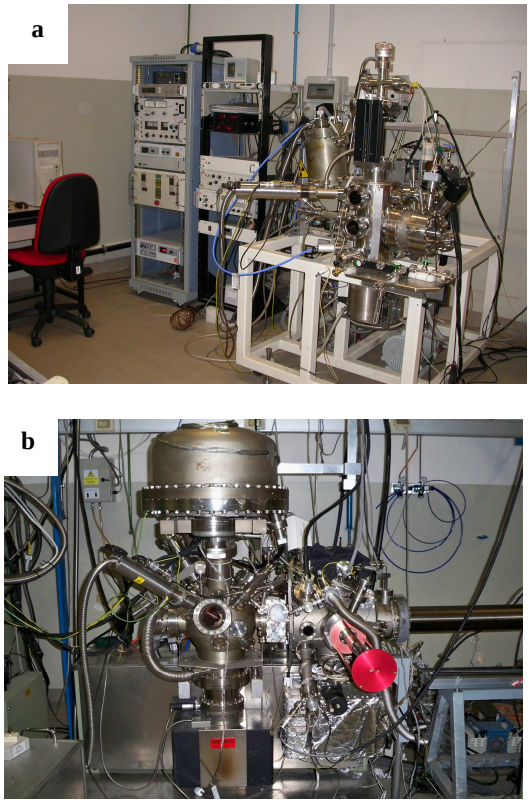

Figure II.5 (a) The TPD UHV chamber setup (Padova); (b) The HR-XPS and AR-XPD UHV chamber setup (Padova).

Other, hereafter reported, experiments were performed in collaboration with the University of Brescia (Brescia NanoLab, Dr. L. Gavioli)[9] for the model catalysts STM and during measurements beamtimes carried out at the Elettra Synchrotron facility in Trieste. In particular our user dedicated measurement times were spent at the Material Science[10] and at the BACH[11] beamlines.

References

[1] P. W. Woodruff, T. A. Delchar, *Modern Techniques in Surface Science*, Cambridge University press, New York, 1986.

[2] L. C. Feldman, J. W. Mayer, *Introduction of Surface Science and Thin Films Analysis*, Elsevier Science publishing, 1986.

[3] G. A. Somorjai, *Introduction to Surface Chemistry and Catalysis*, Wiley, New York, 1994.

[4] S.L.M.Schroeder, M.Gottfried, *Lecture Notes*, FU Berlin, 2002.

[5] C.S.Fadley, Basic Concepts of X-Ray photoelectron Spectroscopy, in Electron Spectroscopy, Theory, Techniques and Applications, Ed C.R.Brundle, A.D.Baker, Pergamon Press, 1978.

[6] G. Granozzi and M. Sambi, *Adv. Mat.*, 1996, **8**, 315.

[7] C.Davisson, L.H.Germer, *Nature* 1927, **119**, 558; *Phys. Rev.*, 1927, **29**, 908.

[8] C. J. Chen, *Introduction to Scanning Tunneling Microscopy*, Oxford University Press, 1993.

[9] http://www.dmf.unicatt.it/~gavioli/nano/

[10] http://www.elettra.trieste.it/experiments/beamlines/ms/index.html.

[11] http://www.tasc.infm.it/research/bach/scheda.php.

Section 2

TiO_x Ultrathin films on Pt (111)

Chapter III

State of the art 1: TiO_x ultrathin films on Pt (111)

III.1 Introduction: the TiO_x/Pt (111) phase diagram

Titania (TiO_2) is one of the most prominent materials for applications in technologically important areas like photo-assisted oxidation[1], heterogeneous catalysis (used both as an active catalysts as well as a support for metal catalysts),[2,3] gas sensors,[4] wastewater remediation,[5] optical devices (optical filters and optical waveguides),[6,7] antireflective coatings[8] and photovoltaic devices.[9] Since most of such peculiar properties are surface dependent, a detailed description of the surface properties of titania[10] is crucial to exploit the full potential of these systems in innovative devices. Moreover, a rapidly expanding subset of studies is focusing on the innovative properties that can be introduced when nano-dimensional titania phases are considered, e.g. nanosheets, nanotubes, nanorods and nanoclusters.[11]

Because Ti can be present in several different oxidation states, most common being Ti^{2+}, Ti^{3+} and Ti^{4+}, many different oxides (TiO_x) are observed in the nature, ranging from fully oxidized (x=2) to reduced ones ($1<x<2$).[12] The basic building block of all these oxides is a Ti centred octahedron whose connectivity with adjacent octahedra is highly variable. The most common bulk phases are TiO, Ti_2O_3 and TiO_2, which have been intensively studied, while other phases like Ti_3O_5, Ti_4O_7, Ti_5O_9, Ti_6O_{11} and Ti_8O_{15}[13,14] also exist. In addition to phases that have a well defined stoichiometry, there is a strong tendency to form non-stoichiometric phases, i.e. phases presenting a variable stoichiometry where x can vary in a limited range while maintaining the same basic structure. Another peculiarity of the reduced titania phases is the formation of the so-called Magnéli phases, formed through the creation of crystallographic shear planes.[15] However, relatively few studies have been carried

out on the investigation of their structural and electronic properties due to the difficulty of their preparation. Recently, a report has been published where the surface properties of reduced TiO_x phases and the corresponding peculiar electronic and structural properties have been discussed.[16] As in all oxides, the structure and dynamics of defects play a relevant role to tailor the properties of the titania and such aspects have been recently reviewed.[17,18] All these aspects, nanodimensionality, reduced stoichiometry and defects can be addressed by studying titania in the form of ultrathin (UT) films (the term ultrathin means a thickness in the nm range, i.e. a few monolayer). This motivates the intense activity that has been focused on the fabrication and characterization of TiO_x UT films with a large range of x values. In a recent review article, the field of UT TiO_x films on metal substrate has been discussed.[19]

Within this context, UT TiO_x films deposited on a Pt single crystal have been widely studied; the choice of the Pt substrate was originally stimulated by the promotion properties of Pt in photocatalysis[20] and by the fact that TiO_x/Pt system is a prototypical example of the strong metal support interaction (SMSI) effect.[21] These combined effects provoked a big interest in the scientific community, that tied to understand the reasons at the base of this behaviour. The Surface Science group where this thesis has been developed has given a strong contribution to the field. In the following it will be briefly summarized in order to facilitate the reader of the present thesis.

The TiO_x/Pt(111) system was first studied by Boffa *et al.* in 1995, when they have reported on the preparation and characterization (by XPS, LEED, STM and LEIS) of UT TiO_x films up to 5 ML range.[22] However, with respect to the two phases reported by Boffa, a more complex situation with plenty of different phases has been described: after a long and patient search,[23] optimized experimental conditions have been found, which revealed as effective recipes for preparing seven different almost pure (as judged by LEED and spot STM images) UT phases of TiO_x ($1.2 \leq x \leq 2$) on Pt(111). In the following discussion we will use the TiO_x formula for sub-stoichiometric phases ($1.2<x<2$) and the TiO_2 formula for the stoichiometric ones.

All the resulting phases have been characterized by different surface science techniques, i.e. photoemission from core and valence levels (including synchrotron radiation studies), LEED, PD, STM and models have been obtained by DF

calculations (see section 2.2 for the adopted theoretical framework) so that reliable stoichiometries were derived.[23, 24, 25, 26, 27, 28, 29, 30, 31]

The standard deposition method used to obtain all the titania phases is the following:

- Pt (111) surface preparation by means of Ar^+ sputtering followed by annealing cycles up to 1000 K
- Ti reactive deposition from an e-beam evaporator in a O_2 environment (typical pressure range from 10^{-7} to 10^{-5} mbar)
- annealing (in O_2 pressure or UHV depending on the phase) up to 950 K.

Depending on the amount of evaporated Ti, the temperature and the O_2 partial pressure (the guidelines are reported below) it is possible to obtain several different phases. For convenience, all the amounts of deposited Ti are expressed in equivalents monolayers (ML), where 1 ML corresponds to 1.5 x 10^{15} atoms/cm^2.

$$\text{Pt(111) + 0.4 ML Ti} \xrightarrow{823\text{K}, p_{O_2}=10^{-7}...10^{-8}\,mbar} k\text{-TiO}_x\text{/Pt(111)} \qquad \text{(II.1)}$$

$$\text{Pt(111) + 0.8 ML Ti} \xrightarrow{823\text{K}, p_{O_2}=10^{-8}\,mbar} z\text{-TiO}_x\text{/Pt(111)} \qquad \text{(II.2)}$$

$$\text{Pt(111) + 0.8 ML Ti} \xrightarrow{823\text{K}, p_{O_2}=10^{-10}\,mbar} z'\text{-TiO}_x\text{/Pt(111)} \qquad \text{(II.3)}$$

$$\text{Pt(111) + 1.0 ML Ti} \xrightarrow{973\text{K}, p_{O_2}=10^{-6}\,mbar} rect\text{-TiO}_2\text{/Pt(111)} \qquad \text{(II.4)}$$

$$\text{Pt(111) + 1.2 ML Ti} \xrightarrow{873\text{K}, p_{O_2}=10^{-7}\,mbar} w\text{-TiO}_x\text{/Pt(111)} \qquad \text{(II.5)}$$

$$\text{Pt(111) + 1.2 ML Ti} \xrightarrow{923\text{K}, p_{O_2}=10^{-10}\,mbar} w'\text{-TiO}_x\text{/Pt(111)} \qquad \text{(II.6)}$$

$$\text{Pt(111) + } \geq 2\text{ ML Ti} \xrightarrow{873\text{K}, p_{O_2}=5\cdot10^{-6}\,mbar} rect'\text{-TiO}_2\text{/Pt(111)} \qquad \text{(II.7)}$$

Each TiO_x phase has a peculiar reconstruction, which is outlined by a specific LEED pattern (phase diagram reported in picture III.1) and STM topography (phase diagram reported in picture III.2).

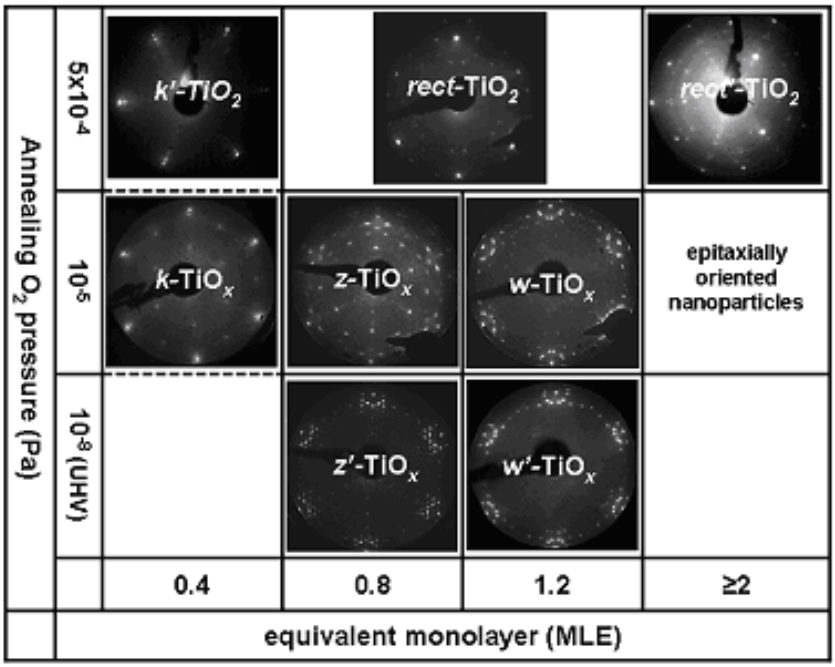

Figure II.1.

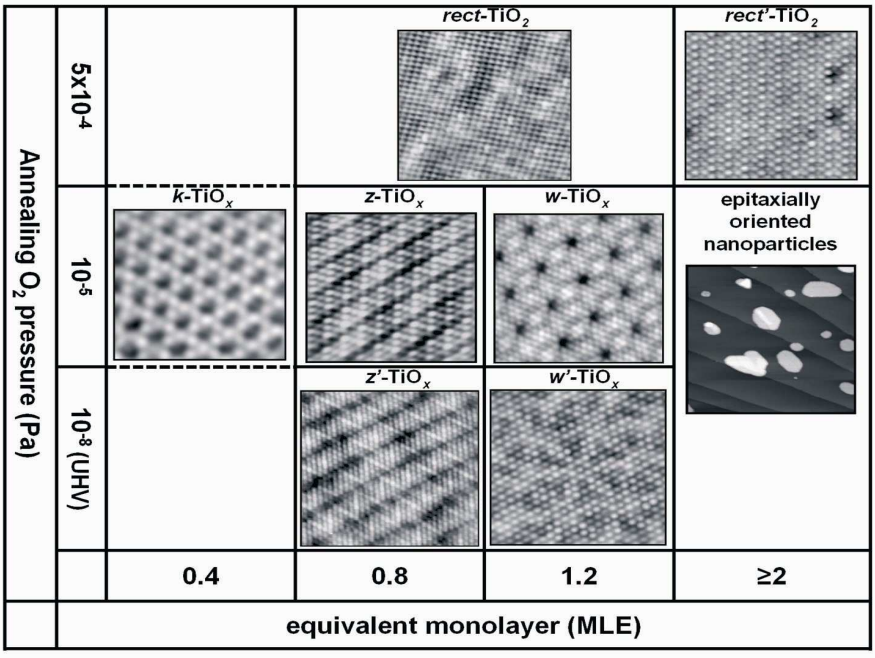

Figure II.2.

Each of the previous figures report a phase diagram where the annealing O_2 pressure is reported as a function of the amount of deposited Ti (in ML). All the different phases have been labelled basing on the structural characteristics put in light by atomically resolved STM pictures: the *k* label stands for *kagomè* (a Japanese word

which means ”bamboo basket”), *z* stands for *zig-zag*, *w* stands for *wagon-wheel* and *rect* stands for *rectangular*.

The Ti $2p_{3/2}$ and O 1s XPS line shape and binding energies have been analyzed for all the observed phases: the table reported in figure II.3 reports the BE positions of the Ti 2p core levels regarding all the possible Ti oxidation states.

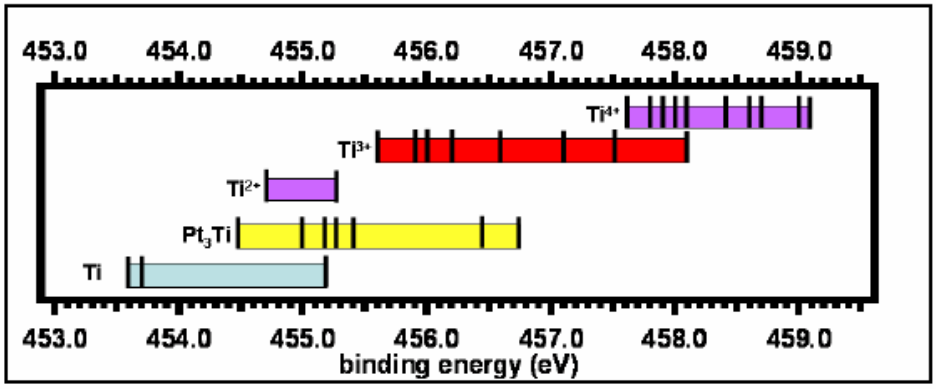

Figure III.3. Binding energy ranges for all the Ti oxidation states.

The Ti 2p peak energy ranges reported in figure III.3 take into account all the literature reports about metallic Ti, the Pt_3Ti surface alloy, the reduced Ti^{2+} states, the Ti^{3+} states and the Ti^{4+} core level components referring to TiO_2 NPs, TiO_2 single crystals and policrystalline TiO_2 films.[32,33,34,35,36, 37,38,39,40] The obtained TiO_x phases can be assembled in two major groups basing on the Ti oxidation state: reduced TiO_x phases (*z*, *z’*, *w*, *w’*and *k*) and stoichiometric TiO_2 phases (*rect* and *rect’*).

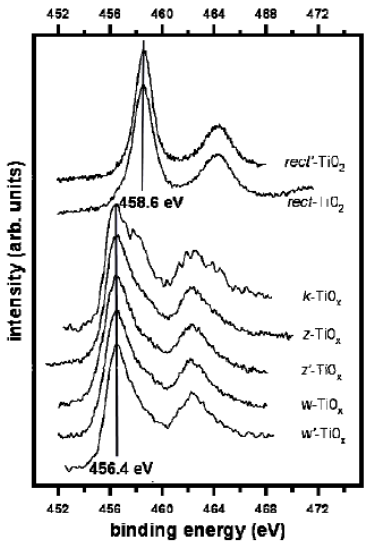

Figure III.4. XPS spectra for all the characterized TiO_x UT films

The XPS spectra reported in figure III.4 refer to all the titania phases reported before and put in evidence the two main peak components contribution: the first one, at a lower BE (about 456.5 eV), can be assigned to the reduced, three-fold coordinated Ti atoms (Ti^{3+}) and the second one, at higher BE (about 458.5 eV), can be assigned to four-fold coordinated Ti atoms (Ti^{4+}). The reduced phases obtained at higher coverages (*w'* and *w*-TiO_x) and the *k*-TiO_x might also show a higher BE contribution, due to the formation of TiO_2 clusters during the Ti reactive deposition. Nevertheless it is not easy to make a precise determination of the overall phases oxidation state, since these TiO_x phases are vertical nanostructures supported on the Pt(111) metal surface. Hence, the interaction between the metal and the substrate results in not negligible final state effects, due to reduced screening and relaxation and perturbing the shift of the BE due to chemical effects.[41]

All the TiO_x phases have also been analyzed by Angle Scanned Photoelectron Diffraction (AS-PD), since this technique is very sensitive to the short range order and then the vertical arrangement of ultrathin structures. Considering that if an ordered grid of scatterers is interposed between the emitter atoms and the detector, an intensity modulation in polar (θ) - azimuthal (φ) angles occurs while, if the emitters are located on the topmost layer, no modulation is possible, some AS-PD experiments were carried on both on the Ti 2p and on the O 1s signals. The scans, reported in figure III.5, reveal that all the reduced TiO_x/Pt (111) phases (herein we report the scans for the *w*-TiO_x phase, figure III.5(a)) are not Ti terminated: the Ti 2p azimuthal scan (APD) shows 2 clear features with a 60° periodicity. On the contrary, the APD scan based on the O 1s signal shows no modulation, thus suggesting that all the reduced TiO_x reconstructions are a bilayer, where the Ti atoms are at the interface with the Pt while the O atoms form the topmost layer.

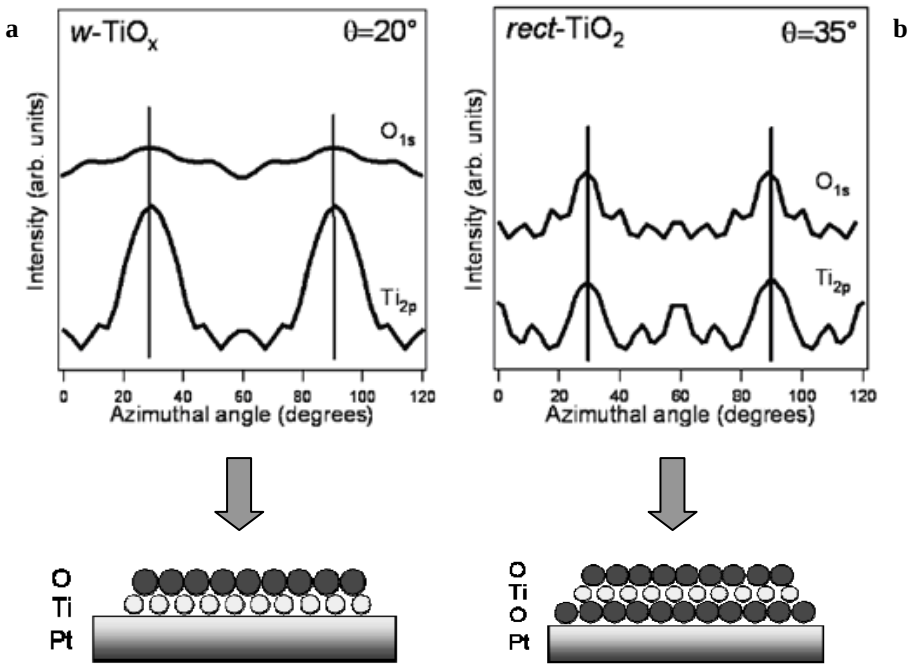

Figure III.5. APD scans for the (a) reduced w'-TiO_x UT film and (b) the stoichiometric rect-TiO_2 UT film.

If we move to figure III.5(b) it is possible to see that for a stoichimetric phase (herein we report a scan taken for the *rect*-TiO_2) both the O 1s and the Ti 2p signals are modulated with a 60° periodicity. This implies the presence of 2 oxygen layers, one in direct contact with the Pt and the other belonging to the topmost layer (the overall layout is then Pt/O-Ti-O).

The TiO_x phases used during my PhD were the reduced sub-stoichiometric *z'*-TiO_x and *w'*-TiO_x and the stoichiometric *rect*-TiO_2 and *rect'*-TiO_2. In the next paragraphs we will focus on the description of these films.

III.2 Reduced TiO_x/Pt (111) phases

III.2.1 The *z'*-TiO_x phase

The *z'*-TiO_x phase is obtained through reactive deposition at room temperature of about 0.8 ML_{eq} of Ti in an O_2 atmosphere and then annealing the system above 823 K in UHV. The phase has been characterized in deep both experimentally and theoretically.

The STM and LEED experiments have revealed that it is characterized by a commensurate superstructure with a $\begin{bmatrix} 6 & 0 \\ 3 & 6 \end{bmatrix}$ (also labelled as (6 x 3 √3)-rect) LEED pattern and with a unit cell of 16.6 x 14.4 Å.[2, 5, 7] The phase grows as a continuous film portion completely wetting the Pt substrate surface (hereafter indicated by *stripes*) and parallel dark rows (hereafter indicated as *troughs*) spaced by 14.4 Å (as it is clearly visible in figures III.6 a, b, c, d). This spacing is consistent with the short lattice constants extrapolated by LEED (figure II.6 e). The *troughs* are visible independently of the applied bias voltage and its sign. If we look the *troughs* in more detail it is possible to note that they have different sizes, so that wide and thin *troughs* (WT and TT) are present (outlined respectively with dotted rectangles and ellipses in figure III.6 a,b). Focusing on figure III.6 c it is possible to note that the phase *zig-zag* motif on the *stripes* consist of four bright protrusions (named narrow-*stripes*, NSs) and W shaped kinks. Moreover, there are some portions in the *stripes* where 5 bright protrusions are present (named as large-*stripes*, LSs) and where the kinks are both W and V shaped. Therefore, if we focus on the WTs, the high resolution STM images (III.6 c, d) show a series of elliptical black features with alternating orientations, with no long range periodicity, so that the WTs appearance is wavy. The circles in fig III.6 c outline some larger round holes inside the WT, whose density, together with the other elliptical features, strongly depends on the duration of the phase annealing procedure. A longer post-annealing time, as the one reported in figure III.6 d, creates a smaller amount of elliptical and round holes, converting the WTs in NTs, and at the same time the amount of LSs and alternating W and V shaped kinks is strongly increased.

Theoretical density functional (DF) calculations were performed to obtain a model for the *z'*-TiO_x phase in agreement with the previously reported experimental

evidences. Assuming that the phase is a Ti-O monolayer where Ti atoms are at the interface with the Pt and O atoms form the topmost layer, a natural arrangement for the Ti layer might continue the fcc stacking of the Pt(111) substrate. However, the optimal lattice parameter of such titania phase is between 2.9 and 3.3 Å,[9] thus larger than that of the Pt (111) (2.775 Å). This problem can be solved with the creation of denser Ti (*stripes*) separated by less dense regions (*troughs*), while the oxygen topmost layer forms dislocation lines within the *stripes* in order to solve the crowding problems. The dislocation lines are formed by 4-fold oxygen coordinated Ti atoms (Ti_4, more positively charged) separating triangles of 3-fold oxygen coordinated Ti (Ti_3).

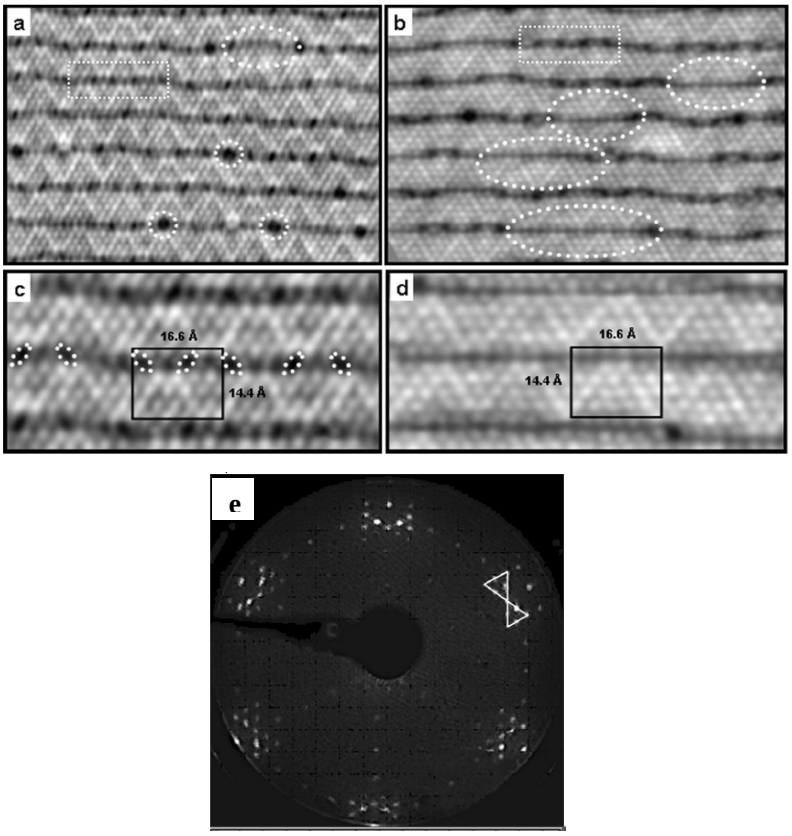

Figure III.6.(a) Large scale 140 x 100 Å^2, V=0.8 V, I=1.5 nA after 30' annealing at 673 K, (b) 150 x 100 Å^2, V=0.6 V, I=1.6 nA after 110 min annealing at 673 K and (e) LEED pattern

The different charge in Ti_4 and Ti_3 reflects in their density of empty electronic states above the Fermi energy and explains the appearance of the *zig-zag* like motif in the STM images.[9] DF calculations were performed in order to provide a model in tune with the STM images both for the *stripes* and the *troughs* and the final results fits

well with the experimental (figure III.7). The best agreement between the simulated and the experimental structure has been found using a O:Ti ratio of 1.25 (figure III.7 a), that has the lowest energy among the several tried models.

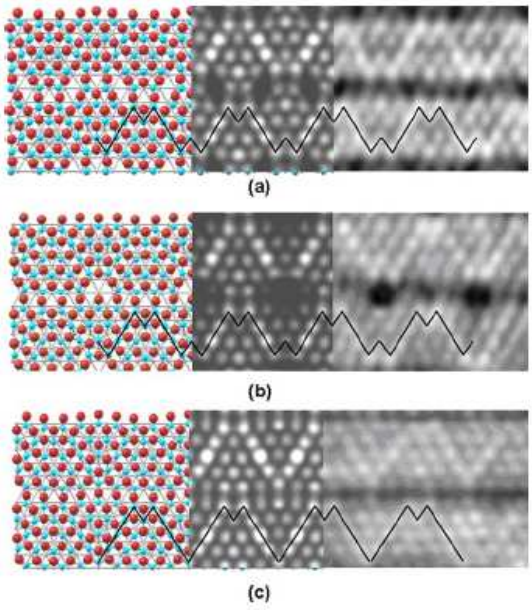

Figure III.7.Theoretical "ball and sticks" simulations, Thersoff-Hamann approximation and experimental STM images for the z'-TiO_x UT film.

The structure can be described as a NS/WT alternation where all the kinks of the *zig-zag*-like motif are W shaped. The other images (b and c) reported in figure III.7 have been calculated to fit the STM pictures taken after prolonged thermal treatments. It has been found that the elliptical black features, which are clearly visible in figure III.7 b, are true holes (named *picoholes*) where the underlying Pt substrate is left uncovered. The simulated structure for the STM picture taken after the longest annealing (III.7 c) has a final stoichiometry of $TiO_{1.2}$, and reproduces perfeclty the observed sequence LSs/TTs. Hence a $TiO_{1.25} \rightarrow TiO_{1.2}$ tranformation occurs after heating the system for long periods, in tune with the thermodynamical predictions of the ΔG between the two structures.

III.2.2 The *w'*-TiO_x phase

The *w'*-TiO_x phase is obtained after a Ti deposition of ca. 1.2 ML_{eq} in a reactive O_2 pressure of $1 \cdot 10^{-7}$ mbar and a subsequent annealing in UHV at about 920 K.[24] Its distinctive LEED pattern is reported in figure III.8 a and reveal the commensurate superstructure $\begin{bmatrix} 8 & 3 \\ -3 & 5 \end{bmatrix}$ or (7 x 7)R 21.8° (in the Wood notation) and an hexagonal unit cell with a periodicity of 19.4 Å. The term *w'* comes from the distinctive *wagon-wheel* motif observed through STM and clearly visible in figure II.8 b.

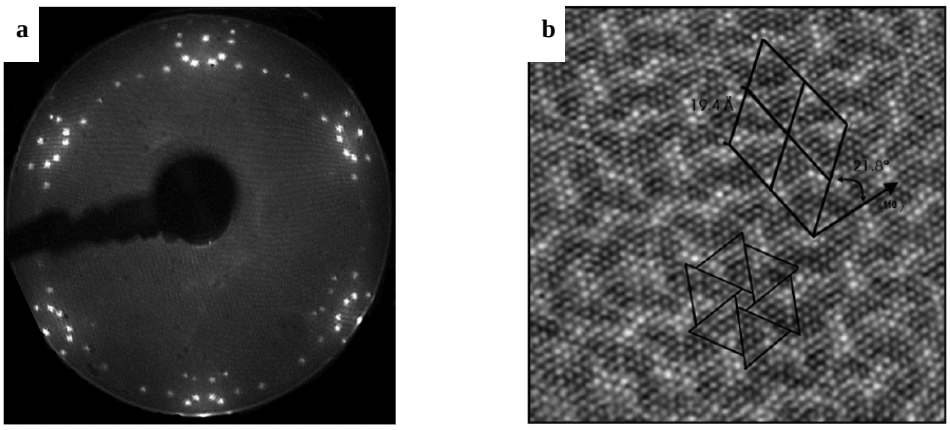

Figure III.8. (a) LEED pattern of the w'-TiO_x phase taken at 51 eV, (b) High resolution (126 x 126 Å^2; V = 0.2 V, I = 1.0 nA) STM picture of the w'-TiO_x phase.

The *w'*-TiO_x give rise to a flat and continuous film wetting the Pt (111) substrate surface. In the atomically resolved STM figure (III.8 b) it is possible to note the hexagonal unit cell (marked) and the lattice vectors fits well with the calculated LEED cell dimensions. Since also this film was found to be formed by a Ti-O layer with the Ti at the interface with the Pt, it shows the same apparent height as the one observed for the *z'*-TiO_x. The large hexagonal unit cells can be interpreted as resulting from a Moirè pattern, arising from the long range coincidence of the Pt(111) lattice with the oxide super-lattice. No theoretical calculations have been carried out until now, in order to simulate the experimental STM and LEED evidences. Nevertheless, the main difference between the *z'* and the *w'*-TiO_x is that no defect sites (round or elliptical *picoholes*) are found on the latter.

III.3 Stoichiometric TiO_2/Pt (111) phases

III.3.1 The *rect*-TiO_2 phase

The *rect*-TiO_2 phase is obtained depositing Ti in the ML_{eq} range in a reactive O_2 pressure of $5 \cdot 10^{-6}$ mbar and then annealing it up to 970 K keeping the O_2 pressure in order to avoid a partial Ti reduction. In this case, as already outlined in section III.1, the phase is a O-Ti-O layer. The interfacial oxygen make the *rect*-TiO_2 different from the reduced TiO_x phases, since a Pt/O interface is present instead of a Pt/Ti, making the interaction of the phase with the substrate weaker. The LEED pattern, reported in figure III.9 a, can be attributed to an incommensurate overlayer, having a rectangular unit cell of 3.8 x 3.0 Å^2.[8] The unit cell axes are rotated by an angle of 8.3° with respect to the principal directions of the Pt (111) substrate. Since the phase is not commensurated to the Pt (111) and is weakly interacting, no strain is expected to be present on it.

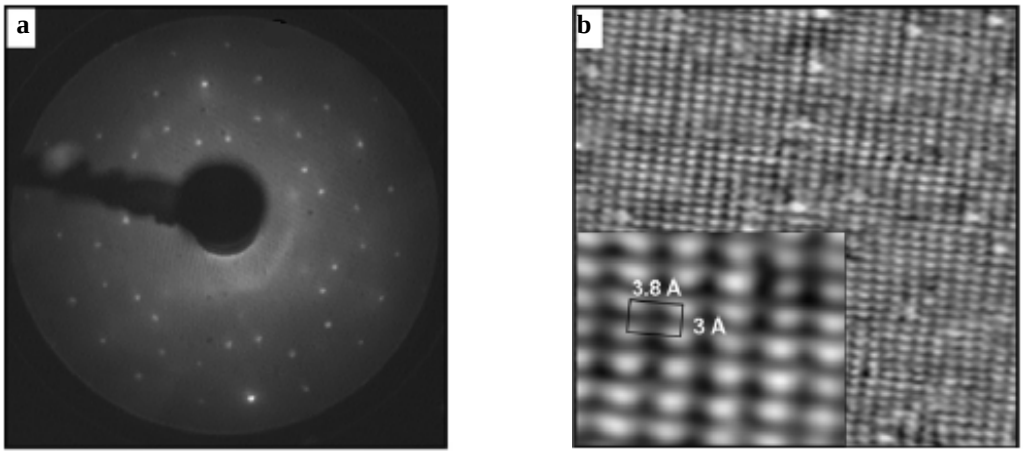

Figure III.9. (a) LEED pattern of the rect-TiO_2 phase taken at 51 eV, (b) High resolution (125 x 125 Å^2; V = 0.8 V, I = 0.9 nA) STM picture of the rect-TiO_x phase.

The rectangular unit cell is also marked on the HR-STM image, and is in complete agreement with the LEED predictions.

To furnish a complete overview of the phase structure, a complete theoretical simulation based on DF theory of it was performed.[8] All the previously reported experimental results lead to a matching between our *rect*-TiO_2 structure and a TiO_2 overlayer with a *lepidocrocite*-like structure matched to the size of the Pt (111) substrate. The best theoretical simulations and geometry optimizations were made

using an unstrained TiO_2 layer keeping the *lepidocrocite*-like structure. Since no distortions were induced in the oxide layer (all the lattice parameters were kept fixed), being the strained one not representative of our experimental data, a strain was induced in the Pt (111) metal support (see figure III.10 a).

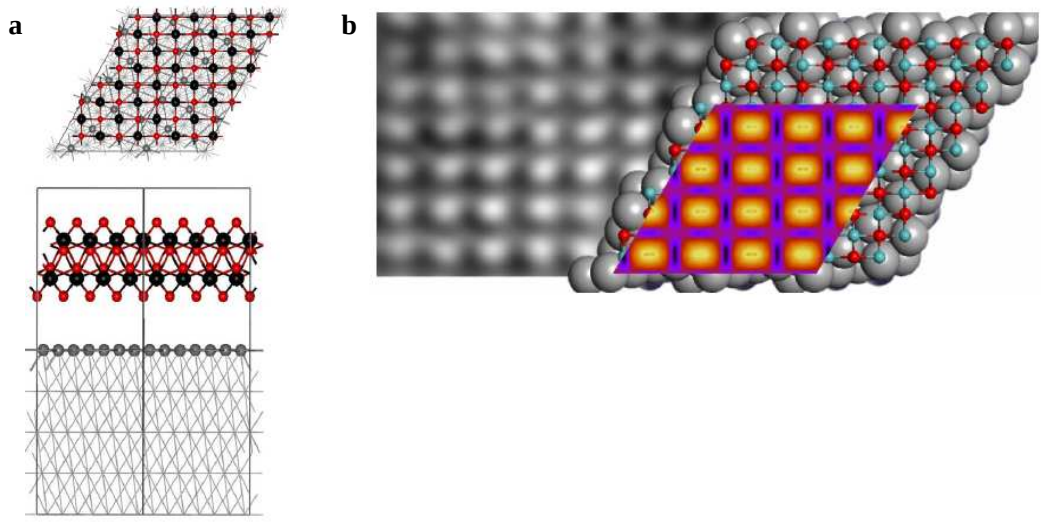

Figure III.10. (a) Top-view and side-view calculated structure of the rect-TiO_2 nanophase. Case where the Pt(111) substrate is strained, corresponding to a supercell with a1 = 7.466A ˚ , a2 = 7.116A ˚ , and an internal angle of 58.4°. (b) Simulated STM image for the rect-TiO_2/Pt(111) nanophase taken at a bias of V = +0.8 V.

This setup yields a less distorted structure than the other based on the TiO_2 overlayer strain, so that the Ti atoms are allowed to maintain the six-fold coordination while the O atoms at the interface with Pt are three-fold coordinated (a double coordination with Ti atoms and a bond with the Pt substrate). The so calculated interface distance is long (3.13 Å), so that the adhesion energy is weak.

Using the Tersoff-Hamann approximation[42] the simulated STM images were obtained using the model discussed above at a voltage of 0.8 V, the same used in the STM experiment. In figure III.10 b the bright spots correspond to the Ti 3d empty states while the dark features are due to the oxygen atoms. The match found between the experimental and the simulated images is fine.

III.3.2 The *rect'*-TiO_2 phase

The *rect'*-TiO_2 phase is obtained depositing more than 1 ML_{eq} of Ti in a reactive O_2 pressure of $5 \cdot 10^{-6}$ mbar and then annealing the system at 870 K keeping the O_2 pressure in the chamber. The LEED pattern (reported in figure III.11 a) is attributed to an incommensurate $\begin{bmatrix} 1.37 & 0.0 \\ 1.95 & 2.55 \end{bmatrix}$ overlayer and corresponds to a primitive unit cell with a a_2 = 6.3 Å and a_1 = 3.7 Å (or, alternatively a rectangular centred unit cell with 3.7 x 12.2 $Å^2$) separated by an angle of 73°.

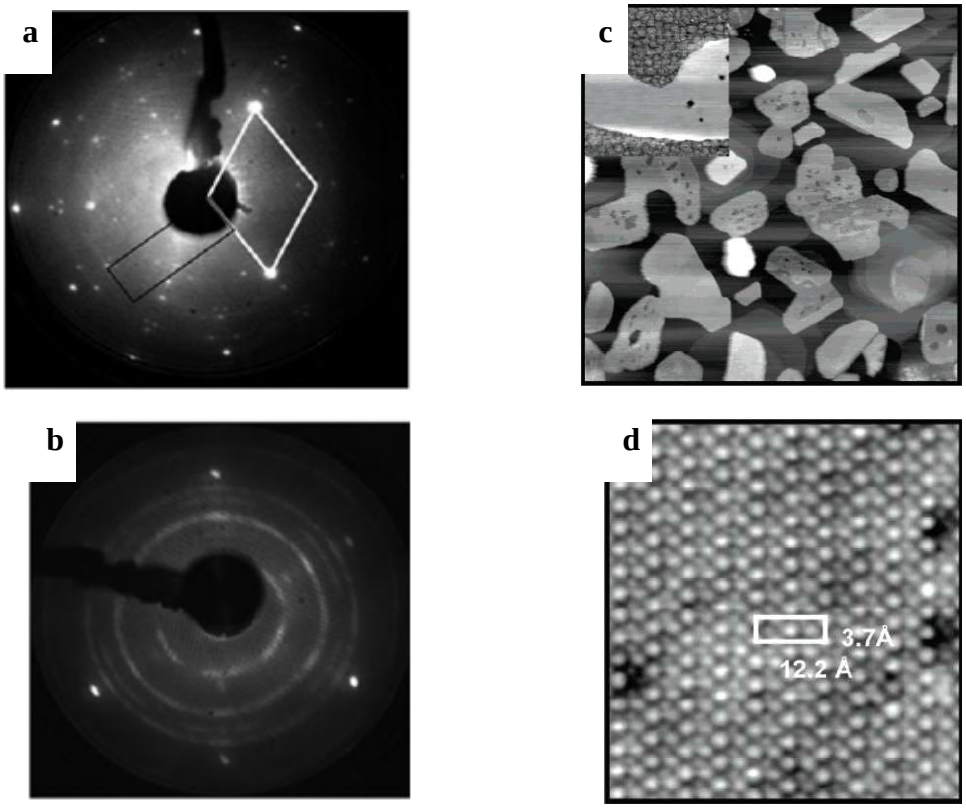

Figure III.11. (a) LEED pattern of the rect'-TiO_2 taken at 196 and (b) 50 eV corresponding to 2 different amounts of deposited Ti (resp. 2 and 11 ML_{eq}). (c) Large scale STM image of the rect'-TiO_2 growing on a wetting k-TiO_x layer (500 x 500 nm2; V = 1.2 V, I = 1.2 nA) (d) High resolution STM image of the rect'-TiO_2 (61 x 6.1 A^2; V = -0.7 V, I= 0.66 nA).

Increasing the Ti coverage, the LEED pattern changes drastically: as shown in figure III.11 b for a coverage of about 11 ML_{eq}. In this pattern, the characteristic phase

spots are substituted by concentric circles, indicating that at high coverage the unit cell lose any preferential azimuthal orientation with respect to the Pt (111) substrate.
The large scale STM picture reported in figure III.11 c shows that the *rect'*-TiO_2 phase is formed by big flat and regularly shaped islands. As long as the deposited Ti amount is increased, also the islands increase their thickness. This 3D Vollmer-Weber growth is certainly a consequence of the weak interaction between the TiO_2 and the substrate, since the overlayer is never able to totally cover the substrate and the motif of the *k*-TiO_x phase is visible all around the islands. A high resolution STM image is reported in figure III.11 d and both the primitive oblique and rectangular cells perfectly match the LEED values.
As a part of this thesis, a complete re-evaluation of the *rect'*-TiO_2 phase structure has been carried out in 2010, which will be reported in Chapter IV.

III.4 The templating effect of the *z'*-TiO_x/Pt(111) film

One of the main issues in the modern nanoscience and nanocatalysis is to obtain ordered arrays of well-defined and almost uniformly sized nanostructures, whose controlled nucleation processes and dimensions might create potentially innovative optical,[43] magnetic[44] and catalytic[45] properties. Many strategies have been developed during these years, in order to obtain such ordered arrays of nano-aggregates, e.g. by nanolithigraphic methods, by atomic manipulation through STM[46] or by size selected cluster deposition (in this case cluster ordering is more difficult to achieve).[47] Furthermore, another promising method is to obtain such ordered nanostructures by a parallel self-assembly fast process. Using long-range self-assembled structures (e.g. surface oxides, that are commonly used in many industrial applications) having ordered arrays of defects, which can act as templates for the preferential nucleation phenomenon, is one of the most simple and promising approach. This approach has been widely investigated using reconstructed single crystal metal surfaces[48] so that a large number of defects (steps, kinks, misfit dislocations, vacancies and different stacking) have been found to be templating sites for the metal-based nanostructures growth. However, such metal-based templates are far from an hypothetical real world application, since in most cases they do not survive outside the UHV conditions.

Oxide-based templates are more promising, because in many cases they can maintain their properties also in real conditions. For these purposes, metal nanoparticles (NPs) growth on templating oxide surfaces is currently an active field of research,[49,50] and many examples have been reported where oxide-based UT films act as templates for NPs[51,52,53,54] or even single atoms growth.[55] In recent years, many research groups have spent their efforts in order to investigate the effect of the NPs size and the role of the support on the catalytic activity. In particular, both the development of model systems as near as possible to the real working catalysts, and the design of new catalysts, tailored for a desired specific reaction, have been taken into consideration.[56] As an example, nano-sized Au exceptional reactivity, especially towards selective oxidation reactions (as will be widely discussed in chapter V) is a living topic of great interest in the scientific community. A real improvement in the explanation of the step processes that are at the base of such catalytic activity, could be achieved using well characterized oxide substrates acting, through the presence of ordered defects, as templates for the Au NPs growth.

Considering these evidences and using the previously reported TiO_x UT films characterized in my group as a substrate, a study has been carried on about Au NPs deposition upon them.[57] In particular, two reduced UT films, the *z'*-TiO_x and the *w'*-TiO_x, have been chosen, since they have many similarities (they are a Ti-O bilayer, where the Ti atoms are at the interface with the Pt while the O constitute the topmost layer) but, as a consequence of the slightly higher amount of Ti used to grow the *w'*-TiO_x, a different stoichiometry leading to *z'*-$TiO_{1.25}$ and *w'*-$TiO_{1.20}$. Thence dislocation lines are present on the former, where ordered arrays of defects (*picoholes* where the Pt substrate is left uncovered) are found. Such defects have demonstrated to be effective nucleation sites for the Au, leading to the formation of NPs with a narrow size dispersion and growing aligned on the phase *troughs* (figure III.12 b). On the contrary, when the Au has been deposited on the *w'*-TiO_x phase, being no preferential nucleation sites present, the NPs have grown almost randomly (figure III.12 a). This has been the first evidence of the templating effect shown by one of our well characterized TiO_x UT films. Therefore, the *z'*-TiO_x phase has been extensively used during my PhD (see Chapter VI), to determine the electronic and morphological differences between the metal NPs growing either on a templating or a not-templating substrate.

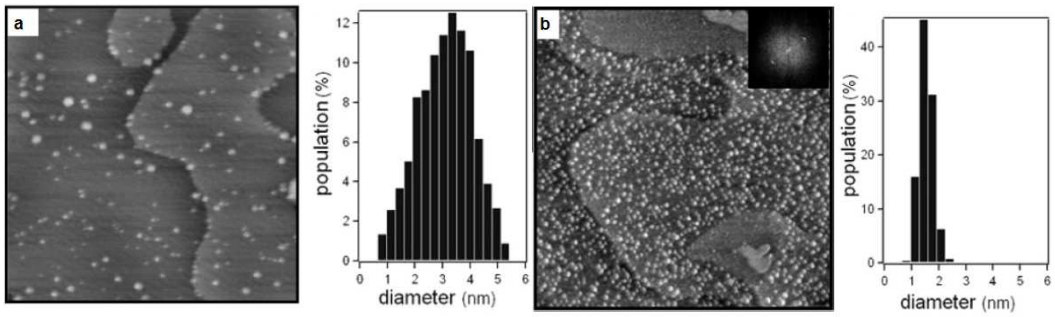

Figure III.12. STM images and corresponding histograms of the distribution of Au NPs for the (a) the Au/w'-TiO_x system (0.2 ML Au, 100 x 94 nm^2, V=1.5 V, I=0.2 nA; (b) the Au/z'-TiO_x system (0.35 ML Au, 100 x 100 nm^2, V=0.6 V, I=0.6 nA).

References

[1] C.-G. Wu, C.-C. Chao and F.-T. Kuo, Catalysis Today 2004, **97**, 103.

[2] D.W. Flaherty, Z. Dohnalek, A. Dohnalkova, B.W. Arey, D.E. McCready, N. Ponnusamy, C.B. Mullins and B.D. Kay, J. Phys. Chem. C 2007, **111**, 4765.

[3] I.N. Remediakis, N. Lopez and J.K. Norskov, Angew. Chem., Inter. Ed. 2005, **44**, 1824.

[4] M. Sanchez, R. Guirado and M.E. Rincon, J. Mater. Sci.: Mater. Electro. 2007, **18**, 1131.

[5] Y.S. Mok, J.-O. Jo and C. Woo, J. Adv. Oxid. Tech. 2007, **10**, 439.

[6] H.-Y. Zheng, H.-X. Qian and W. Zhou, Appl. Surf. Sci. 2008, **254**, 2174.

[7] A. Pillonnet, J. Mugnier, V. Le Bihan, C. Leluyer, G. Ledoux, C. Dujardin, B. Masenelli, D. Nicolas and P. Melinon, J. Luminescence 2006, **119**, 560.

[8] R. Kishore, S.N. Singh and B.K. Das, Renewable Energy 1997, **12**, 131.

[9] W.X. Que, A. Uddin and X. Hu, J. Power Sources 2006, **159**, 353.

[10] U. Diebold, *Surf. Sci. Rep.* 2003**, 48**, 53.

[11] X. Chen and S.S. Mao, Chem. Rev. 2007, **107**, 2891.

[12] G.V. Samsonov, *The Oxide Handbook* (2nd ed.) (IFI/Plenum Press, New York, 1982).

[13] J.F. Baumard, D. Panis and A.M. Anthony, J. Solid State Chem. 1977, **20**, 43.

[14] C. Picard and P. Gerdanian, J. Solid State Chem. 1975, **14**, 66.

[15] L. A. Bursill and B.G. Hyde, Prog. Solid State Chem. 1972, **7**, 177.

[16] M. Bowker, Cur. Opin. Solid State Mat. Sci. 2006, **10**, 153.

[17] M.K. Nowotny, L.R. Sheppard, T. Bak and J. Nowotny, J. Phys. Chem. C 2008, **112**, 5275.

[18] M.V. Ganduglia-Pirovano, A. Hofmann and J. Sauer, Surf. Sci. Rep. 2007, **62**, 219.

[19] Q-H. Wu, A. Fortunelli, G. Granozzi, *Inter. Rev. Phys. Chem.* 2009, **28**, 517-576.

[20] O. Carp, C. L. Huisman and A. Reller, Prog. in Solid State Chem. 2004, **32**, 33.

[21] S.J. Tauster, S.C. Fung and J. Garten, J. Am. Chem. Soc. 1978, **100**, 170.

[22] A.B. Boffa, H.C. Galloway, P.W. Jacobs, J.J. Benitez, J.D. Batteas, M. Salmeron, A.T. Bell and G.A. Samorjai, Surf. Sci. 1995, **326**, 80.

[23] F. Sedona, Ph. D. thesis, University of Padova, 2005.

[24] F. Sedona, G. A. Rizzi, S. Agnoli, F.-X. Llabre's i Xamena, A Papageorgiou, D. Ostermann, M. Sambi, P. Finetti, K. Schierbaum and G. Granozzi, *J. Phys. Chem B* 2005, **109**, 24411.

[25] G. Barcaro, S. Agnoli , F. Sedona, G.-A. Rizzi, A. Fortunelli, G. Granozzi, *J. Phys. Chem C* 2009, **113**, 5721.

[26] F. Sedona, G. Granozzi , G. Barcaro, A. Fortunelli, *Phys. Rev. B* 2008, **77**, 115417.

[27] Y. Zhang, L. Giordano, G. Pacchioni, A. Vittadini, F. Sedona, P. Finetti, G. Granozzi, *Surf. Sci.* 2007, **601**, 3488.

[28] G. Barcaro, F. Sedona, A. Fortunelli, G. Granozzi, *J. Phys. Chem. C* 2007, **111**, 6095.

[29] P. Finetti, F. Sedona, G.-A. Rizzi, U. Mick, F. Sutara, M. Svec, V. Matolin, K. Schierbaum, G. Granozzi, *J. Phys. Chem. C* 2007, **111**, 869.

[30] F. Sedona, S. Agnoli, G. Granozzi, *J. Phys. Chem. B* 2006, **110**, 15359.

[31] F. Sedona, M. Eusebio, G.-A. Rizzi, G. Granozzi, D. Ostermann, K. Schierbaum, *Phys. Chem. Chem. Phys.* 2005, **7**, 697.

[32] D. Robba, *Surf. Sci.* 1997, **380**, 311.

[33] U. Bardi, *Catal. Lett.* 1990, **5**, 81.

[34] S. Ringler, E. Janin, M. Boutonnet-Kizling, M. Goethelid, *Appl. Surf. Sci.* 2000, **190**, 162.

[35] W. Chen, L, Severin, M. Goethelid, M. Hammar, S. Cameron, J. Paul, *Phys. Rev. B.* 1994, **50**, 5620.

[36] D.-R. Jennison, O. Dulub, W. Hebenstreit, U. Diebold, *Surf. Sci.* 2001, **492**, L677.

[37] D.-F. Dwyer, S.-D. Cameron, F. Gland, *Surf. Sci.* 1985, **159**, 430.

[38] T. Matsumoto, M. Batzill, S. Hsieh, B. Koel, *Surf. Sci.* 2004, **572**, 127.

[39] Q. Guo, W.-S. Oh, D.-W. Goodman, *Surf. Sci.* 1999, **437**, 49.

[40] Z.-M. Liu, M.-A. Vannice, *Surf. Sci.* 1996, **350**, 45.

[41] F.-P. Netzer, *Surf. Rev. And Lett.* 2002, **9**, 1553.

[42] J. Tersoff, D.R. Hamann, *Phys. Rev. Lett.* 1983, **50**, 1998.

[43] E. Ozbay, *Science* 2006, **311**, 189.

[44] G. Reiss, A. Hutten, *Nat. Mater.* 2005, **4**, 725.

[45] A. T. Bell, *Science* 2003, **299**, 1688.

[46] R. Garcia, R. V. Martinez, J. Martinez, *Chem. Soc. Rev.* 2006, **35**, 29.

[47] S. Lee, S. Fan, T. Wu, S. L. Anderson, *J. Am. Chem. Soc.* 2004, **126**, 5682.

[48] H. Brune, *Surf. Sci. Rep.* 1998, **31**, 121.

[49] H. J. Freund, *Surf. Sci.* 2002, **500**, 271.

[50] W. T. Fallace, B. K. Min, D. W. Goodman, *Top. Catal.* 2005, **34**, 17.

[51] S. Degen, C. Becker, K. Wandelt, *Faraday Discuss.* 2004, **125**, 343.

[52] N. Berdunov, G. Mariotto, K. Balakrishnan, S. Murphy, I. V. Shvets, *Surf. Sci.* 2006, **600**, L287.

[53] G. Hamm, C. Becker, C. R. Henry, *Nanotechnology* 2006, **17**, 1943.

[54] K. Jordan, S. Murphy, I. V. Shvets, *Surf. Sci.* 2006, **600**, 5150.

[55] N. Nilius, E. D. L. Rienks, H. P. Rust, H. J. Freund, *Phys. Rev. Lett.* 2005, **95**, 66101.

[56] D. W. Goodman, *J. Catal.* 2003, **216**, 213.

[57] F. Sedona, S. Agnoli, M. Fanetti, I. Kholmanov, E. Cavaliere, L. Gavioli, G. Granozzi, *J. Phys. Chem. C* 2007, **111**, 8024-8029.

Chapter IV

Update on the stoichiometric *rect* and *rect'*-TiO_2 UT films

In this chapter I will attach a published paper reporting on the structural model of two different stoichiometric UT films: the *rect* and the *rect'*-TiO_2. An in deep analysis joining both experimental data (STM and LEED) and theoretical DFT simulations will be reported in order to provide a precise model of the UT films and an idea of the stability sequence of the TiO_2 polymorphs at the bottom of the nanoscale.

IV.1 Reprint of the paper: Stability of TiO_2 Polymorphs: Exploring the Extreme Frontier of the Nanoscale

ARTICLES

DOI: 10.1002/cphc.200900872

Stability of TiO_2 Polymorphs: Exploring the Extreme Frontier of the Nanoscale

Andrea Vittadini,[b] Francesco Sedona,[a] Stefano Agnoli,[a] Luca Artiglia,[a] Maurizio Casarin,[a] Gian Andrea Rizzi,[a] Mauro Sambi,[a] and Gaetano Granozzi*[a]

Dedicated to Prof. Dr. R. Jürgen Behm on the occasion of his 60th birthday

The structure of two ordered stoichiometric TiO_2 nanophases supported on Pt(111) and (1×2)-Pt(110) substrates, prepared by reactive evaporation of Ti in a high-oxygen background, is compared by discussing experimental data (i.e. low-energy electron diffraction, scanning tunneling microscopy) and density functional theory calculations. Two rectangular phases, called *rect*-TiO_2 and *rect'*-TiO_2 were obtained on both the hexagonal Pt(111) and the rectangular (1×2)-Pt(110) substrates, generally suggesting that they are weakly interacting with the substrates. The *rect*-TiO_2 phase is actually confined to a TiO_2 double layer, while the *rect'*-TiO_2 can extend up to a thickness of several layers and is obtained when higher Ti doses are evaporated. While the *rect*-TiO_2 is best described as a thickness-limited lepidocrocite-like nanosheet, growing as a single-domain-commensurate (14×4) phase on (1×2)-Pt(110) and as a six-domains-incommensurate phase on Pt(111), the thicker *rect'*-TiO_2 phase can be best described as a TiO_2*(B)* supported nanolayer (NL). This represents the first example of the TiO_2*(B)* phase in the form of a supported NL, whose properties are still largely unexplored. The important point is that, because of the weak interaction between the oxide NLs and the Pt surfaces, the substrate does not play a role in stabilizing the 2D nanostructures. Rather, it acts as a sort of lab bench where sub-nanosized titania crystallites self-assemble, so that the final NLs are representative of 2D confined titania at the bottom of the nanoscale.

1. Introduction

Titanium dioxide is a highly strategic multi-functional material of interest in areas including photocatalysis, photovoltaic cells, electronic devices, and sensors.[1] The semiconducting properties of TiO_2 are essential to accomplish these functions and several approaches have been proposed to enhance its promise by controlling its size and/or shape down to the nanometer range.[1] Actually, increasing the surface area and changing the photochemical or photophysical properties (e.g. the electron–hole recombination rate) can have a strong influence on the applications.

Titania and titanate 2D nanosheets (NSs) have recently gained great attention because they are likely to be intermediates during transformation among different titania polymorphs.[2] In addition, NSs are also interesting because they can be considered as precursors[3,4] of another important group of materials such as titania nanotubes (NTs), which in turn can be used for further assembling of nanostructured materials with different morphologies, such as boat-like, comb-like, sheet-like, leaf-like, quadrate, rhombic, and wire-like.[5]

One of the key factors for the success of NSs as building blocks in titania-based nanotechnology relies on the possibility to easily prepare large quantities of NSs by simple exfoliation of titanate in alkaline solutions.[6] However, from the point of view of the comprehension of the chemistry involved, this represents a complication because the processes occurring in solution are often rather complex. As a matter of fact, the actual structure of hydrated NSs as well as the mechanism at the origin of their self-wrapping to form NTs is still a matter of debate in the scientific community.[4,7] In addition, successful application of NSs also requires detailed information on their electronic, mechanical, and electric properties. All these considerations strongly motivate a basic study of the structure and properties of single NSs. In this context, it is of particular interest to clarify how and to what extent the 2D structures are related to standard 3D titania polymorphs (i.e. anatase, rutile and brookite).

We have recently demonstrated that a bottom-up preparative route of supported NSs, alternative to the top-down exfoliation of layered titanates, is possible by self-assembly of the constituent elements on metallic substrates, such as single-crystal Pt(111) and (1×2)-Pt(110) surfaces (for a recent overview see ref. [8]). This route offers clear advantages when a detailed characterization is the final goal, since it allows the *in-situ* application of highly advanced and informative surface science tools. In particular, we have demonstrated that under strictly

[a] *Dr. F. Sedona, Dr. S. Agnoli, Dr. L. Artiglia, Prof. M. Casarin, Prof. G. A. Rizzi, Dr. M. Sambi, Prof. G. Granozzi*
Dipartimento di Scienze Chimiche and INSTM Research Unit
University of Padova
Via Marzolo 1, 35131 Padova (Italy)
Fax: (+39) 0498275161
E-mail: gaetano.granozzi@unipd.it

[b] *Dr. A. Vittadini*
Istituto di Scienze e Tecnologie Molecolari del CNR (CNR-ISTM) and CR-INSTM "Village"
Dipartimento di Scienze Chimiche, University of Padova
Via Marzolo 1, 35131 Padova (Italy)

controlled experimental conditions with a low oxygen background, several interface-stabilized understoichiometric TiO_x ($2 > x > 1.2$) monolayers (MLs) can be prepared, which completely wet the substrate as a consequence of the presence of a direct Pt–Ti interface.[9,10] On the other hand, when a higher oxygen background is used, fully stoichiometric NSs of different thickness can be prepared, where oxygen atoms are located at the interface with the Pt substrate.[11–13]

In particular, we have already shown that a lepidocrocite-like[14] fully stoichiometric NS (named *rect*-TiO_2 according to the previously reported nomenclature) can be formed under strongly oxidative conditions ($P_{O2} = 1 \times 10^{-4}$ Pa) on both Pt(111) and (1×2)-Pt(110) surfaces:[11–13] On the former it has been found that the NS is characterized by a rectangular unit cell and that the film is incommensurate with respect to the substrate.[11] The same lepidocrocite-like structure with an almost identical unit cell has also been found in the early stages of epitaxy on (1×2)-Pt(110) under the same preparative conditions; however, in this case, the NS forms a 14×4 commensurate superstructure with respect to the substrate.[12,13]

Herein we extend the previous work to a thicker nanolayer (NL) [hereafter referred to as *rect'*-TiO_2] obtained by longer reactive deposition of Ti in an O_2 background both on the Pt(111) and (1×2)-Pt(110) surfaces, and we discuss its structure and morphology in detail, on the basis of low-energy electron diffraction (LEED), scanning tunneling microscopy (STM) experimental data and theoretical density functional theory (DFT) simulations. Moreover, the observed experimental data have been directly compared with the predictions of theoretical calculations on the self-standing NLs.[15,16] Although some photoemission spectroscopic data[17] and a short report on STM data and DFT calculations of the *rect'*-TiO_2 on Pt(111) were already reported in a preliminary letter focusing on the mobility of Au nanoparticles on *rect'*-TiO_2,[18] the complete set of LEED and STM data on the *rect'*-TiO_2 on both Pt(111) and (1×2)-Pt(110) substrates and the structural details of *rect'*-TiO_2 are reported here for the first time.

In addition, herein we also draw several general conclusions on the different NLs on Pt substrates, which lead us to discuss the stability of titania phases at the nanoscale down to the extreme region of 2D confinement. This connection between the data on supported NLs and those on unsupported titania is ultimately allowed by the weak interaction between the Pt substrate and the fully oxidized NLs, which makes the Pt substrate play the role of an almost inert physical support where titania nanostructures self-assemble.

Experimental and Computational Section

The experiments were performed in a UHV custom-designed system with a base pressure of 5×10^{-9} Pa, dedicated to STM. The substrates used were Pt(111) and Pt(110) single crystals. The Pt(111) surface was prepared by several Ar^+-sputtering (KE = 2 keV) and annealing cycles at 870 K until the C 1s signal was below the detection limit of XPS. The subsequent inspection with LEED showed a clear (1×1) diffraction pattern. The (1×2)-Pt(110) surface was prepared by repeated cycles of Ar^+ sputtering and annealing at T = 970 K with subsequent cooling down in oxygen ($p(O_2) = 5 \times 10^{-5}$ Pa) to 700 K. The cleaning cycles were repeated until a clean and well-ordered (1×2) reconstructed surface was obtained as judged by the LEED pattern. The mesoscopic morphology of (1×2)-Pt(110) surface consists of islands elongated in the $[1\bar{1}0]$ direction and characterized by varying degrees of the typical fish-scale reconstruction.[19]

The *rect*-TiO_2 and *rect'*-TiO_2 overlayers were grown in the same conditions, that is, by depositing Ti at room temperature (RT) by means of an electron beam evaporator in an oxygen partial pressure of 1×10^{-4} Pa, followed by a post-annealing treatment in the temperature range of 800–900 K and cooling down in oxygen ($p(O_2) = 1 \times 10^{-4}$ Pa) to improve the long-range order of the deposited layer, and to allow the complete oxidation of Ti. The estimated deposition rate resulting from this treatment was ≈ 0.075 nm min^{-1} of Ti, as determined by quartz microbalance calibrations. In order to maintain a unique coverage unit for both substrates and overlayers, we have adopted the definition of one monolayer equivalent (ML_{eq}) assuming the growth of an anatase TiO_2 (001) bilayer with a distance between adjacent planes of 0.24 nm (1/4 of the unit-cell dimension in the [001] direction, equal to 0.951 nm). By adopting such an assumption, the growth of a full bilayer (i.e. the one representing the *rect*-TiO_2 film) is achieved when a coverage of 2 ML_{eq} is reached. The complete oxidation of the overlayers was checked by core level photoemission.

STM images were obtained by means of an Omicron variable-temperature STM, operating in constant-current mode at RT using electrochemically etched Pt–Ir tips. The scanner was calibrated in the z-direction with respect to the step edge of a clean Pt(111) surface. For the lateral calibration the (1×2)-Pt(110) reconstructed surface was used.

DFT calculations were performed with the Quantum-ESPRESSO code (QE),[20] using the generalized-gradient approximation (GGA), adopting the Perdew–Burke–Ernzerhof exchange–correlation functional.[21] One-electron wavefunctions were expanded in plane waves, using Vanderbilt ultrasoft pseudopotentials,[22] and explicitly treating the semi-core 3s and 3p Ti electrons. For a better comparison, we took care of using a computational setup as close as possible to those already used (and tested) in previous calculations on titania bulk and surface systems.[23] Thus, we used a set of pseudopotentials developed by P. Giannozzi and M. Lazzeri, which are not part of the QE database. Furthermore, the KE cutoff for the smooth and for the augmented electron density was 25 Ry and 200 Ry, respectively, while surface Brillouin zones (SBZs) were sampled at points distributed by the Monkhorst-Pack (MP) scheme.[24] In detail, this translates into a (4×2) MP grid for the SBZ of (001)-oriented TiO_2(*B*) slabs. Doubling the density of sample points yielded differences of the order of 0.1% in the surface energies. On the other hand, due to the large size of the models, SBZs of metal-supported systems were sampled only at the Γ-point, also adopting a cold smearing to populate the one-electron levels. In all the calculations, the convergence thresholds of the residual atomic forces in the optimized structures was 0.03 eV/Å.

The equilibrium shapes of TiO_2 crystals were computed, in the spirit of the Wulff construction[25] as the interior envelope of planes normal to the vectors of the low-index stoichiometric surfaces and passing at a distance from the origin taken to be proportional to the appropriate surface energy. In the case of lepidocrocite-like TiO_2, which has an intrinsically 2D structure (one of the surfaces has practically zero energy) the equilibrium shape was determined by using only two surfaces. All the slab models of the metal-sup-

ported layers were built by assuming the theoretical ($a = 0.3957$ nm) Pt lattice constant, and by including five Pt atomic layers. Only the upper part of the slab was used to simulate the surface, while Pt atoms belonging to the two bottom layers were kept fixed in their bulk positions. The structure and the surface energies of the clean (1×1)- and (1×2)-reconstructed Pt(110) surfaces were found to be in good agreement with previous DFT calculations.[26,27] Simulated STM images were obtained within the Tersoff–Hamann approach.[28]

2. Results and Discussion

At low Ti coverages ($< 2\ ML_{eq}$) we obtain flat nanoislands of *rect*-TiO_2, which progressively enlarge their lateral sizes, while maintaining the same thickness up to a coverage of $2\ ML_{eq}$, where an almost full NS is covering the substrate. When the total coverage goes beyond $2\ ML_{eq}$, thicker nanoislands with a different structure (the *rect'*-TiO_2 phase) start to grow, which are not thickness-limited. As already mentioned in the Introduction, herein we concentrate on new data on the *rect'*-TiO_2 phase. However, as one of our main goals is also to discuss the structural evolution of the different overlayers, in order to allow the reader to follow such changes, we first briefly summarize what is already known about thickness-limited *rect*-TiO_2 NS.

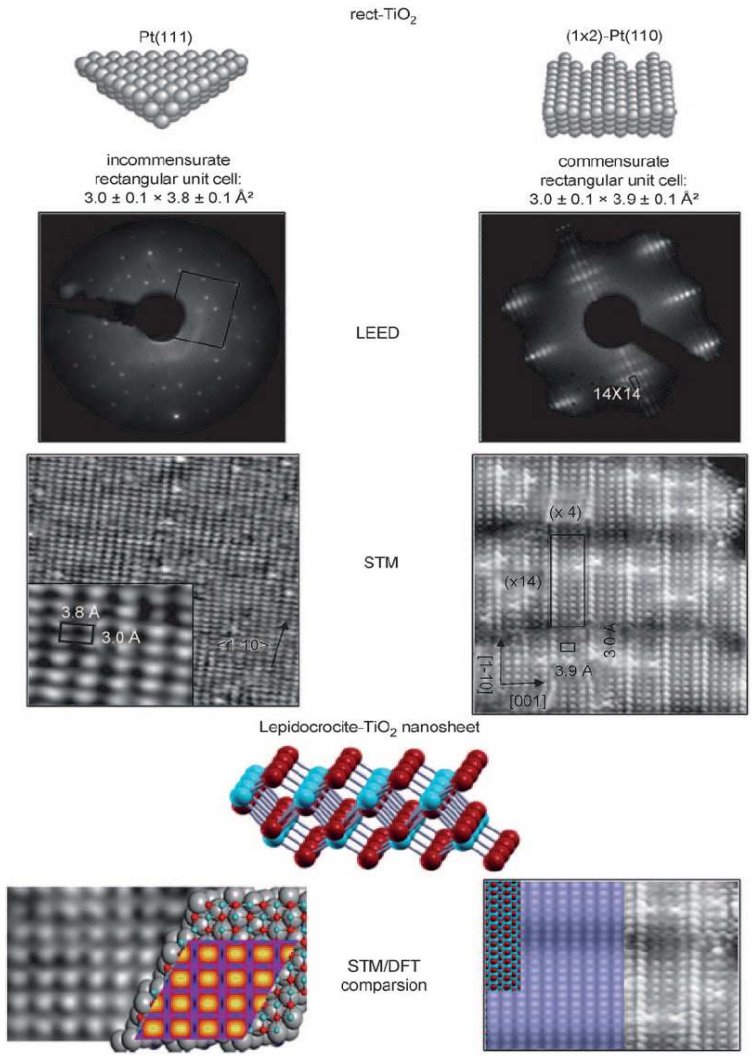

Figure 1. Summary of the most significant literature structural data[11–13] on the *rect*-TiO_2 ultrathin film on Pt(111) [left] and (1×2)-Pt(110) [right] substrates. The size of the unit cells derived by LEED are reported and compared with the corresponding high-resolution STM images. A lateral view of the lepidocrocite-like structural model derived by DFT calculations[13] is reported (oxygen: red, titanium: blue). The experimental high-resolution STM images are compared with the DFT derived simulations obtained adopting the Tersoff–Hamann model.[28]

2.1. A Thickness-Limited Nanophase: The *rect*-TiO_2 Case

Figure 1 contains the most relevant structural data (LEED, STM and DFT) so far published on the *rect*-TiO_2 system on the two Pt(111) and (1×2)-Pt(110) substrates, to be compared with the *rect'*-TiO_2 phase whose properties are described in Section 2.2. The *rect*-TiO_2 phase is observed with almost identical cell parameters (see Figure 1) both on the Pt(111)[11] and (1×2)-Pt(110)[12,13] substrates, and tends to grow as flat ad-islands on the substrate. On Pt(111), an incommensurate structure (with six different domains) is formed which can be described by the $\begin{bmatrix} 1.16 & 0.18 \\ 0.58 & 1.56 \end{bmatrix}$ matrix. On the (1×2)-Pt(110) substrate, single-domain (14×4) commensurate ad-islands are formed which almost completely cover the metallic substrates when the total coverage of $2\ ML_{eq}$ is reached. The commensurate overlayer on the (1×2)-Pt(110) substrate is due to the compatibility of the two rectangular meshes (the substrate and the oxide), and it has been interpreted as the result of a specific Ti–Pt interaction occurring at the anticoincidence sites of the oxide overlayer with the substrate.[13] A detailed angle-scanned photoelectron

CHEMPHYSCHEM

diffraction (XPD) study on the single-domain NS obtained on the (1×2)-Pt(110) substrate has provided a definitive assessment of the structural details of the NS, demonstrating a lepidocrocite-like structure.[12] DFT calculations have validated such an assignment: in Figure 1 we report the DFT-refined structural model and the comparison between the experimental and DFT-simulated STM data (for details, see the caption to Figure 1 and the references reported therein).[13] It is also interesting to compare the shape of the TiO_2 islands experimentally observed on the (1×2)-Pt(110) substrate at low coverage (1 ML_{eq}) [Figure 2] with the theoretical equilibrium shape of a

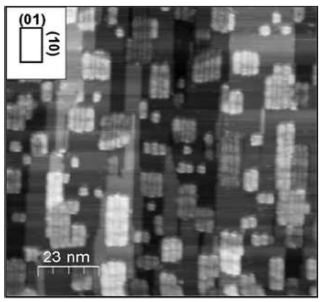

Figure 2. STM image of the *rect*-TiO_2 ultrathin film (1 ML_{eq}) on (1×2)-Pt(110) [1100×1100 Å^2, V = 1.9 V, I = 1.5 nA].[13] Rectangular islands of lepidocrocite-TiO_2 are observed whose shape is in agreement with the equilibrium shape predicted by DFT calculations (insert).

self-standing lepidocrocite-TiO_2 NS, obtained by computing by DFT its 2D-Wulff shape (Figure 2, insert). The observed correspondence lends support to the hypothesis that the substrate is weakly perturbing the oxide overlayer.

2.2. A Multilayer Nanophase: The *rect'*-TiO_2 Case

When the Ti coverage is well beyond 2 ML_{eq}, that is, above the coverage needed to prepare an almost complete lepidocrocite-TiO_2 NS, a new *rectangular* phase (named *rect'*-TiO_2) starts to appear, which can be obtained in a large interval of coverages on both Pt(111) and (1×2)-Pt(110) substrates. This phase can be described as a multilayer NS. For this reason it should be rather considered as a NL. As already mentioned in the Introduction, only preliminary data on this phase on Pt(111) have been reported so far. In the following we report and discuss the whole set of LEED and STM data relative to the *rect'*-TiO_2 NL on both the Pt(111) and (1×2)-Pt(110) substrates.

2.2.1. LEED Data

The LEED pattern (E_k = 196 eV) of the *rect'*-TiO_2 NL supported on Pt(111) is reported in Figure 3 for a coverage of 3.5 ML_{eq}. A sharp and contrasted pattern is observed, indicating the formation of sufficiently large (see STM data in Section 2.2.2) and azimuthally aligned incommensurate islands (Figure 3a). It is important to outline that in the several preparation attempts of the *rect'*-TiO_2 NL, we never observed spots to be assigned to the *rect*-TiO_2 NS. This is a strong indication for a phase transformation of the *rect*-TiO_2 NS into the new higher coverage *rect'*-TiO_2 NL under the chosen experimental conditions (800–900 K). DFT calculations are in progress in order to clarify the mechanism for this peculiar phase transition. The observed pattern can be interpreted in terms of a centred rectangular unit cell (see the real-space drawing in Figure 3b). The best fit with the experimental data is obtained using a centred unit cell with dimensions: 3.7±0.1 Å×12.2±0.1 Å. Three different domains are observed on Pt (111). However, we have found that, changing the deposition conditions, the LEED pattern of *rect'*-TiO_2 can also be obtained with a full set of rotationally equivalent domains, as indicated by the formation of characteristic bright circles (Figure 3c). In Figure 3c some spots to be assigned to a wetting layer of reduced TiO_x with a *kagomé*-like structure (*k*-TiO_x)[9] are also observed. This is in agreement with some preliminary STM data[18] (for further discussion, see Section 2.2.2).

Also in the case of the (1×2)-Pt(110) substrate we observe the formation of a distinct LEED pattern (E_k = 138 eV) [Figure 3d]. This can be explained by considering an incommensurate rectangular centred unit cell having almost the same size (3.6±0.1×12.0±0.4 Å^2) of the one found on Pt(111) [Figure 3e]. In the present case, however, because of the twofold symmetry of the substrate, only two equivalent rotated do-

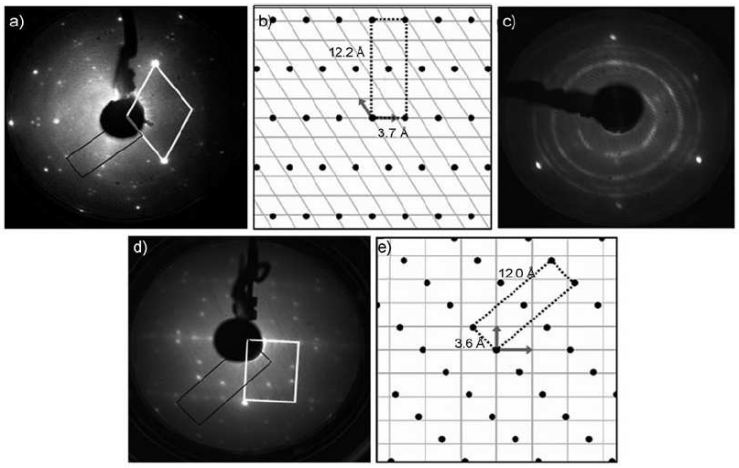

Figure 3. a) LEED pattern (E_k = 196 eV) of the *rect'*-TiO_2 ultrathin film (3.5 ML_{eq}) on Pt(111). The unit cell of the substrate (white) and of one domain of the centred rectangular supercell (black) are shown. b) Real-space superstructure of the incommensurate unit cell. c) LEED pattern (E_k = 50 eV) of the *rect'*-TiO_2 ultrathin film (10 ML_{eq}) on Pt(111) showing an azimuthal relaxation of the domains. d) LEED pattern (E_k = 138 eV) of the *rect'*-TiO_2 ultrathin film (3.5 ML_{eq}) on (1×2)-Pt(110). The unit cell of the substrate (white) and of one domain of the centred rectangular supercell (black) are shown. f) Real-space superstructure of the incommensurate unit cell.

mains are observed (see one in Figure 3d), that is, the sides of the rectangular unit cell are rotated by $\pm 45^\circ$ with respect to the [001] direction of the Pt(110) substrate. At variance with the Pt(111) substrate, on Pt(110) we have not observed the formation of azimuthally relaxed domains. Some streaking along the [001] surface is also observed, which is probably due to another low-order phase (see Section 2.2.2).

2.2.2. STM Data

Under the conditions reported in the experimental section, the formation of the *rect'*-TiO_2 NL is observed on Pt(111) for coverages >2 ML_{eq}. In Figure 4 large-scale STM images taken at

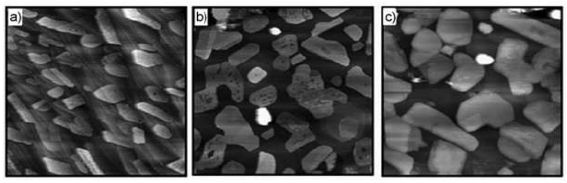

Figure 4. Large-scale STM constant-current image of the *rect'*-TiO_2 ultrathin films for a nominal coverage of a) 3.5 ML_{eq} (4700×4700 Å^2, $V=0.45$ V, $I=0.56$ nA), b) 10 ML_{eq} (4700×4700 Å^2, $V=1.2$ V, $I=1.5$ nA), c) 18 ML_{eq} (4700×4700 Å^2, $V=1.1$ V, $I=1.4$ nA).

three different nominal coverages are reported. They indicate that *rect'*-TiO_2 NL is formed by flat and regularly shaped islands, which progressively increase their lateral size and thickness as a function of the Ti coverage. This is typical Vollmer–Weber 3D growth that can be interpreted as the result of a weak interaction between the overlayer and the substrate. In agreement with the LEED pattern, it is evident that, for *high* Ti coverage as well, the overlayer does not completely cover the Pt(111) surface.

At *low* coverage (3.5 ML_{eq} in Figure 4a), the islands have an apparent step height of about 5 Å with respect to the surroundings, while for the highest coverage (18 ML_{eq} in Figure 4c) they reach an apparent height in the range of 20–25 Å. We point out here that the apparent height seen in the STM images can be associated with a real physical step only in the absence of electronic factors (typically when the step is occurring between two surfaces with the same electronic nature). This is not the case for the *rect'*-TiO_2 islands, which are seen amid a wetting layer of TiO_x (Section 2.2.1). However, it is interesting to note that, as shown in Figure 4b, the surface of the islands sometime shows ledges ca. 5 ± 1 Å deep. One can also easily observe that some islands assume an almost hexagonal shape.

As already pointed out,[18] these *rect'*-TiO_2 islands grow directly on top of the bare platinum surface and amid a reduced TiO_x wetting layer. This is a rather unexpected behaviour which is most probably due to the important role that kinetic factors can play. Very recently, Agnoli et al.[29] have reported a study where the combined use of low-energy electron microscopy (LEEM) and μ-LEED allowed the *in situ* monitoring of dynamic processes at the TiO_x/Pt(111) interface. The transformations between different phases were investigated and a general outcome of this study was that kinetic factors have a relevant role in the preparation of such ultrathin films and must be taken into account in order to explain the observed transformations. In particular, heat-induced mass transport of Ti atoms in and out of the substrate bulk has to be hypothesized to clarify some observed coverage-dependent phenomena.

In Figure 5 we report two high-resolution STM pictures, taken at opposite bias values with respect to the Fermi edge on the top of a *rect'*-TiO_2 island (3.5 ML_{eq}) having an apparent

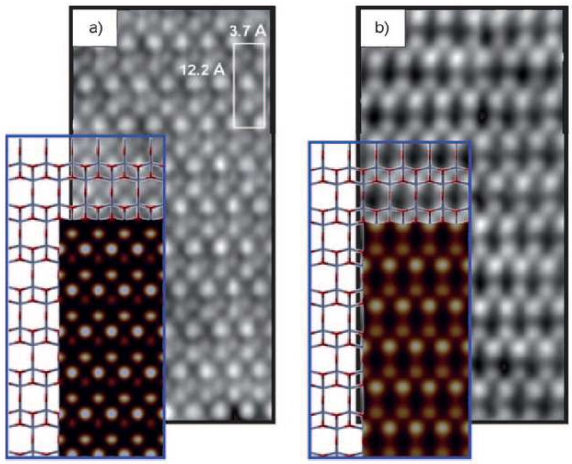

Figure 5. High-resolution STM images taken at the top of a *rect'*-TiO_2 island on Pt(111) with an apparent height of ca. 5 Å (3.5 ML_{eq}) [27×60 Å^2] with opposite bias : a) $V=-0.7$ V, $I=0.66$ nA; b) $V=0.7$ V, $I=0.66$ nA. The centred rectangular unit cell is outlined. The two insets show the projection of the surface atoms of the adopted TiO_2(*B*) slab model and the Tersoff–Hamann[28] computed STM maps at the two chosen bias values (oxygen: red, titanium: blue).

height of ca 5 Å. For both biases a centred rectangular motif can be observed, which nicely fits with the unit cell dimensions determined by LEED. Bias dependent features are seen in the two images, which points to the role of electronic effects in determining the overall STM contrast (Section 2.2.3).

Passing now to the (1×2)-Pt(110) substrate, once the coverage of 2 ML_{eq} is exceeded, some strand-like structures, running parallel to the $[1\bar{1}0]$ direction, are formed and some new regularly shaped islands can be evidenced at the same time (see Figure 6). Atomic resolution on the strand-like structure was impossible as well as the individuation of a characteristic LEED pattern (apart from streaks running parallel to the [001] direction which are spaced ×1 along the $[1\bar{1}0]$ direction). At the moment we have no well-defined model for these strongly anisotropic features. However, on the bigger islands atomic resolution has been achieved (Figure 6, inset), evidencing the distinctive motif of the *rect'*-TiO_2 phase already seen on the Pt(111) substrate and in good agreement with the unit cell and orientation determined by means of LEED. In general, these islands are 10–30 nm wide and adopt an approximately hexago-

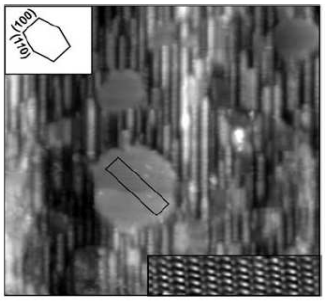

Figure 6. STM image of a 6 ML_{eq} deposit on (1×2)-Pt(110). Some randomly spaced titania strands run parallel to the $[1\bar{1}0]$ direction. Several large hexagonal islands are visible (640×640 Å^2; V=0.48 V, I=1 nA). The low right corner inset shows a high-resolution image of one of the hexagonal islands (76×18 Å^2; V=0.7 V, I=1.5 nA); the high left corner inset shows the theoretical equilibrium shape of a TiO_2(*B*) crystal oriented as indicated by the STM image.

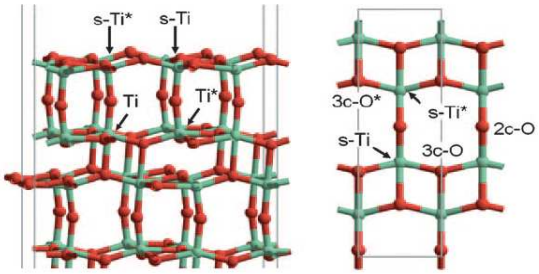

Figure 7. Model of the DFT-derived model of a relaxed (001) surface of TiO_2(*B*). Left: perspective view; right: top view.

nal shape. Moreover, they present a corrugation very similar to that observed along the surrounding titania strands. This suggests that by increasing the titania dose, some strands merge and form a first nucleus of a *rect'*-TiO_2 island, which grows in due course. It is worth mentioning, however, that it is not possible to obtain a full layer of *rect'*-TiO_2 phase on (1×2)-Pt(110). Rather, some titania strands always remain on the surface.

2.2.3. DFT Data and Structural Description

In a previous letter,[18] where the mobility of Au nanoparticles on *rect'*-TiO_2 nanoislands on Pt(111) was investigated, we preliminarily described the structure of the *rect'*-TiO_2 NL on the basis of a "pentacoordinated phase" (PP) model, uniquely made of five-fold coordinated Ti ions arranged in two Ti_2O_3 layers, where the "top" Ti ions are connected to the "bottom" ones by two-fold coordinated interlayer oxygen ions (i.e. Ti_2O_3—O_2—Ti_2O_3). Though the PP model successfully reproduces the main features of the STM images (unit cell size and symmetry, position of the spots), it fails in describing some details: for instance, STM images taken at positive bias show spots with two distinct intensities (Figure 5b), whereas the spots of the PP-based simulations are all identical.[18]

A careful re-examination of the PP structure revealed that it is nothing but a (001)-oriented slice of TiO_2(*B*), a polymorph whose bulk and surface properties have recently been investigated with DFT calculations.[30,31] Interestingly, the stability of TiO_2(*B*) is comparable to that of rutile and anatase, while its (001) surface is computed to have a low surface energy (0.40 J m^{-2}).[31] These features make the (001)-oriented TiO_2(*B*) slabs natural candidates to explain the multilayer growth of the *rect'*-TiO_2 phase. The slabs can be obtained by stacking the Ti_2O_3—O_2—Ti_2O_3 PP tri-layer units described above. It should be noted, however, that whereas in the PP model the Ti ions are all equivalent, in TiO_2(*B*)-(001) slabs two sets of Ti ions are present (see Figure 7 for the labelling): a set of six-fold coordinated (Ti) and a set of five-fold coordinated cations (Ti*) interconnected by an oxygen bridge. This makes the surface Ti cations (s-Ti) non-equivalent, as some of them (s-Ti) are connected through a second layer of oxygen to a third layer of five-fold coordinated ion (Ti*), whereas the others (s-Ti*) are connected to a third layer of six-fold coordinated ion (Ti). Consistently, three different types of O ions are also exposed at the surface (Figure 7, right): two of them are three-fold coordinated, and bridge two s-Ti ions (3c-O), and two s-Ti* ions (3c-O*), respectively. The third O surface species is two-fold coordinated, and bridges s-Ti and s-Ti* cations. It should be emphasized that though both s-Ti and s-Ti* cations are five-fold coordinated, only the former, strictly speaking, carry dangling bonds, as s-Ti* species derive from cations (Ti*) that are already five-fold coordinated in the bulk. This non-equivalence is reflected in the final relaxed structure (s-Ti ions are 0.01 Å deeper than s-Ti* ones) and in their electronic properties, giving rise to differences in the STM brightness of the spots which nicely match the experimental ones (Figure 5). Because the experimental STM images were found to be unaffected by the film thickness, in order to compare the experimental STM contrast with the theoretical one, the simulations were performed on an *unsupported* film model made of three Ti_2O_3—O_2—Ti_2O_3 tri-layer units, which gave a converged surface energy for the (001) surface of TiO_2(*B*).[31] The agreement between theoretical and experimental images is remarkable (Figure 5), for both positive and negative bias. In particular, it is found that the brightest spots observed for positive bias are associated to the (slightly) deeper s-Ti surface cations. Even stronger electronic effects are found at negative bias. In fact, spots localized at the 3c-O* species are even brighter than those at the 2c-O anions. In contrast to that, 3c-O anions are rather faint. This effect can be ascribed to the different hybridization occurring between the anions and the s-Ti/s-Ti* ions. In conclusion, both at positive and at negative bias, the STM contrast largely arises from *electronic* rather than *geometric* effects.

A further point to be addressed concerns the presence of the 5±1 Å deep ledges in Figure 4. In fact these structures can hardly derive from (001) steps, as in this case they should be 6.376 Å high. However, we point out that two stoichiometric terminations are possible for the (001) surface of TiO_2(*B*):[31] the most stable one [type (001)-I], which has been considered so far, and a titanyl-terminated one [type (001)-II], obtained by cutting the solid along a plane passing through the two-fold coordinated oxygen. The Δz between the exposed Ti cations

in a hypothetical structure where (001)-II ledges are introduced in a (001)-I terrace is 4.4 Å if relative to the bulk structure. This would be compatible with the experimental depth of the ledges, keeping also into account that whereas the cations at the (001)-I surface remain practically unrelaxed, those at the (001)-II one are instead predicted to relax inward by 0.2 Å.[31] Ultimately, the ledges could thus be described as regions where only the bottom half of the topmost PP layer has been formed.

Finally, it is also interesting to compare the shape of the large island reported in Figure 6 with the projection of the theoretically computed thermodynamic Wulff shape (note that the alignment between the crystallographic axes of the experimental and theoretical shapes is allowed by the information provided by the high-resolution STM image reported in the low-right corner inset). The agreement between the two shapes is only partial. In particular, it should be noted that the borders running parallel to the strands correspond to {010} planes are absent in the Wulff shape, and are possibly stabilized by specific interactions between the surface and the edge atoms of the overlayer island. However, weak interactions may be sufficient to achieve this result, as the energy difference between the (110) and the (010) surfaces of $TiO_2(B)$ is rather small (0.61 vs 0.69 $J\,m^{-2}$).[31]

2.2.4. Implications for the Energetics of TiO_2 Nanocrystals

We now discuss the relevance of the results described above, which refer to 2D Pt-*supported* phases, for the comprehension of the properties of 3D *unsupported* nanostructured TiO_2.

Three main bulk polymorphs (i.e. anatase, rutile and brookite) have been thoroughly investigated in the literature, and their relative energies and shapes have been demonstrated to be strongly dependent on the actual crystallite sizes. Ranade et al.[32] suggested that this can be related to the increasing weight of surface energy in determining the crystallite stability when the size is reduced. Actually, DFT calculations confirm this picture,[23,33,34] as the average surface energy of TiO_2 crystallites are predicted to decrease in the order: rutile > brookite > anatase.

Conventional studies based on the synthesis and characterization of nanocrystals in massive quantities can be difficult however, due, for example, to the effect of impurities and to the formation of multiple species. These difficulties obviously increase when we approach the extreme region of the nanoscale. On the other hand, accuracies granted by currently available density functionals do not allow one to reach clear conclusions when bulk energies and average surface energies are similar for the compared polymorphs. This is the case of TiO_2-(*anatase*) and $TiO_2(B)$, which were computed to have practically identical surface energies.[31]

Results obtained from UHV investigations on supported nanocrystals are on the other hand affected by the interfacial energy term introduced by the interaction between the nanocrystals and the support, which in principle affects the results. However, herein this seems not to be the case. In fact we observe that:

1) the formation of nanocrystals of both lepidocrocite and $TiO_2(B)$ phases occur in the same conditions on two substrate with rather different structures;
2) the shape of the nanocrystals is the same as the equilibrium one as predicted by DFT calculations (Figures 2 and 6), which also explicitly predict a weak (~0.01 eV $Å^{-2}$) overlayer–substrate interaction;
3) recent LEEM data, where the growth of the *rect*-TiO_2 NS on Pt(111) has been monitored in situ, indicate that the overlayer is rapidly expanding over the substrate by floating over its step bunches.[29]

Such evidence indicates that the Pt surface actually plays the role of a nanolab bench, where the intrinsic properties of nanocrystals can be studied. In other words, the overlayer–substrate interactions are just capable to order the overlayer domains azimuthally, but do not play a fundamental role in stabilizing the 2D nanophases. Under these fortunate circumstances we have the opportunity to monitor the growth and to determine the structure of the titania phases down to the extreme 2D nanoscale level by using the powerful tools provided by modern surface science.

The emerging picture suggests that $TiO_2(B)$ layers are actually more stable than anatase when the thickness regime up to few layers is considered, while at the bottom a lepidocrocite-like NS is preferred. On the basis of our results, we therefore propose that the complete sequence of stability to be expected on decreasing the crystal size is the one reported in Figure 8.

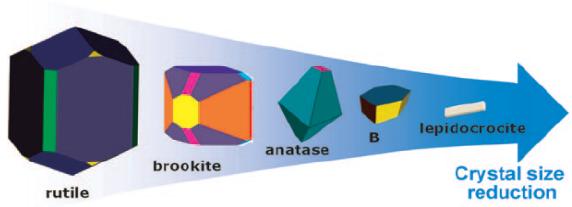

Figure 8. Stability trend of unsupported titania phases with crystal size reduction that can be inferred by comparing the results herein study with literature data.

As a closing remark, we point out that both the structures observed herein are in close relation with the anatase polymorph. As suggested on the basis of DFT calculations,[12,16] lepidocrocite-like TiO_2 NSs can be obtained from the spontaneous rearrangement of (001)-oriented anatase slabs, whereas (001)-oriented $TiO_2(B)$ layers can be formed from the rearrangement of (101)-oriented anatase slabs. This lends further support to our conjecture.

3. Conclusions

In conclusion, we have performed an integrated theoretical and experimental study on the formation of 2D TiO_2 phases supported on two different Pt surfaces. The combined use of

DFT calculations and experiments shows that, irrespective of the surface used as the support, the same TiO_2 phases are formed. In particular, nanosheets with a lepidocrocite-like structure are obtained at the beginning of the deposition process, whereas, at higher coverages, multilayer flat islands are formed, which have been identified as (001)-oriented $TiO_2(B)$ nanocrystals. The similarity of the results obtained for both Pt substrates indicates that the support plays the role of an (almost) inert observer, where the TiO_2 structures self-assemble on the basis of their intrinsic stability. On this ground, we propose that on reducing the size of TiO_2 crystallites the stability sequence of the TiO_2 polymorphs, is rutile→brookite→anatase→$TiO_2(B)$→lepidocrocite.

Acknowledgements

This work has been funded by the European Community through two STRP projects: GSOMEN and NanoChemSens within the SIXTH FRAMEWORK PROGRAMME, by the Italian Ministry of Instruction, University and Research (MIUR) through the fund PRIN-2005, project title: "Novel electronic and chemical properties of metal oxides by doping and nanostructuring" and by the University of Padova, through the grant CPDA071781. Computational resources and assistance were provided by the "Laboratorio Interdipartimentale di Chimica Computazionale" (LICC) at the Department of Chemistry of the University of Padova, and by CINECA (Bologna, Italy).

Keywords: density functional calculations · nanostructures · scanning probe microscopy · thin films · titanium dioxide

[1] X. Chen, S. Mao, *Chem. Rev.* **2007**, *107*, 2891 – 2959.
[2] M. Gateshki, S. Yin, Y. Ren, V. Petkov, *Chem. Mater.* **2007**, *19*, 2512 – 2518.
[3] R. Ma, Y. Bando, T. Sasaki, *J. Phys. Chem. B* **2004**, *108*, 2115 – 2119.
[4] A. Vittadini, M. Casarin, A. Selloni, *ACS Nano* **2009**, *3*, 317 – 324.
[5] P. Wen, H. Itoh, W. Tang, Q. Feng, *Langmuir* **2007**, *23*, 11782 – 11790.
[6] H.-H. Ou, S.-L. Lo, *Separation and Purification Technology* **2007**, *58*, 179 – 191.
[7] D. V. Bavykin, J. M. Friedrich, F. C. Walsh, *Advanced Materials* **2006**, *18*, 2807 – 2824.
[8] Q-H. Wu, A. Fortunelli, G. Granozzi, *Int. Rev. Phys. Chem.* **2009**, *28*, 517 – 576.
[9] F. Sedona, G. A. Rizzi, S. Agnoli, F. X. Llabrés i Xamena, A. Papageorgiou, D. Ostermann, M. Sambi, P. Finetti, K. Schierbaum, G. Granozzi, *J. Phys. Chem. B* **2005**, *109*, 24411 – 24426.
[10] G. Barcaro, S. Agnoli, F. Sedona, G. A. Rizzi, A. Fortunelli, G. Granozzi, *J. Phys. Chem. C* **2009**, *113*, 5721 – 5729.
[11] Y. Zhang, L. Giordano, G. Pacchioni, A. Vittadini, F. Sedona, P. Finetti, G. Granozzi, *Surf. Sci.* **2007**, *601*, 3488 – 3496.
[12] T. Orzali, M. Casarin, G. Granozzi, M. Sambi, A. Vittadini, *Phys. Rev. Lett.* **2006**, *97*, 156101 1 – 4.
[13] S. Agnoli, T. Orzali, M. Sambi, A. Vittadini, M. Casarin, G. Granozzi, *J. Phys. Chem. C* **2008**, *112*, 20038 – 20049.
[14] I. E. Grey, C. Li, I. C. Madsen, J. A. Watts, *J. Solid State Chem.* **1987**, *66*, 7 – 19.
[15] A. Vittadini, M. Casarin, A. Selloni, *Theor. Chem. Acc.* **2007**, *117*, 663 – 671.
[16] A. Vittadini, M. Casarin, *Theor. Chem. Acc.* **2008**, *120*, 551 – 556.
[17] P. Finetti, F. Sedona, G. A. Rizzi, U. Mick, F. Sutara, M. Svec, V. Matolin, K. Schierbaum, G. Granozzi, *J. Phys. Chem. C* **2007**, *111*, 869 – 876.
[18] F. Sedona, M. Sambi, L. Artiglia, G. A. Rizzi, A. Vittadini, A. Fortunelli, G. Granozzi, *J. Phys. Chem. C* **2008**, *112*, 3187 – 3190.
[19] P. Hanesch, E. Bertel, *Phys. Rev. Lett.* **1997**, *79*, 1523 – 1526.
[20] P. Giannozzi, S. Baroni, N. Bonini, M. Calandra, R. Car, C. Cavazzoni, D. Ceresoli, G. L. Chiarotti, M. Cococcioni, I. Dabo, A. Dal Corso, S. Fabris, G. Fratesi, S. de Gironcoli, R. Gebauer, U. Gerstmann, C. Gougoussis, A. Kokalj, M. Lazzeri, L. Martin-Samos, N. Marzari, F. Mauri, R. Mazzarello, S. Paolini, A. Pasquarello, L. Paulatto, C. Sbraccia, S. Scandolo, G. Sclauzero, A. P. Seitsonen, A. Smogunov, P. Umari, R. M. Wentzcovitch, *J. Phys. Condens. Matter* **2009**, *21*, 395502, 1 – 19.
[21] J. P. Perdew, K. Burke, M. Ernzerhof, *Phys. Rev. Lett.* **1996**, *77*, 3865 – 3868.
[22] D. Vanderbilt, *Phys. Rev. B* **1990**, *41*, 7892 – 7895.
[23] M. Lazzeri, A. Vittadini, A. Selloni, *Phys. Rev. B* **2001**, *63*, 155409, 1 – 9.
[24] H. J. Monkhorst, J. D. Pack, *Phys. Rev. B* **1976**, *13*, 5188 – 5192.
[25] G. Wulff, *Z. Kristallogr. Mineral.* **1901**, *34*, 449 – 530.
[26] J. I. Lee, W. Mannstadt, A. J. Freeman, *Phys. Rev. B* **1999**, *59*, 1673 – 1676.
[27] S. J. Jenkins, M. A. Petersen, D. A. King, *Surf. Sci.* **2001**, *494*, 159 – 165.
[28] J. Tersoff, D. R. Hamann, *Phys. Rev. Lett.* **1983**, *50*, 1998 – 2001.
[29] S. Agnoli, T. O. Menteş, M. A. Niño, A. Locatelli, G. Granozzi, *Phys. Chem. Chem. Phys.* **2009**, *11*, 3727 – 3732.
[30] M. B. Yahia, F. Lemoigno, T. Beuvier, J.-S. Filhol, M. Richard-Plouet, L. Brohan, M.-L. Doublet, *J. Chem. Phys.* **2009**, *130*, 204501.
[31] A. Vittadini, M. Casarin, A. Selloni, *J. Phys. Chem. C* **2009**, *113*, 18973 – 18977.
[32] M. R. Ranade, A. Navrotsky, H. Z. Zhang, J. F. Banfield, S. H. Elder, A. Zaban, P. H. Borse, S. K. Kulkarni, G. S. Doran, H. J. Whitfield, *Proc. Nat. Ac. Sci.* **2002**, *99*, 6476 – 6481.
[33] M. Ramamoorthy, RD. Vanderbilt, D. King-Smith, *Phys. Rev. B* **1994**, *49*, 7709–7715.
[34] XQ. Gong, A. Selloni, *Phys. Rev. B* **2007**, *76*, 235307.

Received: November 11, 2009
Published online on ■■ ■■, 2010

Section 3

Au Based Model Catalysts

Chapter V
State of the art 2: Au at the nanoscale

V.1 Introduction

In this chapter I will summarize on the state of the art regarding gold nanoparticles (NPs) reactivity and catalysis, especially regarding the CO oxidation. After this brief general introduction I will focus on gold surfaces, gold NPs and at the end on model catalysts.

I give first some important information on the elemental, chemical and physical properties, since there is a strong relationship between the atomic structure, the dimensions and the catalytic activity. Gold atom has a large nucleus (Z = 79) and nuclear charge; as a consequence of this, relativistic effects[1] play an important role so that the *s* and *p* orbitals are contracted, while the *d* and *f* orbitals are in fact expanded. Thereby, the *5d* band assumes a great relevance in terms of a large participation of the orbitals in the metallic bond and affects the metal behaviour (larger cohesion energy than the other transition metals). Moreover, gold has the highest Pauling electronegativity value in the group d elements (2.4), so a high electron affinity (EA) value of 2.31 eV and ionization potential (9.22 eV). Hence gold is the only transition metal that have not a stable oxide (Au_2O_3 is only metastable) and is capable to interact with itself in so an effective way that its bond is called *aurophilic*.[2]

Gold has always been considered as a noble element, and it is very difficult to adsorb any kind of molecule on its surfaces. In 1987 Masatake Haruta started to report about his studies about gold NPs, focusing on the ones with a diameter smaller than 5 nm, which showed an intense catalytic activity.[3, 4, 5, 6, 7]

Since 1987 many efforts in the surface science and catalysis research communities have been dedicated to gold NPs and the catalytic systems obtained using them.
Many common reactions demonstrated to be well catalyzed by gold:
- low temperature (LT) CO oxidation[8]
- selective oxidation of propene to propene oxide[9]
- water gas shift reaction[10]
- NO_x reduction[11]
- selective hydrogenation of poli-alkenes and alkynes.[12]

In particular, LT CO oxidation assumed an important role, as a consequence of the catalytic system application in the air purification[13] and fuel cells (prevention of CO poisoning in protonic exchange membranes).[14]
In the last 20 years the chemical properties of gold and gold-based catalysts have been extensively studied, so that it is difficult to summarize all the literature. For convenience, the reader can find more information in some complete reviews[15] and books.[16]

V.2 Chemistry of Au surfaces

The study of gold have started from the analysis of its surfaces (single crystals) chemical reactivity and then extended to the NPs, following the evolution of the nanoscience.
In 1995 Hammer and Nørskov theoretically analyzed the chemistry of dissociation of H_2 on Au(111), pointing out on 2 main factors determining the activation barrier entity and the interaction between the metal and the adsorbate.[17] First, being Au a coinage metal, it has a totally filled *d* band that originates a repulsion during the interaction with an adsorbate (such ad H_2) as a consequence of the antibonding orbital filling. The second factor, always regarding Au chemical nature, is due to the large overlap between the *s* and *d* orbitals, that leads to a high energy value demand for molecules adsorption. Starting from these assumptions, Mavrikakis et al. extended the research to other adsorbates, such as CO, O_2 and molecular oxygen.[18]
DFT calculations show that CO adsorbs preferentially on rich step surfaces, e. g. Au(211), instead of more regular ones (e.g. the large terraces on the hexagonal Au(111)), binding to under-coordinated sites through a bridge bond. Atomic oxygen

was also found to prefer stepped surfaces, while O_2 adsorbs on surface steps but with a very weak interaction that implies its desorption before any possible dissociation reaction. Hence, steps are an important parameter for a surface reactivity, especially for NPs, whose step density increases as reported in figure V.1. For convenience, in the same figure it is reported the reactivity of the Au NPs vs their dimension found by Haruta.

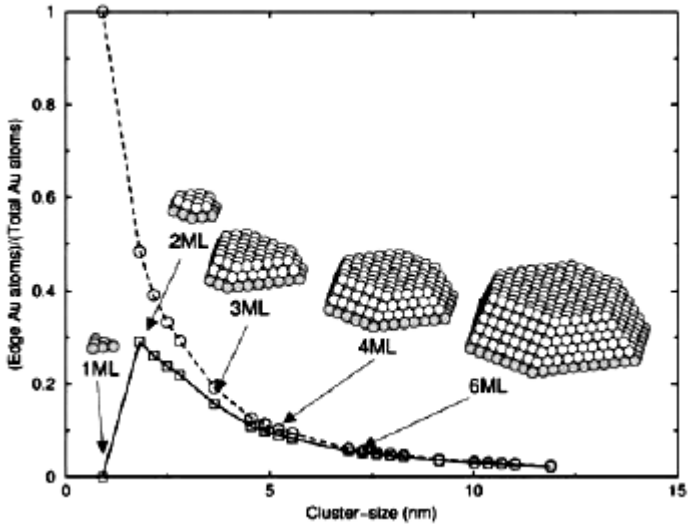

Figure V.1. Schematic representation of the step density and reactivity vs. the NPs dimensions [3-6]

Nørskov et al. obtained good theoretical results demonstrating how on Au monolayer (ML) islands a smaller amount of oxygen atoms is adsorbed than on multilayer islands. If Au is deposited on a metal substrate that induces some strain, then the reticular parameters are affected by this interaction and theoretical simulations show how in this case the interaction with some gases is enhanced (higher reactivity). An Au (211) surface with a 10% strain has a doubled binding energy towards O_2 with respect to the single crystal, causing a decrease in the activation energy (E_a) for the dissociation (from 1.12 to 0.63 eV).[19]

Mills et al. studied the O_2 adsorption on flat Au (111) surfaces and on the same islands containing islands of Au adatoms.[20] Au islands are used to induce a larger roughness on the surface, and the results put in evidence how the presence of a large number of under-coordinated Au atoms is able to induce a higher adsorption. Theoretical calculation have been used to show that an highly localized HOMO, allowing an easy charge transfer to the O_2 π^* orbitals, is able to enhance the reactivity

of rough Au surfaces. On the contrary, on flat surfaces (or anyway surfaces where large terraces are foud), the HOMO results to be de-localized and it is not possible to coordinate O_2.

Liu et al. examined the adsorption and reactivity of CO and O_2 on Au surfaces and their results show a higher reactivity on the steps than on the kinks.[21] This seems to apparently contradict what was reported before about the high reactivity of under-coordinated sites. The calculated E_a for O_2 dissociation on steps was 0.93 eV, a value which is lower than the calculated E_a on a 12 atoms NP. Then the probability to obtain O_2 dissociation on an Au (211) was calculated, leading to a value of 10^{-21} (gas considered as ideal, room temperature), that demonstrate how on single crystal Au (211) surfaces the dissociation does not take place on average. Considering that, as already reported by Mavrikakis, also the CO preferentially adsorbs on step rich surfaces, the authors finally consider the CO oxidation reaction on Au (221), based on the theoretical models already reported in the literature and involving CO and molecular oxygen coordinated to the bridge sites along step edges (figure V.2).

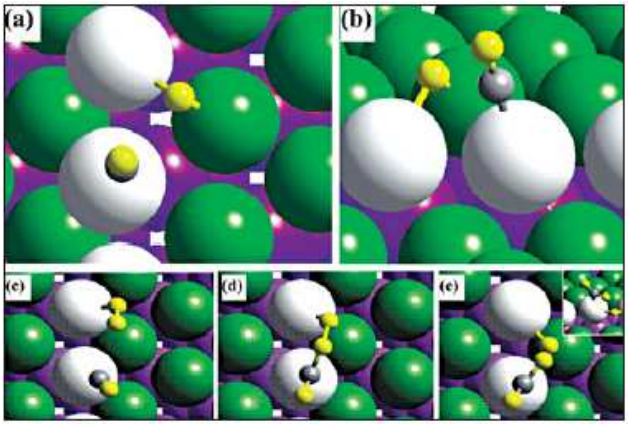

Figure V.2.Theoretical model for the CO oxidation reaction on Au(221) [34]

In the transition state, CO migrates on-top along the step edge while oxygen goes in a bridge site placed between a step and a terrace atom. The reaction leading to the final product (CO_2) has a E_a of 0.25 eV. The suggested overall reaction pathway is based on an Eley-Rideal mechanism where O_2 in the gas phase reacts with CO coordinated on a step edge, leaving on the surface an O atom available for the next cycle. The proposed E_a value for this mechanism is 0.59 eV, and reduces to 0.46 if a second adsorbed CO molecule is present, showing how the CO coverage is essential for the reaction outcome. In this last discussion both the CO adsorption and the O_2

dissociation were not correlated with the particle dimensions: all the data were based on the step density. In real catalysts the support could have a role in making the oxygen adsorption easier.

Other research groups focused their work on gold NPs shape and their interactions with different adsorbates. Using DFT calculations and ionic mobility measurements, Furche et al. stated that anionic Au_n NPs ($n \geq 11$) prefer a planar arrangement.[22] The authors also say that in the case of Au the transition between a planar and a three-dimensional arrangement is found so late as a consequence of the high relativistic nature of the metal (see V.1). Wang et al. report that small neutral Au NPs are planar up to 6 atoms, while adding more atoms a three-dimensional structure is favoured.[23] Between 10 and 14 Au atoms the energetically more stable structure is a flat cage while for NPs with more than 15 atoms a sphere is favoured. In any case it is really difficult to determine the balance structure for small dimensions NPs, especially because many transitions happen during the calculations, that are mainly due to the substrate.[24] Another interesting research topic is related to the electronic nature of bi-dimensional NPs. Zhao et al. developed some calculations on planar particles in order to determine their polarizability.[25] They found that along lateral dimensions the polarizability values result to be high (comparable to a typical metal value) although the NPs show a non-metallic behaviour along the normal direction. For bi-dimensional NPs the polarizability calculated in the normal direction is similar to a semi-conducting (like the Si) one. Theoretical calculations were then developed to foresee very large (up to 1000 atoms) NPs behaviour and different results are reported, including disordered structures[26, 27] and faceted particles.[28, 29] Of particular interest is the transition between fcc structures, which were seen for very large NPs, and decahedral-icosahedral particles, which are typical for very small particles. There are many manuscripts in the literature trying to predict the transitions in the structure of metal NPs as a function of the Au atoms content, especially because the structure seems to have strong implications for NPs reactivity.

V.3 Chemistry of Au NPs

In one of the first studies on gold catalytic activity towards CO oxidation, Huber et al.[30] report about the condensation of single gold atoms on a 1:1 matrix of CO:O_2 at 10 K. They obtain a new species, called *carbonylgold(II)peroxyformate*, decomposing after subsequent heating at 30-40 K developing CO_2. Starting from this experiment, many others research groups focused their attention on the reactivity of free Au NPs. In particular, Cox at al. report about the adsorption of D_2, CH_4 and O_2 on Au NPs with different sizes.[31, 32] They demonstrate that D_2 is well adsorbed on positively charged NPs and on neutral NPs built with 3 or 7 atoms, while negatively charged NPs are inert. CH_4 behaviour is similar to the one described for H_2, while O_2 adsorbs on cationic NPs with 10 Au atoms, on anionic NPs with an even number of Au atoms (no adsorption observed with NPs built with an odd number of Au atoms). These evidences suggest a correlation between the NPs EA and their reactivity: NPs with a high EA are more reactive towards D_2 and CH_4 whereas the ones with lower EA react with O_2. The previously mentioned relativistic effects, which cause a decrease in the energy gap between *s* and *d* orbitals, are responsible for the oscillations (up to 1.0 eV) observed in the EA between NPs with an odd or even number of Au atoms.[33] A further explanation of the interaction between the O_2 and the NPs, based on the molecular orbitals (MO) theory, has been proposed: the bond takes place between a π^* antibonding electron of the O_2 and the NP HOMO. This hypothesis could explain why O_2 adsorbs only on NPs with an odd number of atoms, whose HOMO is occupied with an unpaired electron. Salisbury et al., using a flow bed reactor, examined the adsorption of O_2 on anionic NPs with an even number of Au atoms, obtaining a fast reaction validating the MO hypothesis.[34] Moreover, the Au_n^- NPs valence band, studied by UPS, shows a clear evolution after the adsorption of O_2: the band attributed to the NPs HOMO vanishes, bearing out the charge transfer (back bonding) from the NPs to the molecules.[35] Stolcic et al. extend the study of unsupported Au NPs to aggregates with more than 20 atoms demonstrating that such larger NPs are almost inert towards O_2, most probably as a consequence of the high value of EA, that make impossible the back-bonding from the NPs to the molecules.[36]

Basing on the MO theory, it is also possible to analyze the CO interaction with Au NPs. In this case the bond takes place between the NPs LUMO, through electron

donation from the CO σ orbitals, and π back-bonding from the *d* orbitals of the Au NPs. Both of these are weak interaction, that should not depend on the NPs structure as previously seen with O_2. Wallace and Whetten reports about the adsorption of CO on anionic Au NPs obtaining, as a consequence of their interaction, the formation of some preferential products: Au_5CO, $Au_{11}CO$, $Au_{15}CO$ and $Au_{15}(CO)_2$.[37, 38] Hence, differently from what was predicted by the MO theory, also the CO seems to have a sensibility towards the Au NPs structure. The previously indicated complexes remain stable also after exposure to higher amounts of CO, thus suggesting that the NPs available active sites are already saturated at low exposures.

Probably considering what we have just reported about O_2 and CO adsorption on Au, Hagen et al. started some experiments dosing both the gases on 2 or 3 atoms Au NPs.[39] In this case, since the reaction rate between the Au and the O_2 result to be at least one order of magnitude larger than the one with CO, no formation of Au carbonyls is observed. After the formation of a $Au_3(CO)(O_2)$ complex a second molecule of oxygen adds to form $Au_3(CO)(O_2)_2$, indicating the presence of a cooperative adsorption process, O_2 and CO competing for the active bonding site. The same authors extended the work to larger NPs, showing evidences of the formation of CO_2.[40] In fact, exposing Au_6^- species to a flux of CO they created a wide distribution of complexes $[Au_6(CO)_n]^-$, that were then exposed to O_2. This results in the formation of $[Au_6(CO)_{n-1}O^-]^-$ like complexes, indirectly indicating the oxidation of one CO molecule and the formation of CO_2. A catalytic analysis of the entire process shows that the overall reaction rate is 100 times lower than the one observed with real catalysts and that in one catalytic cycle the NPs lose their activity.

In a further study, Landman et al, using an octupole mass spectrometer at the end of the reactor, report about the formation of different products exposing to CO/O_2 mixture Au_2^- NPs: Au_2^-, $Au_2O_2^-$ and $Au(CO)O_2^-$.[41] The overall reaction mechanism proposed by these authors is the following:

$$Au_2^- + O_2 \rightarrow Au_2O_2^-$$
$$Au_2O_2^- + CO \rightarrow Au_2(CO)O_2^-$$
$$Au_2(CO)O_2^- + CO \rightarrow Au_2^- + 2CO_2$$

This results allowed the first calculation of the turnover frequency (TOF) for Au_2^-. Density Functional Theory (DFT) based calculations indicated that the most stable

reaction intermediate should form as a consequence of a CO Eley-Rideal insertion in between the O-O bond in the $Au_2O_2^-$ complex, originating a carbonate like specie. Wallace et al. investigated the role of moisture on the reactivity of Au NPs, discovering that the presence of water in the reaction environment leads to the formation of Au_nOH^- complexes; the subsequent exposure to oxygen produce opposite results to the ones outlined before: anionic NPs with an odd number of atoms react well.[42] The authors explain this evidence as a consequence of the high –OH group EA, that leads to an electron transfer to the Au NPs, so that their HOMO has an unpaired electron available for bonding.

V.4 Model catalysts

Many real catalysts are based on metal supported on high surface area substrates that can be more or less inert. A common method to bypass all the problems related to the complexity of such systems is to re-create on a conductive planar surface (a metal single crystal) on an oxide thin film and then to deposit the metal onto it. The so obtained system is called planar model catalysts and allow the scientist to use common surface science techniques (XPS, STM or AFM, LEED, TPD, FT-IRAS) to analyze it. Model systems are very useful devices in studying and understanding the elemental mechanisms of catalytic processes. Surface Science techniques applied to model catalysts allow us to recover important indications about the chemical composition, morphology, reactivity and life. Many real systems have been analyzed through the creation of the corresponding model catalyst, for convenience we will focus on the titania substrate and report the main outcomes.

V.4.1 Au NPs on titania

Amongst all the Au/TiO_2 systems, the most studied is the Au deposited on TiO_2 rutile (110). One of the most complete review regarding this system has been written by Cosandey and Madey.[43] The rutile (110) surface has been deeply analyzed by STM and the results show that the (1x1) termination is formed by alternating Ti and O atoms rows, where half of the Ti atoms are linked to a bridging oxygen.[44] Hence, it is possible to find six- (like in the bulk phase) and five-fold coordinated Ti atoms and

five- (like in the bulk phase) and three-fold coordinated (bridging) oxygen atoms (see figure V.3).

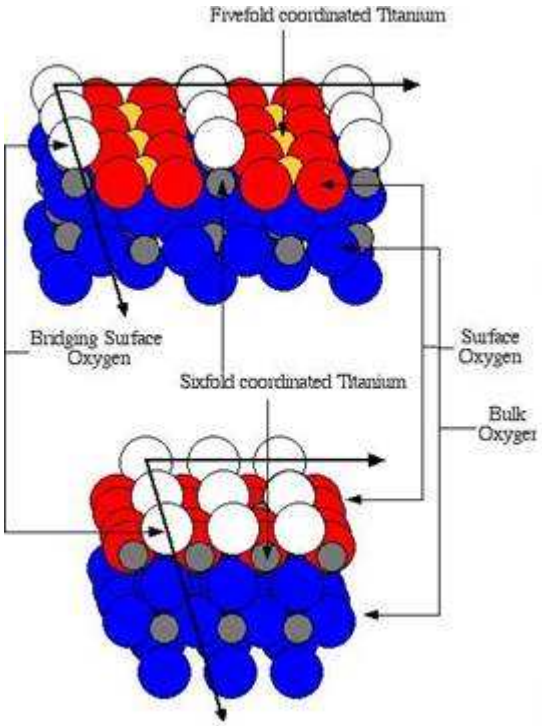

Figure V.3.[44]

It is now well established that the bridging oxygen, as a consequence of the under-coordination, are easier to remove and contribute to the creation of either point defect or F centres, depending on how the O atom is removed (O^-, O^+ or O^*). Pacchioni, through quantum-mechanic simulations, reports that after an O atom is removed from TiO_2, a charge re-distribution on the Ti ions all around the vacancy takes place, so that the five-coordinated Ti electron Binding Energies (BE) shift to more negative values with respect to the six coordinated ones.[45]

Since there is a direct connection between defects and nucleation, the TiO_2 phase preparation is fundamental for the Au NPs growth. In fact there is a real evidence that F centres act as preferential nucleation sites, making NPs more stable. Lai et al., through STM, show how at extremely low Au coverages (about 0.1 ML) the TiO_2 (110) surface appears to be without defects.[46] The suggested explanation has been associated to a preferential Au nucleation on phase defects. Several studies outlined how gold grows in 2D or quasi 2D way at low coverages (<0.15 ML) while at higher coverages the growth is three-dimensional.[46, 47] Hence, there could be a direct

correlation between the defect concentration and the NPs nucleation way. Parker et al. show how TiO_2 (110) ion bombardment produces defects that are directly related to the nucleation of gold.[48] On the clean surface, the transition from 2D to 3D growth is at ca. 0.09 ML gold coverage, while on the bombarded surface the value raise to 0.22 ML. The temperature is a second important parameter influencing the nucleation: the experiments made at 160 K on the clean surface show a 2D to 3D transition at 0.19 ML coverage, a higher value than the one reported before at room temperature (0.09 ML). These evidences show that higher temperatures promote 3D growth. A more detailed STM investigation of the correlation between Au nucleation and O vacancies on TiO_2 (110) has been proposed by Wahlström et al..[49] The amount of vacancies reduces after Au deposition, even if the metal occupies only a small part of the surface.

DFT calculations bear out the experimental evidences, putting in light that Au atoms prefer to bond to oxygen vacancies by 0.45 eV with respect to the other titania active sites. An oxygen vacancy can adsorb up to 3 metal atoms and a 2D to 3D transition is observed. There are many hypothesis regarding the preferential nucleation, and Lopez and Nørskov concluded that the coordination site depends on the Au coverage, explaining many of the obtained results.[50] Au has a weaker interaction with TiO_2 compared to other coinage metals like Cu or Ag, and this probably affect the interaction mode. An explanation could arise from the high Au electronegativity and ionization potential values, making it a poor electron donor.

Therefore, Madey et al. examined the growth and nucleation of Au on TiO_2 (110) at high coverages using high resolution (HR) SEM,[51] showing that after the deposition of a 1.5 nm (more than 5 ML thick) film of Au a new growth state begins, where the NPs form worm-like islands. Continuing the deposition, the Au island density decreases as a consequence of their coalescence, until the complete connection, which takes place at about 8 nm thickness. A further Au deposition results in a granular Au film, whose average thickness is about 12 nm. At the same time the researchers performed annealing experiments on the worm-like islands, obtaining a steady gold islands density, a parallel increase in the average thickness, a gradual islands faceting and an higher percentage of the exposed TiO_2 surface.

The last reported evidences are clearly in contrast with the annealing of small Au NPs. In that case coalescence and Ostwald ripening processes lead to a decrease in the average NPs density and an increase in their thickness. HR-SEM images obtained

during different growth steps show that many Au NPs nucleate in a semi-epitaxial way.[52, 53] Au NPs with (111) orientation are observed when Au grows on top of the bridging oxygen TiO_2 rows. Theoretical calculations demonstrate that along the TiO_2 (100) direction the reticular mismatch with Au is by 2.6%, conversely in the perpendicular direction (110) the misfit between two bridging O of a row and four deposited Au atoms along it is by 14.3%. The growth of Au (112) rows along the (110) direction has then been studied: in this configuration Au atoms lay atop five-coordinated Ti atoms, decreasing the mismatch to 8.4%. It is also interesting to report that, in disagreement with the latter calculations, a very small Au lattice distortion has been observed despite of the strain between the Au and the TiO_2 substrate. This is a clear consequence of the small overall interaction between the Au and the support, also confirmed by the XPS Ti 2p and O1s peaks that do not show any remarkable variation neither in the shape nor in the position.[54] A different behaviour has been observed growing Au on the TiO_2 anatase phase, where HREM images stress a strong epitaxial relation between the Au and the substrate, mainly due to the small misfit (0.9%) between the Au (111) and TiO_2 (112).[55] Anyway, even if theoretical simulations predicted decahedric or icosahedric shapes for small NPs, the structural relationship between the Au and the TiO_2 is strong enough to allow the NPs epitaxial growth until large dimensions,[52] both for rutile and anatase.[56] A comparison between the experimental and theoretically simulated images found the best result for strained NPs where the Au lattice constants are superimposed to the ones of the substrate. In this way, the Au(110) grows along the TiO_2(110) facet, so that the distances between the atoms are strained by 5.3% along Ti rows and expanded by 12.5% between them. This growth way continues as long as Au reaches the 4^{th} layer.

After a brief description of the nucleation and growth of Au on TiO_2 it is important to examine the thermal evolution of the systems in order to obtain important information to shift to the real catalysis world. As a consequence of the temperature increase, Au NPs are inclined to agglomeration. Edgell et al., through STM, report about a clearly visible Ostwald ripening during the annealing of Au NPs on TiO_2 (110): larger NPs grow including the smaller ones.[57] After the deposition of 0.15 ML of Au at room temperature a NPs size distribution centred at about 2.7 nm has been observed. After 7 hours heating of the surface at 750°C, the size distribution has a bimodal behaviour that is typical of a ripening process with a first peak centred at ca.

2 nm and a second one at 4 nm. The coalescence process could happen after transport or migration of Au atoms from the NPs edges. This can be related to the low melting temperature of the Au NPs. It is also very important to evaluate the Au NPs behaviour in reactive environments. Once exposed to 10 torr O_2, Au NPs deposited on TiO_2 in UHV, undergo a process similar to the previously reported Ostwald ripening.[58] After exposure to a reactive environment (10 torr, 2:1 CO/O_2), the effect is more pronounced, as reported in figure V.4. Au NPs, which at the beginning are centred at 2.6 nm with an apparent height of 0.7 nm, after exposure to a reactive environment move to 3.6 mean size diameter with an apparent height of 1.4 nm and at the same time NPs with a smaller diameter are observed (1.5 nm) giving rise to a bimodal size distribution.

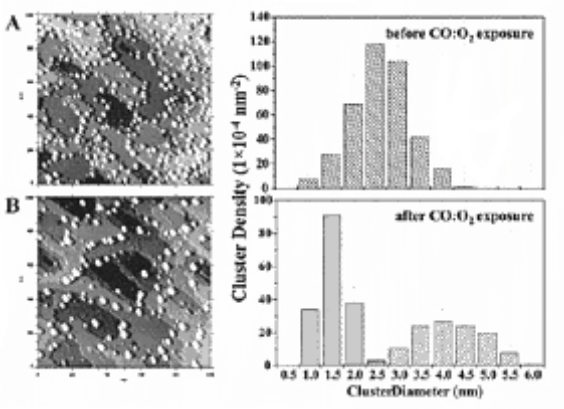

Figure V.4. STM images and Au NPs sizes profiles before and after HP exposure to $CO:O_2$ mixture[58]

Exposing larger supported Au NPs (mean diameter 4.2 nm) to 10 torr O_2 at RT no ripening was observed. This fact indicates that the Ostwald ripening process is mainly related to the NPs reactivity, although the real mechanism at the base of it is still not clear. Wilneff et al. noted that when Au_2O_3 is exposed to CO at about 400°C some not clearly identified volatile species are formed, that are able to transport the Au, since the oxide itself is not volatile.[59] If the TiO_2 (110) substrate surface is pre-functionalized with defects (O_2 vacancies produced by electron bombardment) before Au deposition, the NPs show a higher stability in an oxygen environment, most probably as a consequence of the high interaction between Au and the phase defects. An *in situ* measurement of Au NPs supported on TiO_2 (110) behaviour in reactive environment (1:1 CO/O_2) has been performed by Kolmanov and Goodman.[60, 61] At the beginning the system has a uniform size distribution but after a treatment at 720

Pa and 450 K a fast Ostwald ripening is observed. As expected, an increase in the temperature corresponds to an acceleration of the overall process. Moreover the authors affirm that O_2 acts weakening the Au-Au bond, thus promoting the NPs coalescence.

V.4.2 Electronic properties of supported Au NPs

It is noteworthy that nano-sized particles supported on oxides substrates can exhibit electronic, magnetic and optical properties different from their bulk counterparts. This is really important for gold, and many researchers believe that these changes are at the base of the Au exceptional catalytic activity. Although in many cases Au based catalysts show weak interactions with the substrate,[62] its role influence the Au electronic nature through charge transfer. Valden et al., using Scanning Tunneling Spectroscopy (STS), demonstrated that the highest activity for the system Au/TiO_2 (110) is found when the transition metal → semiconductor is observed (figure V.5).[63]

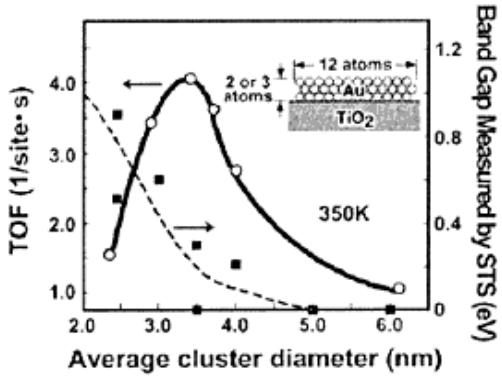

Figure V.5. Plot of the reactivity vs. the Au NP dimensions[63]

A band gap starts to be visible at about 3.2 nm diameter and 1 nm Au NPs and increases as the NPs dimensions decrease until a top value is reached at 2 nm diameter. Au NPs have a so high activity as a consequence of their small dimensions (some authors also speculate a connection with their thickness). Hence, the research for the precise point where the metal → non-metal transition is observed is very interesting.

Using XPS, Berry et al. put in light how, supporting size selected Au NPs on amorphous carbon, significant binding energy (BE) shift from the core levels value are observed for Au_n with $n<34$.[64] These shifts are related to the presence of Au

atoms with different coordination numbers. Through data extrapolation it was possible to find the limit between metallic and non-metallic NPs when the number of Au atoms corresponds to about 150. Similar experiments were performed with different spectroscopic techniques and allowed the scientists to find the NPs "limit dimension" on many substrates. A shift from the core value in the BE can be interpreted as a consequence of quantum effects due to the low particles dimensions and structure relaxation. Both of these effects are directly related to the nature of the oxide support.[65, 66] Therefore, it is important to consider that metal NPs have a high value of surface atoms that, having a lower coordination number, give raise to a shift in the *d* band with respect to the Fermi level and a parallel decrease in the core photoelectron BE. For Au this shift is by about 0.4 eV.[67]

Finally, it is necessary to consider the role of the substrate. The metal can have a different affinity with the substrate: Chusuei et al. measured the shifts in the BE in the Au 4f peak for Au NPs supported on both SiO_2 and TiO_2 pointing out big differences between the 2 systems (0.8 eV shift for Au/TiO_2 and 1.6 eV shift for Au/SiO_2).[68] These evidences suggest that Au NPs interaction with the substrate might influence their electronic properties and such BE shifts have been associated by Yang and Wu to the interaction between the Au and the O vacancies on the oxide surfaces.[69] This kind of interaction has also been observed by Howard et al. through the creation of defects on a TiO_2 (110) surface made by Ar^+ ion bombardment.[70] After the Au deposition the Ti 2p XPS peak component relative to Ti^{3+} (the phase defects) disappears, thus suggesting that these centres act as preferential nucleation sites. The charge transfer from the substrate to the NPs is then able to cause a shift in the BE that is in tune with the one observed by Valden.[63]

V.4.3 Reactivity of supported Au NPs

As reported in the previous paragraph, the surface oxide defects play a key role both for the nucleation and the electronic properties of the Au NPs. Many literature reports, using STM, focused on the surface defects characterization and their interaction with the metal particles (figure V.6).[71]

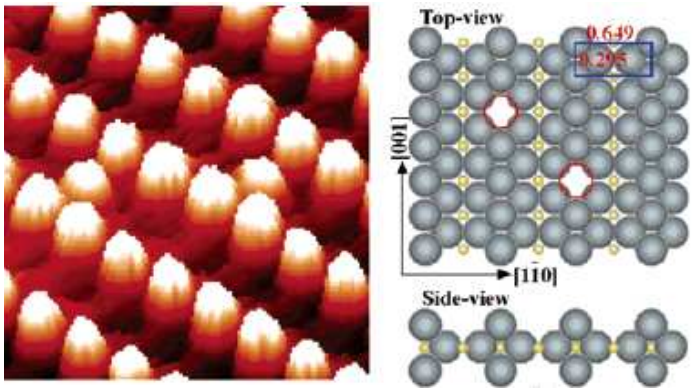

Figure V.6.[71]

In figure V.6 it is reported an STM picture of a TiO_2 (110) single crystal where the hot-spots are the five-coordinated (under-coordinated) Ti sites. The additional spots between the straight lines have been identified as oxygen vacancies (defects, outlined by circles in the right schematic picture). This kind of defects can be created after Ar^+ sputtering of the surface at low energy and it has been demonstrated that they contribute to modify the Au NPs adsorption energy, shape and structure, thence the catalytic activity.[63,71] Considering that it is very important for a catalyst to be stable, especially towards the sinterization process, many experiments focused on the achievement of substrates with nucleation sites similar to the just described ones.[72, 73]
Highly dispersed Au NPs activity towards the CO oxidation reaction is strongly related to their dimensions. Basing our discussion on the data obtained by Goodman,[63] the highest TurnOver Frequency (TOF, expressed as reaction rate by active surface site by second) value for an Au/TiO_2(110) system is obtained with a NPs average diameter by 3 nm (figure V.5). Moreover, catalytic activity has been observed just for Au NPs with a diameter size smaller than 8 nm (changing the substrate also these values can vary).
In order to summarize what was reported in this paragraph and in the previous we can speculate that 3 main parameters contribute to the exceptional Au NPs catalytic activity.
1) The presence of Au sites with a low coordination number.
Since it has been reported that the edges, corners and superficial atoms density increase as long as the NPs average sizes decrease and the catalytic activity appears only with NPs diameters less than 8 nm we can conclude that edges, corners and superficial atoms can act as active sites.[74, 75, 76] Also the calculated values for the interactions between the CO, O_2 and these active sites result to be smaller than the

ones with planar surfaces.[74, 75] DFT calculations showed that CO and O_2 molecules are adsorbed only on Au atoms with a coordination number smaller than 8.[77] The TOF, shown in figure V.5, starts to decrease under 3 nm NPs diameter and this is in tune with an increase of the Au under-coordinated exposed and available for molecules adsorption.

2) Charge transfer between Au and the substrate.

It has been already shown how the interaction with the substrate changes dramatically the Au NPs electronic structure, promoting their activity towards the CO oxidation reaction at low temperatures. The defects play a fundamental role, anchoring the NPs, making them more stable and transferring electron density to the Au.[63, 72, 73] The NPs electronic state can be analyzed using CO as a chemical probe and IRAS as an analysis technique. In this way it has been demonstrated that the CO vibrational frequency (ν_{CO}) shifts, with respect to its value for bulk Au, to smaller values for electron rich NPs and to higher ones for electron poor NPs. Au NPs were found to be electron rich in many of the analyzed systems, as a consequence of the charge transfer from the substrate to the metal, and always considering the Au chemical nature.[78, 79] These NPs effectively adsorb O_2 and can activate the O-O bond through a charge transfer that contributes to the creation of a *superoxo* specie.[80] This intermediate is stable for the Au/TiO_2 system and reacts directly with the CO to form CO_2 even if the complete dissociation of O_2 has never been observed.

3) Quantum effects due to the NPs dimensions.

NPs dimension is a fundamental parameter because it affects the electronic properties.[63, 81] Through photoemission techniques and DFT calculations, a big difference between bulk gold and a 20 atoms (taken as a model) Au NP has been outlined. As previously reported, a transition between metallic and non-metallic behaviour is observed in a NPs diameter range between 2 and 3 nm.[81] The catalytic activity is then affected by the Au NPs lateral dimensions, whose values must be between 2 and 8 nm.

References

[1] K. Pitzer, *Acc. Chem. Res*, 1979, **12**, 271.

[2] H. Schmidbaur, *Gold Bull.*, 2000, **33**, 3.

[3] M. Haruta and N. Yamada, *Chem. Lett.*, 1987, 405 – 408.

[4] M. Haruta, *Catalysis Today*, 1997, **36**, 153.

[5] M. Haruta and M. Date, *Appl. Catal. A*, 2001, **222**, 427.

[6] M. Haruta, CATTECH, 2002, **6,** 102.

[7] M. Haruta, *Chemical Record*, 2003, **3**, 75.

[8] M .Haruta, N. Yamada, T. Kobayashi and S. Lijima, *J. Catal.*, 1989, **115**, 301.

[9] T. Hayashi, K. Tanaka and M. Haruta, *J. Catal.*, 1998, **178**, 566.

[10] D. Andreeva, V. Idakiev, T. Tabakova, A. Andreev and R. Giovanoli, *Appl. Catal. A: General*, 1996, **134**, 275.

[11] A. Ueda and M. Haruta, *Gold. Bull.*, 1999, **32**, 3.

[12] G. C .Bond, P. A. Sermon, G. Webb, D. Buchanan and P. B. Wells, *J. Chem. Commun.*, 1973, 444.

[13] G. Srinivas, J. Wright, C. S. Bai and R. Cook, *Studies in Surface Science and Catalysis*, 1996, **101**, 427.

[14] T. V. Choudhary and D. W. Goodman, *Catalysis Today*, 2002, **77**, 65.

[15] (a) R. Meyer, C. Lemire, Sh. K. Shaikhutdinov and H. J. Freund, *Gold Bull.*, 2004, **37**, 72; (b) M. Haruta, *Gold Bulletin* 2004, **37**, 27; (c) A. S. K. Hashmi, *Chemical Reviews*, DOI: 10.1021/cr000436x; (d) F. Cinquini, C. Di Valentin, E. Finazzi, L. Giordano, G. Pacchioni, *Theor Chem. Acc*, 2007, **117**, 827.

[16] G. C. Bond, C. Louis, D. T. Thompson, *Catalysis by Gold*, Catalytic Science Series, Vol. 6, ed. G.J. Hutchings, Imperial College Press, 2006.

[17] B. Hammer and J. Nørskov, *Nature*, 1995, **376**, 238.

[18] M. Mavrikakis, P. Stolze and J. Norskov, *Catal. Lett.*, 2001, **64**, 101.

[19] Y. Xu and M. Mavrikakis, *J. Phys. Chem. B*, 2003, **107**, 9298.

[20] G. Mills, M. S. Gordon and H. Metiu, *J. Chem .Phys.*, 2003, **118**, 4198.

[21] Z. P. Liu, P. Hu and A. Alavi, *J. Am. Chem. Soc.*, 2002, **124**, 14770.

[22] F. Furche, R. Alrichs, P. Weis, C. Jacob, S. Gilb, T. Biereweiler and M. M. Kappes, *J. Chem. Phys.*, 2002, **117**, 6982.

[23] J. Wang, G. Wang and J. Zhao, *Phys. Rev. B*, 2002, **66**, 035418.

[24] H. Häkkinen and U. Landman, *Phys. Rev. B*, 2000, **62**, R2287.

[25] J. Zhao, J. Yang and J. G. Hou, *Phys. Rev. B*, 2003, **67**, 085404.

[26] I. L. Garzon, K. Michaelian, M. R. Beltràn, A. Posada Amarillas, P. Ordejon, E. Artacho, D. Sanchez-Portal and M. Soler, *Phys. Rev. Lett.*, 1998, **81**, 1600.

[27] I. L. Garzon, K. Michaelian, M. R. Beltràn, A. Posada Amarillas, P. Ordejon, E. Artacho, D. Sanchez-Portal and M. Soler, *Eur. Phys. J. D.*, 1999, **9**, 211.

[28] J. Li, X. Li, H. J. Zhai and L. S. Wang, *Science*, 2003, **299**, 864.

[29] O. D. Haberlen, S. C. Chung, M. Stener and N. Rösch, *J. Chem. Phys.*, 1997, **106**, 5189.

[30] H. Huber, D. McIntosh and G. Ozin, *Inorganic Chemistry*, 1977, **16**, 975.

[31] D. M. Cox, R. O. Brickman, K. Creegan and A. Kaldor, *Metal Res. Society Proceedings*, 1991, **206**, 43.

[32] D. M .Cox, R. Brickman, K. Creegan and A. Kaldor, *Z. Phis. D*, 1991, **19**, 353.

[33] K. J. Taylor, C. L. Petiette Hall, O. Cheshnovsky and R. E. Smalley, *J. Chem. Phys.*, 1992, **96**, 3319.

[34] B. E. Salisbury, W. T. Wallace and R. L. Whetten, *Chem. Phys.*, 2000, **262**, 131.

[35] Y. D. Kim, M. Fischer and G. Gantefor, *Chem. Phys. Lett*, 2003, **377**, 170.

[36] D. Stolcic, M. Fischer, G. Gantefor, Y. D. Kim, Q. Sun and P. Jena, *J. Am. Chem. Soc*, 2003, **125**, 2848.

[37] W. T. Wallace and R. L. Whetten, *J. Phys. Chem. B*, 2000, **104**, 10964.

[38] W. T. Wallace and R. L. Whetten, *European Journal of Physics D*, 2001, **16**, 123.

[39] J. Hagen, L. D. Socaciu, M. Elijazyfer, U. Heiz, T. M. Bernhardt and L. Wöste, *Phys. Chem. Chem. Phys.*, 2002, **4**, 1707.

[40] W. T. Wallace and R. L Whetten, *J. Am. Chem. Soc.*, 2002, **124**, 7499.

[41] L. D. Socaciu, J. Hagen, T. M. Bernhardt, L. Wöste, U. Heiz, H. Hakkinen and U. Landman, *J. Am. Chem. Soc*, 2003, **125**, 10437

[42] W. T. Wallace, R. B. Wrywas, R. L. Whetten, R. Mitri and V. Bona Kouteck, *J. Am. Chem. Soc*., 2003, **125**, 8408.

[43] F. Cosandey and T. Madey, *Surf. Rev. Lett.*, 2001, **8**, 73.

[44] U. Diebold, *Surf. Sci. Rep.*, 2003, **48**, 53.

[45] T. Bredow and G. Pacchioni, *Chem .Phys. Lett*, 2002, **355**, 417.

[46] X. Lai, T. P. St. Clair, M. Valden and D. W. Goodman, *Surf. Sci.*, 1998, **59**, 25.

[47] L. Zhang, R. Persaud and T. E. Madey, *Phys. Rev. B*, 1997, **56**, 10549.

[48] S. C. Parker, A. W. Grant, V. A. Bondzie and C. T. Campbell, *Surf. Sci.*, 1999, **441**, 10.

[49] E. Wahlström, N. Lopez, R. Schaub, P. Thostrup, A. Rønnau, C. Africh, E. Laegsgaard, J. K. Norskov and F. Besenbacher, *Phys. Rev. Lett*, 2003, **90**, 026101.

[50] N. Lopez and J. K. Nørskov, *Surf. Sci.*, 2002, **515**, 175.

[51] L. Zhang, F. Cosandey, R. Persaud and T. E.Madey, *Surf. Sci.*, 1999, **439**, 73.

[52] F. Cosandey, L. Zhang and T. E. Madey, *Surf. Sci*., 2001, **474**, 1.

[53] F. Cosandey and P. Stadelmann, *Mas. Res. Soc. Symp. Proc.*, 2001, **589**, 235.

[54] D. W. Goodman, *J. Phys. Chem.*, 1996, **100**, 13090.

[55] T. Akita, K. Tanaka, S. Tsubota and M. Haruta, *J. of Electron Microscopy*, 2000, **49**, 657.

[56] S. Giorgio, C. R. Henry, B. Pauwels and G. Van Tendeloo, *Materials Science and Engineering A*, 2000, **297**, 197.

[57] C. E. J. Mitchell, A. Howard, M. Carney and R. G. Edgell, *Surf. Sci.*, 2001, **490**, 196.

[58] X. Lai and D. W. Goodman, *J. Mol. Catal. A: Chem.*, 2000, **162**, 33

[59] E. A. Willneff, C. Klanner and S. L. M. Schroeder, *Chem. Commun.*, 2003, 258.

[60] A. Kolmakov and D. W. Goodman, *Catal. Letters.*, 2000, **70**, 93.

[61] A. Kolmakov and D. W. Goodman, *Surf. Sci.*, 2001, **490**, L597.

[62] A. G. Shastri, A. K. Dayte and J. Schwank, *J. Catal.*, 1984, **87**, 265.

[63] M. Valden, X. Lai and D. W. Goodman, *Science*, 1998, **281**, 1647.

[64] S. B. DiCenzo, S. D. Berry and E. H. Hartford, *Phys. Rev. B*, 1988, **38**, 8465.

[65] M. Baumer and H. J. Freund, *Prog. Surf. Sci.*, 1999, **61,** 127.

[66] P. H. Citrin and G. K. Wertheim, *Phys. Rev. B*, 1983, **27**, 3176.

[67] P. H. Citrin, G. K. Wertheim and Y. Baer, *Phys. Rev. Lett.*, 1978, **41**, 1425.

[68] C. Chusuei, X. Lai, K. Luo and D. W. Goodman, *Top. In Catal.*, 2001 **14**, 71.

[69] Z. Yang and R. Wu, *Phys. Rev. B*, 2003, **67**, 081403.

[70] A. Howard, D.N.S. Clark, C.E.J. Mitchell R.G. Egdell and V.R. Dhanak, *Surf.Sci*., 2002, **518**, 210.

[71] M. Chen and D. W. Goodman, *Surface Science*, 2004, **306**, 252-255.

[72] M.Chen, D. W. Goodman, *Surf. Sci.*, 2005, **574**, 259-268.

[73] B. K. Min, W. T. Fallace and D. W. Goodman, *J. Phys. Chem. B*, 2004, **108**, 14609-14615.

[74]N. Lopez, T. V. W. Janssens, B. S. Clausen, Y. Xu, M. Mavrikakis, T. Bligaard, J. K. Norskov, *J. Catal.*, 2004, **223**, 232-235.

[75] N. Lopez, T. V. W. Janssens, J. K. Norskov, A. Carlsson, A. Puig.Molina, B. S. Clausen, J. D. Grunwaldt, *J. Catal*, 2004, **225**, 86-94.

[76] J. D. Stiehl, T. S. Kim, S. M. McClure, C. B. Mullins, *J. Am. Chem. Soc.*, 2004, **126**, 13574-13575.

[77] N. Lopez, J. K. Norskov, *J. Am. Chem. Soc.*, 2002, **124**, 11262-11263.

[78] G. Mills, M. S. Gordon, H. Metiu, *J. Chem. Phys.*, 2003, **118**, 4198-4205.

[79] S. T. Daniells, A. R. Overweg, M. Makkee, J. A. Moulijin, *J. Catal.*, 2005, **230**, 52-65.

[80] B. Yoon, H. Hakkinen, U. Landman, *J. Phys. Chem. A*, 2003, **107**, 4066-4071.

[81] Y. Maeda, M. Okumura, S. Tsubota, M. Kohyama, M. Haruta, *Appl. Surf. Sci.*, 2004, **222**, 409-414.

Chapter VI

Results on the Au/TiO_x/Pt(111) model catalysts

In this chapter I will report on the work done on the Au/TiO_x/Pt(111) model catalysts during my PhD. Since all the collected results have been already published, I will directly attach the paper reprints. In paragraph VI.1 the CO chemisorption properties of different Au based model catalysts, studied by TPD, will be taken into consideration, while in paragraph VI.2 a STM study of the mobility of Au NPs on both reduced and stoichiometric TiO_x substrates will be pointed out. In paragraph VI.3 I will focus on a HR-XPS and PD study of the Au NPs growth on the templating *z'*-TiO_x UT film. In the end, in paragraph VI.4, I will report on a high pressure PM-IRAS study, made in collaboration with the University of Ulm, of different UT TiO_x films and the corresponding model catalysts in different reactive atmospheres.

VI.1 Reprint of the paper: Chemisorption of CO on $Au/TiO_x/Pt(111)$ Model Catalysts with Different Stoichiometry and Defectivity

In this paper we present a TPD investigation of model catalysts prepared depositing Au on three different well characterized $TiO_x/Pt(111)$ ultrathin films. CO is used as a probe molecule and its interaction with the metal is followed by thermal desorption experiments in order to outline the dependence between the desorption profiles and the amount of deposited metal. Moreover, we have investigated three different model systems where the Au NPs nucleate and grow differently depending on the TiO_x phase structure and stoichiometry.

Our data clearly demonstrate that the desorption profile is modified by both the morphology of the metal NPs (so that it is Au coverage dependent) and the TiO_x phase stoichiometry. In particular, Au NPs growing on reduced TiO_x substrates (the *w* and *w'*-TiO_x UT films), having a stronger interaction with the TiO_x than the ones growing on the stoichiometric TiO_2 substrate (the *rect'*-TiO_2 UT film), show both a smaller average diameter and apparent heights distribution. These characteristics affect the way the Au NPs can interact with the CO, making the larger and higher Au NPs more suitable for the gas adsorption.

Journal of
Nanoscience and Nanotechnology
Vol. 8, 3595–3602, 2008

Chemisorption of CO on Au/TiO$_x$/Pt(111) Model Catalysts with Different Stoichiometry and Defectivity

Luca Artiglia, Gian Andrea Rizzi, Francesco Sedona, Stefano Agnoli, and Gaetano Granozzi*

Dipartimento di Scienze Chimiche, Unità di Ricerca CNR-INFM and INSTM, Università di Padova, Via Marzolo 1, I-35131 Padova, Italy

Au/TiO$_x$/Pt(111) model catalysts were prepared starting from well characterized TiO$_x$/Pt(111) ultrathin films, according to an established procedure consisting in a reactive evaporation of Ti, subsequent thermal treatment in O_2 or in UHV, and final deposition of submonolayer quantities of Au. Temperature Programmed Desorption measurements were performed to compare the interaction of CO in the case of two reduced TiO$_x$/Pt(111) substrates (indicated as *w*-TiO$_x$ and *w'*-TiO$_x$, being the former characterized by an ordered array of defects that can act as template for the deposition of a stable array of Au nanoparticles), with the case of a stoichiometric *rect'*-TiO$_2$/Pt(111) substrate. It was found that in all cases CO is molecularly adsorbed and two different desorption peaks are detected: one at ≈140 K corresponding to CO desorption from less active adsorption sites (terraces) of the Au nanoparticles and one at ≈200 K corresponding to CO desorption from Au nanoparticles step sites. After annealing at 770 K, the high temperature CO desorption peak is still present in the case of the defective reduced *w*-TiO$_x$ phase, supporting the good templating and stabilizing effect of such phase. On the *rect'*-TiO$_2$ stoichiometric phase, the CO uptake decreases after annealing but only to a minor extent.

Keywords: CO Chemisorption, Au Nanoparticles, Titania Templates, Ultrathin Films, TPD, Model Catalyst.

RESEARCH ARTICLE

1. INTRODUCTION

One of the main problems to be addressed in nanoscience is related to the instability of matter when dimensions are in the nanometric range. Nanoparticles (NPs) are intrinsically unstable objects because their high surface/volume ratio enhances the surface energy contribution; they can, in principle, be kinetically stabilized if a sufficiently high kinetic barrier turns them into meta-stable systems. Therefore, development of strategies to stabilize NPs against agglomeration is a strategic issue to turn to reality the expectations from nanoscience and nanocatalysis.[1]

When dealing with supported NPs, the support-NP interaction is a very important parameter to play with in order to avoid NPs agglomeration. It is well known that point (vacancies) and extended defects (steps, dislocations etc.) are capable of pinning NPs, so that a possible strategy to stabilize them is to use a substrate presenting an array of defects. On such surfaces, a bottom-up self-assembling process takes place, since each defect acts as a preferential nucleation site for the NP growth. If the defect array is spatially ordered (often called a templating substrate), the resulting NP collection will result ordered as well.

This approach has been widely studied in the case of reconstructed metallic surfaces presenting nanopatterns.[2] However, these systems are far from the real world because, in most cases, the template itself is stable only in ultra high vacuum (UHV) conditions. To this regard, templates based on oxide structures seem to be more promising because in many cases they are stable even at ambient condition (i.e., atmospheric pressure), and examples of oxides ultrathin films acting as effective template for the growth of ordered metal NPs (MNPs) or even single metal atoms have been recently reported.[3–9] It turns out that an ordered array of defects can narrow the size distribution of the MNPs down to less than 10% with respect to 25–40% expected for random nucleation.

Our research group has focused recently on nanostructured ultrathin films of TiO$_x$ ($1.2 \leq x \leq 2$) grown on a Pt(111) surface: several different nanophases have been obtained, which are characterized by different stoichiometries and defects distribution.[10] The preparation procedure consists in a reactive evaporation of Ti on a Pt(111) surface in an O_2 pressure of 10^{-5} Pa, followed by thermal treatments at different temperatures and O_2 pressures ($5 \times 10^{-4} \leq P_{O_2} \leq 10^{-8}$ Pa). All these phases have been characterized by different surface science techniques, like X-ray photoemission spectroscopy

*Author to whom correspondence should be addressed.

(XPS),[10a] ultraviolet photoemission spectroscopy (UPS),[10b] low energy electron diffraction (LEED),[10a–c] photoelectron diffraction (PED),[10a] scanning tunneling microscopy (STM),[10] and models have been obtained by Density Functional Theory (DFT) calculations.[10d–e]

In Figure 1 we report a summary of the different TiO$_x$ nanophases so far characterized: the reported STM images furnish a rationale for the labels used to identify each one of them (*k* stays for *kagomè*, i.e., in Japanese bamboo basket, *z* and *z'* stay for *zig-zag*, *w* and *w'* stays for *wagon-wheel*, *rect* and *rect'* stay for rectangular).

These TiO$_x$ phases can be divided into two groups depending on the oxidation state of Ti. The *w*, *w'*, *z* and *z'* phases are reduced phases, characterized by a Ti2p XPS binding energy (BE) at 456.4 eV, while the *rect* and *rect'* phases correspond to a fully oxidized Ti with a BE at 458.6 eV. The reduced phases consist in a Ti–O double layer, where Ti is at the interface with Pt. The oxidized phases have, on the contrary, an O–Pt interface and are formed by, at least, 3 atomic layers (O–Ti–O). Some of these phases (*w* an *z'*) are characterized by ordered arrays of defects, as can be easily guessed from the STM images (Fig. 1), where the dark spots or *troughs* form a regular pattern. These dark features, as proven by DFT calculations,[10e, 11] correspond to Ti vacancies, so that in the case of *w* and *z'* phases an effective template effect for MNP growth has been anticipated and demonstrated.[3, 12]

The ideal metal to test the possibility to obtain stabilized MNP arrays is gold. In fact, since 1987, after the historical report of Haruta,[13] supported Au NPs have been extensively studied because of their outstanding catalytic performances induced by their nanosize.[14, 15] Among the many reactions that can be effectively catalyzed by Au NPs, the low temperature oxidation of CO to CO_2 if the most studied one.[16] Thence, in order to study in detail the size-dependent catalytic properties of Au NPs, the most obvious test to start with is the adsorption of CO with Au NPs of different sizes.

This paper reports about the adsorption of CO, studied by Thermal Programmed Desorption (TPD), on Au NPs deposited on different TiO$_x$ ultrathin films, that are examples of oxidized and reduced phases with or without point defects (*w*, *w'* and *rect'*). The TPD results are related with NP sizes and shapes obtained by previous STM images. The main value of this study is associated to the degree of structural knowledge of the investigated systems which allows a detailed interpretation of the TPD data. As it will be shown, the dimensions and temperature stability of Au NPs depend not only on the interaction with the defects, but also on the oxidation state of Ti. On the other hand,

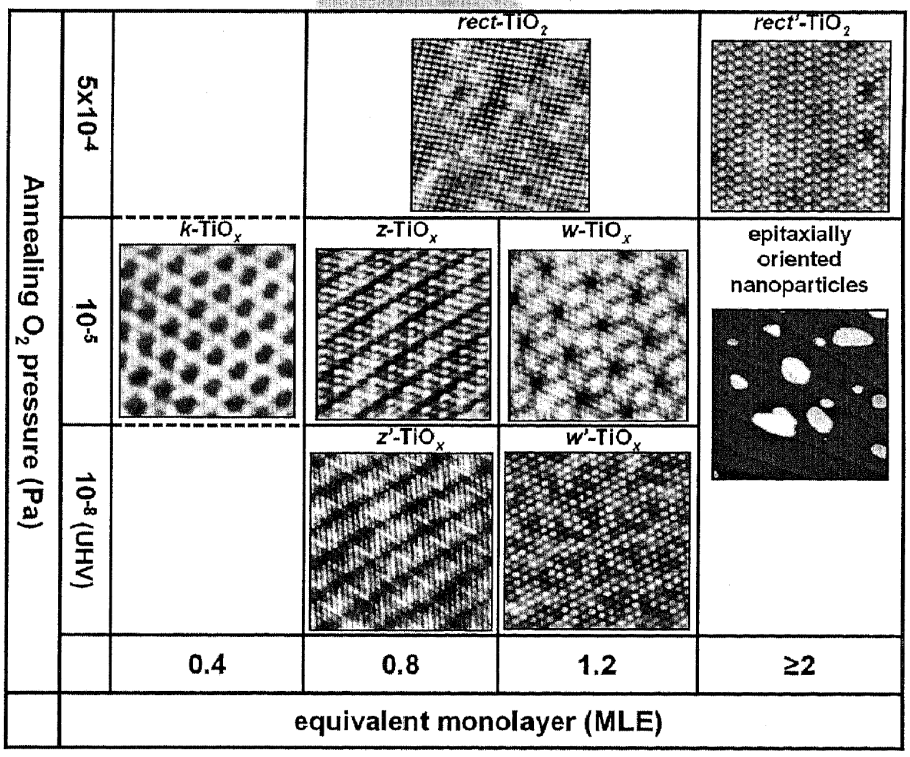

Fig. 1. Summary of the STM constant-current images of the TiO$_x$/Pt(111) nanophases so far characterized:[10] the different phases are categorized according to the oxygen pressure of the annealing procedure and to the nominal coverage in MLE (see text). *k* = *kagomé*; *z* = *zigzag*-like; *w* = *wagon-wheel*-like; *rect* = rectangular.

the ability to adsorb CO does not depend only on the size of the Au NPs, but especially on their morphology.

2. EXPERIMENTAL PROCEDURES

All the experiments have been carried on using an UHV chamber with a base pressure of $3.0 \cdot 10^{-8}$ Pa, equipped with a sputter gun, an electron beam evaporator, a four-grid LEED optics (Omicron Spectaview), a hemispherical energy analyzer (VG CLAM2), an X-ray double anode source (Omicron Dar400) and a TPD (Hyden Quadrupole Mass Spectrometer) facility.

The Pt(111) substrate has been cleaned by cycles of Ar^+ sputtering and UHV annealing at 920 K (until the C 1s signal was below the detection limit of XPS) and finally exposing it to a O_2 pressure of $5.0 \cdot 10^{-5}$ Pa for 30 seconds before the cool-down. The subsequent inspection with LEED shows a well defined (1×1) diffraction pattern. The preparation and structural characterization of the different TiO$_x$/Pt(111) phases have been reported in details elsewhere.[10a]

They are basically obtained in two steps:
—the formation at room temperature (RT) of an intermediate film on the Pt(111) single crystal by electron-beam evaporation from a Ti wire in an oxygen background ($p_{O_2} = 10^{-5}$ Pa). The different TiO$_x$ phases are prepared by varying the amount of the deposited Ti, given in MLE, where 1 MLE corresponds to $1.5 \cdot 10^{15}$ atoms cm^{-2}, as determined with a quartz microbalance. This number corresponds to the surface density of Pt atoms per unit area of Pt(111) 1×1 (cm^2 units);
—the annealing of this intermediate film at 900 K in different conditions reported in Table I. The presence of a particular phase has been checked by comparison with the LEED literature data.[10]

Gold has been evaporated from a Omicron EFM3/4 evaporator using a filament basket directly on the TiO$_x$/Pt(111) film held at RT in UHV. The amount of gold deposited has been determined by using a TPD calibration procedure reported by Somorjai et al.[17]

The TPD spectra were taken in the UHV chamber exposing the sample at low temperature (140 K) to CO introduced by a leak valve. In order to analyze all the products desorbed from the sample, it was then heated, close to a QMS, with a rate of 1 K/s to reach a final temperature of 373 K.

The STM images have been obtained in constant current mode at RT in two different systems operating at a base pressure of 5×10^{-9} Pa. Tunneling voltages are given with respect to the sample. The tunneling parameters are reported in the corresponding captions of the reported STM images. Experimental details are reported in Refs. [3, 21].

Table I. Experimental condition adopted to obtain the TiO$_x$ phases used in the present study.

TiO$_x$ phase	Annealing conditions	Thickness (MLE)
w	900 K, $p_{O_2} = 1.0 \cdot 10^{-5}$ Pa	1.2
w'	900 K in UHV	1.2
rect'	900 K, $p_{O_2} = 1.0 \cdot 10^{-4}$ Pa	2.0

3. RESULTS

The TPD curves were obtained monitoring the m/e = 28 amu (CO) signal in the temperature interval 140–370 K range. Unfortunately, the lowest temperature reachable by the used equipment is not enough to completely include the lowest desorption peak, whose maximum is usually found around 130–140 K.[18] For this reason in many of the reported cases we will only see a declining background in the lowest temperature range.

The CO TPD data for the system Au/*w*-TiO$_x$/Pt(111) after a CO exposure of 2 L are shown in Figure 2. On the clean *w*-TiO$_x$ phase there is only one broad and weak feature in the low temperature region (at about

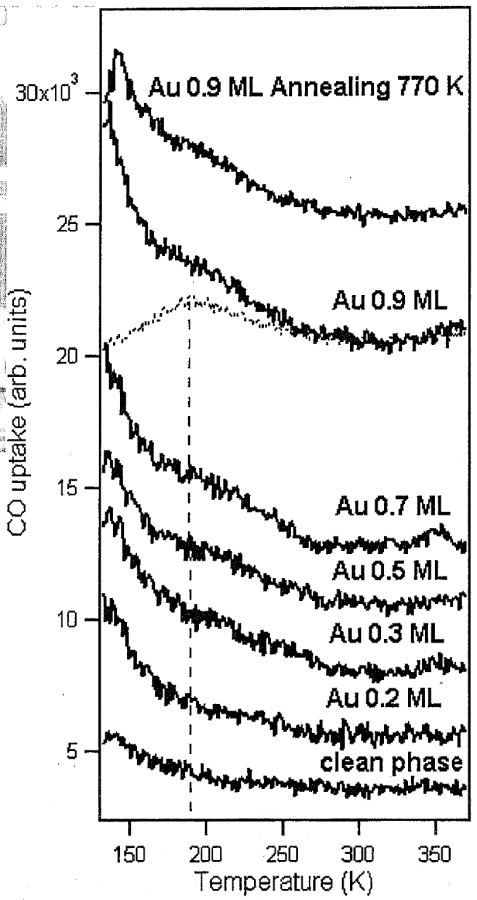

Fig. 2. CO TPD data of Au/*w*-TiO$_x$/Pt(111) at different Au coverages for a CO exposure of 2 L. The dotted curve (at a Au coverage of 0.9 ML) corresponds to an exposure of 0.1 L of CO.

140–150 K). After Au deposition (in the Au coverage range of 0.2–0.9 ML), two desorption peaks are observed whose intensity increases with the amount of deposited Au: the first one is in the same region of the feature seen on the clean substrate, while the second, very wide, is found at higher temperature. For the low coverages it is difficult to clearly detect a peak maximum, which progressively shift toward lower T with the Au coverage, reaching the value of about 190 K for 0.9 ML (see dotted vertical line in Fig. 2). In the Figure 2, the same high T peak can be singled out (see dotted curve) during a measurement obtained after sample exposure to only 0.1 L of CO in order to saturate only the higher temperature sites (190 K). The same peak is observed also in a TPD experiment carried out on the Au/w-TiO$_x$/Pt(111) system after annealing it at 770 K for 20 minutes (see upper curve in Fig. 2). Using a Redhead approximation,[19] an approximate value of the desorption energy ($\Delta E_{des} = 54.4 \pm 4$ KJ/mol) has been obtained assuming for the pre-exponential factor a value of $\nu_1 = 1.0 \cdot 10^{-14}$ s^{-1}.

The CO TPD data collected for the Au/w'-TiO$_x$/Pt(111) system are shown in Figure 3. Also in this case the curve obtained for the clean support presents only a declining background in the lowest temperature region. As in the previous system, Figure 3 shows that, when Au is deposited, two different desorption peaks are observed whose intensity increases with the Au coverage (from 0.2 ML to 1.0 ML): one centred at about 140 K, similar to the one described above and a second one (rather broad) centred at ca. 200 K when the highest Au coverage is examined. An exposure to 0.2 L of CO was sufficient to saturate only desorption sites corresponding to the peak centred at ca. 200 K (dotted curve in Fig. 3). Differently from the case of the Au/w-TiO$_x$ system, this peak almost disappears in a TPD experiment carried out after annealing at 770 K for 20 minutes. The Redhead equation, with the same approximation used in the previous example, furnishes a value of the desorption energy of $\Delta E_{des} = 56.4 \pm 4$ KJ/mol.

The CO TPD curves collected for the system Au/*rect'*-TiO$_2$/Pt(111) are shown in Figure 4. The curve corresponding to the clean support shows an increasing background in the low temperature region, very similar to the one

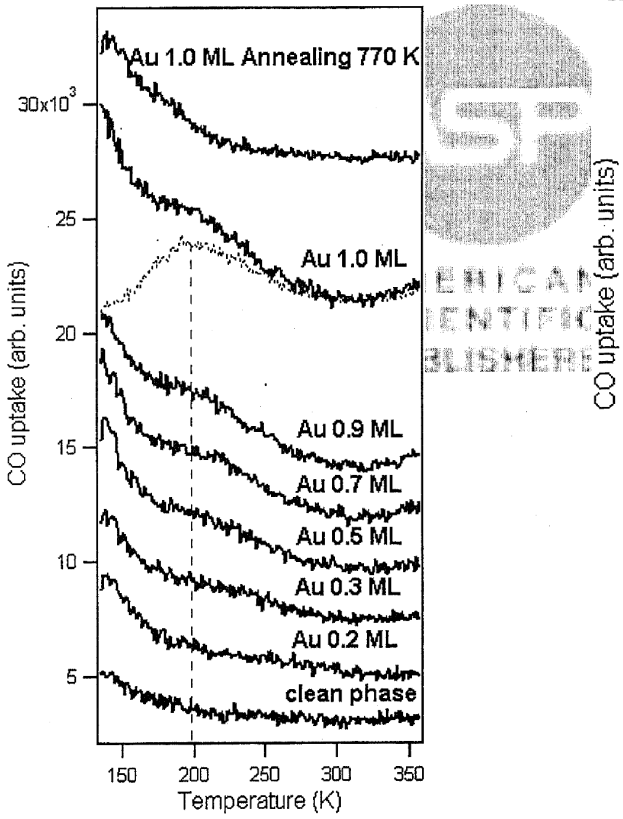

Fig. 3. CO TPD data of Au/w'-TiO$_x$/Pt(111) at different Au coverages for a CO exposure of 2 L. The dotted curve (at a Au coverage of 1.0 ML) corresponds to an exposure of 0.2 L of CO.

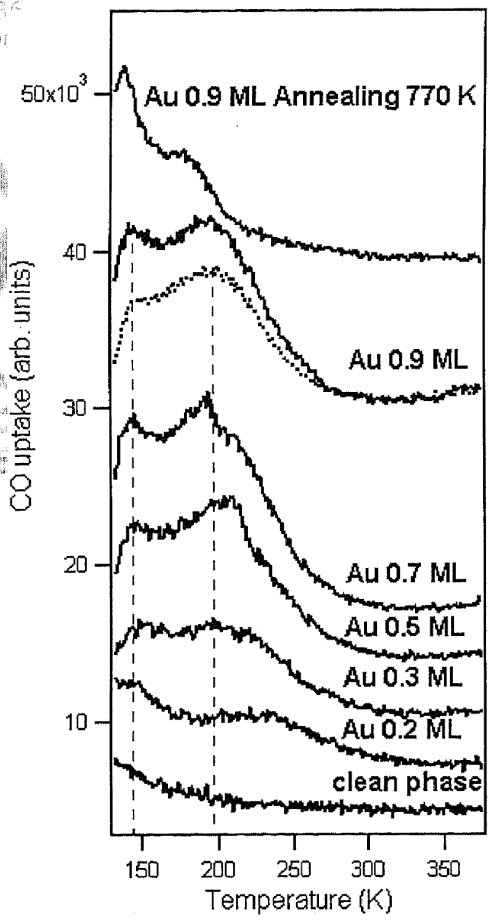

Fig. 4. CO TPD data of Au/*rect'*-TiO$_x$/Pt(111) at different Au coverages for a CO exposure of 6 L. The dotted curve (at a Au coverage of 0.9 ML) corresponds to an exposure of 0.5 L of CO.

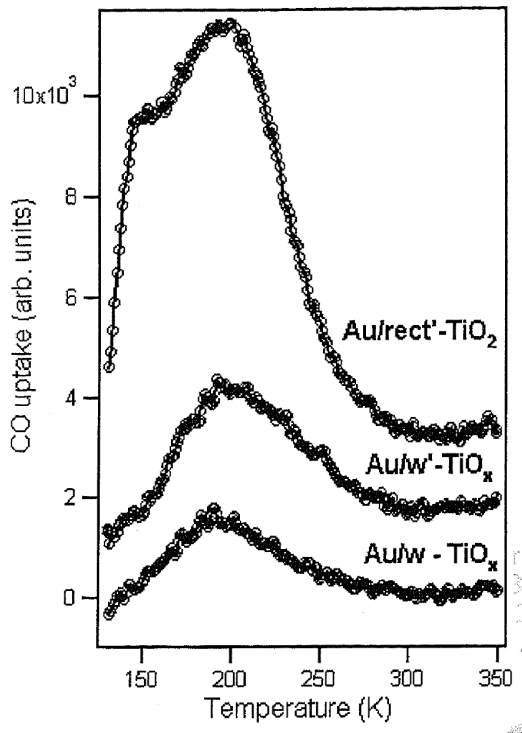

Fig. 5. Comparison between the dotted curves reported in Figures 2, 3 and 4 for the three analyzed Au/TiO$_x$/Pt(111) systems.

seen in the w'-TiO$_x$ phase (see Fig. 3). After Au deposition, there are two different desorption peaks: the one described before and a second wide peak at higher temperature (centred at about 196 K for the highest Au coverage), whose intensity increases with the amount of deposited gold (0.2–0.9 ML). Differently from the previous cases, the low temperature peak shifts to higher temperature as the amount of Au increases and for a coverage of 0.9 ML is centred at about 144 K. An exposure to 0.5 L of CO was necessary to saturate the peak centred at 196 K (shown in Fig. 5 by a dotted line). This peak is found also in a CO TPD experiment carried out after annealing the system at 770 K for 20 minutes, although shifted to lower temperature. The desorption energy obtained by the Redhead approximation is $\Delta E_{des} = 55.4 \pm 4$ KJ/mol.

In order to evaluate the relative CO uptake of the three different systems, in Figure 5 the three dotted curves reported in Figures 2, 3 and 4 are compared. Their relative areas have been evaluated: on the *rect'*-TiO$_x$/Pt(111) system, a CO uptake 700% greater than on w-TiO$_x$/Pt(111) and 300% greater than on w'-TiO$_x$/Pt(111) is observed.

4. DISCUSSION

An interesting study on the interaction of CO with Au/TiO$_x$/Ru(0001) model catalysts has been already reported,[18] where a similar approach was used to discuss the NP size effect and the role of the substrate. The present study can be considered as a follow up of such study to model catalysts having a better defined structural characterization. Actually, for two of the herein investigated substrates, detailed structural models (w-TiO$_x$ [10a–c, 11] and *rect'*-TiO$_2$[20]) and electronic structure data[10b] have been already discussed, whereas their interaction with Au has been examined in details.[3, 21] Before discussing the reported data, we will summarize the principal structural results of relevance for the herein reported TPD data of the Au/TiO$_x$/Pt(111) systems.

As well evident in Figure 1, the w-TiO$_x$ substrate has an ordered array of black spots that have been interpreted as Ti vacancies,[10c, 11] which can actually work as preferential nucleation sites for the Au NPs. According to the theoretical model, the w-TiO$_x$ phase is associated to a reduced oxide ($x \approx 1.2$).[11] Recently, a system based on an alumina ultrathin phase on $Ni_3Al(111)$ has been found to exhibit a similar pattern of defective holes that act as nucleation centers.[22] An ordered hexagonal array of size selected and stabilized Au NPs (Au islands with size distribution peaked at ca. 1.3 nm with a narrow dispersion and with a maximum height of 0.4 nm, i.e., 2 MLs) was recently observed after annealing at 600 K a linear array of Au NPs grown on the z'-TiO$_x$ phase (see Fig. 6(a)).[3] This hexagonal ordered array has been interpreted as deriving from a Au and temperature induced transformation of the z'-TiO$_x$ phase into the w-TiO$_x$ one.

On the other hand, the w'-TiO$_x$ and *rect'*-TiO$_2$ substrates are examples of reduced and stoichiometric substrates, respectively, where there is no long-range ordered defectivity: larger Au NP sizes were obtained at RT (mean sizes: w'-TiO$_x$ $\approx$ 3.5 nm,[3] *rect'*-TiO$_2$ $\approx$ 5–6 nm,[21] with larger dispersions, see Figs. 6(b, c)), which can be interpreted as a consequence of a change of Au mobility on titania related substrates along the sequence:[21] reduced defective < reduced *defect-free*[23] < stoichiometric *defect-free*. The Au NP nucleation on the w'-TiO$_x$ phase is random, occurring on both terraces and steps (Fig. 6(b)). On the *rect'*-TiO$_2$ phase larger 3D NPs are clearly seen (Fig. 6(c), where the NP have a 1.5 nm mean height[21]) almost independent on the Au coverage. It is quite plausible that annealing the w'-TiO$_x$ and *rect'*-TiO$_2$ systems at high temperatures would provide a coarsening of the Au NPs, as a consequence of the higher NP mobility. So the three investigated systems, namely w-TiO$_x$, w'-TiO$_x$ and *rect'*-TiO$_2$, are examples of NP arrays of different sizes with a different dynamics with respect to temperature raise.

Let us start from these considerations to discuss the CO TPD curves for the different Au/TiO$_x$/Pt(111) phases.

We first discuss the lowest explored temperature range before Au deposition: for the clean w'-TiO$_x$ and *rect'*-TiO$_2$ phases, the TPD curves (bottom of Figs. 3 and 4) show a declining background, probably due to a peak centred

RESEARCH ARTICLE

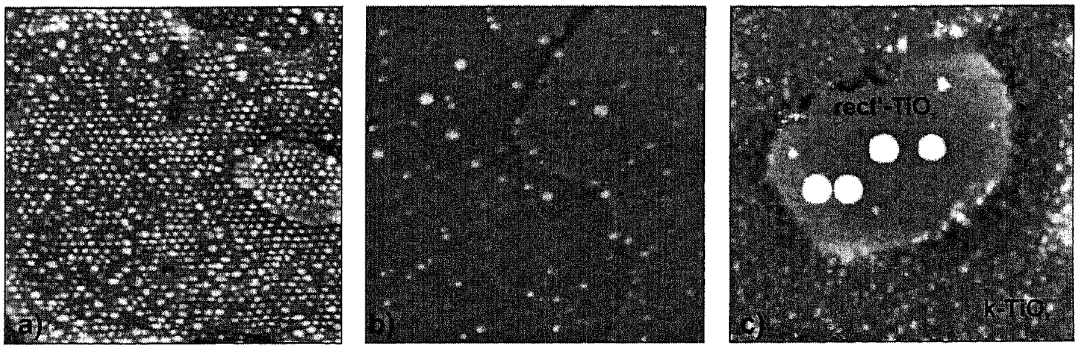

Fig. 6. STM images of: (a) an hexagonal array of Au NPs on the *z'*-TiO$_x$ monolayer phase on Pt(111) annealed at 600 K after deposition of 0.35 MLE of Au (80 nm × 80 nm, $V = 1.0$ V, $I = 0.4$ nA) (see text for discussion), (b) a *w'*-TiO$_x$ wetting monolayer on Pt(111) after deposition of 0.2 MLE of Au (82 nm × 82 nm, $V = 1.5$ V, $I = 0.2$ nA).[3]

between 130 and 140 K (just below the probed temperature region), while in the *w*-TiO$_x$ clean phase (see Fig. 2) the curve appears to be slightly shifted to higher temperatures. In all three cases, such low intensity feature can be safely assigned to CO desorbed from defective sites of the clean TiO$_x$ substrate, as already observed in similar systems.[18] These defects could therefore be potential adsorption sites for CO where a stronger interaction could be inferred. Unfortunately the investigated temperature range does not allow to draw any definite conclusion.

When Au is progressively deposited on the different substrates, low temperature TPD features are present, but their intensity increases with the Au coverage. Thus, it is clear that they contain a contribution of CO desorption from the Au NPs. Similar features have already been observed assigned to CO desorption from Au terraces.[18,24,25] The intensity increase, observed at higher Au coverages, can be explained with the expected increase of both the size and number of Au NPs (and therefore of terraces) deposited on the oxidic substrate. Subtle changes of these features in the different systems can be related to the different interaction and morphologies of Au NPs with the supporting phases. For example, our TPD data suggest that in the case of the Au/*rect'*-TiO$_2$/Pt(111) system, the low temperature peak is shifted to higher temperatures (ca. 140–150 K, Fig. 4) with respect to the other two cases (Figs. 2 and 3). Our STM data[21] show clearly that, for the same Au coverage, the NPs deposited on the *rect'*-TiO$_2$/Pt(111) have a larger size with respect to the other two systems (see Fig. 6 and Refs. [3, 21]). Thus, the shift of the TPD curve to higher temperatures could be a consequence of larger Au terraces.

Similar considerations can be used to explain the nature of the CO desorption peak which is present at higher temperature, whose intensity increases with the amount of deposited Au. This peak has already been observed in similar systems[18,26,27] and assigned, by means of IRAS measurements, to CO chemisorption on Au NP defective sites. It is also reported that this peak is strongly influenced by the NP size and its intensity is strongly dependent on the number of step sites in the NPs.[28] It is not completely clear whether the sites at the interface between the oxide film and the NPs contribute to this high temperature CO desorption peak.[29]

Referring to Figure 5, both the Au/*w*-TiO$_x$ and Au/*w'*-TiO$_x$ systems show a definitely smaller CO uptake with respect to the Au/*rect'*-TiO$_2$ system. This behaviour can be explained by considering the different Au NP morphology and dimension on the three phases, as emerging from the discussed STM data.[3,21] For the fully developed 3D NPs obtained in the Au/*rect'*-TiO$_2$ system, a higher number of defective stepped sites can be inferred; thence, the CO desorption peak at about 200 K is expected to be more intense than in the case of the other two systems.

The STM data are also useful to explain the TPD spectra collected after annealing the Au/oxide systems at 770 K (see top of Figs. 2, 3 and 4). In the case of the Au/*w*-TiO$_x$ system, the CO high temperature desorption peak at 200 K (although of low intensity) is unchanged after annealing (Fig. 2); this is in tune with the templating/stabilizing effect of the *w*-TiO$_x$ phase towards Au NPs which avoids a temperature induced agglomeration. On the contrary, the Au/*w'*-TiO$_x$ system shows (Fig. 3) that the CO desorption peak almost vanishes after annealing, in agreement with the hypothesis that temperature induced NPs agglomeration is occurring (larger NP mobility on *w'*-TiO$_x$ than in *w*-TiO$_x$).[3] The TPD data of the Au/*rect'*-TiO$_2$ system behaves differently: the larger Au NPs (5–6 nm average size) have a full 3D shape (with a 1.5 nm mean height) at low temperature and it is expected that such 3D shape would be maintained also after annealing, even if the temperature treatment would partially flatten the NPs. Consequently, the high temperature CO desorption peak from Au/*rect'*-TiO$_2$ is still present after annealing, although less intense and shifted to lower temperature.

If we consider the interaction between Au NPs and the oxidic support, it is quite clear from the data reported in the literature, that it is stronger in the case of reduced

RESEARCH ARTICLE

phases.[30,31] According to our data (see the Redhead approximation derived ΔE_{des} values and the higher temperature peak maxima), there is no clear and distinct trend in the examined systems.

One further effect to be mentioned is the observed shift at lower temperature of the peak centred at ≈200 K when the Au coverage is increased (see curves in Figs. 2, 3, and 4). There are two hypotheses that may explain this effect: the first one associates this shift to the increasing of the Au NPs dimensions.[18,24] The second one considers that on larger NPs there is a larger number of adsorbed CO so that there is a inter-adsorbate repulsion effect. The ΔE_{des} values reported in the Section 3 have been calculated at the maximum Au coverage (which means maximum NPs dimensions) and they are in good agreement with the ones reported for a similar Au(1.5 ML)/TiO_2/Ru(0001) sample investigated by Zhao et al.[18]

Finally, we want to mention some XPS data collected at low temperature (140 K) for the three systems (data not reported). There is no visible difference in the peak shape between the Au4f and Ti2p spectra collected before and after exposure to 6 L of CO. However, the Au4f/Ti2p intensity ratio, before and after CO exposure, shows some variations. For Au NPs supported on the two reduced phases (w-TiO_x and w'-TiO_x) there is no appreciable change in the ratio value (less than 2% for both systems). On the contrary, for the oxidized *rect*-TiO_2 one, we observe an increase in the Au4f/Ti2p intensity ratio of about 20%. This variation may indicate that CO chemisorption on Au NPs causes a change in their surface energy, and that the high Au mobility on the *rect*-TiO_2 phase[21] may induce some flattening of the 3D NPs. On the contrary, on the reduced supports this shape modification could be inhibited by the higher NP-substrate interaction.

5. CONCLUSIONS

Au NPs deposited on well characterized TiO_x ultrathin grown on Pt(111) have been examined by low temperature CO TPD and XPS to study the effect of the NP sizes and morphologies on the CO chemisorption. We found that CO is molecularly adsorbed and two different desorption peaks are detected. The low temperature one (≈140 K) corresponds to CO desorption from less active adsorption sites (terraces) of the Au NPs, while the high temperature one (≈200 K) corresponds to CO desorption from Au NPs step sites. We also found that Au NPs deposited on reduced substrates (w-TiO_x and w'-TiO_x) present a lower CO uptake than the one deposited on the oxidized stoichiometric phase (*rect*-TiO_2). On the basis of previous STM investigations, we associate such differences to the different sizes of Au NPs. The increase in the XPS peaks intensity ratio Au4f/Ti2p observed after CO dosing in the case of Au/*rect*-TiO_2 system suggests that some CO-induced flattening of the Au 3D NPs is occurring. Experiments are in progress to substantiate such hypothesis.

The annealing of the samples at 770 K for 20 minutes has been used to test the NP stability towards agglomeration processes. The high temperature CO desorption peak (assigned to desorption from steps and defects) is still present, after thermal treatment, in the case of the w-TiO_x reduced phase, demonstrating the very good templating and stabilizing effect of such phase. To our knowledge this is the first example of Au NP stabilization obtained by a self-assembling process of the metal NPs on an ordered nanoarray of defects. On the *rect*-TiO_2 stoichiometric phase, the CO uptake decreases after annealing but only to a minor extent.

Acknowledgments: This work has been funded by European Community through two STRP projects (NanoChemSens, *Nanostructures for Chemical Sensors*, and GSOMEN, *Growth and Supra-organization of Transition and Noble Metal Nanoclusters*), and by the Italian Ministry of Instruction, University and Research (MIUR) through the fund "Programs of national relevance" (PRIN-2003, PRIN-2005).

References and Notes

1. (a) A. T. Bell, *Science* 299, 1688 (**2003**); (b) R. Schlogl and H. Abd, *Angew. Chemie Int. Ed.* 43, 1628 (**2004**); (c) T. E. Madey, K. Pelhos, Q. Wu, R. Barnes, I. Ermanoski, W. Chen, J. J. Kolodziej, and J. E. Rowe, *Proc. Nat. Acad. Sci.* 99, 6503 (**2002**).
2. H. Brune, *Surf. Sci. Reports* 31, 121 (**1998**).
3. F. Sedona, S. Agnoli, M. Fanetti, I. Kholmanov, E. Cavaliere, L. Gavioli, and G. Granozzi, *J. Phys. Chem. C* 111, 8024 (**2007**).
4. H. J. Freund, *Surf. Sci.* 500, 271 (**2002**).
5. W. T. Fallace, B. K. Min, and D. W. Goodman, *Top. Catal.* 34, 17 (**2005**).
6. S. Degen, C. Becker, and K. Wandelt, *Faraday Discuss.* 125, 343 (**2004**).
7. N. Berdunov, G. Mariotto, K. Balakrishnan, S. Murphy, and I. V. Shvets, *Surf. Sci.* L287, 600 (**2006**).
8. G. Hamm, C. Becker, and C. R. Henry, *Nanotechnology* 17, 1943 (**2006**).
9. K. Jordan, S. Murphy, and I. V. Shvets, *Surf. Sci.* 600, 5150 (**2006**).
10. (a) F. Sedona, G. A. Rizzi, S. Agnoli, F. X. Llabrés i Xamena, A. Papageorgiou, D. Ostermann, M. Sambi, P. Finetti, K. Schierbaum, and G. Granozzi, *J. Phys. Chem. B* 109, 24411 (**2005**); (b) P. Finetti, F. Sedona, G. A. Rizzi, U. Mick, F. Sutara, M. Svec, V. Matolin, K. Schierbaum, and G. Granozzi, *J. Phys. Chem. C* 111, 869 (**2007**); (c) F. Sedona, S. Agnoli, and G. Granozzi, *J. Phys. Chem. B* 110, 15359 (**2006**); (d) G. Barcaro, F. Sedona, A. Fortunelli, and G. Granozzi, *J. Phys. Chem. C* 111, 6095 (**2007**); (e) F. Sedona, G. Granozzi, G. Barcaro, and A. Fortunelli, *Phys. Rev. B* 77, 115417 (**2008**).
11. F. Sedona, G. Barcaro, S. Agnoli, G. A. Rizzi, A. Fortunelli, and G. Granozzi, to be submitted.
12. Actually, the templating effect of the w-TiO_x phase has been demonstrated indirectly by STM by observing an hexagonal array of Au NPs after annealing a deposit on the z'-TiO_x phase (see Ref. [3]).
13. M. Haruta and N. Yamada, *Chem. Lett.* 16, 405 (**1987**).
14. M. Haruta, *Nature* 437, 1098 (**2005**).
15. S. C. Parker and C. T. Campbell, *Top. Catal.* 44, 3 (**2007**).

RESEARCH ARTICLE

16. G. C. Bond and D. T. Thompson, *Gold Bulletin* 33, 41 (**2000**).
17. P. M. Davies, M. A. Quinlan, and G. A. Somorjai, *Surf. Sci.* 121, 290 (**1982**).
18. Z. Zhao, T. Diemant, D. Rosenthal, B. Christmann, J. Bansmann, H. Rauscher, and R. J. Behm, *Surf. Sci.* 600, 4992 (**2006**).
19. P. A. Redhead, *Vacuum* 12, 203 (**1962**).
20. A. Vittadini, A. Selloni, and M. Casarin, *Theor. Chem. Acc.* 5–6, 663 (**2007**); A. Vittadini and M. Casarin, *Theor. Chem. Acc.* (**2008**), in press.
21. F. Sedona, M. Sambi, L. Artiglia, G. A. Rizzi, A. Vittadini, A. Fortunelli, and G. Granozzi, *J. Phys. Chem. C* 112, 3187 (**2008**).
22. M. Schmid, G. Kresse, A. Buchsbaum, E. Napetschnig, S. Gritschneder, M. Reichling, and P. Varga, *Phys. Rev. Lett.* 99, 196104 (**2007**).
23. For *defect-free* we mean substrates where ordered arrays of defects are not observed in the corresponding STM images.
24. C. Lemire, R. Meyer, S. K. Shaikhutdinov, and H. J. Freund, *Surf. Sci.* 552, 27 (**2004**).
25. C. Winkler, A. J. Carew, S. Haq, and R. Raval, *Langmuir* 19, 717 (**2003**).
26. L. Zhang, R. Persaud, and T. E. Madey, *Phys. Rev. B* 56, 10549 (**1997**).
27. G. B. Raupp and J. A. Dumesic, *J. Phys. Chem.* 89, 5240 (**1985**).
28. M. Haruta and N. Yamada, *Chem. Lett.* 2, 405 (**1987**).
29. M. C. Kung, R. J. Davis, and H. Kung, *J. Phys. Chem. C* 111, 11767 (**2007**).
30. C. T. Campbell, A. W. Grant, D. E. Starr, S. C. Parker, and V. A. Bondzie, *Top. Catal.* 14, 43 (**2001**).
31. M. Sterrer, M. Yulikov, E. Fishbach, M. Heyde, H. P. Rust, G. Pacchioni, T. Risse, and H. J. Freund, *Angew. Chemie Int. Ed.* 45, 2630 (**2006**).

Received: 12 February 2008. Accepted: 20 March 2008.

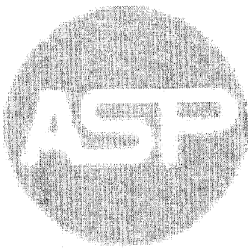

VI.2 Reprint of the paper: Mobility of Au on TiO_x Substrates with Different Stoichiometry and Defectivity

In this paper we present a STM study of a model catalyst obtained depositing Au on a stoichiometric TiO_2/Pt(111) UT film. The stoichiometric *rect'*-TiO_2 UT film does not grow completely wetting the Pt(111) support. It creates large islands that are separated by a wetting layer of a reduced TiO_x film (the *k*-TiO_x phase) with a honeycomb structure. The coexistence of such 2 UT film, whose structure and chemical properties are completely different, also reflects on the Au NPs nucleation and growth. In fact, as already specified in paragraph VI.1, Au interacts stronger with a reduced substrate than with a stoichiometric one. Such a difference in the metal-oxide interaction leads to the formation of smaller (average diameter of ca. 1.5-2 nm) and flatter (average apparent height of ca. 0.2 nm) Au NPs on the *k*-TiO_x phase than the ones formed on the *rect*'-TiO_2 (average diameter of ca. 5-6 nm and average apparent height of ca. 1.5 nm). Moreover, the weak interaction between the Au and the stoichiometric UT film is also outlined by the STM tip scan, which is able to manipulate the Au NPs moving them on the *rect'*-TiO_2 islands.

The experimental results presented in this study are supported by theoretical DFT calculations that, based on the structure of the 2 UT films, predict the interaction between them and the Au. Also the theoretical evidences put in light how the mobility of the Au on the stoichiometric film is higher than the one calculated on the reduced *k*-TiO_x.

THE JOURNAL OF PHYSICAL CHEMISTRY C LETTERS

3187

2008, *112*, 3187−3190
Published on Web 02/07/2008

Mobility of Au on TiO$_x$ Substrates with Different Stoichiometry and Defectivity

Francesco Sedona,[†] Mauro Sambi,[†] Luca Artiglia,[†] Gian Andrea Rizzi,[†] Andrea Vittadini,[‡] Alessandro Fortunelli,[§] and Gaetano Granozzi*,[†]

Dipartimento di Scienze Chimiche, Unità di Ricerca CNR-INFM and INSTM, Università di Padova, Via Marzolo 1, I-35131 Padova, Italy, Dipartimento di Scienze Chimiche, ISTM-CNR and INSTM, Università di Padova, Via Marzolo 1, I-35131 Padova, Italy, and IPCF-CNR, via Giovanni Moruzzi 1, I-56124 Pisa, Italy

Received: December 16, 2007; In Final Form: January 24, 2008

Au nanoparticles deposited on titania films, where two nanophases of different stoichiometry and defectivity are co-present, were imaged on the same spot by scanning tunneling microscopy. The observed sizes are rather dissimilar as a consequence of the different mobility of Au on the two surfaces. The role of the stoichiometry, which can influence the Au−substrate interaction, and of the defects, which can trap the metal atoms, is discussed on the basis of theoretical calculations of diffusion energy barriers on the two surfaces.

One important issue in surface chemistry and catalysis is to clearly identify the effect of dimensionality on the chemical reactivity of heterogeneous systems, and this has produced the new field of nanocatalysis.[1] It is well-known that new, or improved, chemical and catalytic properties are obtained when metallic nanoparticles (NPs) in the range of 1−5 nm are supported on a dispersing support, typically a metal oxide. A major general problem that needs to be overcome is related to the intrinsic instability of the NPs: due to their high surface/volume ratio, NPs tend to decrease their energy by coalescing into larger particles (Ostwald ripening and sintering processes). This makes their characterization difficult and the exploitation of their innovative properties on a long time scale or under realistic reaction conditions uncertain. Being intrinsically unstable, NPs can only survive in the presence of kinetic barriers which avoid mass transfer and agglomeration processes or when stabilized by specific NP−substrate interactions. As defects in oxides have been demonstrated to be effective in stabilizing NPs, ultrathin films containing ordered arrays of defects have been used as templates for the growth of size-selected and ordered NPs arrays.[2−8]

In this context, Au NPs supported on reducible metal oxides represent a case of particular relevance because they are very active catalysts for a variety of reactions. A paradigmatic example in this sense is the catalytic activity toward CO oxidation at low temperature discovered for Au grown on reduced titania surfaces, whose explanation, however, is still the object of debate.[9−14] Controlling the Au mobility on titania surfaces is particularly important in relation to the goal of stabilizing the Au NPs. Indirect evidence has been reported according to which Au NPs are less mobile on reduced titania surfaces with respect to stoichiometric ones, based on the NP size observation by scanning tunneling microscopy (STM) on surfaces of different stoichiometry,[15] but a direct and simultaneous observation of differently sized NPs on different TiO$_x$ substrates having a well-defined stoichiometry is still lacking. In the present Letter, we report such a STM study, where Au NPs were deposited and observed on two ultrathin TiO$_x$ films on Pt(111) which have well-defined and different stoichiometries and defect structures.[16] What is most interesting is that the two different oxide nanophases are co-present in the same STM images, thus allowing a direct comparison of both the Au NP size and mobility at different temperatures free from errors due to tip and scanning parameter differences.

In recent years, some of us have managed to prepare and characterize several nanophases of TiO$_x$ on Pt(111) having rather different STM topographies and stoichiometries and distinct low energy electron diffraction (LEED) patterns.[16] For some of them, we have recently demonstrated that they are good templates for metal-cluster growth.[2] The two nanophases used in the present study have been termed as *k*-TiO$_x$ (*k* stands for *kagomé*[17] and $x \approx 1.5$)[16] and *rect*′-TiO$_2$ (*rect*′ stays for rectangular),[16b] respectively.

The preparation and the structural characterization of the different TiO$_x$ nanophases on Pt(111) have been reported in detail elsewhere.[16] Ti was evaporated at room temperature (RT) onto the clean Pt(111) surface, in an oxygen background pressure (P_{O_2}) of 1×10^{-4} Pa. In order to obtain a well-defined and ordered TiO$_x$ nanophase, the amount of deposited Ti, the substrate temperature, and the oxygen pressure during the postannealing have to be optimized. However, if the preparation is carried out under nonoptimized conditions (in the present case 950 K $P_{O_2} = 10^{-6}$ Pa for 10′), different phases can be co-present and the LEED pattern may result in the superimposition of different patterns typical of each phase. In these cases, looking at the surface by STM, regions where the different nanophases are adjacent can be imaged.

Au has been evaporated from a filament basket on the substrate held at RT under UHV conditions (without further annealing), with a typical deposition rate of about 0.3 ML/min. The STM images have been obtained in constant-current mode

* To whom correspondence should be addressed. E-mail: gaetano.granozzi@unipd.it.
[†] Unità di Ricerca CNR-INFM and INSTM, Università di Padova.
[‡] ISTM-CNR and INSTM, Università di Padova.
[§] IPCF-CNR.

10.1021/jp711801w CCC: $40.75

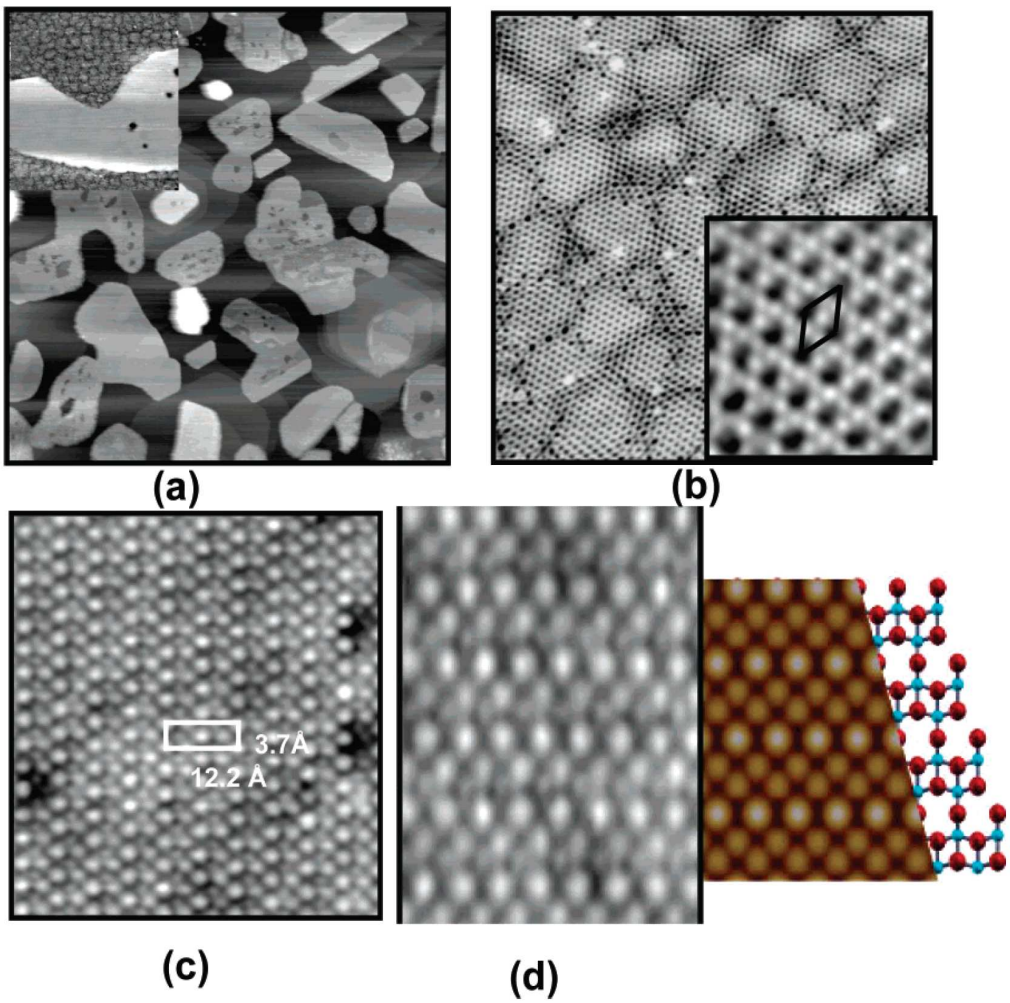

Figure 1. STM constant-current image of (a) *rect*′-TiO_2 islands grown on the *k*-TiO_x monolayer (500 × 500 nm^2; $V = 1.2$ V, $I = 1.2$ nA). In the inset, a close-up of an island is shown (80 × 80 nm^2; $V = 2.0$ V, $I = 1.0$ nA). (b) The wetting monolayer of *k*-TiO_x (30 × 30 nm^2; $V = 1$ V, $I = 1$ nA) and (inset) its atomically resolved image (3 × 3 nm^2; $V = -0.4$ V, $I = 1.06$ nA). (c) The top of a *rect*′-TiO_2 island (6.1 × 6.1 nm^2; $V = -0.7$ V, $I = 0.66$ nA). (d) The comparison between a close-up of a STM image and a simulation obtained from a "pentacoordinated nanosheet" model where Ti atoms are reported as light blue spheres and O atoms as red spheres.

at RT in an Omicron VT-STM system operating at a base pressure of 5×10^{-9} Pa. Tunneling voltages are given with respect to the sample. The tunneling parameters are reported in the corresponding captions of the reported STM images. Experimental details were similar to those in ref 16a.

In Figure 1a, we report the STM image of a spot of the sample where *rect*′-TiO_2 large islands are evident on a substrate covered by a wetting monolayer (ML) of the *kagomé-like* *k*-TiO_x phase. The *rect*′-TiO_2 islands have sizes in the range 50−100 nm and an apparent height in the order of 0.5 nm. If one looks carefully at the inset in Figure 1a, the typical pattern of the *k*-TiO_x nanophase can be easily recognized.[16a] For comparison, in Figure 1b, we report the STM image of the *k*-TiO_x phase, taken in a different experiment on a single *k*-TiO_x nanophase sample:[16a] a patched but clearly two-dimensional hexagonal overlayer with a long-range Moirè-like modulation is observed, where the surface mesh has a periodicity of approximately 6.0 Å, in good agreement with the hexagonal 2.15 × 2.15 mesh seen by LEED.[16a] Atomically resolved images (see the inset in Figure 1b) allowed us to demonstrate that a *kagomé-like* ML is present, based on hexagons which are interconnected through their vertices. A structural model implying a Ti_2O_3 stoichiometry for the *k*-TiO_x nanophases has been suggested, which has been recently corroborated by density functional theory (DFT) calculations.[18]

In Figure 1c, we report a close-up of the *rect*′-TiO_2 island, where the outlined centered rectangular unit cell (3.7 × 12.2 Å^2) is in good agreement with the LEED pattern of a single *rect*′-TiO_2 phase.[16b] A model of this phase has been recently proposed, which consists of a 2-ML-thick nanosheet composed of 5-fold coordinated cations connected by an intermediate layer of 2-fold coordinated oxygens. In spite of the low ion coordination number, this structure is remarkably stable (only 0.18 eV/TiO_2 above bulk anatase), and is readily obtained starting from a 4 ML (101)-oriented anatase slab.[19]

In Figure 1d, we report a comparison between the simulated and experimental STM map for the top of the *rect*′-TiO_2 island. We point out that the theoretical map was obtained from an unsupported film. To correct for the absence of the support−overlayer charge transfer, the empty states closest to the Fermi level were excluded from the Tersoff−Hamann procedure.

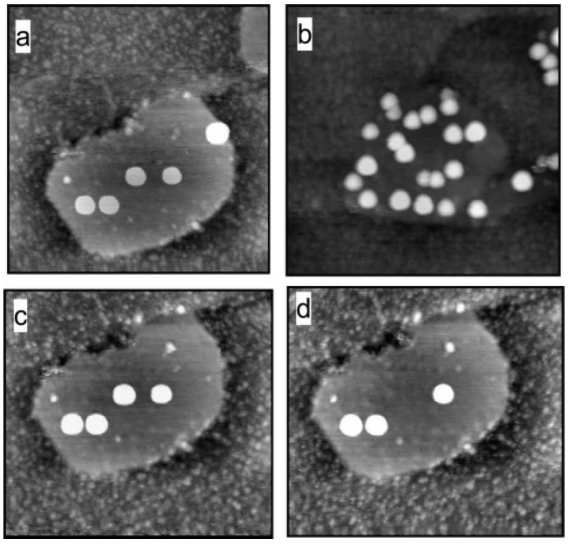

Figure 2. STM constant-current image of the *rect*′-TiO_2/*k*-TiO_x system after the deposition of Au NPs: (a) 0.2 ML of Au (82 × 82 nm^2; V = 1.5 V, I = 1.5 nA); (b) 0.8 ML of Au (82 × 82 nm^2; V = 1.5 V, I = 1.5 nA); (c and d) the same as part a in successive scans, demonstrating a tip-induced mobility.

As to the relevance to the present report, the important point is that we have the co-presence of two adjacent, well-characterized phases having rather different stoichiometry (i.e., Ti_2O_3 and TiO_2) and topography (a *kagomé-like* defective and a completely oxygen terminated surface, respectively). The STM image reported in Figure 2a shows the *rect*′-TiO_2/*k*-TiO_x system after the deposition of 0.2 ML of Au.[20] As it can be easily observed, there is a striking difference between the dimensions of the Au NPs imaged on the stoichiometric *rect*′-TiO_2 surface and those covering the reduced *k*-TiO_x surface. The particles deposited on the *rect*′-TiO_2 phase show an apparent height of ca. 1.5 nm and a diameter of ca. 5−6 nm. In contrast, on the reduced *k*-TiO_x phase, the Au NPs are characterized by a definitely smaller mean apparent height (0.2 nm) (with a larger spread in the height distribution) and diameter (1.5−2 nm). Since the flux of Au particles impinging on the sample surface is statistically the same (the *k*- and *rect*′-phases are co-present on the same spot of the Pt(111) surface), the fact that on the stoichiometric *rect*′ phase the Au NPs are characterized by a larger mean cluster size than on *k*-TiO_x strongly suggests a larger mobility of Au on the *rect*′-TiO_2 phase with respect to the *k*-phase, which favors the agglomeration and formation of larger Au NPs. When the Au coverage is increased to 0.8 ML, one observes an increase in the particle density of the NPs on the *rect*′-phase, even though their shape and dimensions are similar to those obtained at lower coverage (see Figure 2b). Considering the NPs on *k*-TiO_x, their mean apparent height (0.25 nm) and diameter (2.5 nm) are somewhat larger in the 0.8 ML system, even if the actual sizes are difficult to be precisely measured because many NPs are barely resolved.

To corroborate this analysis, adsorption energies and diffusion pathways and activation energy barriers for a single Au atom on both the *k*- and *rect*′-TiO_2 surfaces have been calculated via a DFT approach.[21,22] First, the optimal adsorption sites of Au atoms on the two titania surfaces have been found, and—starting from these sites—the diffusion mechanisms and the corresponding energy barriers have been calculated using a nudged elastic band (NEB) approach.[23] A striking difference was found for the two phases. A gold atom interacts very weakly with the *rect*′-phase, with a maximum adsorption energy on top of an oxygen atom of 0.30 eV. Correspondingly, the barriers for the two possible diffusion mechanisms by which the Au atom can jump from an oxygen site to the two neighboring ones are extremely small: 0.05 and 0.06 eV, respectively (see Figure 3a). It can be concluded that diffusion of Au single atoms (and presumably small clusters[21a]) is extremely fast on this phase, and that even medium-sized clusters can be mobile if subjected to sufficiently strong forces.

In contrast, a gold atom easily penetrates into the "holes" exposing the bare Pt(111) surface which characterize the *k*-phase and is strongly adsorbed there (with adsorption energies of 2.96 eV in the center of the hole), and the jump out of a hole into the nearest neighbor is energetically costly, with an activation energy barrier of about 2.4 eV (see Figure 3b). It is thus to be expected that significant diffusion of Au atoms on the *k*-phase can only occur at RT if they are not trapped into the holes but are kinetically hopping on top of the oxygen atoms in a metastable state (the corresponding adsorption energies and energy barriers were also calculated, finding values similar to those on the *rect*′-phase). Our results of a substantial influence of mobility on the growth of metal clusters are consistent with recent experimental data of MBE experiments of Au on the TiO_2(110) surface.[24] Note that the presence of some small and

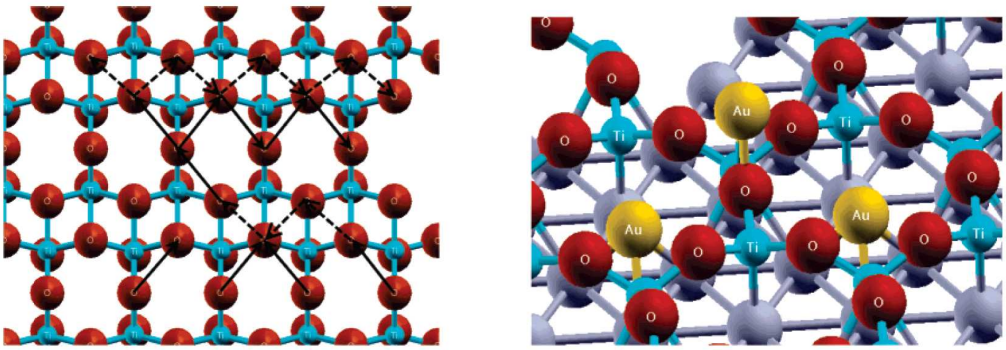

Figure 3. Diffusion mechanisms of a Au atom on the (a) *rect*′-TiO_2 and (b) *k*-TiO_x phases. Ti atoms are reported as light blue spheres, O atoms as red spheres, and Au atoms as golden spheres. On the *rect*′-phase, diffusion occurs through two different nearest-neighbor jumps, highlighted as full and dotted arrows in part a. On the *k*-phase, the initial, saddle-point, and final positions of a Au atom hopping from a hole into the next neighbor are shown in part b.

a few large Au NPs at the borders of the *rect'* islands in Figure 2 suggests that a step-edge (Ehrlich−Schwoebel) barrier is effective, which is consistent with the large mean size of the NPs and with a constant NP size as a function of coverage.[25]

Another interesting feature concerning the Au NP mobility on top of the *rect'*-TiO_2 surface is shown in Figure 2c and d, where we report the image of the same island taken after some tip passages: a tip-induced extraction of the NPs from the surface is clearly evident. This cannot be due to a simple movement out of the picture frame but is probably due to the fact that Au NPs can get attached to the STM tip.[26]

The present experimental data clearly show to what extent the different stoichiometry and defect structure of an oxide surface can influence the interaction with a metal.[27] In the case of Au on titania, a very weak interaction with TiO_2 stoichiometric surfaces is documented, with cluster nucleation occurring only in the presence of undercoordinated Ti atoms (e.g., step-edge decoration). It is quite clear from our data that undercoordinated Ti atoms are rare on the oxygen terminated surface of the stoichiometric *rect'*-TiO_2 islands. On the contrary, the peculiar *kagomé-like* structure of the wetting ML offers potential nucleation sites in the center of each hexagon. In this connection, we recall that an example of Au NPs deposited on a reduced *w'*-TiO_x ($x \approx 1.2$) ML phase has recently been published,[2] where the outermost layer is also a complete oxygen layer exhibiting a close-packed structure with virtually no defects. In that case, the mean diameter of the Au NPs was ≈3.5 nm, a value lower than that found on the *rect'*-TiO_2 island. The smaller size of the Au NP is to be attributed either to confinement effects[25] or to a lower Au mobility on the defect-free reduced *w'*-TiO_x phase with respect to the defect-free oxidized *rect'*-TiO_2 phase, a fact that can be rationalized by assuming a larger Au−substrate interaction in the reduced surface. A way to rationalize this larger interaction could be related to charging of the Au atoms on the *w'*-TiO_x phase, similar to what was proposed for analogous ultrathin systems.[28]

Acknowledgment. This work has been funded by European Community through two STRP projects (NanoChemSens, *Nanostructures for Chemical Sensors*, and GSOMEN, *Growth and Supra-organization of Transition and Noble Metal Nanoclusters*), by the Italian CNR through the project SSATMN within the framework of the ESF EUROCORES SONS, and by the Italian Ministry of Instruction, University and Research (MIUR) through the fund "Programs of national relevance" (PRIN-2003, PRIN-2005). Part of the calculations were performed at the Cineca Supercomputing Center within an agreement with Italian INFM-CNR.

References and Notes

(1) (a) Bell, A. T. *Science* **2003**, *299*, 1688. (b) Schlogl, R.; Abd, H. *Angew. Chem., Int. Ed.* **2004**, *43*, 1628. (c) Madey, T. E.; Pelhos, K.; Wu, Q.; Barnes, R.; Ermanoski, I.; Chen, W.; Kolodziej, J. J.; Rowe, J. E. *Proc. Natl. Acad. Sci. U.S.A.* **2002**, *99*, 6503.

(2) Sedona, F.; Agnoli, S.; Fanetti, M.; Kholmanov, I.; Cavaliere, E.; Gavioli, L.; Granozzi, G. *J. Phys. Chem. C* **2007**, *111*, 8024.

(3) Freund, H. J. *Surf. Sci.* **2002**, *500*, 271.

(4) Fallace, W. T.; Min, B. K.; Goodman, D. W. *Top. Catal.* **2005**, *34*, 17.

(5) Degen, S.; Becker, C.; Wandelt, K. *Faraday Discuss.* **2004**, *125*, 343.

(6) Berdunov, N.; Mariotto, G.; Balakrishnan, K.; Murphy, S.; Shvets, I. V. *Surf. Sci.* **2006**, *600*, L287.

(7) Hamm, G.; Becker, C.; Henry, C. R. *Nanotechnology* **2006**, *17*, 1943.

(8) Jordan, K.; Murphy, S.; Shvets, I. V. *Surf. Sci.* **2006**, *600*, 5150.

(9) Chen, M. S.; Goodman, D. W. *Science* **2004**, *306*, 252.

(10) Lopez, N.; Janssens, T. V. W.; Clausen, B. S.; Xu, Y.; Mavrikakis, M.; Bligaard, T.; Nørskov, J. K. *J. Catal.* **2004**, *223*, 232.

(11) Chen, M. S.; Goodman, D. W. *Acc. Chem. Res.* **2006**, *39*, 739.

(12) Chen, M.; Cai, Y.; Yan, Z.; Goodman, D. W. *J. Am. Chem. Soc.* **2006**, *128*, 6341.

(13) Hernandez, N. C.; Sanz, J. F.; Rodriguez, J. A. *J. Am. Chem. Soc.* **2006**, *128*, 15600.

(14) Kung, M. C.; Davis, R. J.; Kung, H. *J. Phys. Chem. C* **2007**, *111*, 11767.

(15) Chen, M. S.; Luo, K.; Kumar, D.; Wallace, W. T.; Yi, C.-W.; Gath, K. K.; Goodman, D. W. *Surf. Sci.* **2006**, *601*, 632.

(16) (a) Sedona, F.; Rizzi, G. A.; Agnoli, S.; Llabrés i Xamena, F. X.; Papageorgiou, A.; Ostermann, D.; Sambi, M.; Finetti, P.; Schierbaum, K.; Granozzi, G. *J. Phys. Chem. B* **2005**, *109*, 24411. (b) Finetti, P.; Sedona, F.; Rizzi, G. A.; Mick, U.; Sutara, F.; Svec, M.; Matolin, V.; Schierbaum, K.; Granozzi, G. *J. Phys. Chem. C* **2007**, *111*, 869.

(17) Mekata, M. *Phys. Today* **2003**, *56*, 12.

(18) Fortunelli, A.; Barcaro, G.; Sedona, F.; Granozzi, G. Manuscript in preparation.

(19) Vittadini, A.; Selloni, A.; Casarin, M. *Theor. Chem. Acc.* **2007**, *5−6*, 663. Vittadini, A.; Casarin M. *Theor. Chem. Acc.*, in press.

(20) The Au coverage has been determined by analyzing the STM images of Au on clean Pt(111). The typical deposition rate is about 0.3 ML/min.

(21) The computational details are similar to those used in previous work: (a) Barcaro, G.; Fortunelli, A.; Nita, F.; Ferrando, R. *Phys. Rev. Lett.* **2005**, *95*, 246103. (b) Barcaro, G.; Sedona, F.; Fortunelli, A.; Granozzi, G. *J. Phys. Chem. C* **2007**, *111*, 6095.

(22) Baroni, S.; dal Corso, A.; de Gironcoli, S.; Giannozzi, P.; Cavazzoni, C.; Ballabio, G.; Scandolo, S.; Chiarotti, G.; Focher, P.; Pasquarello, A.; Laasonen, K.; Trave, A.; Car, R.; Marzari, N.; Kokalj, A. http://www.p-wscf.org/.

(23) This method searches for the minimum energy path between two local minima by creating a fixed number of intermediate configurations (images) which are linked to each other by elastic springs. The image highest in energy does not feel the spring forces along the band; instead, the true force at this image along the tangent is inverted. In this way, the image tries to maximize its energy along the band, and thus, when this image converges, it is at the exact saddle point. See: Henkelman, G.; Uberuaga, B. P.; Jònsson, H. *J. Chem. Phys.* **2000**, *113*, 9901.

(24) Matthey, D.; Wang, J. G.; Wendt, S.; Matthiesen, J.; Schaub, R.; Laegsgaard, E.; Hammer, B.; Besembacher, F. *Science* **2007**, *315*, 1692.

(25) Krug, J.; Politi, P.; Michely, T. *Phys. Rev. B* **2000**, *61*, 14037.

(26) Durston, P. J.; Palmer, R. E.; Wilcoxon, J. P. *Appl. Phys. Lett.* **1998**, *72*, 176.

(27) Fua, Q.; Wagner, T. *Surf. Sci. Rep.* **2007**, *62*, 431 and references therein.

(28) Pacchioni, G.; Giordano, L.; Baistrocchi, M. *Phys. Rev. Lett.* **2005**, *94*, 226104.

VI.3 Reprint of the paper: Au Nanoparticles on a Templating TiO_x/Pt(111) Ultrathin Polar Film: a Photoemission and Photoelectron Diffraction Study

In this paper we present a detailed study, by mean of HR-XPS, ES and AS-PD, UPS and STM performed on a series of model catalyst obtained depositing Au on the reduced templating *z'*-TiO_x/Pt(111) UT film at different metal coverages. The spectroscopic and ES-PD data were collected at the Elettra synchrotron facility. The STM put in light how the Au NPs grow aligned along straight lines (the *z'*-TiO_x phase *troughs*) where they find preferential nucleation sites. The NPs average height population depends on the Au coverage: as long as the metal coverage is increased also the 2 and 3 layers thick NPs population increase. The PD data put in light that the ordered portion of the NPs grow in a (111) registry with the Pt support, in spite of the presence of the TiO_x UT film. This is probably due to the fact that the metal nucleates and grows in a direct contact with the Pt through the phase active sites (*picoholes* inside the phase *troughs*). Moreover, the AS-PD modulation observed for a 0.7 ML Au/*z'*-TiO_x/Pt(111) model system is in tune with the presence of a 3 layers Au NPs population, as observed with STM. The HR-XPS data suggest us the presence of 2 components in the Au 4f core peaks: a lower BE one (83.5 eV) due to the Au growing in direct contact with the phase oxygen topmost layer (high affinity) and a higher BE one (ca. 84.0 eV, a value typical for the bulk Au) due to the Au external layers. The higher BE component intensity increases as long as the Au coverage is increased and almost totally disappear after a thermal treatment of the sample, as a consequence of the NPs flattening.

The templating effect of the *z'*-TiO_x UT film has also been observed by mean of theoretical calculations. Based on the model proposed for the UT film, Au NPs with different dimensions were put on the TiO_x surface and showed a higher adsorption energy for the active sites (*picoholes*) that are present inside the phase *troughs*.

PAPER www.rsc.org/pccp | Physical Chemistry Chemical Physics

Au nanoparticles on a templating TiO$_x$/Pt(111) ultrathin polar film: a photoemission and photoelectron diffraction study

Gian Andrea Rizzi,[a] Francesco Sedona,[a] Luca Artiglia,[a] Stefano Agnoli,[a] Giovanni Barcaro,[b] Alessandro Fortunelli,[b] Emanuele Cavaliere,[c] Luca Gavioli[cd] and Gaetano Granozzi*[a]

Received 6th November 2008, Accepted 8th January 2009
First published as an Advance Article on the web 9th February 2009
DOI: 10.1039/b819791a

We present an in-depth investigation of Au nanoparticles self-assembled on a zigzag-like TiO$_x$/Pt(111) ultrathin polar film, whose structure is known in great detail. The peculiar pattern of defects (picoholes) templates a linear array of size-selected (*ca.* 1 nm) Au nanoparticles without disruption of the titania layer, as observed by scanning tunneling microscopy. Their structure and electronic properties have been investigated by several large-area spectroscopic tools, *i.e.* high-resolution core and valence level photoemission and angle-scanned and energy-scanned photoelectron diffraction. The comparison between experimental data and density functional theoretical calculations indicates that the Au atoms landing on the oxide film are rather mobile, and that the picoholes can act as effective trapping and nucleation centers for the growth of the Au nanoparticles. All the experimental results are in concord in indicating that the Au NPs are flat islands with a maximum thickness of 2–3 layers exposing the (111) surface.

1. Introduction

Metal nanoparticles (NPs) present many interesting and innovative properties that can find applications in fields such as photonics,[1] sensors and biosensors,[2,3] magnetism[4] and catalysis.[5] These properties strongly depend on the structure of the NPs at the atomic level. In order to take advantage of these properties for technical applications it is mandatory to find easy and reproducible synthesis routes and characterization techniques to accurately control the size and shape of the NPs.

With respect to the typical top-down sequential nanofabrication approaches, a simpler and more efficient method to obtain arrays of NPs relies on the bottom-up self-assembling approach.[6] When a templating substrate is adopted, usually a film with an ordered array of defects acting as preferential nucleation sites, an ordered array of NPs with reproducible size and structure over macroscopic sample areas could be obtained.[7] In this respect, oxide-based templates are more promising than metallic substrates because in many cases they are stable systems which survive at ambient conditions. For these reasons metal NP growth on nanostructured oxide surfaces is currently a very active field of research,[8,9] and several examples have been reported where oxide-based ultrathin films act as templates for NP[10–16] or even single metal atom growth.[17,18]

[a] *Dipartimento di Scienze Chimiche and ISTM-CNR, CNR-INFM and INSTM Research Units, Università di Padova, Padova. E-mail: gaetano.granozzi@unipd.it*
[b] *Istituto per i Processi Chimico-Fisici (IPCF) del CNR, via Giovanni Moruzzi 1, I-56124 Pisa, Italy*
[c] *Dipartimento di Matematica e Fisica, Università Cattolica, via dei Musei 41, Brescia, I-25121, Italy*
[d] *Laboratorio Nazionale TASC-INFM-CNR, SS 14, Km 163.5, Basovizza (TS), IT-34012, Italy*

We have recently focused our attention on the growth and characterization of several understoichiometric TiO$_x$/Pt(111) ultrathin films:[19] the structure of such reduced TiO$_x$ phases consists of a Ti/O double layer, with the Ti atoms at the interface with Pt (hence a polar film), presenting different defect motifs. Using STM we have demonstrated that a zigzag-like phase, having a unit cell of 1.66 × 1.44 nm^2 (hereafter z'-TiO$_x$/Pt(111)),[19,20] can effectively act as a template for Au NPs in a self-assembling process.[14] The STM data of the ultrathin film clearly reveal the presence of dark rows (troughs), spaced by 1.44 nm, whose structure and origin has been described in great detail:[20] it has been proposed that the picoholes present within the troughs could act as nucleation sites, driving the formation of Au NPs which are ordered along straight lines with the same periodicity of the troughs. However, the local information deduced by STM limits the possibility of understanding the epitaxial relationship of the NPs with the substrate, their growth mechanism and crystallinity.

In the present study we extend our previous STM investigation on the Au/z'-TiO$_x$/Pt(111) system[14] by using several large-area spectroscopic techniques, such as high-resolution core (HR-XPS) and valence level (VB-UPS) photoemission and angle-scanned (AS) and energy-scanned (ES) photoelectron diffraction (PD). The added value of the present study consists of using a range of structural probes applied to Au deposition on a substrate whose structure is known in great detail.[19,20] The PD technique[21] can provide information on the epitaxial relationship between the Au NPs and the substrate and some indication about the onset of 3D NP formation. The HR-XPS and VB-UPS measurements, carried out with synchrotron radiation, were used to characterize the electronic properties of the Au NPs deposited on the z'-TiO$_x$/Pt(111) substrate. Actually, peculiar electronic properties of Au

NPs (if compared with Au deposited on a TiO_2 substrate) are expected due to the low (between +2 and +3) oxidation state of Ti in the substrate and the presence of a metallic surface just a few Å below the oxide surface. The discussion of the present results will take advantage of density functional (DF) calculations which allowed us to derive some hints on the mobility of Au atoms and the preferential nucleation sites on such a strongly anisotropic system.[22]

II. Experimental and computational details

The Pt(111) substrate (MaTecK disk of 8 mm diameter and 3 mm thickness cut and mechanically polished with accuracy better than 0.1° with respect to (111) surface plane) was cleaned by several cycles of Ar^+ sputtering, ultra high vacuum (UHV) annealing at 900 K and then exposed to a pressure of 5×10^{-4} Pa of oxygen before cooling down. The subsequent low energy electron diffraction (LEED) inspection revealed a well defined (1 × 1) diffraction pattern.

The preparation and structural characterization of z'-TiO$_x$/Pt(111) have been reported in detail elsewhere.[19,20] The prepared ultrathin films were completely wetting the substrate surface as checked by using CO as chemisorption probe. Au has been evaporated from an e-beam evaporator directly on the TiO$_x$/Pt(111) films held at room temperature (RT). The amount of Au deposited was determined using angle resolved XPS, based on the layer by layer growth of Au on Pt(111). Coverage values expressed in monolayer equivalents (MLeq) are calculated assuming the growth of Au(111) and an interlayer distance between adjacent plane of 0.235 nm.

All the AS-PD spectra were collected in a UHV VG ESCALAB MK II (Vacuum generators, Hastings, England) system (base pressure of 5×10^{-8} Pa) consisting of two separate chambers: an analysis and a preparation chamber. The system is equipped with a four grids rear view LEED, an electron beam evaporator with an integrated flux monitor, a mass quadrupole, a twin (Mg/Al) anode X-ray source with hemispherical electrostatic analyzer with a five channeltrons detector. The binding energy (BE) calibration was carried out using the 4f peaks of the Pt(111) sample. The angular acceptance of the analyzer can be varied between 1.5° and 8° (for the current AS-PD experiments a value of 3.5° has been used). The sample was mounted on a two-axis goniometer which allowed the sweeping of the electron emission direction with an angular resolution of ±1° both in polar angle (θ, defined with respect to the surface) and in azimuthal angle ϕ.

All the HR-XPS, VB-UPS and ES-PD measurements were carried out at the Materials Science Beamline, Synchrotron Elettra in Trieste, Italy, operated by the Charles University of Prague, Academy of the Sciences of the Czech Republic and Sincrotrone Trieste S.p.A. The UHV analysis chamber had a base pressure of 1×10^{-8} Pa. The temperature was measured with a K-type thermocouple attached to the rear surface of the crystal. The system was equipped with an hemispherical electron analyzer Phoibos 150 (Specs, Berlin) which operated in fixed analyzer transmission mode. For photoemission measurements the adopted geometry implies $\theta = 30°$ for photon incidence and $\theta = 90°$ for electron emission angles and the monochromator, designed according to the SX 700 concept, permitted to select the photon energy in the range of 22 to 1000 eV from the bending magnet. In our experiment we used the following photon energies, representing the best compromise to maximize both photon flux and photoemission cross sections: 40 eV (VB-UPS) and 130 eV (Au 4f, Pt 4f), with the total resolution of 0.06 and 0.1 eV, respectively. ES-PD measurements were performed on the Au 4f line by collecting photoelectron energy distribution curves (EDCs) approximately 9.0 eV wide and covering the photon energy range between 120 eV and 270 eV in steps of 0.05 eV. Measurements were made at normal emission, with p-polarised photons incident onto the sample at an angle of $\theta = 30°$. Integrated areas were calculated after a fitting procedure and plotted as a function of electron kinetic energy to produce PD curves with modulations characteristic of the local structural environment of the Au emitters. Non-diffraction contributions to these modulations due to parameters such as the variation in the transmission of the beamline, atomic photoemission cross-sections, analyser transmission and decay in photon flux with time were removed by fitting the raw data with third order polynomial splines, thus obtaining I_0 curves for each scan. Final results are displayed as $\chi(E)$ modulation curves, where $\chi(E) = (I(E) - I_0)/I_0$. All photoemission data were acquired at RT.

The STM data were acquired in an Omicron Multiscan Lab system (University of Brescia), operating in UHV conditions (with a base pressure $< 5 \times 10^{-9}$ Pa) and equipped with surface preparation facilities. The STM images were obtained in constant current mode at RT, with tip to sample bias ranging from 0.4 to 1.5 V and tunnelling current ranging from 0.2 to 0.8 nA.

DF calculations were performed using the same approach previously reported in detail:[23] the PWscf (plane-wave self-consistent field) computational code[24] was adopted, employing ultrasoft pseudopotentials[25] and the PW91 exchange–correlation functional.[26] A value of 30 Ryd for the energy cutoff on the wave function, a value of 150 Ryd for the energy cutoff on the electronic density, about 8–10 Å of empty space between replicated cells, a metal support described using 2 layers of Pt, and a (2,4,1) k_{mesh} grid for the sampling of the first Brillouin zone were used. All the calculations were performed spin-unrestricted. The z'-TiO$_x$/Pt(111) phase has a commensurate rectangular unit cell aligned along a $<1\bar{1}0>$ direction of the Pt(111) surface and $Ti_{24}O_{30}$ stoichiometry. The Car–Parrinello (CP) simulations of the diffusion of a single Au atom were performed using the ESPRESSO software.[27] The time step was set to 25 au, the electron mass to 3500 au, a CP run consisted of: 500 minimization steps, 200 MD steps starting with null velocities at 300 K, and a variable number of production MD steps at the chosen temperature for a total simulation time of 5 ps using a Nosé thermostat for the kinetic energy of the electronic wave function.

III. Results

III.1 Photoemission data

In Fig. 1 we report the HR-XPS Au 4f spectra at different coverage (0.1–0.9 MLeq) of Au/z'-TiO$_x$/Pt(111), collected

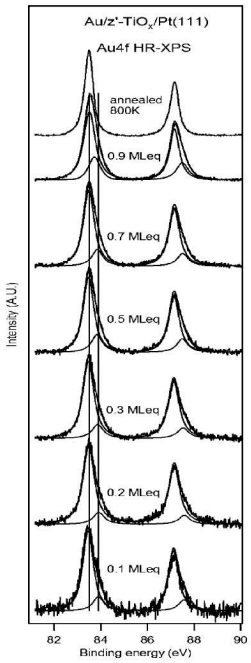

Fig. 1 Au 4f HR-XPS data of Au/z'-TiO$_x$/Pt(111) $h\nu$ = (130 eV) as a function of the Au coverage. The spectrum of the 0.9 MLeq sample after a UHV annealing at 800 K is also reported.

with a photon energy of 130 eV, together with the results of a fitting analysis. The Au 4f peaks can be fitted with two components: the first one centered at a BE of 83.5 eV and a second one at 83.9–84.0 eV. We do not observe any energy variation in the two components up to a coverage of 0.7 MLeq. At the maximum coverage (0.9 MLeq) the high BE component is slightly shifted towards lower BE. In Fig. 1 we also show for comparison the Au 4f peak at the highest coverage (0.9 MLeq) after a thermal treatment at 800 K in UHV. After the annealing, the Au 4f peak can be fitted with a single component at BE = 83.6 eV.

The VB-UPS data at different coverage (0.1–0.9 MLeq) of Au/z'-TiO$_x$/Pt(111) are reported in Fig. 2a, as well as the data of the clean ultrathin film (dotted line). In order to outline the contribution from the Au NPs, the VB-UPS data obtained by subtracting the VB-UPS profiles of the clean z'-TiO$_x$/Pt(111) film for each spectrum are also reported in Fig. 2b. The subtracted contribution has been attenuated by a progressively decreasing factor, obtained by measuring the intensity decrease of the Pt 4f$_{7/2}$ photoelectrons (taken with a photon energy of 130 eV so that their kinetic energy is *ca.* 55 eV), as the Au coverage was increased. It is important to note that the error introduced by the attenuation factor (we have tested changes of the attenuation factor by ±20%) modifies only to a negligible extent the shape of the VB-UPS profile in the region of interest, *i.e.* beyond 2 eV of BE. As explained in the Discussion section, the analysis of the 5d Au electronic levels allow us to obtain some insight into the Au NPs physical state. The profile obtained at a Au coverage of *ca.* 0.9 MLeq is characterized by two strong features centered at about 3.3 (A$_1$) and 5.5 eV (A$_2$) (Fig. 2). With increasing the Au coverage, the

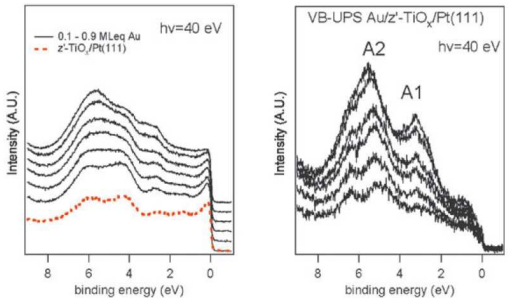

Fig. 2 VB-UPS data of Au/z'–TiO$_x$/Pt(111) ($h\nu$ = 40 eV) as a function of the Au coverage (0.1, 0.2, 0.3, 0.5, 0.7 and 0.9 MLeq): (a) raw data together with the data of the clean z'-TiO$_x$/Pt(111) film (bottom, dotted line). (b) the VB-UPS profiles after subtracting the VB-UPS data of the corresponding z'-TiO$_x$/Pt(111) film (see the text for the subtraction procedure).

A$_1$ peak stays almost unshifted, while the A$_2$ peak shifts from 4.9–5.0 eV to 5.5 eV. A third component, well resolved at low coverage at about 6.5 eV, merges in the A2 peak at higher coverage.

III.2 Photoelectron diffraction data

A simple way to obtain crystallographic information on the Au NPs and to detect any possible epitaxial ordering is to perform AS-PD experiments where both the substrate Pt 4f and the NPs Au 4f signals are acquired during the same run. In Fig. 3 we report the 2π angular intensity plots for the Au 4f peak at a Au coverage of 0.7 MLeq and the corresponding Pt 4f plot.[28] In this type of presentation the centre of the plot corresponds to the surface normal, the radial section displays a polar scan and the circular section an azimuthal scan. The photoelectron intensity is given by the corresponding value of the color scale. After having acquired single azimuthal scans for an angle range of about 150° and verified the existence of a symmetry plane every 120°, which implies the existence of a C_3 axis, the data were acquired in a 126° range in ϕ, and for θ spanning from 66° to 26° (to reduce the total acquisition time) and finally were averaged through the symmetry plane. The final plot, where the whole 2π range is shown, was obtained by simply repeating three identical set of data covering a 120° range in ϕ. It is immediately evident (Fig. 3) that the Pt 4f and Au 4f plots presents only minor differences. It is important to remind that in the case of Au 4f and Pt 4f the diffraction pattern can be directly compared without the aid of

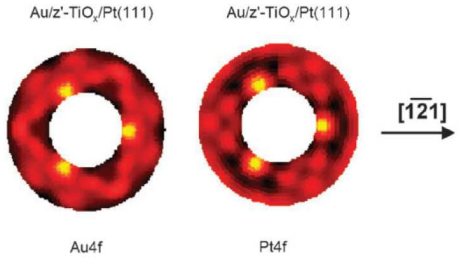

Fig. 3 AS-PD 2π plots of the intensity of the Au 4f peak of Au/z'-TiO$_x$/Pt(111) at a coverage of 0.7 MLeq. The analogous plot for the Pt 4f peak is reported for comparison.

calculations since the kinetic energies of the photoelectrons differ only by 13 eV. The three intense peaks due to M–M forward-scattering (FS)[21] along $\langle 1\bar{2}1\rangle$ directions (at an ideal polar angle of $\theta = 55^\circ$) due to atoms in adjacent layers are found also in the Au 4f 2π plots so that it is straightforward to take for granted that Au NPs having a double layer (see Discussion section) and exposing the (111) plane represent a statistically significant subset of the NPs array at a coverage of 0.7 MLeq. In addition, a preferential azimuthal alignment of the Au NPs with respect to the Pt(111) substrate can be observed within the experimental error ($\pm 1.5^\circ$), with the simple epitaxial relation (111) $[1\bar{2}1]$//(111) $[1\bar{2}1]$.

Further information comes from the detailed analysis of the single polar curves (not reported). The actual position of the FS peak is observed at a polar angle close to 55° and this can be taken as an indication that the Au NP grow with a bulk-like structure without any in-plane strain.[21]

Interestingly, the AS-PD curves recorded for the O 1s peak do not show any measurable intensity oscillation, and considering the fact that the oxygen layer is the top-layer this would imply either that the oxygen emitters are spatially disordered after Au NPs nucleation or that they are intrinsically unequivalent emitters so averaging to zero the resulting diffraction. This fact might be in relation with the observed fading of the LEED pattern after the Au deposition, even in the low coverage range.

In Fig. 4 we report a series of ES-PD Au 4f $\chi(E)$ curves on Au/z'-TiO$_x$/Pt(111) for the coverage range analysed in this paper. These data can provide further information on the onset of 3D growth of the Au NPs. The data are characterized by two intense features at about 190 and 245 eV, that increase as the growth proceeds. Both features start to be evident at coverage higher than 0.2 MLeq. In Fig. 4 we also report for comparison the corresponding Pt 4f $\chi(E)$ curve taken in the identical experimental conditions on the Pt(111) substrate, showing that the peaks at 190 and 245 eV are representative of a 3D bulk-like structure of an fcc metal. Therefore our experimental data suggest that the onset of the 2nd Au layer occurs at a coverage between 0.2–0.3 MLeq.

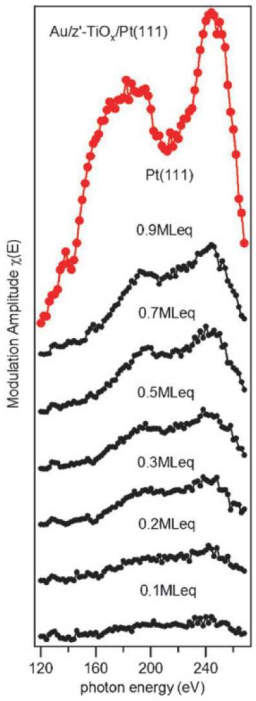

Fig. 4 Plot of the ES-PD Au 4f $\chi(E)$ curves of Au/z'-TiO$_x$/Pt(111) where the Au coverage was varied from about 0.1 to 0.9 MLeq. The corresponding Pt 4f $\chi(E)$ curve of the clean Pt(111) substrate is also reported for comparison (upper curve).

IV. Discussion

Before discussing the data reported in the previous section, it is useful to summarize what is known on the structure of the z'-TiO$_x$/Pt(111) ultrathin polar film. The starting point is the experimental demonstration by AS-PD data[19] that such polar reduced films can be described as a bilayer, where the Ti atoms are at the interface with the Pt(111) surface, while the O atoms form the topmost layer. According to the model structure derived by DF calculations,[20] the Ti atoms are not allowed to continue the fcc stacking of the Pt(111) surface due to mismatch considerations. Hence the Ti layer grows creating denser stripes separated by less dense regions (the dark troughs in the STM image), while the O atoms solve the overcrowding problem with the formation of dislocation lines within the stripes. In the end, the z'-TiO$_x$/Pt(111) film has been described as constituted by TiO$_{1.20}$ stripes, aligned with the $[1\bar{1}0]$ direction of the Pt substrate, coupled by 2 Ti_2O_3 units per unit cells, so that a final stoichiometry of TiO$_{1.25}$ is obtained.[20]

The zigzag-like pattern seen in the STM images has been explained by the presence of two different Ti atoms, *i.e.* 4-fold oxygen-coordinated Ti atoms and 3-fold oxygen-coordinated Ti atoms. The former Ti atoms are more oxidized (more positively charged) than the latter ones, thus having a greater density of empty electronic states above the Fermi energy, which explains why they appear as brighter spots in the experimental STM images at positive bias. High-resolution STM images clearly show that a series of elliptical black features with alternating orientation can be resolved along the troughs: such black features do not have a long range periodicity and they have been described as picoholes, where the TiO$_x$ layer is left with uncovered Pt areas of different size, depending on the annealing temperature.[20]

A theoretical study of the interaction of a single Au atom with the z'-TiO$_x$/Pt(111) film has been already reported.[22] There, it was shown that Au has a higher affinity for the defective sites (basically, Ti vacancies or picoholes inside the troughs and exposing the bare Pt(111) substrate) than for the zigzag-like stripe regions. With the latter regions, Au was found to interact according to two different regimes: (1) a weak interaction regime on top of the overlayer oxygens, in which the Au atom remains essentially neutral and exhibits a rather low adsorption energy (less than 0.2 eV); (2) a strongly interacting regime on top of the Ti atoms, in which Au extracts a Ti atom from the interface, with a strong perturbation of the TiO$_x$ bilayer and a correspondingly much larger (around 0.8 eV) final adsorption energy. This phenomenon bears similarity with other examples in the literature.[29,30] It should

be noted, however, that Au atoms are mobile even in the strongly interacting regime. We performed in fact short runs (typically, few ps) of CP simulations at 600, 900 and 1200 K on a single Au atom adsorbed on the center of the stripe of the z'-TiO$_x$/Pt(111) phase and estimated that the corresponding diffusion energy barrier is about 0.4–0.5 eV, and is thus compatible with finite mobility at RT. More complicated effects, such as a step-edge (Ehrlich–Schwoebel) barrier at the border of the stripes as found in an analogous system,[31] have not been investigated. From these numerical results it is suggested that Au atoms landing on the oxide stripes are rather mobile and that the picoholes along the troughs can act as effective trapping and nucleation centers for the growth of Au NPs. This is confirmed by the fact that DF calculations on Au dimers and trimers adsorbed on the compact, stripe regions of z- and z'-TiO$_x$/Pt(111) films do NOT present a disruption of the TiO$_x$ structure with the formation of Au–Ti bonds typical of the strongly interacting regime: the strong Au–Au bonding competes with the Au–Ti bond and weakens the metal–surface interaction (at least in such small clusters).

The first point we want to address is the size and morphology of the Au NPs, by cross checking the AS-PD and ES-PD data with the STM data. In Fig. 5 we report two STM color images taken on the Au/z'-TiO$_x$/Pt(111) system at two different Au coverage (0.35 MLeq (a) and 0.70 MLeq (b), as derived from the analysis of the STM images).[32] Comparing Fig. 5a and b it can be deduced that the coverage increase does not substantially affect the Au NP size, while the NP density is almost doubled. The apparent NP mean size is *ca.* 1.3 nm, even though a precise size determination is hampered by tip convolution factors. Taking into consideration that the lateral size inferred from the STM data is an upper limit, a rule of thumb evaluation tells us that the Au$_N$ clusters observed in our experiments are expected to be in the range of $10 < N < 40$. In any case, the STM data are compatible with an ordering effect along the troughs which is maintained even at the higher coverage (0.7 MLeq). The image color scale of Fig. 5 has been chosen to highlight the height distribution of the NPs: in fact the observed apparent heights are compatible with NPs one and two monolayer high, while three monolayer high NPs are only rarely observed at 0.3 MLeq coverage. This is consistent with the appearance in the PD spatial integrated measurements (Fig. 3 and 4) of features attributable to 3D Au NPs starting from 0.2–0.3 MLeq coverage. Moreover, the intensity increase of such PD features as a function of increasing Au coverage is reflected in the evolution of the NP distribution observed by STM. In fact the NPs do not grow laterally but increase in density, with the presence of three monolayer thick NPs statistically more abundant at higher coverage (Fig. 5b). As far as the shape of the NP is concerned, despite tip-convolution effects, one can observe that the smallest NPs in Fig. 5a also appear slightly elongated in the direction of the troughs, whereas the larger NPs in Fig. 5a and b exhibit a more rounded shape. This would suggest that a shape transition is occurring for Au NPs, presumably when the N value of Au$_N$ passes from the lower limit ($N \sim 10$) to the higher one (see considerations reported in the following).

As a whole, the comparison of the PD and STM data indicates that the Au NPs are at least two monolayers thick and grow exposing a (111) stacking. In addition, the Au NPs keeps the in-plane lattice constant very close to the value of bulk Au. In fact, there is no evidence of any measurable trigonal distortion of the cell as proven by the position of the Au–Au FS peak found at $\theta = 55°$ from the surface.

Further information on the NP morphology can be deduced by comparing the experimental data of Fig. 3 with the results of a theoretical simulation of the PD pattern, carried out within the frame of the multiple scattering cluster (MSC) theory.[33] In Fig. 6 we report a comparison between the 2π plot AS-PD data of the Au(0.7 MLeq)/z'-TiO$_x$/Pt(111) system (Fig. 6b) and two different simulations carried out on a cluster having either two (Fig. 6a) or three (Fig. 6c) Au atomic layers. The MSC simulations were obtained from the EDAC software package,[34] using a 60 atoms cluster with a 13 Å diameter. It is well evident that the three atomic layers thick model better reproduces the experimental fine structure. This is a strong evidence for the presence at the 0.7 MLeq coverage of truly 3D Au NPs with a not negligible contribution from a 3rd layer.

The second point we want to address is the epitaxial ordering of the Au NPs. The AS-PD data reported in the previous section (Fig. 3) clearly show that the Au NPs are exposing the Au(111) surface with a preferential azimuthal

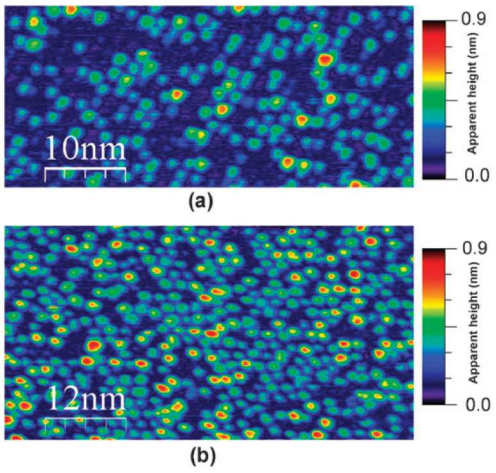

Fig. 5 Color STM pictures of Au/z'-TiO$_x$/Pt(111) at different coverage: (a) 0.35 MLeq (50 × 28 nm, $V = 0.6$ V $I = 0.6$ nA), (b) 0.70 MLeq (48 × 31 nm, $V = 1$ V $I = 0.5$ nA).

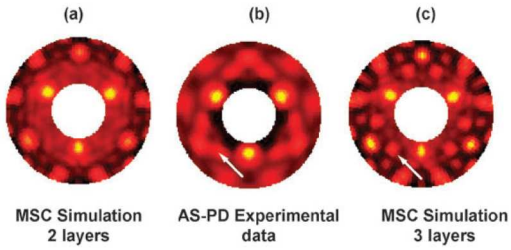

Fig. 6 Comparison between the experimental AS-PD 2π plot of the intensity of the Au 4f peak of Au(0.7 MLeq)/z'-TiO$_x$/Pt(111) system (b) and two MSC simulations obtained with a Au cluster having 2 (a) or 3 (c) Au layers. The arrows indicate the features associated to the presence of the 3rd layer.

alignment along the low index direction of the underlying Pt(111) substrate, *i.e.* implying the epitaxial relation (111) [1$\bar{2}$1]//(111) [1$\bar{2}$1].[35] We remind here that PD technique provides structural information on the ordered portions of a system, summing up coherently their contributions.[21] For this reason we cannot exclude that part of the Au NPs are randomly oriented in the azimuthal direction. The question to be answered is the origin of such epitaxial ordering. A naïve interpretation would suggest that the Au islands are in direct contact with the Pt(111) substrate, after having partially or completely disrupted the TiO$_x$ ultrathin film. This mechanism has been invoked to explain the behavior of more reactive metals deposited on oxide ultrathin films, *i.e.* Fe on TiO$_x$/Pt(111)[36] and Co on VO$_x$/Rh(111),[37] where the higher reactivity of the adsorbed metals gives rise to a competition for the oxygen atoms with the metal of the oxide film (Ti, V). According to existing STM and photoemission data, the ultrathin films is either restructured[36] or displaced[37] and the deposited metal goes directly in contact to the interface with the substrate. Similarly, in the case of Ag/c(4 × 2)NiO$_x$/Pd(100) system, a (100)[001]//(100)[001] epitaxial relation of the Ag NPs with the Pd(100) substrate has been demonstrated,[38] but evidence from XPS and AS-PD data suggested the possibility that the c(4 × 2)-NiO$_x$ phase was altered after the Ag deposition.

However, according to our STM data, this is not the case when the noble Au metal is deposited on the z'-TiO$_x$/Pt(111) substrate (Fig. 5):[14] at the very early stage of deposition Au islands are nucleated within the troughs of the layer, their shape appears elongated along them, and no evidence is seen of any disruption of the template itself around the Au islands and/or encapsulation of the Au islands. In addition, as already pointed out above, the Au NPs have a rather uniform size even at a coverage up to 0.7 MLeq (*i.e.* increasing the Au coverage a higher density of almost identical Au NPs is observed) and they keep growing along the troughs even though their shape is no more elongated along them. Again, this is in keeping with the fact that—according to DF calculations—Au dimers and trimers adsorbed on the stripe regions of the z'-TiO$_x$/Pt(111) film do not present a strongly interacting regime (see above). The upholding of the Au/oxide/Pt stacking is also in agreement with previous studies for Au NPs deposited on TiO$_x$/Ru(0001) films, where the authors exclude any evidence of Au encapsulation by TiO$_x$ suboxides.[39] Incidentally, adsorption of CO, studied by thermal programmed desorption (TPD),[40] on Au NPs deposited on different TiO$_x$ ultrathin films is in agreement with the hypothesis that the Au NPs are not directly bound to the Pt(111) substrate. So, the preferential alignment of the Au(111) islands along the Pt(111) directions must be motivated by more subtle factors than the direct contact with the Pt(111) substrate.

Some speculation on the origin of the azimuthal alignment of the Au NPs can be done on the basis of theoretical simulations, *i.e.* DF ones on the preferred Au$_N$ cluster structural arrangements and MSC ones for the AS-PD patterns. If we take into consideration the suggestions coming from the DF simulations on the interaction of single Au atoms with the z'-TiO$_x$/Pt(111) phase,[22] and the previously reported calculations on single-atom diffusion and Au$_2$ and Au$_3$ adsorption on the z'-TiO$_x$ stripes, there is little doubt about the hypothesis that the preferential attachment sites for single Au atoms are the picoholes within the troughs. The open question is the actual shape of the NPs and their epitaxial relationships to the substrate. Even if rigorous DF predictions on this system are complicated by the large size of the unit cell and the intrinsic difficulties of structure predictions for supported metal clusters, some indications can be drawn from exploratory DF calculations. In principle, a first-principles systematic search would be in order, similar to the one recently reported for the first time for supported metal clusters.[41] Preliminary calculations using this protocol have been conducted on the smallest sizes of Au$_N$ clusters by supposing that the oxide substrate can locally relax but is not disrupted by the interaction with Au atoms.[42] Two typical configurations obtained for Au$_3$ and Au$_8$ clusters are shown in Fig. 7. It can be noted that the clusters grow around the oxide picohole and have a basically planar structure oriented along the troughs. Note that the height of these clusters is about 4 Å. This might be consistent with the experimental STM images at the lowest coverage,[14] and also with the fact that gas-phase Au clusters are planar up to size Au$_{13}$.[43] It is known, however, that even in the gas-phase a structural transition occur for $N > 13$, from planar to cage configurations. A similar transition can be hypothesized to occur also for supported clusters, and we would expect that this transition would cause an increase in the apparent height and a transition toward more rounded NPs similar to the one discussed above and reported in Fig. 5. It can be noted in this connection that an analysis of the electronic density and the density of states of adsorbed Au$_2$–Au$_8$ clusters similar to that conducted in ref. 29 for a single adsorbed Au atom shows that no charging of Au atoms in clusters bound to the defective hole of the z'-TiO$_x$/Pt(111) film seems to occur in this system, *i.e.*, the Au charge state seems to be essentially neutral.[44] This is in keeping with expectations based on the polar nature of the oxide layer and the high work function of the underlying Pt support:[20,23] at variance with non-polar ultrathin films, metallization of the oxide layer is the actual depolarization mechanism for these phases, which in turn entails a constancy of the high work function and scarce polarizability of the Pt support and thus a minor role of charging/image-charge-stabilization effects. It can also be added that CO binds to the least-coordinated sites of the Au clusters with binding energies very similar to those found for gas-phase clusters.

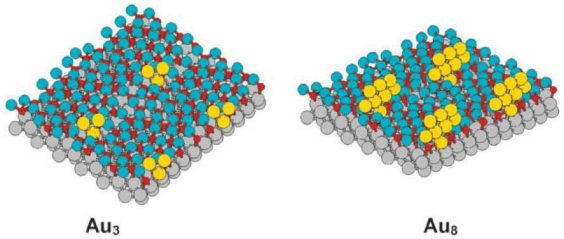

Fig. 7 DF optimized structures for the adsorption of Au$_N$ clusters on the z'-TiO$_x$/Pt(111) phase: platinum atoms are grey, oxygen atoms are light blue, titanium atoms are red, gold atoms are yellow.

On the other hand, MSC simulations of the AS-PD pattern carried out with model systems implying Au_N planar structures oriented along the troughs (and summed up for the three equivalent domains rotated by 120°) have furnished an AS-PD pattern which is not far the experimental one observed at higher coverage (0.7 MLeq). So we could speculate that the transition from elongated NPs toward more round shaped NPs observed by STM might reflect such intrinsic shape transformation from a planar structure oriented along the troughs (see Fig. 7) toward more isotropic 3D NPs.

This type of scenario can be checked against the HR-XPS and VB-PES data reported in Fig. 1 and 2. Our HR-XPS Au 4f data (Fig. 1) clearly show the coexistence of two types of Au states, shifted by a value of *ca.* 0.3–0.5 eV: one centred at 84.0 eV and a second one, more intense, at about 83.5 eV. In literature there are several studies that relate BE shifts of the Au 4f peak to size and substrate effects.[45] Summarizing the literature data, we can say that Au NPs have a shift toward higher BE with respect to bulk Au due to final state effects (reduced intra-atomic relaxation due to spatial confinement). Such a shift seem to be reduced in the case of interacting substrates (*e.g.* TiO_2) with respect to inert ones (*e.g.* SiO_2).[46] In addition, charge transfer effects (*e.g.* Au NPs on reduced substrates like TiO_x, the ones of this study) can partially cancel out the shift toward higher BE.[39,47] According to the mentioned literature data it would be plausible to assign the lower BE component at 84.0 eV to Au NPs of smaller size, while the component centered at 83.5 eV should correspond to larger Au NPs. The rather low energy shift value assigned to larger Au NPs is compatible with the value measured by other authors for Au deposited on TiO_2 and TiO_x films grown on Ru(0001).[37] Such interpretation would be consistent with the STM results discussed above, since a minority of smaller NPs can be easily seen in Fig. 5.

The HR-XPS data obtained after the annealing treatment at 800 K are reported on top of Fig. 1: interestingly, the position and shape of the lower BE component at 83.5 eV is perfectly coincident with the position and shape of the Au 4f peak after annealing at 800 K. On the other hand, we know from STM that after the annealing at 800 K, single layer Au islands wetting the TiO_x surface are actually imaged.[14,48] This evidence leads us to propose an alternative interpretation of the HR-XPS data which relates the Au 4f component at 83.5 eV to Au atoms at the interface with the TiO_x substrate, while the component at 83.9–84.0 eV could be assigned to undercoordinated Au atoms of the external layers. Such an interpretation is in tune with the data recently reported for Au NPs on a templating h-BN nanomesh on Rh:[49] the BE values of the two components are coincident with those reported in literature and the intensity ratio between them were interpreted by the authors as indicative of Au islands presenting one or two atomic layers. In addition, at the highest coverage herein studied (0.9 MLeq) the component at 84.0 eV slightly shifts to lower BE and increases its intensity with respect to the lower coverage data; this probably reflects the presence of a 3rd layer of Au atoms, in agreement with the discussed STM and PD diffraction data reported in Fig. 5 and 6. A further evidence which supports this interpretation comes from the analysis of the HR-XPS Au 4f peak after dosing CO (10 L at 140 K) (Fig. 8): the appearance of a higher BE peak (*ca.* 84.5 eV) is observed after CO dosing which is in tune with a shift of the component due to undercoordinated Au sites as a consequence of the charge flow from Au → CO. The preferential binding of CO with undercoordinated Au atoms is very well documented.[50,51] On the other hand, the same experiment carried out after the annealing treatment at 800 K does not show any evidence of adsorbed CO, as expected for a 2D Au NP.[52]

Finally we discuss the VB-UPS data reported in Fig. 2. It has been demonstrated that the actual VB profile due to Au 5d states contains information on the size of the Au system.[53] Since the VB features of the Au NPs overlap with the features from the TiO_x/Pt(111) substrate, the Au 5d states in our investigated systems at different coverage have been put in evidence by the subtraction procedure described in the previous section 3 (Fig. 2b). One simple interpretation (usually applied in the XPS regime) correlates the profile with a simple valence bonding theory assuming that the Au 5d shell, even if contributing to the VB, shows a residual atom-like spin orbit splitting into $5d_{5/2}$ and $5d_{3/2}$ components. An alternative interpretation, based on a delocalized molecular orbital (MO) like elementary theory, associates the lower BE component to antibonding MOs and the higher BE one to their bonding counterpart. It has been proposed that the splitting between the two $5d_{5/2}$ and $5d_{3/2}$ components correlates rather well with the number of Au NN:[53] in the case of a free atom the value of the splitting is about 1.4 eV and this value increases almost linearly with the numbers of Au NN, up to 2.8 eV for bulk Au. In terms of the MO theory, this can be related to the fact that the low BE antibonding MOs shift more than their bonding counterpart MOs when increasing the number of NN.

Our results show a different behaviour since the component at low BE (A1 in Fig. 2b) does not present any shift by increasing the Au coverage, while the component A2 does. However a comparison of our data with the VB spectra obtained from a Au(111) bulk surface with a similar photon energy[54] shows a rather good agreement although it is difficult to distinguish all the features reported in the case of the

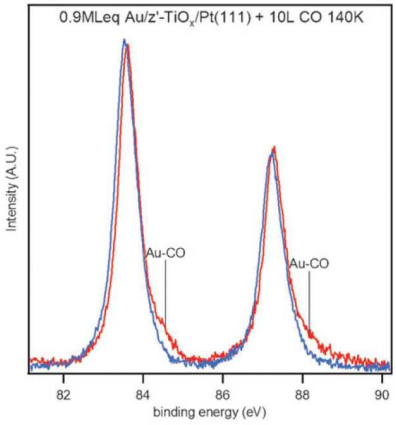

Fig. 8 Au 4f HR-XPS data ($h\nu$ = (130 eV) of Au(0.9 MLeq/z'-TiO_x/Pt(111) before and after dosing of 10 L of CO at 140 K.

Au(111) bulk surface, probably because of the background subtraction procedure. The A1 and A2 bands (at 3.3 and 5.5 eV at a coverage of 0.9 MLeq) are found at 3.5 and 5.9 eV in the case of bulk Au(111), respectively.[54] As described in section III.1, the A2 component progressively shifts from 4.9 to 5.5 eV as long as the growth proceeds and this trend could be explained with the developement of 3D Au NPs.

V. Conclusions

By capitalizing on the in depth knowledge built on the structure of the z'-TiO$_x$/Pt(111) ultrathin film,[19,20] in the present paper we were able to discuss in great detail the growth and the morphology of an ordered array of Au NPs in the range size of one nm.

The first Au atoms arriving on the highly anisotropic oxide layer find a landscape (the oxygen terminated surface) where they can easily move (see the DFT computed diffusion barriers of about 0.4–0.5 eV, compatible with finite mobility even at RT) and eventually be trapped on the existing picoholes, which can then be considered as preferential nucleation sites where the successive arrival of Au atoms produces size-selected and linearly arranged Au NP arrays. The large-area PD tools used in the present study have further shaped our knowledge: in the coverage range herein explored the Au NPs are effectively almost flat islands exposing the (111) surface with a thickness up to 3 ML. High resolution photoemission data (both from core and valence level) taken with synchrotron radiation have been interpreted in the light of the previously reported STM and of the herein reported structural data. They provide a picture where the tiny Au islands are strongly interacting with the oxidic substrate (which is actually in a reduced TiO$_x$ state where the original film has a TiO$_{1.25}$ stoichiometry). The high BE component observed in the HR-XPS Au 4f spectra was interpreted as the fingerprint of the presence of undercoordinated Au atoms.

Acknowledgements

This work has been funded by the European Community through two STRP projects: GSOMEN and NanoChemSens within the SIXTH FRAMEWORK PROGRAMME, by the Italian Ministry of Instruction, University and Research (MIUR) through the fund PRIN-2005, project title: "Novel electronic and chemical properties of metal oxides by doping and nanostructuring" and by the University of Padova, through the grant CPDA071781. We thank the staff of the Material Science Beamline (Elettra, Trieste) for technical assistance during the beamtime. We thank the DEISA Consortium (co-funded by the EU, FP6 project 508830) for support within the DEISA Extreme Computing Initiative (www.deisa.org).

References

1 E. Ozbay, *Science*, 2006, **311**, 189.
2 J. Homola, *Chem. Rev.*, 2008, **108**, 462.
3 M. E. Stewart, C. R. Anderton, L. B. Thompson, J. Maria, S. K. Gray, J. A. Rogers and R. G. Nuzzo, *Chem. Rev.*, 2008, **108**, 494.
4 G. Reiss and A. Hutten, *Nat. Mater.*, 2005, **4**, 725.
5 A. T. Bell, *Science*, 2003, **299**, 1688.
6 S. Kinge, M. Crego-Calama and D. N. Reinhoudt, *ChemPhysChem*, 2008, **9**, 20.
7 H. Brune, M. Giovannini, K. Bromann and K. Kern, *Nature*, 1998, **394**, 451.
8 H. J. Freund, *Surf. Sci.*, 2002, **500**, 271.
9 W. T. Fallace, B. K. Min and D. W. Goodman, *Top. Catal.*, 2005, **34**, 17.
10 S. Degen, C. Becker and K. Wandelt, *Faraday Discuss.*, 2004, **125**, 343.
11 N. Berdunov, G. Mariotto, K. Balakrishnan, S. Murphy and I. V. Shvets, *Surf. Sci.*, 2006, **600**, L287.
12 G. Hamm, C. Becker and C. R. Henry, *Nanotechnology*, 2006, **17**, 1943.
13 K. Jordan, S. Murphy and I. V. Shvets, *Surf. Sci.*, 2006, **600**, 5150.
14 F. Sedona, S. Agnoli, M. Fanetti, I. Kholmanov, E. Cavaliere, L. Gavioli and G. Granozzi, *J. Phys. Chem. C*, 2007, **111**, 8024.
15 M. Schmid, G. Kresse, A. Buchsbaum, E. Napetschnig, S. Gritschneder, M. Reichling and P. Varga, *Phys. Rev. Lett.*, 2007, **99**, 196104.
16 E. Napetschnig, M. Schmid and P. Varga, *Surf. Sci.*, 2007, **601**, 3233.
17 N. Nilius, E. D. L. Rienks, H. P. Rust and H. J. Freund, *Phys. Rev. Lett.*, 2005, **95**, 66101.
18 T. Risse, S. Shaikhutdinov, N. Nilius, M. Sterrer and H. J. Freund, *Acc. Chem. Res.*, 2008, **41**, 949.
19 F. Sedona, G. A. Rizzi, S. Agnoli, F. X. Llabrés i Xamena, A. Papageorgiou, D. Ostermann, M. Sambi, P. Finetti, K. Schierbaum and G. Granozzi, *J. Phys. Chem. B*, 2005, **109**, 24411.
20 F. Sedona, G. Granozzi, G. Barcaro and A. Fortunelli, *Phys. Rev. B*, 2008, **77**, 115417.
21 G. Granozzi and M. Sambi, *Adv. Mater.*, 1996, **8**, 315.
22 G. Barcaro, A. Fortunelli and G. Granozzi, *Phys. Chem. Chem. Phys.*, 2008, **10**, 1876.
23 G. Barcaro, A. Fortunelli, F. Sedona and G. Granozzi, *J. Phys. Chem. C*, 2007, **111**, 6095.
24 S. Baroni, A. Dal Corso, S. de Gironcoli and P. Giannozzi, 2007, http://www.pwscf.org.
25 D. Vanderbilt, *Phys. Rev. B*, 1990, **41**, 7092.
26 J. P. Perdew, J. A. Chevary, S. H. Vosko, K. A. Jackson, M. R. Pederson, D. J. Singh and C. Fiolhais, *Phys. Rev. B*, 1992, **46**, 6671.
27 http://www.quantum-espresso.org.
28 AS-PD measurements require extremely long acquisition times so that satisfactory statistics is not obtained at lower coverages.
29 N. Nilius, M. V. Ganduglia-Pirovano, V. Brázdová, M. Kulawik, J. Sauer and H.-J. Freund, *Phys. Rev. Lett.*, 2008, **100**, 096802.
30 M. Chen and D. W. Goodman, *Chem. Soc. Rev.*, 2008, **37**, 1860.
31 F. Sedona, M. Sambi, L. Artiglia, G. A. Rizzi, A. Vittadini, A. Fortunelli and G. Granozzi, *J. Phys. Chem. C*, 2008, **112**, 3187.
32 The coverage deduced by the analysis of the STM images is in a very good agreement with the MLeq coverage adopted in the present paper.
33 F. J. Garcia de Abajo, M. A. Van Hove and C. S. Fadley, *Phys. Rev. B*, 2001, **63**, 75404.
34 Electron Diffraction in Atomic Clusters (EDAC) software: http://maxwell.optica.csic.es/software/edac/index.html.
35 In any case, we underline that possible small rotations of the epitaxial matching cannot be seen in our AS-PD data, as a relatively large step (3°) was used in acquiring the AS-PD data in order to maintain an affordable acquisition time for the AS-PD measurements.
36 L. Artiglia, S. Agnoli, G. A. Rizzi, E. Cavaliere, L. Gavioli and G. Granozzi, manuscript in preparation.
37 G. Parteder, F. Allegretti, S. Surnev and F. P. Netzer, *Surf. Sci.*, 2008, **602**, 2666.
38 S. Agnoli, M. Sambi, G. A. Rizzi, G. Parteder, S. Surnev, F. P. Netzer and G. Granozzi, *Surf. Sci.*, 2008, **602**, 499.
39 Z. Zhao, T. Diemant, D. Rosenthal, K. Christmann, J. Bansmann, H. Rauscher and R. J. Behm, *Surf. Sci.*, 2006, **600**, 4992.

40 L. Artiglia, G. A. Rizzi, F. Sedona, S. Agnoli and G. Granozzi, *J. Nanosci. Nanotechnol.*, 2008, **8**, 3595.
41 G. Barcaro and A. Fortunelli, *Chem.–Eur. J.*, 2007, **13**, 6408.
42 G. Barcaro and A. Fortunelli, unpublished results.
43 J. C. Idrobo, W. Walkosz, S. F. Yip, S. Öğüt, J. Wang and J. Jellinek, *Phys. Rev. B*, 2007, **76**, 205422, and references therein.
44 This is in good agreement with preliminary FT-IRAS data taken on the CO/Au/z'-TiOx system.
45 R. Meyer, C. Lemire, Sh. K. Shaikhutdinov and H.-J. Freund, *Gold Bull.*, 2004, **37**, 72.
46 C. Chusuei, X. Lai, K. Luo and D. W. Goodman, *Top. Catal.*, 2001, **14**, 71.
47 J. Radnik, C. Mohr and P. Claus, *Phys. Chem. Chem. Phys.*, 2003, **5**, 172.
48 After annealing at 800 K the Au/z'-TiOx/Pt(111) undergoes a substantial restructuring of the oxide ultrathin film as discussed in ref. 14.
49 M. L. Ng, A. B. Preobrajennski, A. S. Vinogradov and N. Mårtensson, *Surf. Sci.*, 2008, **602**, 1250.
50 E. A. Willneff, S. Braun, D. Rosenthal, H. Bluhm, M. Havecker, E. Kleimenov, A. Knop-Gericke, R. Schlogl and L. M. Schroeder, *J. Am. Chem. Soc.*, 2006, **128**, 12053.
51 S. Lee, C. Fan, T. Wu and S. L. Anderson, *Surf. Sci.*, 2005, **578**, 5.
52 Actually, adsorption of CO on large Au terraces occurs atlower temperature (100–130 K) (see ref. 39).
53 M. G. Mason, *Phys. Rev. B*, 1983, **27**, 748.
54 K. A. Mills, R. F. Davis, S. D. Kevan, G. Thornton and D. A. Shirley, *Phys. Rev. B*, 1980, **22**, 581.

VI.4 Reprint of the paper: Stability and Chemisorption Properties of Ultrathin $TiO_x/Pt(111)$ films and $Au/TiO_x/Pt(111)$ Model Catalysts in Reactive Atmospheres

In the following paper we "fill" the pressure gap for some $TiO_x/Pt(111)$ UT films and $Au/TiO_x/Pt(111)$ model catalysts. Through a collaboration between the Surface Science group of the University of Padova and the Institute of Surface Chemistry and Catalysis of the University of Ulm (Germany) it was possible to combine a UHV chamber for the *in-situ* preparation of the UT films and the model catalysts to a HP-cell where PM FT-IRAS experiments were carried on up to 10^2 mbar range in controlled conditions (both pure CO and $CO:O_2$ 1:1 atmospheres).

Three TiO_x UT films have been grown, based on their structures and oxidation states: 2 reduced UT films, the *z'* (templating substrate where the metal NPs grow ordered along straight lines) and the *w'*-TiO_x (where no ordered defects are present, so that the metal NPs are free to nucleate and grow randomly) and a stoichiometric UT film, the *rect'*-TiO_2. These systems have been used as substrates for the Au NPs growth at different coverages.

The FT-IRAS outputs, together with the XPS, LEED and STM collected in UHV after the HP treatments, show that both the three UT films and the corresponding model catalysts are stable in pure CO HP atmospheres. On the contrary, when the two reduced UT films are exposed to HP in the presence of oxygen ($CO:O_2$ 1:1 environment) they strongly modify, leading to the Pt support dewetting as a consequence of the formation of TiO_2 clusters. The stoichiometric *rect'*-TiO_2 UT film is stable also in the presence of oxygen HP. The instability of the reduced substrates also reflects on the corresponding model catalyst, so that when the Au/*z'*-$TiO_x/Pt(111)$ and the Au/*w'*-$TiO_x/Pt(111)$ systems are treated in a $CO:O_2$ HP a, Au/TiO_2 nano-composite is formed. The Au/*rect'*-TiO_2 model catalyst remain stable also in $CO:O_2$ HP.

In the paper, also the UHV thermal evolution (up to 1000 K) of the two reduced UT films is presented, as studied by XPS and STM after the HP treatment in a $CO:O_2$ mixture. The outputs show that while at high temperature the *z'*-TiO_x restores its original structure and oxidation state through a progressive oxygen loss, the *w'*-TiO_x never restores completely.

PAPER www.rsc.org/pccp | Physical Chemistry Chemical Physics

Stability and chemisorption properties of ultrathin TiO$_x$/Pt(111) films and Au/TiO$_x$/Pt(111) model catalysts in reactive atmospheres†

Luca Artiglia,[a] Thomas Diemant,[b] Heinrich Hartmann,[b] Joachim Bansmann,[b] R. Jürgen Behm,[b] Luca Gavioli,[cd] Emanuele Cavaliere[cd] and Gaetano Granozzi*[a]

Received 14th January 2010, Accepted 16th March 2010
First published as an Advance Article on the web 11th May 2010
DOI: 10.1039/c000884b

The stability of three ultrathin TiO$_x$/Pt(111) films with different stoichiometry and defectivity and the corresponding Au/TiO$_x$/Pt(111) model catalysts in CO or a CO–O$_2$ (1 : 1) gas mixture up to a pressure of 100 mbar has been investigated. According to previous studies, the ultrathin films proved to be effective substrates to deposit in UHV Au nanoparticles with specific morphologies and lateral sizes ranging between 1 and 6 nm. The films have been characterized before and after the exposure using X-ray photoemission spectroscopy (XPS), low-energy electron diffraction (LEED) and scanning tunnelling microscopy (STM). Additional *in situ* measurements of the CO chemisorption behavior were performed using polarization-modulation infrared reflection–absorption spectroscopy (PM-IRAS). A fully oxidized film is stable in CO and CO–O$_2$ (1 : 1) ambient, while the reduced films undergo an oxidative dewetting process at RT in the latter atmosphere. This process ultimately produces a nano-composite surface, where very tiny (from 0.5 to 3 nm lateral sizes) titania nanograins are mixed with open, uncovered areas of the Pt substrate. IRAS measurements on the corresponding Au/TiO$_x$/Pt(111) model catalysts demonstrated that the CO chemisorption strongly depends on the Au nanoparticle size and morphology, while the actual Ti oxidation state of the oxide support does not seem to play a significant role.

I. Introduction

Triggered by the outstanding catalytic activity of nanosized gold ($d < 5$ nm) reported by Haruta,[1] systems formed by Au nanoparticles (NPs) on transition metal oxide supports have been the object of intensive research efforts during the past 20 years. Several reactions take place on Au based catalysts with a high and specific activity, and the interest towards them is linked to a long life-time.[2–4] Most of the work was focused on the CO oxidation, taken as a prototypical model reaction.

It is now well established that the nature of the oxide support can play a major role, since both the electronic properties, the morphology of the NPs and the resulting catalytic activity are strongly influenced by the nature of the support.[5] A paradigmatic example, in this sense, is the high catalytic activity toward CO oxidation at room temperature (RT) discovered for Au bilayer thick NPs grown on reduced titania (TiO$_x$) surfaces.[6] The explanation of this effect, however, is still under debate.[7,8]

Due to the intrinsic complexity of the individual reaction steps on Au/TiO$_2$ catalysts (and especially on powder catalysts), a deeper understanding of the different physical mechanisms may be reached by investigating planar Au/TiO$_2$ model systems with well-defined structural properties. Ultrathin (UT) transition metal oxide films prepared on single crystal metal substrates combined with the evaporation of metal NPs in ultra-high-vacuum (UHV) provide ideal model systems since the whole ensemble of advanced surface science methods can be applied to investigate these systems.[9] It has been demonstrated that NP nucleation preferentially takes place on topographic defects such as step edges or point defects. When an ordered array of point defects is present on the UT film, it can act as a template for a directed assembling process, eventually providing an ordered array of NPs.[10–19] However, the extrapolation of the properties obtained on such UHV model catalysts to realistic catalytic conditions is an operation which is not necessarily legitimate, and studies checking the validity over the so-called *material* and *pressure* gaps are certainly needed.[20]

In recent years, some of us focused the attention on UT TiO$_x$ films deposited on a Pt(111) single crystal.[21] Depending on the Ti amount deposited in a reactive O$_2$ atmosphere and on the annealing treatment, several UT TiO$_x$ films with different morphologies and stoichiometries were prepared and characterized.[22] Among them, three different TiO$_x$ ($1.2 \leq x \leq 2$) UT films can be considered as representative

[a] *Department of Chemical Sciences, via Marzolo 1, University of Padova, Italy*
[b] *Institute of Surface Chemistry and Catalysis, Ulm University, D-89069 Ulm, Germany*
[c] *Department of Mathematics and Physics, Università Cattolica del Sacro Cuore, via dei Musei 41, I-25121 Brescia, Italy*
[d] *Laboratorio Nazionale CNR-INFM-TASC, S.S. 14 Km 163.5, 34012 Basovizza (TS), Italy*

† Electronic supplementary information (ESI) available: Fig. S1 and S2: Representative Au 4f XPS data of the Au(0.9 ML$_{eq}$)/TiO$_x$/Pt(111) model catalysts before and after pure CO and CO–O$_2$ (1 : 1) HP exposures at 100 mbar. Fig. S3: Representative STM image taken on Au(0.9 ML$_{eq}$)/*w*′-TiO$_x$/Pt(111) exposed to 100 mbar of a CO–O$_2$ (1 : 1) mixture. See DOI: 10.1039/c000884b

model systems for titania supports to study the effects of defectivity and stoichiometry on the growth and properties of Au/TiO$_x$ catalysts. Two of them (labelled as z' and w'-TiO$_x$ following the original nomenclature, where z stands for *zigzag-like* and w for *wagon-wheel-like*) are under-stoichiometric fully wetting TiO$_x$ films,[22,23] and they represent reduced titania supports with (z'-TiO$_x$) or without (w'-TiO$_x$) a long range ordered defectivity. The third is a fully stoichiometric film (*rect*′-TiO$_2$), whose structure has recently been demonstrated to be related to the TiO$_2$(B) bulk polymorph.[24] In addition, the structure and morphology of the Au/TiO$_x$/Pt(111) model catalysts obtained after evaporation of Au in UHV conditions were investigated in depth by using scanning tunnelling microscopy (STM).[17,18,25] In particular, the capability of the z'-TiO$_x$ UT film to produce an ordered array of size-selected Au NPs as a consequence of the ordered defectivity (see below) has been demonstrated.[17,18]

In this paper we want to address the stability of both the TiO$_x$/Pt(111) UT films and Au/TiO$_x$/Pt(111) model catalysts at high pressure (HP) (in the mbar range) by comparing X-ray photoemission spectroscopy (XPS), low-energy electron diffraction (LEED) and STM measurements carried out before and after the exposure to an elevated pressure of pure CO or a CO–O$_2$ (1 : 1) gas mixture (up to 100 mbar), so partially filling the *pressure* gap. In addition, we also analyse their chemisorption properties toward CO by *in situ* polarization–modulation infrared reflection absorption spectroscopy (PM-IRAS) during gas exposure. The analysis of the CO stretching frequency ν(CO) also provides information on the stability and the evolution of the UT clean films and Au/TiO$_x$ systems at HP and on the strength of the Au/CO interaction. Results of a similar HP PM-IRAS study on related model catalysts, *i.e.*, Au/TiO$_2$/Ru(0001), were already reported.[26–28] However, with respect to these studies, the Au/TiO$_x$/Pt(111) systems investigated herein consist of thinner films and the structures are known at an atomic level.[21] Neglecting to a first approximation the effect of the underlying Pt substrate, they can be considered as models for both reduced and fully oxidized titania substrates where defects are also included.

II. Experimental

The preparation procedure of the different TiO$_x$/Pt(111) UT films has been reported in detail elsewhere.[22,29] The clean Pt(111) surface was prepared by cycles of sputtering/flashing to 1000 K before film deposition. The UT films cover the substrate surface almost completely (uncovered surface less than 8%), as evidenced by temperature programmed desorption (TPD) experiments using CO as a chemisorption probe (CO chemisorbs under the chosen conditions, dosing at RT in UHV, only on the exposed Pt spots). Au was evaporated from an e-beam evaporator directly on the TiO$_x$/Pt(111) films held at RT. The amount of Au deposited was determined using angle resolved XPS, based on the layer-by-layer growth of Au on Pt(111). Coverage values expressed in monolayer equivalents (ML$_{eq}$) are calculated assuming the growth of Au(111) and an interlayer distance between adjacent plane of 0.235 nm.

The preparation and the spectroscopic experiments were performed *in situ*, using a UHV system equipped with a high-pressure cell for experiments at elevated pressures (from 10^{-2} to 10^{2} mbar). The UHV chamber (base pressure $<10^{-10}$ mbar), used for film and model catalyst preparation and characterization, is equipped with a LEED, a double anode X-ray source, a hemispherical CLAM 2 electron analyzer (VG), a quadrupole mass spectrometer (QMS 200, Pfeiffer Vacuum) and two e-beam evaporators for metal deposition. All spectroscopic measurements were performed at RT. The temperature was measured with a C-type thermocouple attached to the rear surface of the crystal. The Ti 2p XPS data reported in the present study were obtained using Al-Kα radiation for photoelectron excitation and a pass energy of 50 eV at the electron analyzer. Binding energies (BEs) are referenced to the Pt 4f$_{7/2}$ photoemission peak and the shifts in the Ti 2p peak are taken to monitor the oxidation state changes of the Ti atoms of the films.

The HP cell, described in detail elsewhere,[30] has a PM-IRAS spectrometer and a differentially pumped QMS used for checking gas purity and gas mixture preparation. The XPS and LEED experiments were performed before and after high-pressure exposure in the HP cell. In the following, we refer to them as before and after HP treatments (10^2 mbar). All HP exposures and IRAS measurements were done at RT, starting to expose the films to the gas from 10^{-2} mbar and reaching 10^2 mbar with intermediate steps at 10^{-1}, 1, 10 and 100 mbar.

The STM data were acquired in an Omicron Multiscan Lab system, operating in UHV conditions (base pressure $<5 \times 10^{-11}$ mbar) and equipped with surface preparation facilities. The STM images were obtained in constant current mode at RT, with tip-to-sample bias ranging from 0.4 to 1.5 V and tunnelling current ranging from 0.2 to 0.8 nA. The STM tips were prepared by chemical etching of a Pt/Ir wire in a KCl solution.

III. Results and discussion

III.1 Clean ultrathin TiO$_x$/Pt(111) films

Before entering into the discussion of the herein reported results, it is useful to summarize what is already known for the three UT films which have been used as model systems for the titania support in this study.

The structure of the TiO$_x$/Pt(111) reduced UT films has been recently discussed in detail on the basis of experimental and density functional theoretical (DFT) data: they consist of a Ti/O bilayer where the Ti is at the interface with the Pt substrate.[23] In the specific case of the z'-TiO$_x$ phase (x = 1.25, as determined by the DFT calculations), STM has shown the presence of ordered arrays of defects (*picoholes*), where Pt underneath is left uncovered[31] within the dislocation lines (*troughs*). These play an active role as preferential nucleation sites for the growth of metal NPs (see below).[17,18] For the w'-TiO$_x$ film, having a stoichiometry close to that of the z'-TiO$_x$ phase,[22] the STM data do not show any evidence of ordered arrays of defects.[32] In the fully stoichiometric *rect*′-TiO$_2$ phase,[24] a Pt–O–Ti interface is formed, and, as a consequence of the weaker Pt–O interaction with respect to the Pt–Ti one,[33] a partial dewetting of the film occurs which drives the system toward the formation of flat and regularly shaped

rect'-TiO_2 islands (with a minimum thickness of two bilayers), which progressively increase their lateral size and thickness as a function of the Ti coverage.[24] One important point is that in between the islands, a fully wetting bilayer of a reduced TiO_x phase is observed in the corresponding STM images, so that areas of bare Pt support could not be observed.[25] The actual structure of the *rect'*-TiO_2 islands has recently been analysed in detail; it has been demonstrated that they represent the first example reported in the literature of supported TiO_2(B)-like nanolayers.[24] The islands can be grown up to a thickness of several layers. Also in this case, there is no evidence for a long range ordered defectivity and thus, in the present study, they are taken as a model system for a fully stoichiometric titania support. The average island thickness of the *rect'*-TiO_2 islands investigated in the present study is *ca.* two Ti–O bilayers.

As a first step, we tested the stability of the three clean UT films both in pure CO and in CO–O_2 (1 : 1) HP atmospheres. After pure CO HP exposure, IRAS did not show any detectable ν(CO) signal for all three UT films even at the highest pressure used in this study (100 mbar), thus indicating that bare Pt areas are below the detection limit,[34] in agreement with TPD measurements. From these observations, significant CO-induced dewetting can be excluded for all of these phases. LEED images, collected after the HP treatment, maintained the original pattern typical of the corresponding clean phases,[22,29] and the Ti 2p XPS peak (Fig. 1) showed no change from before to after the HP exposure (see ref. 22 and 29 for a detailed discussion of the respective XPS data). In the same figure, XPS data recorded after annealing the HP exposed films in UHV at 950 K are also presented. No significant change is observed in all three explored cases. These results strongly indicate that all clean UT films investigated are stable during HP exposure to pure CO. Hence, under these conditions, CO is not capable to reduce neither the fully oxidized film nor the reduced films.

In contrast, after exposure to a CO–O_2 (1 : 1) mixture, the systems undergo observable transformations that develop in two different ways depending on the Ti chemical state in the corresponding UT film before HP exposure. The reduced phases (z'-TiO_x and w'-TiO_x) show a clear evolution as outlined by the following experimental data:

(i) The XPS data presented in Fig. 2a and b clearly show a BE shift of the Ti 2p peaks of *ca.* 1.7 eV (from 456.8 to 458.5 eV) upon HP exposure, which suggests an oxidation to Ti^{4+} and the formation of a Pt–O interface layer, according to the interpretation of the XPS data of the whole series of UT films.[29] Moreover, we observe a 10% decrease of the Ti 2p/Pt 4f peaks intensity ratio before and after HP exposure.

(ii) Broad and weak bands centred at *ca.* 2080 cm^{-1} (not reported here) are observed in IRAS spectra of the HP treated films, suggesting that small areas of the Pt substrate become accessible to CO adsorption.

(iii) The LEED patterns of the two reduced UT films (see Fig. 3a and b for the initial LEED patterns) show dramatic changes after CO–O_2 HP exposure: for the z'-TiO_x phase (Fig. 3c) a diffuse ring around the integer spots of the Pt(111) substrate on a high background is observed, while in the case of w'-TiO_x phase a lower background is present. Furthermore, apart from the integer spots of the Pt(111) substrate, very broad spots appear, which are shifted toward the centre of the pattern (Fig. 3d). The LEED pattern of the HP exposed z'-TiO_x phase is very similar to that reported in previous studies (an *in situ* μ-LEED and a low-energy electron microscopy (LEEM) investigation on the formation of TiO_x/Pt(111) films[35]), which was assigned to the so-called *precursor-like* phase. The term *precursor-like* was introduced[35] in order to indicate TiO_2 NPs, originating from the metal deposition under reactive O_2 environment, that have not yet a precise structure and epitaxial relation with the Pt substrate. It has been also demonstrated[35] that this phase successively develops toward different phases depending on the amount of deposited TiO_x and the annealing procedure. On the other hand, the LEED pattern observed for the w'-TiO_x phase after HP exposure is more reminiscent of the one observed for a low-coverage oxidized k'-TiO_x phase,[29] where the structure is probably related to the quasi-hexagonal TiO_2 structure recently reported on Cu(001).[36] We believe that also in this

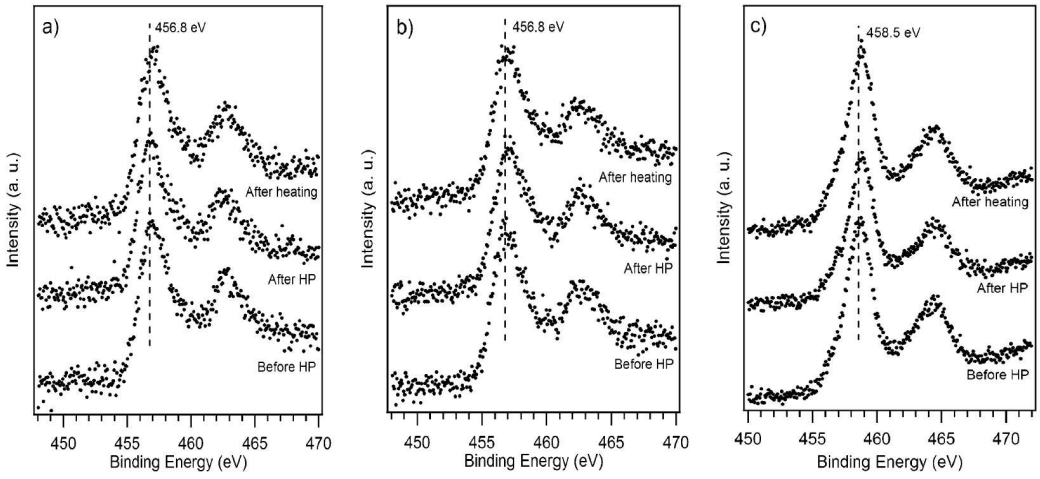

Fig. 1 Ti 2p XPS data of the TiO_x/Pt(111) films before and after CO HP exposure (100 mbar) and after UHV heating at 950 K: (a) z'-TiO_x, (b) w'-TiO_x, (c) *rect'*-TiO_2.

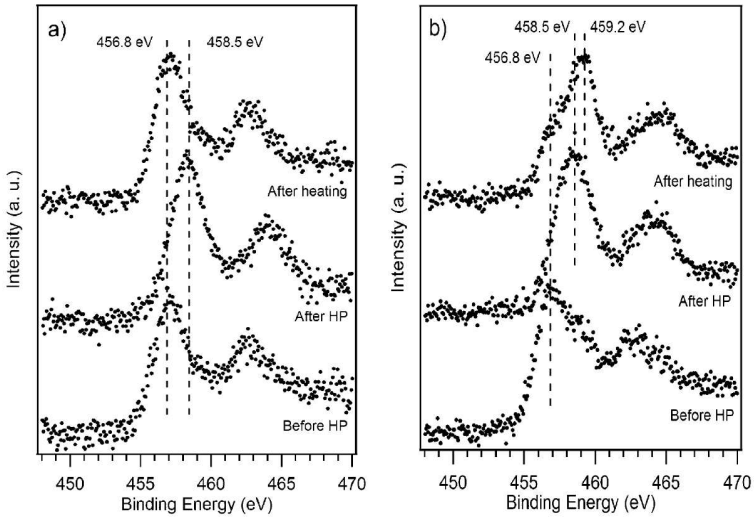

Fig. 2 Ti 2p XPS data of the (a) clean z'-TiO$_x$ and (b) clean w'-TiO$_x$ films collected before CO–O$_2$ (1 : 1) HP exposure (100 mbar), after HP exposure and after UHV annealing to 950 K.

case it is better to refer our LEED pattern to a *precursor-like* phase (different from the one of Fig. 3c) rather than to a specific phase because of the very broad spots which are indicative of very small and disordered nuclei.

(iv) The specific *zigzag-like* and *wagon-wheel-like* STM patterns observed for the two z'-TiO$_x$ and w'-TiO$_x$ films prior to the HP treatment (Fig. 4a and b) are completely lost after the HP treatment. In Fig. 4c and d we show typical surface morphologies as observed after an exposure to 100 mbar of a CO–O$_2$ (1 : 1) mixture (exposure time 5 min). The motif of the oxide layer is no more visible, while the entire surface presents a uniform granularity, with average grain sizes ranging from 0.5 to 3 nm (the rms roughness is about 1 nm). This indicates a clear restructuring of the oxide layer after HP exposure.

Taken together, all experimental results confirm the hypothesis that the reduced UT films undergo an oxidative dewetting when being exposed to CO–O$_2$, leading to the formation of stoichiometric TiO$_2$ nanograins mixed with uncovered parts of the Pt crystal, which become then available for CO adsorption (see the above reported point ii). A similar dewetting was recently reported for the FeO(111)/Pt(111) UT film:[37] however, it should be noted that in this case the dewetting was interpreted as the consequence of the CO + O$_2$ catalytic reaction (40 mbar CO + 20 mbar O$_2$ mixture) taking place at 450 K and that the final highly dispersed iron oxide particles on Pt(111) have larger lateral sizes (8 ± 1 nm in diameter).

On the contrary, the stoichiometric *rect*′-TiO$_2$ film does not show any detectable CO IRAS signal after the HP CO–O$_2$ treatment, its LEED pattern remains unchanged and also the XPS spectra do not show any significant modification. Therefore, the *rect*′-TiO$_2$ film is stable in both an oxidizing and reducing HP environment under present exposure conditions.

We have then analyzed the thermal changes of the HP exposed z'-TiO$_x$ and w'-TiO$_x$ films in UHV from RT to 950 K by LEED, XPS and STM. It should be reminded that in order to prepare each single UT TiO$_x$/Pt(111) phase, carefully optimized conditions have to be adopted, otherwise, a mixture of several phases is obtained under uncontrolled conditions.[22] The LEED patterns show that upon annealing at ~700 K in UHV, the HP treated z'-TiO$_x$ system undergoes a transition to a mixture of different phases (Fig. 3e), as demonstrated by the coexistence of (i) sharp spots located midway between the (0,0) and the (1,0) beams, which are assigned to the reduced *zigzag-like* z-TiO$_x$ phase,[22,38] and (ii) outer rings to be associated to an incipient formation of the z'-TiO$_x$ phase. After annealing to 950 K, the system completely recovers the z'-TiO$_x$ LEED pattern (Fig. 3g). The corresponding STM data are in good agreement with the described trend of the LEED pattern. The granular phase observed after the HP exposure (Fig. 4c) is substantially modified after the annealing step to 700 K (Fig. 4e): one can observe the recovery of a flat morphology where different patches of z-TiO$_x$ and z'-TiO$_x$ are evident (see in Fig. 4e the different patches). Moreover, scattered and brighter islands are observed on the surface, probably reflecting partially oxidized titania surviving the UHV annealing. After annealing to 950 K (Fig. 4g), the surface is predominantly covered by the z'-TiO$_x$ phase, in accordance with LEED and XPS data recorded after 950 K annealing (Fig. 2a), which show a Ti 2p peak shape very similar to the one obtained before the HP treatment (peak maximum at 456.8 eV). In addition, small amounts of bare Pt areas are seen by STM. This might be due to interdiffusion of Ti into the Pt substrate during the UHV annealing procedure, which eventually causes an effective reduction of the TiO$_x$ coverage.[35] Therefore, the experimental results show an oxidation of the z'-TiO$_x$ film after the HP CO–O$_2$ treatment which is largely reversible through a progressive oxygen loss when annealing the sample in UHV.

In contrast, the oxidation of the w'-TiO$_x$ UT film after the HP CO–O$_2$ treatment proceeds in a different, non-reversible, way. The LEED data reported in Fig. 3 clearly show that already after the HP exposure the system is developing along a

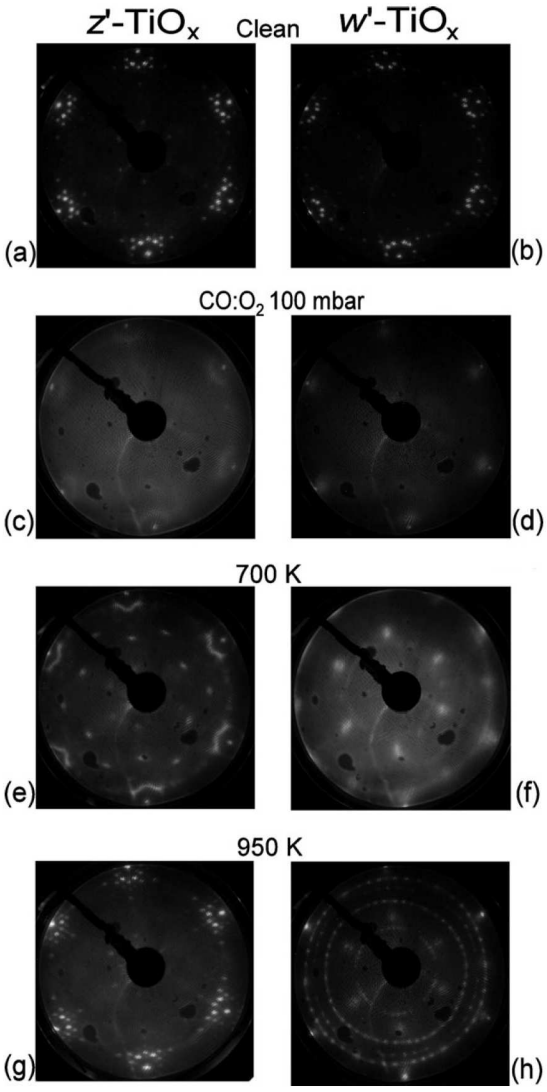

Fig. 3 LEED patterns (45 eV) of the clean z'-TiO$_x$ and w'-TiO$_x$ films (a, b), after HP exposure to 100 mbar of CO–O$_2$ (1 : 1) (c, d) and after UHV annealing at 700 K (e, f) and 950 K (g, h).

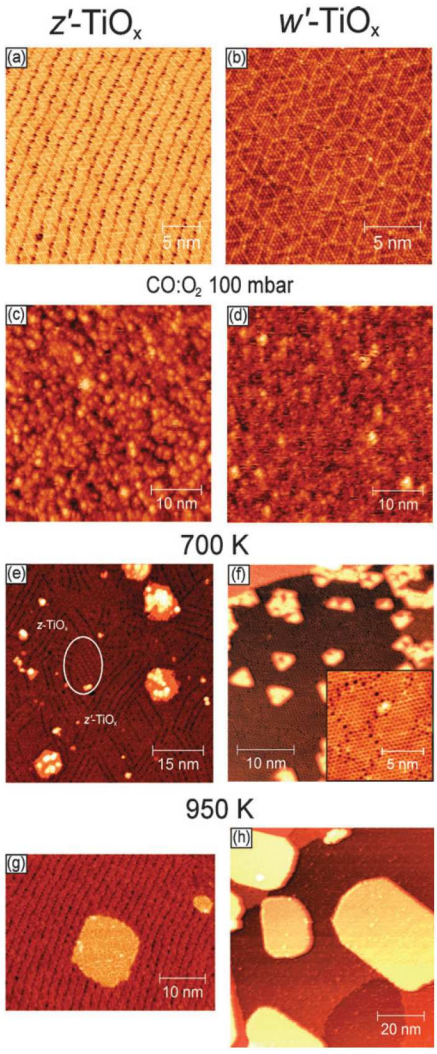

Fig. 4 STM images of the clean z'- and w'-TiO$_x$ phases (a, b), after HP exposure to CO–O$_2$ (1 : 1) (c, d), after UHV annealing at 700 K (e, f) and 950 K (g, h).

different route, since the broad spots observed in Fig. 3d are different from the rings obtained for the HP treated z'-TiO$_x$ film (Fig. 3c). This difference becomes more evident after annealing to 700 K, where a LEED pattern (Fig. 3f) is observed that can be interpreted as a highly defective *kagomé-like* reduced k-TiO$_x$ phase (a quasi-(2 × 2) structure).[35] Finally, the 950 K annealing step (Fig. 3h) provides a LEED pattern which is completely different with respect to that of the pristine UT w'-TiO$_x$ film: we observe the presence of spots related to the reduced k-TiO$_x$ phase, superimposed with a new set of clearly defined spots, whose origin is still unknown. We tentatively assign this complex pattern to a coexistence of TiO$_2$ islands and patches of the k-TiO$_x$ wetting layer. This interpretation is also in agreement with the XPS data of Fig. 2b, where, after thermal treatment in UHV at 950 K, a shoulder at lower BE (associated to a reduced layer having a Ti–Pt interface) is recovered, while the main Ti 2p peak centred at about 459.2 eV (*i.e.*, the Ti^{4+} oxidation state) is still observed at the end of the UHV annealing.

The corresponding STM data are shown in Fig. 4. After the CO–O$_2$ HP treatment, the STM image (Fig. 4d) is almost identical to the one observed in the case of z'-TiO$_x$ (Fig. 4c), *i.e.*, a rough surface with a uniform granularity. The 700 K annealing treatment results in a rather complex situation as shown in Fig. 4f: a wetting layer with a predominant k-TiO$_x$ phase organized in small domains (see the inset),[22,25] in agreement with the quite broad spots observed in the LEED pattern (Fig. 3f), and patches of a different phase that has not been identified up to now. A number of triangularly-shaped islands with an apparent height of about 1 nm are visible on top of the wetting layer, as well as larger and flat islands. These

triangularly shaped islands disappear after the thermal treatment at 950 K (see Fig. 4h), while the large and flat islands increase in density. The flat islands show an internal row-like structure. This may be compatible with the results of a previous investigation where, using angle-scanned photoelectron diffraction (PhD), the presence of rutile-like, flat TiO_2 nanostructures supported on the Pt substrate, with the (100) surface exposed, has been demonstrated.[39,40] In this case both the TiO_2 coverage and the thermal treatment of the system were almost identical to the one described above. Similar rutile-like titania nanostructures with the (100) surface being exposing and typical dimensions of 5–20 nm, have recently been reported on Au(111) after annealing to 900 K.[41]

In conclusion, although both reduced systems seem to follow an oxidative dewetting when being exposed to HP CO–O_2 (1 : 1), the reduction process of the two differently prepared films upon annealing in UHV is rather different: after thermal treatment in UHV up to 950 K, the z'-TiO$_x$ film is brought back to its original oxidation state and structure, while the w'-TiO$_x$ one is not. The difference between the two z'-TiO$_x$ and w'-TiO$_x$ films may either arise from subtle kinetic effects or from an inherently different stability of the two reduced films. Further experiments are in progress to clarify such questions.

III.2 The Au/TiO$_x$/Pt(111) model catalysts

In the following, we will focus on the results obtained from the planar Au/TiO$_x$/Pt(111) model systems. The morphologies of the Au NPs in the three herein studied systems have been previously investigated by STM,[17,18,25] and the main results are briefly outlined in Fig. 5. Since these data are of relevance for the discussion of the reported results, we will briefly summarize in the following the most important points.

As previously outlined in III.1, the z'-TiO$_x$ UT film presents an ordered array of *picoholes* and *troughs*,[31] where the Au NPs preferentially nucleate, resulting in a spatial alignment along the direction dictated by the parallel *troughs* (see Fig. 5a) and, for this reason, a templating function has been assigned to the z'-TiO$_x$ phase.[17,18,19] Moreover, Au NPs grown on this substrate result in a narrow size distribution (1.3 ± 0.4 nm).[17] According to recent PhD data[18] (both angle and energy-scanned), they are best described as flat 2D-like islands, pinned at the *picoholes*, with a maximum thickness of 2–3 layers and exposing the (111) surface. A different behaviour is observed in the case of the w'-TiO$_x$ and *rect*′-TiO_2 phases: these two UT films do not present ordered defect structures and consequently do not behave as templates. Thence, Au NPs with significantly larger lateral sizes and a more 3D-like aspect ratio are observed than on the z'-TiO$_x$ film (Fig. 5b and c) and they are nucleated either at step edges or at randomly distributed defects.[17,25] In addition, on the flat *rect*′-TiO_2 islands, a higher mobility of the Au NPs was demonstrated compared to the reduced wetting films, both experimentally by STM and theoretically by DFT,[25] which is responsible for the agglomeration of Au atoms in larger NPs (see Fig. 5c). The lateral size values, relevant for the following discussion, scale as follows: Au (z'-TiO$_x$, $\sim$1.3 nm) < Au (w'-TiO$_x$, $\sim$3.5 nm) < Au (*rect*′-TiO_2, $\sim$5–6 nm).

We analyzed the behaviour of the Au/TiO$_x$/Pt(111) model catalysts in both pure CO and CO–O_2 (1 : 1) atmospheres up to high pressures for two Au coverages (0.5 and 0.9 ML$_{eq}$). In this case, CO is expected to chemisorb on the Au NPs, where it can be monitored by IRAS.

In Fig. 6, we present IRAS data recorded on the three Au/TiO$_x$/Pt(111) model catalysts with two different Au coverages during exposure to pure CO at different pressures. In the Au/z'-TiO$_x$ system, we find a ν(CO) band at 2123 cm^{-1} for 0.5 ML$_{eq}$ and 2118 cm^{-1} for 0.9 ML$_{eq}$, as shown in Fig. 6a and d, respectively. Both the position and the intensity are relatively independent from the actual pressure conditions, *i.e.*, the signal seems to be already saturated at an intermediate pressure of 1 mbar. The increase in the Au coverage causes a red-shift of 5 cm^{-1} in the band position maxima. In contrast, the Au/w'-TiO$_x$ (Fig. 6b and e) and Au/*rect*′-TiO_2 (Fig. 6c and f) systems show a common behaviour, which is rather different from the one observed for the Au/z'-TiO$_x$ samples: the bands are sharper and more intense, their intensity increases with CO pressure and, in both cases, a small red-shift is found ($\sim$6 cm^{-1}) as a function of the increasing CO pressure. In addition, the ν(CO) wavenumber only shows minor changes with the Au coverage. In all three cases, the corresponding IRAS bands completely disappear when the CO atmosphere is pumped off to UHV, in agreement with a pressure-dependent adsorption–desorption equilibrium on the Au NPs under the present conditions and similar to earlier observations on Au/TiO_2/Ru(0001) model catalysts.[26–28]

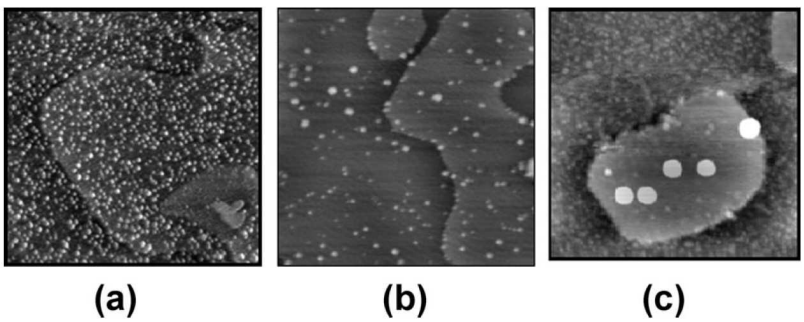

Fig. 5 STM images of (a) Au(0.35 ML$_{eq}$)/z'-TiO$_x$/Pt(111) (100 × 100 nm^2, V = 0.6 V, I = 0.6 nA), (b) Au (0.2 ML$_{eq}$)/w'-TiO$_x$/Pt(111) (100 × 94 nm^2, V = 1.5 V, I = 0.2 nA) and (c) Au(0.2 ML$_{eq}$)/*rect*′-TiO_2/Pt(111) (82 × 82 nm^2; V = 1.5 V, I = 1.5 nA) (from ref. 17, 18 and 25).

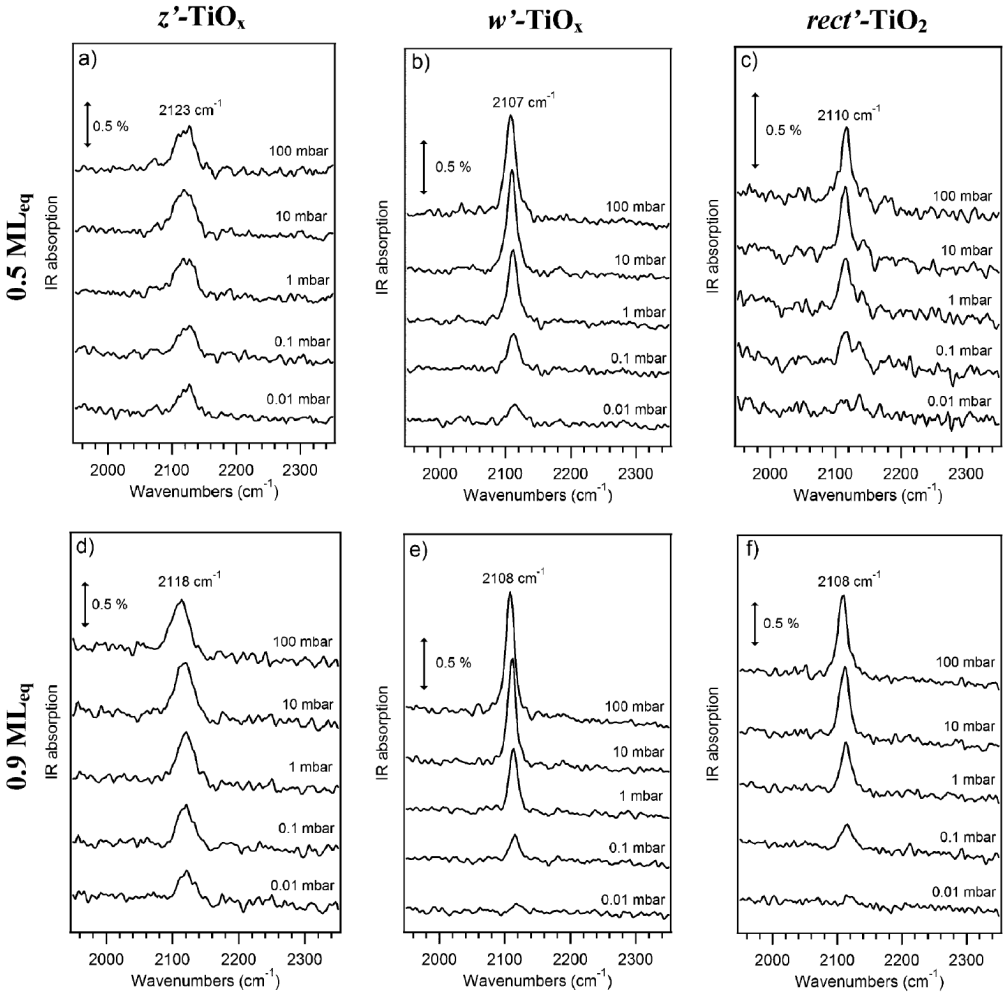

Fig. 6 IRAS data recorded *in situ* during CO exposure at different pressures: (a) Au(0.5 ML$_{eq}$)/*z*′-TiO$_x$, (b) Au(0.5 ML$_{eq}$)/*w*′-TiO$_x$, (c) Au(0.5 ML$_{eq}$)/*rect*′-TiO$_2$, (d) Au(0.9 ML$_{eq}$)/*z*′-TiO$_x$, (e) Au(0.9 ML$_{eq}$)/*w*′-TiO$_x$ and (f) Au(0.9 ML$_{eq}$)/*rect*′-TiO$_2$.

The Ti 2p XPS spectra collected before and after HP exposure to CO revealed for all the model Au/TiO$_x$/Pt(111) systems the same results as already shown in Fig. 1 for the clean films, *i.e.* the films supporting the Au NPs remain stable after the HP CO treatment and no chemical shift is observed. The Au 4f XPS spectra collected before and after HP to CO do not show any significant change in the position/shape of the peaks (see for example the data reported in Fig. S1(a) and S2(a) (ESI†).

Let us now discuss in more detail the behaviour of the ν(CO) IRAS bands in the three different model systems. Starting with the analysis of the band intensities on Au/*z*′-TiO$_x$ (Fig. 6a and d), the ν(CO) band is already visible at the lowest CO pressure (0.01 mbar) and its intensity is relatively constant in the pressure range investigated here, indicating that the active sites of the Au NPs are very soon saturated by CO. In contrast, in the other two systems (Au/*w*′-TiO$_x$ and Au/*rect*′-TiO$_2$, Fig. 6b, c, e and f), a well-defined ν(CO) band starts to develop only at higher pressures (0.1 mbar). In addition, according to the intensity of the ν(CO) band, a larger CO uptake is observed on the Au/*w*′-TiO$_x$ system compared to the Au/*rect*′-TiO$_2$ one. In order to rationalize these data, we have to consider the different NP sizes and morphologies observed by STM (Fig. 5).

The early saturation of the Au/*z*′-TiO$_x$ system can be related to the small size and distinct morphology (flat bi- and trilayer islands) of the Au NPs. In addition, because of the pinning at the *picoholes*, such Au NPs are in a direct contact with the Pt substrate and their under-coordinated peripheral atoms might be only partially available for CO chemisorption. According to the extensive work done in Goodman's group,[6,42–45] bilayer Au islands supported on TiO$_x$/Mo(112) films have the highest affinity for CO adsorption, and similar trends were observed also for Au/TiO$_2$/Ru(0001) model catalysts.[27,46] The interpretation is also in agreement with theoretical predictions,[47] which suggest the Au overlayers to be electron-rich and to have significantly different electronic properties compared with bulk Au.[43] In this respect, it has to be outlined that the bulk

Au(111) surface is not active to CO adsorption under present conditions.[48] Therefore, the onset of CO chemisorption at a comparatively low pressure and the almost pressure independent signal intensity can be interpreted as the result of an enhanced Au–CO interaction which results in rapid saturation of the Au nanostructures already at relatively low CO pressures.

Conversely, in the Au/*w*′-TiO$_x$ and Au/*rect*′-TiO$_2$ systems the ν(CO) IRAS bands are detected only at higher pressures compared to the Au/*z*′-TiO$_x$ model catalyst (Fig. 6). This can be rationalized on the basis of an intrinsically lower affinity of these 3D Au NPs toward CO with respect to the very small Au islands observed on the *z*′-TiO$_x$ film. On the other hand, the higher amount of Au under-coordinated active sites on the Au/*w*′-TiO$_x$ and Au/*rect*′-TiO$_2$ samples allows the NPs to bind a larger amount of CO, explaining the observed difference in the IR signal intensity.

In order to discuss the actual values of the frequencies of the bands in the IRAS data in Fig. 6, we will first summarize relevant results of previous studies. CO adsorption on Au NPs of planar model systems with various oxide film supports, *i.e.* Au/TiO$_2$/Mo(110),[44] Au/TiO$_2$/Ru(0001),[46] Au/Al$_2$O$_3$/NiAl(110)[49] and Au/FeO/Pt(111),[50,51] was already investigated in detail with IRAS under UHV conditions and at low temperature (< 100 K). Especially, a comparison to the results of Lemire *et al.*[50,51] seems worthwhile, since their oxide films had a thickness comparable to that of the *z*′- and *w*′-films used in the present study. For most of the model systems, a single IR band centred between 2100 and 2120 cm^{-1} was detected under these conditions, which can be assigned to CO adsorption on active sites of the Au NPs. In addition, Lemire *et al.*[51] reported the formation of a second IR band at higher wavenumber (~2165 cm^{-1}) for CO adsorption on Au/FeO/Pt(111) model systems formed by deposition of small Au amounts at low temperature (77 K). This feature was assigned to CO adsorption on very small Au clusters and/or isolated Au atoms, which are trapped at defects of the UT FeO film. The shift of the band was explained by charge transfer between the substrate and the small Au aggregates. On Au/TiO$_2$/Mo(110), Meier *et al.* evaluated the CO band at different Au coverages to be centred at ~2122 cm^{-1}.[44] The band position was almost independent of the Au coverage; only for very small Au coverages (and therefore particle sizes), a small shift to lower wavenumbers was detected (to ~2118 cm^{-1}). Therefore, they concluded that the Au NP size does not substantially affect the IR band position. The band shift compared to CO adsorption on bulk Au(110) (2110 cm^{-1})[52] was explained by a substrate effect. To bridge the pressure gap, CO adsorption on Au/TiO$_2$(10 ML$_{eq}$)/Ru(0001) model catalysts was recently studied by IRAS at elevated pressure up to 50 mbar at RT.[26–28] While only a single band at ~2110 cm^{-1} was observed in the presence of CO–O$_2$ gas mixtures and at lower pressures of pure CO (up to 10 mbar), the formation of another, additional feature at lower wavenumbers (2060 cm^{-1}) was detected for higher CO pressures (above 20 mbar). This new feature was attributed to a modification of the electronic properties of the Au NPs (negatively charged) due to a partial local reduction of the titania support upon CO exposure.

Focusing on the present model systems, it is interesting to note that for Au/*z*′-TiO$_x$, the IR band is centred at higher wavenumbers (average measured value of 2120 cm^{-1}) than in the other two cases, where an average value of *ca.* 2108 cm^{-1} is observed. This band shift to higher wavenumbers reminds of the findings observed for the small Au aggregates of the Au/FeO/Pt(111) system[50,51] (albeit with smaller magnitude). Most probably, it can be attributed to a combination of two effects: (i) the significantly lower Au NP size on the *z*′-TiO$_x$ films (ii) a modification of the electronic properties of the Au NPs due to their direct contact with the Pt substrate in the *picoholes*, similar to the case of Au/FeO/Pt(111).[51] Furthermore, the small band shift with increasing Au coverage from 2123 cm^{-1} (0.5 ML$_{eq}$ Au) to 2118 cm^{-1} (0.9 ML$_{eq}$ Au) for the *z*′-TiO$_x$ based model system can be explained by the more 3D-like behaviour. A shift to lower wavenumbers with increasing Au coverage/particle size was observed also in other studies.[53]

For the other model systems, the CO band is centred at ~2108 cm^{-1}, in good agreement with results for other planar Au/metal oxide systems (especially to the HP measurements on Au/TiO$_2$(10 ML$_{eq}$)/Ru(0001)) and bulk Au samples.[26–28] This finding probably reflects the random nucleation process which ultimately takes to more 3D-like Au NPs.

In conclusion, it seems that the actual Ti oxidation state does not play a major role on the band position in the presently studied model catalysts, while morphological aspects, both with regard to film and NP structure, seem to be more relevant. A major point emerging from the present study is that, in contrast to the results from the Au/TiO$_2$(10 ML$_{eq}$)/Ru(0001) system,[26] we do not see the formation of any additional IR feature at lower wavenumbers in a HP CO atmosphere, neither in the case of the Au/*rect*′-TiO$_2$ system nor in the case of Au NPs on the other two reduced UT films. Following the already mentioned interpretation of such band,[26] this would imply that negatively charged Au NPs cannot be created on any of the herein analyzed model systems. We propose two possible explanations for such evidence: (i) the conductive nature of such UT films due to the proximity of the metallic substrate; (ii) the stability of the clean substrates in pure CO atmosphere, which has already been demonstrated in section III.1. In addition, we also want to remind that the *rect*′-TiO$_2$/Pt(111) islands have recently been described as nanolayers of TiO$_2$(B) exposing the (001) surface,[24] whose stability was found to be very high in DFT calculations, with a very low surface energy of 0.40 J m^{-2}.[54] It might be possible that the observed stability of the *rect*′-TiO$_2$/Pt(111) UT film toward CO at high pressures can be traced back also to its specific structure.

Turning now to the small band shifts observed with increasing CO pressure (see Fig. 6), we can imagine the simultaneous action of two counteracting effects: a blue shift due to increasing dipole coupling of CO molecules at larger coverages and a red shift due to a modification of the Au–CO bond (chemical shift), where the latter effect dominates.[55–57] As a consequence of such balance, a small red-shift is observed (between 5 and 7 cm^{-1}) for both the Au/*w*′-TiO$_x$ and Au/*rect*′-TiO$_2$ model catalysts, also in agreement with the results reported for the Au/TiO$_2$(10 ML$_{eq}$)/Ru(0001) model system.[26] The absence of such a red shift in the Au/*z*′-TiO$_x$ system (Fig. 6a and d) is possibly associated with the close contact between the Pt substrate and the Au NPs (see above).

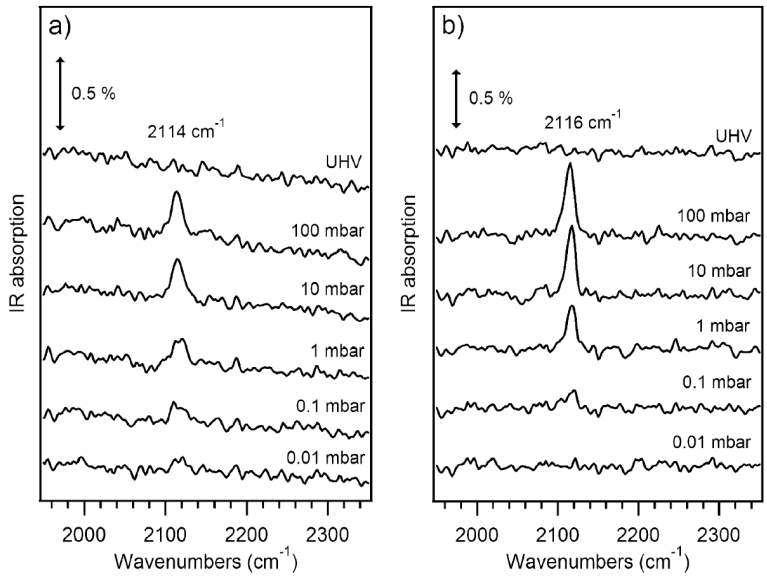

Fig. 7 IRAS data recorded *in situ* during exposure to CO–O$_2$ (1 : 1) mixtures at different pressures: (a) Au(0.5 ML$_{eq}$)/*rect*′-TiO$_2$, (b) Au(0.9 ML$_{eq}$)/*rect*′-TiO$_2$.

We finally discuss the behaviour of the Au/TiO$_x$/Pt(111) model catalysts after exposure to CO–O$_2$ (1 : 1) gas mixtures. Again, model systems with Au coverages of 0.5 and 0.9 ML$_{eq}$ were used.

For the two Au/*z*′-TiO$_x$ and Au/*w*′-TiO$_x$ system (spectra not shown), the IRAS data show the same characteristic features: a very weak ν(CO) band is detected at *ca.* 2088 cm^{-1}, resembling the findings for the pure TiO$_x$ films under similar conditions (see section III.1). This feature is still present after pumping off the system to UHV and is again attributed to adsorption on exposed areas of the Pt substrate, which are uncovered upon gas exposure. Therefore, a similar modification of the film morphology like on the clean UT reduced films can be deduced from these measurements. This is also in agreement with XPS data collected before and after HP exposure of the *z*′- and *w*′-Au/TiO$_x$ model systems, which show a similar modification of the Ti 2p peak shape and position like on the pure TiO$_x$ substrate films: such evidence corroborates the conclusion that the presence of Au NPs does not affect the oxidation and dewetting phenomena occurring for these reduced films. The Au 4f XPS spectra of the Au/*z*′-TiO$_x$ and Au/*w*′-TiO$_x$ system collected before and after HP to CO–O$_2$ (1 : 1) gas mixture do not show any significant change in the position/shape of the peaks (see for example the data reported in Fig. S1(b) and S2(b), ESI†).

A second very weak and broad band is detected at *ca.* 2120 cm^{-1}, which is associated with CO adsorption on the residual oxide supported Au NPs remaining after the oxidative dewetting process. The STM images of the corresponding Au/TiO$_x$ model catalysts after exposure to CO–O$_2$ (1 : 1) gas mixtures have been also recorded (see in Fig. S3 (ESI†) the case of Au/*z*′-TiO$_x$). However, the analysis of the STM images is quite complex because the final composite surface appears to be very rough (TiO$_2$ nanograins, Au NPs and uncovered portions of Pt(111) are exposed). The strong reduction of the ν(CO) band intensity is attributed to the fact that, after the TiO$_x$ film dewetting, most of the Au is probably present in mono- or multilayer islands in direct contact with the Pt underneath, which is inert towards CO adsorption under these conditions. The latter was demonstrated for CO adsorption on a Au monolayer on a Pt(111) surface (in the absence of TiO$_x$), where no CO bands were detected by IRAS.[58]

A different behaviour is observed for the Au/*rect*′-TiO$_2$ model system (Fig. 7): here a distinct ν(CO) band is visible upon exposure to the CO–O$_2$ mixture. Hence, the catalyst is stable under the tested experimental conditions, as already seen for the clean *rect*′-TiO$_2$ UT film. A blue shift of 8 cm^{-1} is observed upon changing from pure CO to the CO–O$_2$ HP exposure, which is typical for such reactive mixtures, and is attributed to the presence of coadsorbed oxygen, which has an electron-withdrawing effect.[59,60] XPS data collected before and after HP exposure to the CO–O$_2$ (1 : 1) mixture for this system revealed no change, neither in the peak position, whose BE value is typical of a stoichiometric TiO$_2$ film, nor in the peak profiles.

In conclusion, the effect on the Au/TiO$_x$/Pt(111) model catalysts of the exposure to CO–O$_2$ (1 : 1) gas mixtures is really dependent on the oxidation state of the oxide support. Reduced supports are transformed into a complex nanocomposite system which can be hardly used as a model catalyst to study the CO + O$_2$ reactivity of well characterized Au NPs, because the model system itself suffers many morphological changes and the chemical nature of the Au sites is thus strongly perturbed.

IV. Conclusion

In order to investigate the potential of ultrathin TiO$_x$ films on Pt(111) for serving as appropriate model systems for a titania support in planar Au/TiO$_2$ model catalysts, we have

investigated the stability of Pt(111) supported TiO_x films with different stoichiometry and defectivity, and of related Au/TiO_x model catalysts under semi-realistic conditions, *i.e.*, in the presence of reactive gases such as oxygen and carbon monoxide at pressures up to 100 mbar.

In the first part of this study, we show that fully oxidized films (*rect*′-TiO_2) are stable in CO and CO–O_2 (1 : 1) atmospheres, while both types of reduced films (z'-TiO_x and w'-TiO_x), undergo an oxidative dewetting process at RT once exposed to the CO–O_2 ambient. This eventually leads to a nanocomposite surface with very small (from 0.5 to 3 nm lateral sizes) titania nanograins coexistent with uncovered parts of the Pt substrate. Albeit in contradiction with the starting goal, this finding (nanocomposite surfaces) might lead to surfaces with new chemical properties as a consequence of the nanoscale dimensionality. Further experiments to explore the design of a Au/titania nanocomposite are in progress, starting either directly from the Au/TiO$_x$/Pt(111) system or by depositing Au on the HP treated UT films.

In the second part, we have tried to relate the chemisorption properties of Au NPs grown on the three investigated UT films up to a CO pressure of 100 mbar with their sizes and morphologies. Actually, the different UT films represent a valuable tool to prepare Au NPs with different shapes and lateral sizes ranging from 1 to 6 nm in UHV. The reported measurements demonstrated that the Au/TiO$_x$/Pt(111) model catalysts are stable in pure CO under HP conditions, allowing us to study the chemisorption properties of the different Au NPs. According to the IRAS measurements, the flat small Au NPs (typical thickness of 2–3 layers) strongly coupled to the reduced z'-TiO_x film and the Pt substrate, present the strongest Au–CO interaction, as evident from the fact that saturation coverage is reached already at *ca.* 1 mbar, which is in agreement with findings in previous studies.[6,27,42] For the more 3D shaped Au NPs formed on the w'-TiO_x and *rect*′-TiO_2 phases, the weaker Au–CO interaction results in a continuous CO_{ad} coverage increase over the entire pressure range. To summarize, the actual Ti oxidation state of the oxide substrate in Au/TiO$_x$/Pt(111) model catalysts does not seem to play a major role for the CO chemisorption on the Au NPs, while morphological aspects, regarding both the film and the Au NPs, are probably more relevant.

On the contrary, the low stability of the reduced Au/TiO$_x$/Pt(111) model catalysts in the presence of oxygen renders such model catalysts hardly usable for studying the size and shape dependent reactivity of Au NPs in CO–O_2 mixtures.

Acknowledgements

This work has been funded by the European Community through two STRP projects: GSOMEN and NanoChemSens within the SIXTH FRAMEWORK PROGRAMME, by the University of Padova, through the Progetto Strategico PLATFORMS (PLAsmonic nano-Textured materials and architectures FOR enhanced Molecular Sensing) and the grant CPDA071781, and by the Deutsche Forschungsgemeinschaft, *via* the collaborative research center (SFB) 569.

References

1 M. Haruta, T. Kobayashi, H. Sano and N. Yamada, *Chem. Lett.*, 1987, 405.
2 M. Haruta, *Catal. Today*, 1997, **36**, 153.
3 M. Haruta, *CATTECH*, 2002, **6**, 102.
4 R. Meyer, C. Lemire, Sh. K. Shaikutdinov and H.-J. Freund, *Gold. Bull.*, 2004, **37**, 72.
5 M. C. Kung, R. J. Davis and H. Kung, *J. Phys. Chem. C*, 2007, **111**, 11767.
6 M. S. Chen and D. W. Goodman, *Science*, 2004, **306**, 252.
7 N. Lopez, T. V. W. Janssens, B. S. Clausen, Y. Xu, M. Mavrikakis, T. Bligaard and J. K. Nørskov, *J. Catal.*, 2004, **223**, 232.
8 N. C. Hernández, J. F. Sanz and J. A. Rodriguez, *J. Am. Chem. Soc.*, 2006, **128**, 15600.
9 H.-J. Freund and G. Pacchioni, *Chem. Soc. Rev.*, 2008, **37**, 2224.
10 S. Kinge, M. Crego-Calama and D. N. Reinhoudt, *ChemPhysChem*, 2008, **9**, 20.
11 S. Degen, C. Becker and K. Wandelt, *Faraday Discuss.*, 2004, **125**, 343.
12 N. Berdunov, G. Mariotto, K. Balakrishnan, S. Murphy and I. V. Shvets, *Surf. Sci.*, 2006, **600**, L287.
13 G. Hamm, C. Becker and C. R. Henry, *Nanotechnology*, 2006, **17**, 1943.
14 K. Jordan, S. Murphy and I. V. Shvets, *Surf. Sci.*, 2006, **600**, 5150.
15 M. Schmid, G. Kresse, A. Buchsbaum, E. Napetschnig, S. Gritschneder, M. Reichling and P. Varga, *Phys. Rev. Lett.*, 2007, **99**, 196104.
16 E. Napetschnig, M. Schmid and P. Varga, *Surf. Sci.*, 2007, **601**, 3233.
17 F. Sedona, S. Agnoli, M. Fanetti, I. Kholmanov, E. Cavaliere, L. Gavioli and G. Granozzi, *J. Phys. Chem. C*, 2007, **111**, 8024.
18 G. A. Rizzi, F. Sedona, L. Artiglia, S. Agnoli, G. Barcaro, A. Fortunelli, E. Cavaliere, L. Gavioli and G. Granozzi, *Phys. Chem. Chem. Phys.*, 2009, **11**, 2177.
19 E. Cavaliere, I. Kholmanov, L. Gavioli, F. Sedona, S. Agnoli, G. Granozzi, G. Barcaro and A. Fortunelli, *Phys. Chem. Chem. Phys.*, 2009, **11**, 11305.
20 R. T. Vang, E. Lægsgaard and F. Besenbacher, *Phys. Chem. Chem. Phys.*, 2007, **9**, 3460.
21 For a recent overview see: Q.-H. Wu, A. Fortunelli and G. Granozzi, *Int. Rev. Phys. Chem.*, 2009, **28**, 517.
22 F. Sedona, G. A. Rizzi, S. Agnoli, F. X. Llabrés i Xamena, A. Papageorgiou, D. Ostermann, M. Sambi, P. Finetti, K. Schierbaum and G. Granozzi, *J. Phys. Chem. B*, 2005, **109**, 24411.
23 G. Barcaro, S. Agnoli, F. Sedona, G. A. Rizzi, A. Fortunelli and G. Granozzi, *J. Phys. Chem. C*, 2009, **113**, 5721.
24 A. Vittadini, F. Sedona, S. Agnoli, L. Artiglia, M. Casarin, G. A. Rizzi, M. Sambi and G. Granozzi, *ChemPhysChem*, 2010, **11**, DOI: 10.1002/cphc.200900872.
25 F. Sedona, M. Sambi, L. Artiglia, G. A. Rizzi, A. Vittadini, A. Fortunelli and G. Granozzi, *J. Phys. Chem. C*, 2008, **112**, 3187.
26 T. Diemant, Z. Zhao, H. Rauscher, J. Bansmann and R. J. Behm, *Top. Catal.*, 2007, **44**, 83.
27 T. Diemant, H. Hartmann, J. Bansmann and R. J. Behm, *J. Catal.*, 2007, **252**, 171.
28 T. Diemant, Z. Zhao, H. Rauscher, J. Bansmann and R. J. Behm, *Surf. Sci.*, 2007, **601**, 3801.
29 P. Finetti, F. Sedona, G. A. Rizzi, U. Mick, F. Sutara, M. Svec, V. Matolín, K. Schierbaum and G. Granozzi, *J. Phys. Chem. C*, 2007, **111**, 869.
30 Z. Zhao, T. Diemant, T. Häring, H. Rauscher and R. J. Behm, *Rev. Sci. Instrum.*, 2005, **76**, 123903.
31 F. Sedona, G. Granozzi, G. Barcaro and A. Fortunelli, *Phys. Rev. B: Condens. Matter Mater. Phys.*, 2008, **77**, 115417.
32 F. Sedona, S. Agnoli and G. Granozzi, *J. Phys. Chem. B*, 2006, **110**, 15359.
33 Y. Zhang, L. Giordano, G. Pacchioni, A. Vittadini, F. Sedona, P. Finetti and G. Granozzi, *Surf. Sci.*, 2007, **601**, 3488.
34 CO adsorption on the UT TiO_x films is not possible under the present experimental conditions.
35 S. Agnoli, T. O. Mentes, N. A. Nino, A. Locatelli and G. Granozzi, *Phys. Chem. Chem. Phys.*, 2009, **11**, 3727.

36 A. Atrei, A. M. Ferrari, P. Finetti, A. Beni and G. Rovida, *J. Phys. Chem. C*, 2009, **113**, 19578.
37 Y. N. Sun, Z. H. Qin, M. Lewandowsky, E. Carrasco, M. Sterrer, S. Shaikhutdinov and H. J. Freund, *J. Catal.*, 2009, **266**, 359.
38 G. Barcaro, F. Sedona, A. Fortunelli and G. Granozzi, *J. Phys. Chem. C*, 2007, **111**, 6095.
39 F. Sedona, M. Eusebio, G. Granozzi, D. Ostermann and K. Schierbaum, *Phys. Chem. Chem. Phys.*, 2005, **7**, 697.
40 D. Ragazzon, Structure and N-doping of titania nanostructures on Pt (111), *Master Degree Thesis*, University of Padova, 2009.
41 D. V. Potapenko, J. Hrbek and R. M. Osgood, *ACS Nano*, 2008, **2**, 1353.
42 M. S. Chen and D. W. Goodman, *Acc. Chem. Res.*, 2006, **39**, 739.
43 M. Chen, Y. Cai, Z. Yan and D. W. Goodman, *J. Am. Chem. Soc.*, 2006, **128**, 6341.
44 D. C. Meier and D. W. Goodman, *J. Am. Chem. Soc.*, 2004, **126**, 1892.
45 M. S. Chen and D. W. Goodman, *Top. Catal.*, 2007, **44**, 41.
46 Z. Zhao, T. Diemant, D. Rosenthal, K. Christmann, J. Bansmann, H. Rauscher and R. J. Behm, *Surf. Sci.*, 2006, **600**, 4992.
47 M. Mavrikakis, P. Stoltze and J. Nørskov, *Catal. Lett.*, 2000, **64**, 101.
48 W.-L. Yim, T. Nowitzki, M. Necke, H. Schnars, P. Nickut, J. Biener, M. M. Biener, V. Zielasek, K. Al-Shamery, T. Klüner and M. Bäumer, *J. Phys. Chem. C*, 2007, **111**, 445.
49 C. Winkler, A. J. Carew, S. Haq and R. Raval, *Langmuir*, 2003, **19**, 717.
50 C. Lemire, R. Meyer, Sh. K. Shaikhutdinov and H.-J. Freund, *Angew. Chem.*, 2004, **116**, 121.
51 C. Lemire, R. Meyer, Sh. K. Shaikhutdinov and H.-J. Freund, *Surf. Sci.*, 2004, **552**, 27.
52 D. C. Meier, V. Bukhtiyarov and D. W. Goodman, *J. Phys. Chem. B*, 2003, **107**, 12668.
53 D. R. Rainer, C. Xu, P. M. Holmblad and D. W. Goodman, *J. Vac. Sci. Technol., A*, 1997, **15**, 1653.
54 A. Vittadini, M. Casarin and A. Selloni, *J. Phys. Chem. C*, 2009, **113**, 18973.
55 J. France and P. Hollins, *J. Electron Spectrosc. Relat. Phenom.*, 1993, **64–65**, 251.
56 F. Boccuzzi, S. Tsubota and M. Haruta, *J. Electron. Spectrosc. Relat. Phenom.*, 1993, **64–65**, 241.
57 P. Dumas, R. G. Tobin and P. L. Richards, *Surf. Sci.*, 1986, **171**, 579.
58 M. Eyrich, H. Hartmann, T. Diemant, J. Bansmann and R. J. Behm, unpublished results.
59 M. A. Bollinger and M. A. Vannice, *Appl. Catal. B*, 1996, **8**, 417.
60 B. Schumacher, Y. Denkwitz, V. Plzak, M. Kinne and R. J. Behm, *J. Catal.*, 2004, **224**, 449.

Section 4

Fe Based Model Catalysts

Chapter VII

State of the art 3: Fe at the nanoscale and SMSI effect

In this chapter I will shortly report on the abundant literature on Fe NPs and their applications. For convenience of the reader, a full overview on this topic can be found in a review article.[1] In addition, I will make a complete treatment of the so called Strong Metal Support Interaction (SMSI), of relevance to discuss the results reported in Chapter VIII.

VII.1 Properties of Fe at the nanoscale

In general, metal NPs can exhibit unique optical, chemical and magnetic properties due to their finite size. In the Fe case, no interest in the scientific community is associated to its optical properties, but the other two are still a living topic. Reducing the size from the bulk material to the NPs range cause a huge increase in the exposed surface area, even if this effect is not the only one leading to the observed reactivity enhancement. A large part of the overall NPs energy is stored as surface free energy, thus leading to a significant catalytic activity and enhanced magnetic properties. Surface defects are believed to be the responsible for the enhanced catalytic activity and NPs have an enormous concentration of these under-coordinated atoms, steps and kinks. Moreover, also the nanoscale effects have a big impact on the electronic structures of the NPs, leading to magnetic properties that are different from the ones of the bulk counterpart. When the NPs dimensions are increased, these peculiar properties tend to converge into the bulk ones. In the following, these two properties, i.e. magnetic and chemical properties, will be further analysed.

In the first half of XX century many studies on iron particles have been reported, focused on their macroscopic magnetic properties (e. g. magnetization) and many theories have been developed, in order to rationalize them. However, it was difficult at that time to have a clear output without a direct correlation with the particles dimensions. Starting from the 1950s and using electron microscopy, it was possible to investigate the Fe NPs based systems in more details. Hence, putting together the theory and the new experimental evidences, a complete theory regarding Fe NPs magnetism was proposed.[2,3,4,5,6] The research on Fe NPs has experienced a renewed interest in the last two decades, as a consequence of their applications in many industrial fields.[7] In fact, magnetic NPs are of great interest today and iron is the most useful and largely available amongst them. Compared to the other, commonly used, magnetic elements (e. g. Co, Ni), Fe has the highest room temperature value for saturation magnetization (σ_s) and a low magnetocrystalline anisotropy, allowing Fe NPs to show *superparamagnetic* behaviour in a wide size range.

VII.1.1 Magnetic properties

NPs made by ferro- or ferrimagnetic material, whose dimensions are below a certain size (10-20 nm) show a unique form of magnetism, called *superparamagnetism*.[8] In the bulk materials, the spins of unpaired electrons undergo spontaneous collective interactions, lowering their average energy by aligning the spins with the neighbouring atoms. Normally, to mediate the overall energy of the system decreasing the magnetic flux leakage, the materials divide into magnetic domains, whose size is determined by the competition between the energy increase due to external magnetic flux and the energy cost of formation of additional domain walls. The walls, dividing the domains, can be modified by the application of an external magnetic field, and their movement give rise to the hysteresis curves typical of the ferromagnetic materials. The magnetic domains size varies depending on the material but usually is in tens of nanometers. Hence, if a NP is smaller than this size, it will contain a single magnetic domain. The single domain NPs are stable because the energy needed to create a new wall would be higher than the energy decrease achieved by the resulting decrease in the magnetic flux.[9,10,11] Moreover it is well known that there is a certain temperature that marks the transition between the

superparamagnetism and ferromagnetism, increasing with the NPs increasing size so that its value could be impractically high for large domain NPs.

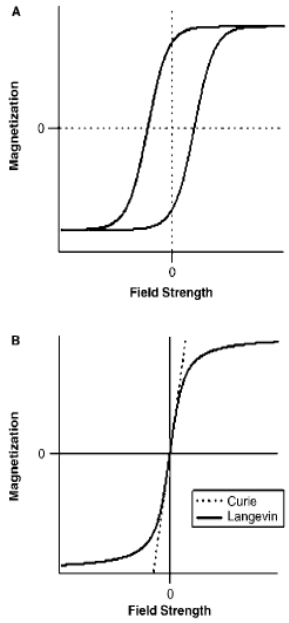

Figure VII.1. Idealized magnetization curves. (A) M versus H for a ferromagnetic (or ferrimagnetic) material. This curve demonstrates the familiar magnetic hysteresis of these systems, and the coercive field (Hc) and remnant magnetization (MR) are labelled; (B) M versus H for a superparamagnetic sample. Curie's law is accurate at low fields, while the Langevin equation fits the magnetization behaviour at all fields. Note the lack of hysteresis

The term *superparamagnetism* has been chosen as a consequence of the similarity to the behaviour of paramagnetic samples. Usually, a paramagnetic ion has no magnetic moment in a zero field even if a weak moment can be induced by applying an external magnetic field. In this case, the particle moment is called induced and its intensity increases as the external field increases, until reaching a limit value. At low fields there is a linear increase of the magnetization, in tune with the Curie's law, while at higher fields the spins approach to their saturation value, leaving the linear correlation with the field: their overall behaviour is predicted by the Langevin equation. The magnetization, in the case of paramagnetic samples, also depends on the temperature as predicted by the Curie's law, decreasing as T^{-1} with the increasing temperature. Paramagnetic ions do not have strong interactions with the neighbours so that a small activation barrier has to be passed in the processes and no hysteresis is observed in figure VII.1 B (a typical hysteresis curve is shown by ferro- and ferromagnetic samples (figure VII.1 A). A *superparamagnetic* sample shares many

macroscopic properties with a paramagnetic one: both of them show Curie's law behaviour at low applied fields and Langevin behaviour at all the other fields, T^{-1} dependence of the magnetization on the temperature and no hysteresis. In the case of *superparamagnetic* particles, the magnetization is larger than the one observed for paramagnetic samples. In spite of all these similarities, the way *superparamagnetic* NPs are able to show their typical behaviour is different from the paramagnetic ones. *Superparamagnetic* NPs have a fixed magnetic moment that only varies in its direction, and their net magnetization at zero field is zero as a consequence of the random orientation of the various particle spins. Thence, *superparamagnetic* NPs spins reorientation is already achieved at relatively low fields, thus meaning that the initial susceptibility values are very high.

Another interesting property distinguishing *superparamagnetic* NPs is that they have no coercivity, so that when the external field is removed, the thermal energy allow them to freely reorient their spins. This phenomenon can occur only in a limited temperature range: hence, below a certain temperature called "blocking temperature" (T_b), the NPs behaviour becomes ferromagnetic (even if the NPs are still single-domain). Thus, the T_b is important since it represent the maximum in the sample susceptibility and the lower limit of the superparamagnetic behaviour.

Studying Fe NPs magnetic properties is very important since they can exhibit the lowest (zero) or higher coercivity depending upon size.

VII.1.2 Chemical properties and catalytic applications

The chemistry of Fe NPs is influenced by the extreme high reactivity with oxidizing agents, so that it is extremely difficult to use Fe based catalyst in the air. Many efforts have been done in order to lower this reactivity, and some strategies are now well known. Pre-oxidation of the NPs is a commonly used technique to handle them, since the magnetite shell formed during this process is strongly adherent to the metal and acts as an oxidation barrier avoiding the direct contact between the Fe and the oxygen. Other methods are the alloying, for example with a noble metal such as Pt to form stable Fe-Pt NPs[12] or the coating, usually done by Au. In any case, all the protection methods significantly alter the Fe chemical properties and are not useful for catalysis purposes.

In spite of its big reactivity towards oxidizing agents, Fe NPs based catalysts can find application in some interesting processes taking place in reducing atmospheres. The most relevant are:

- Fischer – Tropsch synthesis, to obtain hydrocarbons from *syngas*,[7]
- coal liquefaction,[13]
- hydroformilation of an alkene,[14]
- hydrogenation of naphthalene,[15]
- growth of gallium nitride nanostructures,[16]
- growth of carbon nanotubes.[17,18]

It is important to point out our attention on the first process. Coal can be converted through steam reforming into *syngas*, a mixture of CO and H_2. The *syngas* can then be converted into hydrocarbons through the Fischer Tropsch synthesis, a catalytic process involving *syngas* in high pressure and temperature conditions.[7] The critical step in this synthesis is the formation of a new C-C bond on the catalyst surface. For this purpose, the group VII metals demonstrated to have the highest activity and Fe was chosen amongst them for its low price compared to the Ruthenium.[19] The studies on the reactivity of Fe NPs based catalysts for the Fischer – Tropsch synthesis are promising, and a conventional way to obtain such systems is to deposit Fe^{3+} species from a solution and then reduce them to metallic Fe in a hydrogen flux.[20] The observed catalytic activity is six times larger than the one measured on other conventional materials and the main reaction product is methane. The authors explain these evidences considering the small size of Fe NPs, limiting the amount of adsorbing CO molecules. On the other side, H_2 adsorption is favoured, thus leading to the chain termination reaction instead of the C-C chain growth.

VII.2 The Strong Metal Support Interaction (SMSI) effect

The SMSI effect has been reported for the first time in 1978 by Tauster et al., to justify the dramatic reduction in the CO and H_2 chemisorption from metallic NPs supported on TiO_2 after thermal treatment at high temperatures.[21] The authors tried to focus on the metal-substrate interactions, using transition metal oxides as supports and considering that these oxides could show a higher interaction with the metal NPs than the non-transition ones (Al_2O_3, SiO_2, ecc.). In particular, they focused their attention on the overlap between the *d* orbitals of the two transition metals: the metallic atoms belonging to the NPs and the cations belonging to the oxide lattice. In the first work reported by Tauster et al.,[21] the authors show how the chemisorption properties of some metals are altered by the interaction with a TiO_2 surface: after a reducing thermal treatment at 773 K the CO and H_2 adsorption vastly decrease. Electron microscopy and X ray diffraction experiments show neither metal agglomeration nor metal poisoning as a cause of this. Moreover, all the systems totally recovered their adsorption properties after oxidation ad 673 K. Hence, the authors find the only explanation in the strong interaction between the metal NPs and the lattice cations (the term SMSI comes from these first evidences).

In a second work, Tauster started to consider the possibility that also other oxides might show SMSI.[22] In particular, if the "strong interaction" is caused by the lattice cations *d* orbitals, this should limit the reactivity to the transition metals. Starting from these assumptions, the authors made an empiric analysis of various systems formed by metal NPs supported on different oxides (MgO, Sc_2O_3, Y_2O_3, TiO_2, ZrO_2, HfO_2, V_2O_3, Nb_2O_5, Ta_2O_5) and observed that only a part of them were active through SMSI (TiO_2, V_2O_3, Nb_2O_5, Ta_2O_5). The overall conclusions were that, as expected, only the transition metal oxides were able to establish a strong interaction with the metal NPs, even if not all the analyzed transition metal oxide substrate were active. Two of them, the Sc_2O_3 and the ZrO_2 did not show SMSI, and this could be justified considering their refractory behaviour, thus establishing a direct relation between the SMSI activity and the oxide reducibility.

In a third work, published in 1987, on the basis of the observations made during the previous years, Tauster tried to summarize on the SMSI effect.[23] In fact, many experiments showed that some systems (metal NPs/reducible oxide) were perturbed by the temperature, leading to the diffusion of the oxide on the NPs or to a metal

diffusion on the surface in order to increase the oxide coverage. All these events reflected different bonding interaction so that many transition metals, included some "noble" metals, were found to establish interfacial bonds with the reduced transition metal oxides. The fundamental requirement for the SMSI effect resulted to be the surface reduction state of the transition oxide, leading to a spontaneous increase of the metal-oxide interface. In the case of TiO_2, one of the most studied substrates, direct interactions between the metal atoms and the reduced oxide lattice Ti ions were observed through spectroscopic techniques. In any case, all the examples of SMSI involving metal NPs dispersed on an oxide, led to dramatic changes in the overall catalyst morphology through NPs coalescence to form metal thin films or oxide migration on top of the NPs.

In recent years, the interpretation of the SMSI effect have achieved further improvements, leading to the distinction between two factors:

- an *electronic* factor, due to the perturbation of the electronic structure of both the metal and the oxide as a consequence of the charge transfer between them
- a *geometric* factor (*encapsulation*), which is predominant when metal NPs are covered by a reduced thin oxide layer, coming from the oxide substrate and thus blocking all the active sites for catalysis.

VII.2.1 Strong interactions between metals and oxides mixed conductors

The category of oxides that show both electronic and ionic mobility is called "mixed conductors". These materials are able to convert chemical energy in electric energy end vice-versa and thus are used in many applications such as catalysis, photocatalysis, fuel cells, etc. The chemical interactions taking place at the metal/oxide interface can be divided in 4 different groups depending on the products yield:

- *redox reactions*, involving a charge transfer between the metal and the oxide that lead to the NPs oxidation and the oxide partial reduction
- *alloy formation*, producing stable inter-metallic compounds at the interface
- *encapsulation*, generating a mass transfer from the oxide substrate to the metallic NPs surface
- *inter-diffusion*, implying the migration of the metal inside the substrate and vice-versa.[24]

Based on the electronic and geometric factors affecting the SMSI effect, in the following paragraph we will focus on both the thermodynamics and the kinetics governing the *redox reactions* and the *encapsulation* processes.

VII.2.2 Thermodynamic aspects of the SMSI effect

Thermodynamic data regarding reagents and products at the interface are often not available so that, making an approximation, it is necessary to use the thermodynamic data regarding their *bulk* counterparts. The values are different from the ones representing the phases involved in the SMSI, whose chemical composition is frequently unknown. In spite of all these aspects, it is possible to define the fundamental thermodynamic aspects for the redox reactions and the encapsulation processes involving metal NPs supported on an oxide. We will consider TiO_2 as the prototype for these examples, since this oxide is widely used as a substrate in many applications and has been used during our experiments.

- Redox reaction: $M + TiO_2 \rightarrow MO_x + TiO_{2-x}$

To test if the reaction takes place ($\Delta G < 0$) it is enough to consider the heat of formation (ΔH_f^o) of the involved oxides, since the entropy changes in a solid sample are negligible. U. Diebold reports, as a general conclusion, that the redox reactions are favoured when $\Delta H_f^o < -250$ kJ/mol.[25]

- Encapsulation reaction: this reaction can take place mainly through the system surface energy minimization. The general condition to respect is that:

$$\gamma_{Me} + \gamma_{Me-O_x} + \gamma_{Ox-Sub} > \gamma_{Ox} + \gamma_{Ox-Me} + \gamma_{Me-Sub}$$

It has been demonstrated that metals with $\gamma > 2$ J/m are prone to encapsulation reactions.[26]

VII.2.3 Kinetic aspects of the SMSI effect

The kinetics of the interface reactions between a metal and the TiO_2 is determined by mass transfer processes in the oxide surface region. In the TiO_2, the mass transfer processes involve the diffusion of interfacial defects (Ti^{n+}) and oxygen vacancies (V_O^{x+}). The metal oxidation on TiO_2 is controlled by the diffusion of O^{2-} species through the interface while the encapsulation is limited by the diffusion of interstitial Ti^{n+} cations from the bulk to the interface. Many experimental results have shown that the Ti^{n+} species have a large diffusivity in the TiO_2 at high temperatures but, at the same time, metal/TiO_2 reactions at the interface are thermally limited to low temperatures.[26] Hence it is important to consider the kinetics of both the redox reactions and the encapsulation process.

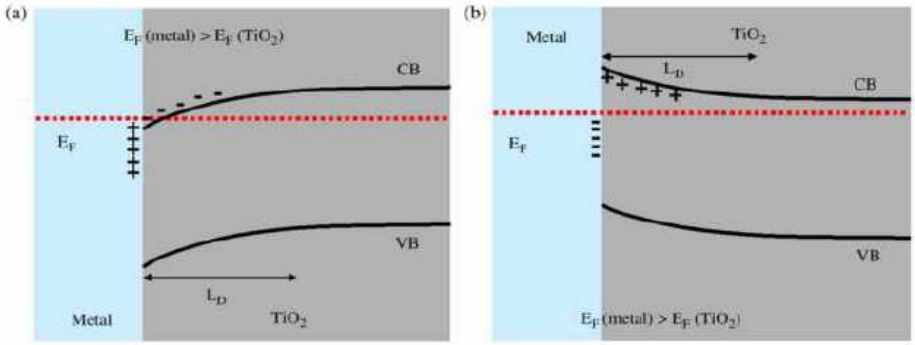

Figure VII.2

- Redox reaction.

When the electronic configuration at the metal/TiO_2 interface is $E_{F(metal)} > E_{F(TiO_2)}$ (figure VII.2 a), the metal/oxide contact causes a charge transfer from the metal to the TiO_2 thus leading to the formation of an overall negative TiO_2 surface charging and a downward band bending of it. This event favour the O^{2-} ions diffusion to the surface, thus leading to a metal oxidation and the consequent oxide partial reduction.[26]

- Encapsulation reaction.

When the electronic configuration at the metal/TiO_2 interface is $E_{F(metal)} < E_{F(TiO_2)}$ (figure VII.2 b), the metal/oxide contact cause a charge transfer from the TiO_2 to the

metal, thus leading to the formation of positive charges at the TiO_2 surface and an upward band bending of it. This event favour the Ti^{n+} cations diffusion and then the metal encapsulation.[26]

Considering that the work-function (φ) is the measured energy difference between an electron in the Fermi level and the same one immediately outside the solid, it is easy to understand that the interaction between a metal deposited on an oxide substrate is influenced by their φ. It is then possible to classify the metal in different group depending on their φ value and thus reactivity (figure VII.3), always considering that $\varphi_{TiO_2} \cong 5.2eV$.

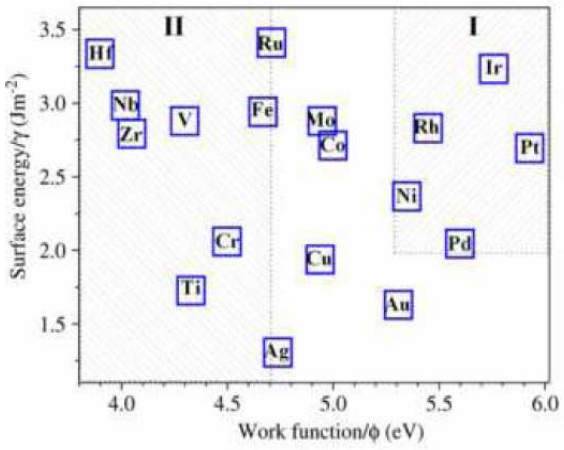

Figure VI.3

- *First and second group metals, with a φ < 3.0 eV* (Cs, K, Na, Ca and Ba). These metals show the highest reactivity towards TiO_2 surfaces, in tune with their high affinity with oxygen and grow forming multilayers of oxidized metals.

-*Metals with a 3.75 eV < φ < 5.0 eV* (Mo, Fe, Cr, V, Ti. Nb, Hf and Al). The redox reaction result to be favoured for this group, as reported by various experimental tests.[26] In particular, Fe has to be considered apart since, as it is possible to note in figure VII.3, its work-function is borderline between the region I and II (encapsulation and redox). In the literature many cases regarding a direct reaction between the Fe and the TiO_2 are reported, even if some cases of encapsulation were found. In fact, if we consider the general inequality regarding the Fe/TiO_2 surface energies:

$$\gamma_{Me} + \gamma_{Me-Ox} + \gamma_{Ox-Sub} > \gamma_{Ox} + \gamma_{Ox-Me} + \gamma_{Me-Sub}$$

and assuming that $\gamma_{Me-Ox} \approx \gamma_{Ox-Me} \approx \gamma_{Ox-Sub}$ (these are all metal/oxide interfaces) and $\gamma_{Me-Ox} \geq \gamma_{Me-Sub}$ (considering Fe electropositivity), the most important terms are γ_{Me} and γ_{Ox} and the inequality becomes:

$$\gamma_{Me} + \gamma_{Me-Ox} > \gamma_{Ox} + \gamma_{Me-Sub}$$

Since, as a general trend, the oxide surfaces free energy is considerably smaller than that of the metal surfaces it is possible that, in the case of Fe, after encapsulation the system reaches an higher stability. These considerations could explain why the Fe/TiO_2 system show both a redox reaction and encapsulation at the interface with TiO_2.

- *Metals with a 4.6 eV < φ < 5.4 eV* (Ag, Au and Cu). The ΔH_f^o of these metals are above the -250 kJ/mol and, as a consequence of this, neither metal oxidation nor TiO_2 reduction is observed at the metal/TiO_2 interface in a wide temperature range.[26]

- *Metals with φ > 5.4 eV* (Pt, Pd, Rh, Ir and Ni). The metals belonging to this group do not react with the TiO_2 substrate, even at high temperatures. A prolonged heating of the systems metal/TiO_2 leads to metal encapsulation.[26]

VII.2.4 The SMSI effect in the Fe/TiO_2 system

In the previous paragraph, we reported about the double nature of the Fe deposited on a reducible oxide like TiO_2. This interaction has been studied by different groups and we will briefly report the main outcomes.

Pan and Madey report a study about the growth and the reactivity of ultrathin Fe films on TiO_2 (110) surface, and, through LEIS and XPS, show how at RT the metal form fully wetting islands on the oxide, even after a few monolayer (ML) deposition.[27] This behaviour is explained as a consequence of the high affinity between the metal and the oxide. For instance, other 3d metal having a lower affinity

for oxygen than Fe (like Cu), grow on TiO_2 forming smaller islands.[28] The same authors also examined the reactivity of this system, observing an oxidation of the Fe adatoms at the interface as a consequence of the large charge transfer from the Fe to the TiO_2. XPS spectra show how, even after the first Fe deposition step, an oxidation reaction takes place, leading to the appearance of a Fe $2p_{3/2}$ peak centred at about 709 eV. If the amount of deposited Fe is increased, a lower BE peak (about 706.5 eV) starts to develop, and is representative of the Fe metallic state (figure VI.4).

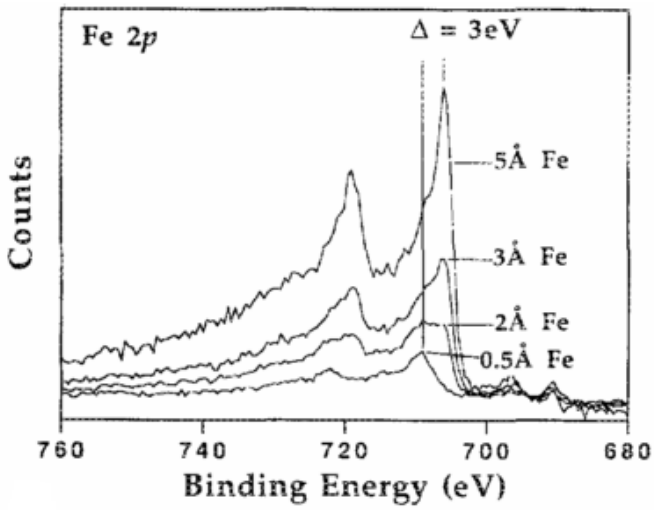

Figure VII.4 [27]

Considering the position of the "high BE" peak and the separation between it and the other component (Δ = 3.0 eV) it is possible to identify the Fe oxidation state (Fe^{2+}).[27] This could be the evidence for the formation of FeO at the interface between the Fe and the TiO_2 after deposition at RT, although no encapsulation is observed. Also Diebold et al. came to the same conclusion in an XPS study of a Fe/TiO_2(110) ultrathin film.[29] Moreover, their analysis shows how a charge transfer between the Fe atoms and the surface O atoms takes place, leading to a reduction of the Ti and an oxidation of the Fe: in particular, the observed Ti oxidation state is comparable to the one obtained after electron bombardment of the TiO_2. Hence, the authors conclude that most probably, during the Fe nucleation, a change in the position of the O atoms from the Ti to the Fe takes place. Nakajima et al. continued and deepened the XPS study analyzing the Fe/TiO_2 system at different coverages.[30] They observed a Fe NPs non-metallic behaviour in the 1.0 to 3.2 ML range coverage and an increasing

metallic component when the amount of Fe is increased and the NPs start to coalesce to form large aggregates and then a film. Focusing on the interaction between the metal and the oxide substrate, Mostèfa-Sba et al. observed an higher redox reactivity (Fe oxidation and, at the same time, TiO_2 reduction) in the 1.0 to 3.0 ML range, when the Fe NPs are still not covering all the TiO_2 surface.[31] When the 3.0 ML coverage is exceeded and a Fe film starts to develop, the interaction between the deposited metallic Fe and the substrate is lower, so that a decrease in the overall reactivity takes place.

The thermal evolution of a Fe/TiO_2 system has then been taken into consideration by Pan and Madey.[32] The collected XPS spectra show how, after an annealing at 773 K, the Fe 2p peak intensity is lower than the one registered at RT and the same peak is also narrowed, as a consequence of an higher metallic component content. Thence, the main difference between the thermal treated sample and the ones analyzed at RT is that the NPs maintain their metallic behaviour, and at the same time a titania sub-oxides migration on top of them is observed (encapsulation). Santos et al. come to the same conclusion considering the CO chemisorption on such a system, observing a progressive decrease of it after the thermal treatment.[33] They interpret this evidence as a consequence of the Fe NPs progressive encapsulation by the TiO_x patches migrating from the oxide substrate and blocking the metal active sites for the CO adsorption. Another interesting study is reported by Petsy et al., as a comparison between the Fe/TiO_2 (110) and the Pt/TiO_2 (110) systems.[34] On the latter, the encapsulation process takes place at relatively low temperatures (450 K), a lower temperature value if compared to the one observed for the Fe/TiO_2 system (800 K). The authors suggest that this event can be interpreted considering the tuning between the wetting properties of the two metals towards the substrate and their tendency to the encapsulation. In fact, if the metal-metal interaction is stronger than the metal-oxide one, then the metal atoms mobility is increased and the wetting tendency is reduced. On the contrary, if the metal-oxide interaction predominates, then the formation of a MeO_x oxide becomes possible, thus disturbing the TiO_x migration on top of the NPs. Therefore, in the case of Pt, the oxidation state of the metal after the annealing is lower than the one of Fe, thus suggesting the preferential formation of Pt-Ti and Fe-O bonds. This different evolution can explain why the Pt encapsulation occurs before the Fe one.

References

[1] D.-L. Huber, *Small* 2005, **1**, 482-501.

[2] C. Kittel, *Phys. Rev.* 1946, **70**, 965–971.

[3] L. Néel, C. R. Hebd, *Seances Acad. Sci.* 1949, **228**, 664–666.

[4] C. Bean, I. Jacobs, *J. Appl. Phys.* 1956, **27**, 1448–1452.

[5] C. Bean, J. Livingston, *J. Appl. Phys.* 1959, **30**, 120S–129S.

[6] I. Jacobs, C. Bean, in *Magnetism*, Vol. III (Eds.: G. T. Rado, H. Suhl), Academic Press, New York, 1963, pp. 271–350.

[7] G. P. Van der Laan, A. A. C. M. Beenackers, *Catal. Rev. Sci. Eng.* 1999, **41**, 255–318.

[8] C. M. Sorensen in Nanoscale Materials in Chemistry (Ed.: K. J. Klabunde), Wiley, New York, 2001, pp. 169–222.

[9] J. Frenkel, J. Dorfman, *Nature* 1930, **126**, 274.

[10] F. Bloch, *Z. Phys.* 1932, **74**, 295.

[11] W. C. Elmore, *Phys. Rev.* 1938, **54**, 1092–1095.

[12] S. Sun, C. Murray, D. Weller, L. Folks, A. Moser, *Science* 2000, **287**, 1989–1992.

[13] A. Martino, M. Stoker, M. Hicks, C. Bartholomew, A. Sault, J. Kawola, *Appl. Catal. A* 1997, **161**, 235–248.

[14] "Preparation of colloidal iron dispersions by the polymer-catalyzed decomposition of iron carbonyl and iron organocarbonyl compounds": T. Smith, USA Patent 4,252,671, 1979.

[15] X. D. Zhan, J. A. Guin, *Energy Fuels* 1994, **8**, 1384–1393.

[16] H.W. Seo, S. Y. Bae, J. Park, H. N. Yang, K. S. Park, S. Kim, *J. Chem. Phys.* 2002, **116**, 9492–9499.

[17] A. Moisala, A. G. Nasibulin, E. I. Kauppinen, *J. Phys. Condens. Matter* 2003, **15**, S3011–3035.

[18] R. Vander Wal, *Combust. Flame* 2002, **130**, 37–47.

[19] M. A. Vannice, *J. Catal.* 1977, **50**, 228–236.

[20] S. G. Marchetti, M. V. Cagnoli, A. M. Alvarez, J. F. Bengoa, N. G. Gallegos, A. A. Yeramian, R. C. Mercader, *Hyperfine Interact.* 2002, **139**, 33–40.

[21] S. J.Tauster, S. C.Fung, R. L.Garten, *J. Amer. Chem. Soc.* 1978, **100**, 170.

[22] S.J.Tauster, S.C.Fung, *J. of Catal.s* 1978, **55**, 29-35.

[23] S.J.Tauster, *Acc. Chem. Res.* 1987, **20**, 389.

[24] Q.Fu, T.Wagner, *Surface Science Reports* 2007, **62**, 431-498.

[25] U.Diebold, *Surface Science Reports* 2003, **48**, 53-229.

[26] Q.Fu, T.Wagner,S.Olliges, H.D.Carstanjen, *Journal of Physical Chemistry B* 2005, **109**, 944-951.

[27] J.-M. Pan, T.E.Madey, *Journal of Vacuum Science Technology A* 1993, **11**, 1667-1674.

[28] J.-M.Pan, B.L.Maschoff, U.Diebold, T.E.Pan, *Surface Science* 1993, **291**, 381-394.

[29] U.Diebold, H.-S. Tao, N.D.Shinn, T.E.Madey, *Physical Review B* 1994, **50**, 14474-14480.

[30] N.Nakajima, H.Kato, T.Okazaki, Y.Sakisaka, *Surface Science* 2004, **561**, 79-86.

[31] H.Mostèfa-Sba, B.Domenichini, S,Bourgeois, *Surface Science* 1999, **437**, 107-115.

[32] J.-M. Pan, T.E.Madey, *Catalysis Letters* 1993, **20**, 269-274.

[33] J.Santos, J.Phillips, J.A. Dumesic, *Journal Of Catalysis* 1982, **81**, 147-167.

[34] F.Pesty, H.-P.Steinrück, T.E.Madey, *Surface Science* 1995, **339**, 83-95.

Chapter VIII
Results on the Fe/TiO_x/Pt(111) model catalysts

In this chapter, the entire set of data collected on the Fe/TiO_x/Pt(111) systems will be presented and discussed in order to provide a full overview about their structural and chemical properties and their evolution as a function of the temperature. Two different Fe/TiO_x/Pt(111) systems will be examined: the Fe/*z'*-TiO_x/Pt(111) and the Fe/*w'*-TiO_x/Pt(111) model catalysts. The former is characterized by a defective and templating UT TiO_x film (see Chapter III), while the latter does not present any periodical defectivity and, therefore, templating effect.
Only a small part of the data is already published (see at the end of the chapter the corresponding reprint) while the unpublished data are the argument of three different manuscripts under development.

VIII.1 The Fe/*z'*-TiO_x/Pt(111) system

In this section I will first report on the data obtained by different surface tools on the Fe/*z'*-TiO_x system, and at the end the current status of understanding emerging from their comparison will be discussed.

VIII.1.1 HR-XPS data for the Fe/*z'*-TiO_x/Pt(111) system

The high resolution XPS data herein presented were obtained at the Beamline for Advanced diCHroism (BACH) of the Elettra Synchrotron (Trieste), using a photon energy of 550 eV to acquire the Ti 2p peaks and of 830 eV to acquire the Fe 2p peaks. The pass energies used were 20 and 50 eV respectively, allowing a total resolution of 0.229 and 0.509 eV, respectively. The experiments at Elettra were

successive to preliminary experiments done at the Surface Science Laboratory in Padova in a standard XPS apparatus (see Chapter II), where the preparation procedure was optimized.

Different amounts of Fe deposited on the ultrathin reduced *z'*-TiO_x phase were taken into consideration, starting from a low coverage (0.1 ML) and then increasing to 0.3, 0.5 and 0.8 ML, where 1 ML (monolayer equivalent) corresponds to $1.5 \cdot 10^{15}\, atoms \cdot cm^{-2}$. Each system was analyzed at room temperature (RT) and after several thermal treatments up to 900 K, maintaining the sample at the desired temperature for 2'. In figure VIII.1 the spectra taken at RT and after thermal treatments at 700 and 900 K, are reported. The whole set of data at intermediate temperatures for the case of Fe(0.5 ML)/*z'*-TiO_x/Pt(111) is reported in the figure 1 of the reprint attached at the end of this chapter.

For convenience, in figure VIII.1a I report only once the Ti 2p spectrum corresponding to the clean TiO_x ultrathin (UT) film, collected before the Fe deposition and used as a reference. Such UT film, behaving as a templating support for the Fe-related nanoparticles (NPs) (see Chapter III), was prepared using the same recipe for each set of experiments.

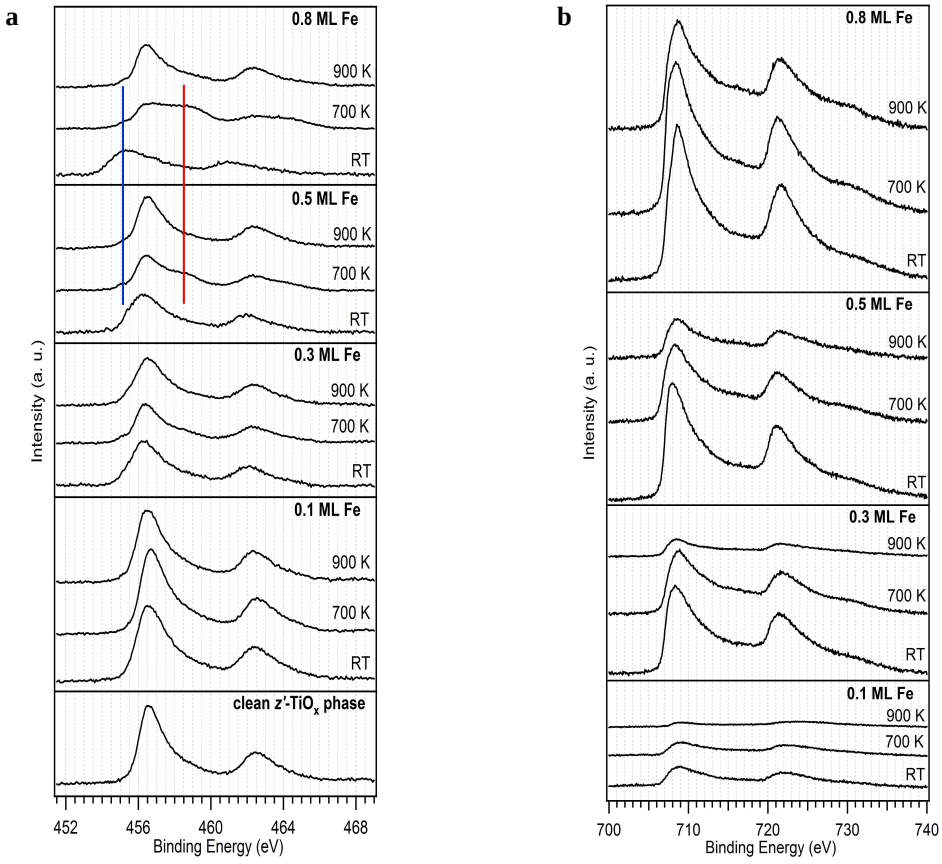

Figure VIII.1 Ti 2p (a) and Fe 2p (b) HR-XPS spectra of the clean z'-TiO$_x$/Pt(111) phase and of the Fe/z'-TiO$_x$/Pt(111) system at 4 different Fe coverages

Focusing on the Ti 2p dataset (figure VIII.1a), it is possible to note that, with respect to the clean *z*'-TiO$_x$ substrate, after the Fe deposition at RT a peak shift is observed. The shift increases with the amount of deposited metal, so that in the case of 0.1 ML of Fe it is difficult to appreciate it but at 0.5 and 0.8 ML is rather evident the presence of a new component at lower binding energy (BE) (blue line reported in figure VIII.1a). Moreover, it is possible to note that, as long as the amount of deposited Fe increases, a high BE shoulder starts to develop in the spectra after the thermal treatment at 700 K (red line reported in figure VIII.1a). This feature almost disappears when the temperature is raised to 900 K and an overall peak shape similar to that of the clean substrate is recovered (900 K spectra). The last evidence is directly related to the Ti 2p intensity: at RT an intensity decrease is observed, whose entity depends on the amount of Fe. When the temperature is raised a progressive increase in the Ti 2p overall intensity is obtained, even if the starting (clean *z*'-TiO$_x$ phase) value is obtained only for the first reported system (0.1 ML Fe). In the other

three cases, the peaks intensity is lower than the one corresponding to the clean phase.

The clean *z'*-TiO_x phase Ti 2p peaks deconvolution (not reported), in line with some previous results,[1] can be properly fitted with two components corresponding to the phase Ti^{3+}, centred at 456.5 eV, and a shoulder (at 458.5 eV) associated to the presence of tetra-coordinated Ti ions contained in some residual TiO_2 particles that are present on the surface after the phase preparation.

The Ti 2p multipeak analysis (figure VIII.2), herein reported after the highest Fe deposition (0.8 ML), clearly shows that immediately after the metal deposition three components are needed to properly fit the spectrum. The lowest BE component (outlined in black), is centred at about 455 eV, a BE value that is in the typical range of a Pt-Ti alloy, while the other two (outlined in blue and green) are centred at about 456.5 (whose BE value corresponds to the one of the Ti^{3+} in the clean *z'* phase, see figure VIII.1 and reference[1]) and 458.1 eV (a BE value typical of Ti^{4+}), respectively. A nice fitting of the spectra collected after thermal treatments of the system at 700 and 900 K is obtained using only the two latter components. Moreover, a 0.5 eV shift in the Ti^{4+} component (from 458.1 to 458.6 eV) is observed when the system undergo the first thermal treatment.

Let us now turn to the Fe 2p HR-XPS dataset reported in figure VIII.1b. Looking at all the examined Fe coverages some common trends can be observed:

i) the peaks have a broad shape, suggesting the presence of several components;

ii) independently from the amount of deposited Fe, a decrease in the overall intensity when the temperature is raised;

iii) focusing on the data taken at RT, the position is slightly shifted to lower BE as long as the amount of Fe is increased.

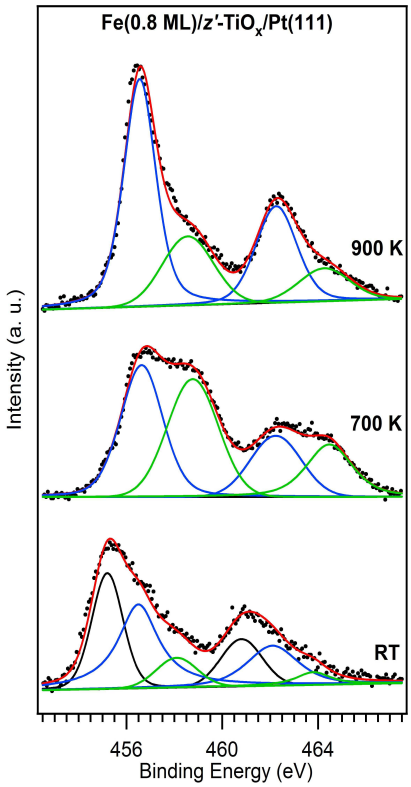

Figure VIII.2 Ti 2p peaks deconvolution for the system Fe(0.8 ML)/z'-TiO$_x$/Pt(111) at room temperature (RT), and thermally treated at 700 and 900 K for 2'.

The Fe 2p multipeak analysis for the Fe(0.5 ML)/TiO$_x$/Pt(111) system at RT is reported in figure VIII.3: it puts in light how complex is the deconvolution procedure since several components are needed to properly fit the experimental data. In particular, the component,(black in the figure) centred at about 707.5 eV (Fe 2p$_{3/2}$), refers to the zero-valent (metallic) Fe, the blue one, centred at about 709.5 eV, is typical of the Fe^{2+} ions, the green one, centred at about 711.5 eV, refers to the Fe^{3+} ions and the brown and grey are the shake-up satellites belonging to the Fe^{2+} and the Fe^{3+} states, respectively.[2] A red, more broad peak, is also present at about 724 eV, and refers to Pt 4s signal, coming out from the Pt(111) single crystal support. After the thermal treatment at 700 K and then at 900 K, a progressive simplification of the spectrum (less components are needed to fit the profile) is observed, together with the overall peaks intensity decrease. It is noteworthy that the metallic component (black) undergo the highest relative decrease: at 900 K it is almost vanished. Also the Fe^{3+} (green) suffers from a considerable reduction, that is clearly visible at 900 K, when its shake-up counterpart (grey) is almost vanished. The Fe^{2+} peak (blue) has the smaller relative decrease so that it becomes predominant at 900 K.

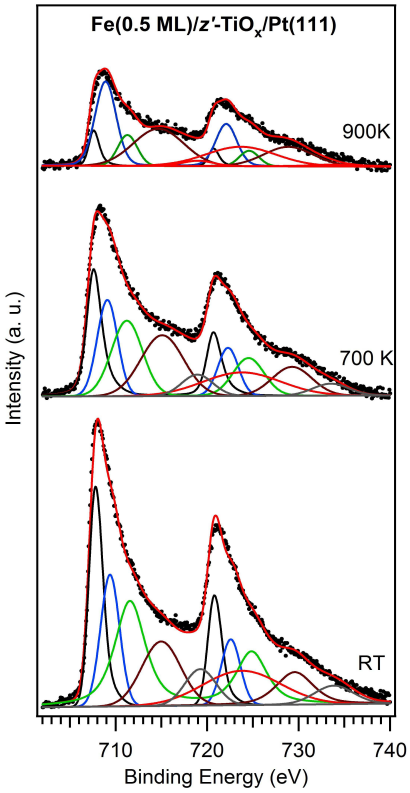

Figure VIII.3 Fe 2p peaks deconvolution for the system Fe(0.5 ML)/z'-TiO$_x$/Pt(111) at room temperature (RT), and thermally treated at 700 and 900 K for 2'.

From the above reported XPS data we can conclude that a quite peculiar redox behaviour of the TiO$_x$ UT film and of the Fe-related NPs is occurring at different temperatures. In addition, the Fe 2p data clearly demonstrate that the Fe-related NPs have a complex and variable stoichiometry, i.e. they are not simple metallic NPs, but are partially oxidized. In order to better study the chemistry of the deposited Fe-related NPs we have undertaken a TPD study, whose main outcomes are reported in the following section.

VIII.1.2 TPD data for the Fe/z'-TiO$_x$/Pt(111) system

The TPD data shown below (figure VIII.4a and b) were acquired in the Surface Science Laboratory of Padova, using a Hiden QMS, cooling down the sample to ca. 120 K, dosing 1.0 L of CO (used as a probe molecule) and then heating up to 500 K with a 2 K/s rate. The z'-TiO$_x$ phase was prepared and then cooled down, in order to use its CO desorption profile as a background for the following experiments. No

specific CO desorption peak is observed apart from a broad tail due to the physisorbed CO. Thence, after the Fe deposition at RT, it was possible to acquire the CO TPD spectra for the model catalyst with the same procedure (120-500 K range) and, after background subtraction, it was possible to single out the Fe contribution to the desorption profile. The model catalyst was then heated at different temperatures (up to 960 K with 50 K steps; not all the acquired spectra are reported in the figures below) for 2' and cooled down to 120 K in order to dose the CO and perform again the desorption experiment.

Figure VIII.4 a shows that for the system at RT, immediately after the Fe deposition, four contributions (labelled as **a**,**b**,**c** and **d** in figure) to the CO desorption profile are present: **a** and **b** (at ca. 142 and 156 K, respectively) are typical of the CO desorption from Fe^{2+} sites, **c** (at ca. 190 K) is assigned to CO desorption from Fe^{3+} sites and **d** (a broad peak centred at 340 K) is typical of CO desorption from metallic Fe sites.[3,4,5]

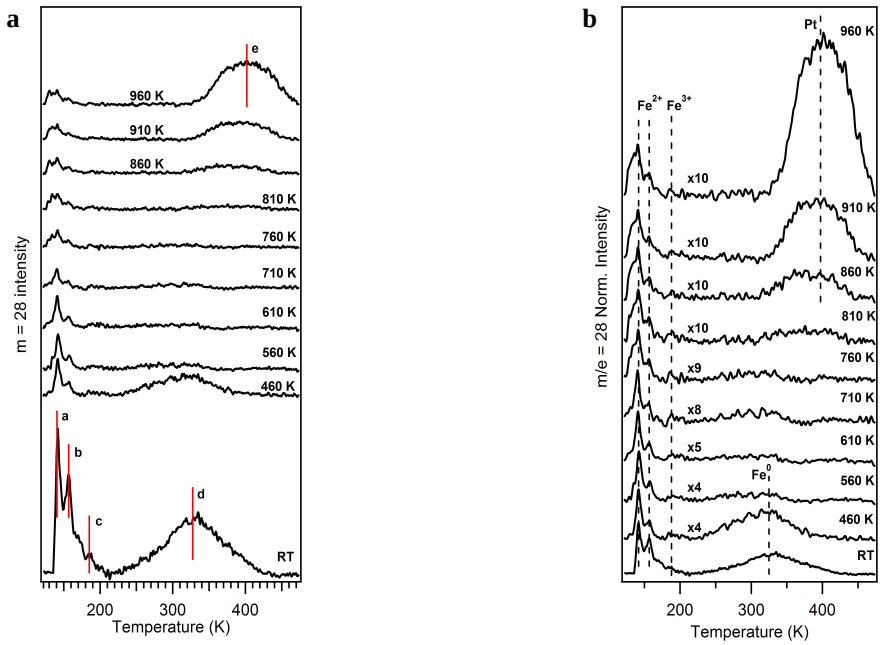

Figure VIII.4 CO-TPD spectra for a Fe(0.5 ML)/z'-TiO$_x$/Pt(111) system collected from RT to 960 K (a) raw data; (b) raw data normalized to the LT peak maximum.

After the first two reported thermal treatments (460 and 560 K) the CO desorption profile outlines strong modifications of the system: all the peaks listed above are reduced. In particular peaks **c** and **d**, corresponding to the CO desorption from the Fe^{3+} and Fe^{0} sites, almost disappear, while peaks **a** and **b** are less intense but still present. Peaks **a** and **b** intensities continue to lightly decrease as long as the

temperature is raised, and after the last thermal treatment (960 K) they behave like a broad and low intensity feature. Starting from 810 K, a new feature develops (for convenience see the normalized spectra in figure VIII.4b), whose shape is clearly distinguishable at both 910 and 960 K. This peak, referenced as **e**, after the 860 K thermal treatment, is centred at about 370 K and shifts to higher T as long as the annealing temperature is increased, so that at 960 K it moves to ca. 405 K. The temperature range is in tune with a CO desorption from Pt on-top sites.[14] In Figure VIII.4 b the above discussed data have been re-normalized to the peak **a** of all the desorption profiles, in order to better outline all the other contributions (in particular peaks **d** and **e**). This process is useful to remark the positive shift in peak **e** when the annealing temperature is raised.

In figure VIII.5 a it is reported the CO desorption profiles corresponding to the system described above (0.5 ML of Fe deposited on the *z'*-TiO_x phase) immediately after Fe deposition (lower profile) and after a 120 L O_2 treatment of the same sample (oxidizing treatment) at RT. These spectra are useful to properly understand the nature of the desorption peaks: in fact, after the oxidation treatment the broad desorption peak centred at about 340 K totally disappears, thus supporting our previous assignment of the peak **e** to Fe^0 adsorption sites, that are no more available after the oxidation. Concurrently, an absolute intensity decrease of the **a** and **b** peaks (Fe^{2+}) is observed, while peak c (Fe^{3+}) completely disappears.

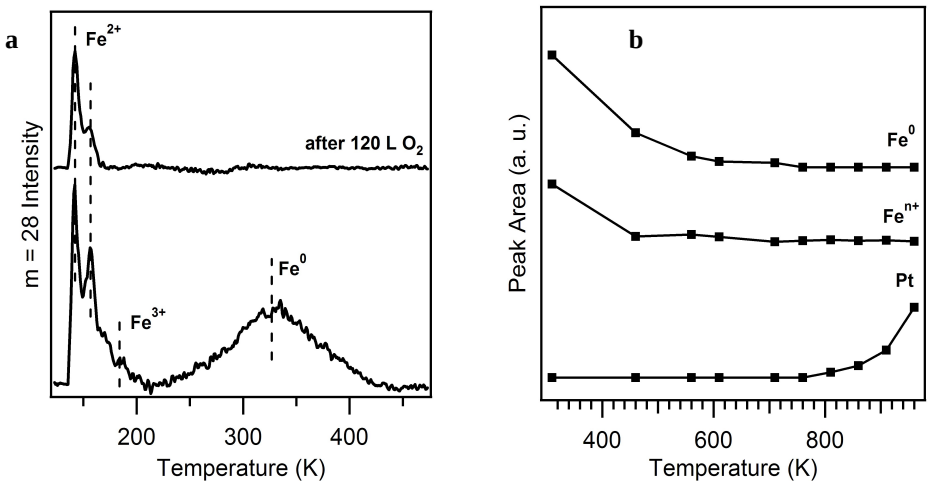

Figure VIII.5 (a) CO TPD spectra of a Fe(0.5 ML)/z'-TiO_x/Pt(111) system collected before and after exposure to 120 L O_2; (b) trend of the Pt, Fe^{n+} and Fe^0 CO TPD desorption peaks areas as a function of the temperature.

The desorption peaks area (figure VIII.4a) was then evaluated and reported as a function of the temperature in order to follow the evolution of the system adsorption sites (figure VIII.5b). Three main groups of peaks were plotted: a first containing all the CO desorption contribution coming from the oxidized Fe sites (labelled Fe^{n+}), a second containing the contribution from the metallic Fe sites (labelled Fe^0) and a third containing the contribution from the uncovered Pt (labelled Pt). The plot shows us that both the Fe^{n+} and Fe^0 intensities decrease as long as the temperature is raised. At the same time, starting from 810-860 K, a sudden increase in the Pt intensity is observed.

VIII.1.3 STM data for the Fe/*z'*-TiO_x/Pt(111) system

The STM images were acquired in the Nanoscience Lab of the "Università Cattolica del Sacro Cuore" of Brescia (Dr. L. Gavioli), using an Omicron multiscan system and collecting the data in constant current mode at RT, with tip to sample bias ranging from 0.3 to 1.6 V and tunneling current ranging from 0.1 to 1.3 nA.

In figure VIII.6 the STM images of the clean *z'*-TiO_x phase and the Fe(0.5 ML)/*z'*-TiO_x/Pt(111) system after five thermal treatments at increasing temperatures (from 410 K to 1000 K) are reported. In figure VIII.6 a the *zigzag-like* pattern of the *stripes* and the *troughs* of the clean *z'*-TiO_x film (see Chapter III) is clearly observed, but completely disappears after the metal deposition at RT. The STM picture taken at 410 K (figure VIII.6b) shows that around some Fe-related NPs (indicated in red-yellow) a partially disordered hexagonal arrangement of the UT TiO_x film is present. Such hexagonal UT film arrangement becomes progressively more visible at higher temperatures (figures VIII.6c,d): at 800 K, also the NPs shape is modified into a more crystalline structure, as shown by the atomic contrast on the largest ones (figure VIII.6d). At 900 K, the UT TiO_x layer clearly reveals the copresence of the new hexagonal phase and the *troughs* typical of *z'*-TiO_x, which eventually at the highest explored temperature (1000 K) is completely recovered, except for the presence of large nanoislands (see figure VIII.6f), whose metallic Pt nature has already been demonstrated by TPD (figure VIII.4a,b).[6]

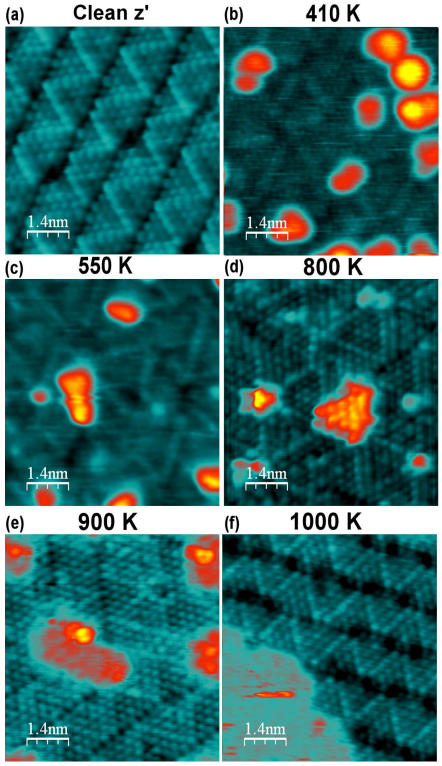

Figure VIII.6 STM images of the clean z'-TiOx/Pt(111) UT film and (a) of the Fe(0.5 ML)/z'-TiOx/Pt(111) system for different annealing temperatures (b-f). The color scale has been chosen to highlight both the oxide layer (green) and the Fe-related nanoparticles (red-yellow).

The Fe/z'-TiO$_x$/Pt(111) systems have also been investigated at different Fe coverages: in figure VIII.7 three different Fe coverages are imaged at RT and after thermal treatment at 900 K. This figure clearly demonstrate that at RT the Fe-related NPs tend to grow aligned on the *z'*-TiO$_x$ *troughs*, i.e. the UT film acts as a template for the NP growth (see Chapter III), even if the long range order is not as good as the one previously reported on the Au/z'-TiO$_x$/Pt(111) systems.[7] This is a direct consequence of the affinity between the Fe and the phase oxygen topmost layer: Fe tends to nucleate on the most active nucleation sites (the *picoholes* inside the phase *troughs*) but also partially grow on the surrounding *stripes*. After a thermal treatment at 900 K for 2', the NPs almost disappear and larger nanoislands are present.

Both the apparent height and the density of such NPs increase as long as the Fe initial coverage is increased. In the case of the 0.3 and 0.5 ML coverages, it is also possible to observe a motif of the UT TiO$_x$ film all around the islands. While in the case of 0.3 ML Fe deposition, the *z'* phase distinctive features (*troughs* and *stripes*) are present on nearly all the uncovered TiO$_x$ surface (some hexagonal patches are

anyway distinguishable), when the Fe coverage is increased to 0.5 ML a mixture of an hexagonal and the *z'* motif is present (as already observed in figure VIII.6).

In figure VIII.7b the histograms relative to the NPs apparent heights are reported. They have been obtained directly from the STM images reported in figure VIII.7 a after thermal treatment at 900 K. The zero of the horizontal scale corresponds to the main peak due to the TiO_x substrate. At 0.3 ML it is possible to observe a NPs apparent height distribution centred at 0.18 nm (black peak) while at 0.5 ML the NPs apparent height has a bimodal distribution centred at 0.18 and 0.36 nm (red peaks). At the highest Fe coverage the NPs apparent height distribution shows again the presence of two peaks centred at the same values reported before, but with an higher percentage of 0.36 nm thick NPs.

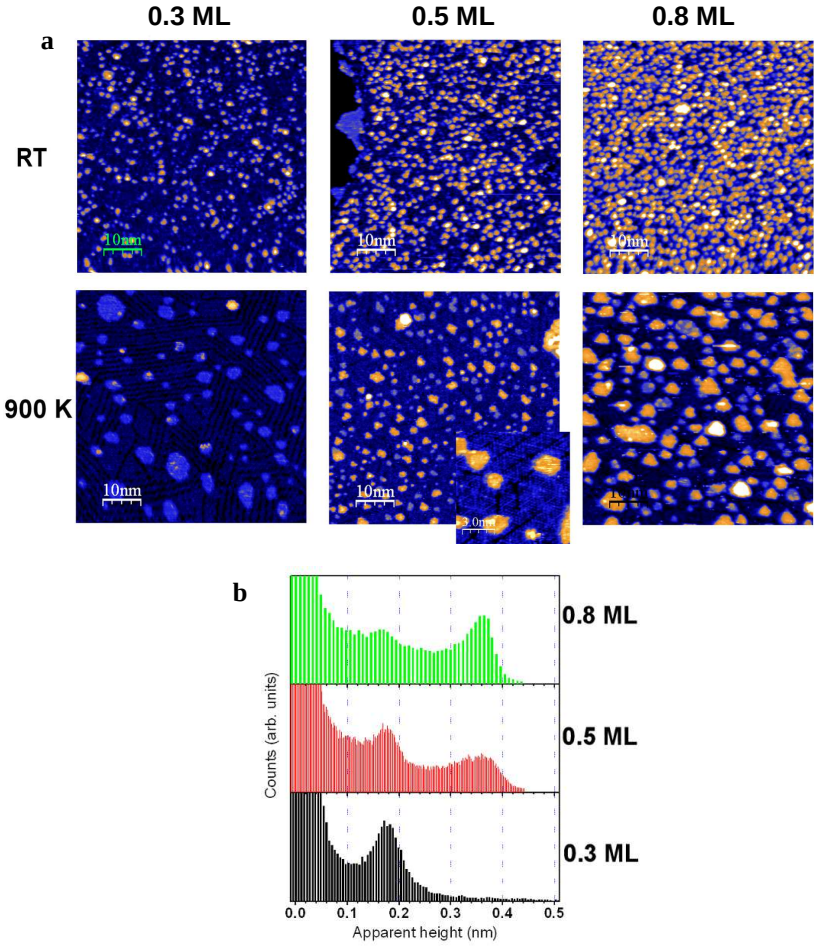

Figure VIII.7 (a) STM images of the Fe/z'-TiO_x/Pt(111) systems reported for three different coverages (0.2, 0.5 and 0.8 ML) at RT and after thermal treatment at 900 K for 2'; (b) histograms of the NPs apparent heights (frequency of each height in the corresponding STM image) after the 900 K thermal treatment.

The large scale image reported in figure VIII.8 (left) shows a Fe(0.5 ML)/z'-TiO$_x$/Pt(111) system after thermal treatment at 100 K. Large islands with triangular or hexagonal shape are clearly visible, and the *z'*-TiO$_x$ motif is observed all around them. The zoom-in reported in Figure VIII.8 (right, bottom) shows the magnification of one island, putting in light a big difference in the contrast between the island top, whose surface can not be clearly resolved, and the *z'*-TiO$_x$ motif, whose *stripes* and *troughs* are very well distinguished. A further magnification of the island allows us to obtain the atomic resolution, whose behaviour is typical of the Pt(111) fcc lattice. The zoom-in reported in Figure VIII.8 (right, top) shows the magnification of another, partially covered, Pt island. The most interesting feature is that the thin oxide layer partially covering such island shows the *z'*-TiO$_x$ motif, thus suggesting a partial re-organization of the pristine film both all around the Pt islands and on top of them.

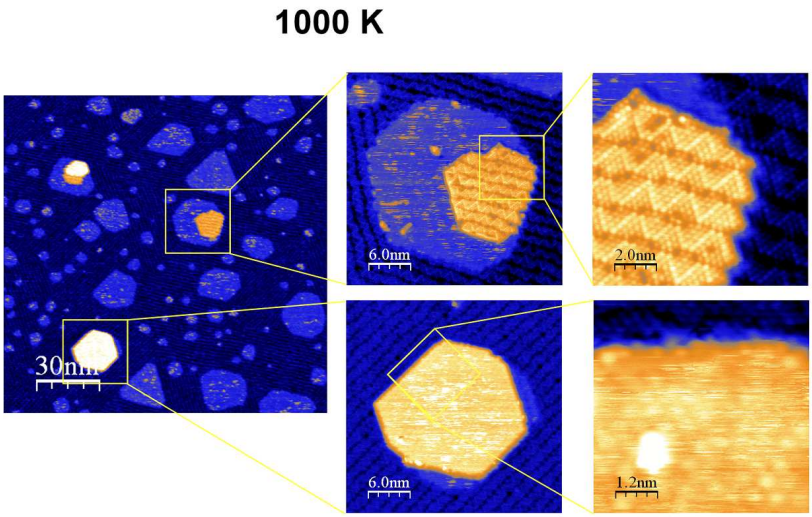

Figure VIII.8 STM images of the Fe(0.5 ML)/z'-TiOx/Pt(111) system thermally treated at 1000 K

VIII.1.4 Discussion of the data on the Fe/*z'*-TiO_x/Pt(111) system

A preliminary report on the thermal evolution of the Fe(0.5 ML)/*z'*-TiO_x/Pt(111) system has been already published (see the reprint at the end of this chapter).[6]

The data reported in the previous paragraphs, together with some new theoretical DFT calculations performed at the "Istituto per i Processi Chimico-Fisici (IPCF)" of CNR, Pisa (Dr. A. Fortunelli), all are concord in giving a consistent and detailed understanding of the processes occurring during the Fe deposition (especially in the first temperature range) and the thermal evolution of the system.

To rationalize the data, three different temperature ranges can be conveniently selected, where some important leading phenomena can be outlined:

1) RT < T < 460 K: in this temperature range a preferential diffusion of the Fe from the Fe-related NPs towards the most favourable sites, i.e. the defect (*picoholes*), occurs and, correspondingly, a partial rearrangement of the *z'*-TiO_x film is observed;

2) 460 < T < 800 K: a reorganization of the *z'*-TiO_x UT film into a new *hexagonal*-TiO_x phase (hereafter *h*-TiO_x) is completed, while some Fe-related NPs are pinned at the apex of the *h*-TiO_x hexagons. Based on the HR-XPS data, showing the appearance of an shoulder associated to an oxidized Ti 2p component, such Fe-related NPs can be associated to a TiO_2/FeO_x mixed oxide.

3) 800 < T < 1000 K: at this high T the Fe is mostly dissolved into the Pt bulk, flat nano-islands of Pt (possibly alloyed with Fe) are extracted at the surface and the very stable *z'*-TiO_x phase is formed again (beside and on top of such nano-islands).

In section VIII.1.1 the BE shifts in the Ti 2p peak position occurring upon Fe deposition has been described: the shift becomes larger as long as the deposited Fe amount increases, and is due to the presence of a low BE component centred at about 455 eV (deconvolution in figure VIII.2), a value that falls in the typical range of a Pt-Ti alloy. At the same time, the analysis of the Fe 2p peak puts in light the co-presence of different Fe oxidation states (Fe^0, Fe^{2+}, Fe^{3+}), even immediately after the metal deposition at RT. The presence of oxidized Fe^{n+} can be rationalized in term of a local redox reaction already occurring at RT between the TiO_x phase and the deposited Fe. This leads to the formation of FeO_x and the reduction of some Ti atoms of TiO_x to Ti, being the latter able to bind to the Pt substrate, thus creating a Pt-Ti surface alloy. When the Fe coverage is raised, the Fe-related NPs cover a larger TiO_x

area (as it is possible to note in figure VIII.7), so that a larger portion of the film undergoes this reaction. This is in tune with the increase of both the intensity of the Fe^{n+} components in the Fe 2p peak and the Pt-Ti component in the Ti 2p peaks. Considering the chemical nature of the so-called Fe-related NPs, the XPS data suggest that both metallic, and oxidised (Fe^{n+}) Fe is present. These data are confirmed by the TPD data reported in figure VIII.4a, showing that after 0.5 ML Fe deposition (RT) the NPs contain both metallic (d) and oxidised (a, b, c) Fe adsorption sites. The metallic peak is predominant at RT and has a broad shape if compared with the literature data reported for CO adsorption of Fe single crystals.[8] This is probably a consequence of a high heterogeneity of the Fe-related NPs, thus having different CO adsorption energies. The peaks a, b and c, corresponding to CO desorption from the Fe^{n+} sites, most probably derive from CO chemisorption sites at the edges of the FeO_x NPs, whereas at RT a large portion of the NPs has a zero-valent metallic nature. To demonstrate further evidence of the metallic nature of peak d, a Fe(0.5 ML)/*z'*-TiO_x/Pt(111) sample has been treated in an oxidizing atmosphere (120 L O_2) at RT and then, after CO exposure, the desorption experiment has been repeated: no peak d was detected, while the ones corresponding to the CO desorption from Fe^{n+} sites remained, even if slightly quenched. Another interesting evidence is about Fe^{3+} sites: after the oxidizing treatment the corresponding c peak almost disappears. It is possible to explain both the intensity reduction of the Fe^{2+} and the disappearance of the Fe^{3+} contribution as a consequence of the Fe oxidation: it is well established from the literature that oxygen terminated FeO_x layers are not able to adsorb CO.[5] Hence, it is possible to suggest a complete Fe NPs oxidation as a consequence of O_2 exposure, that produces oxygen-terminated FeO NPs whose active sites for CO adsorption are only located along their edges.

After the thermal treatments in the low temperature range, the Fe/*z'*-TiO_x/Pt(111) systems show an evident modification both in the electronic properties and in the morphology. These effects are mainly visible at the highest explored Fe coverages (0.5 and 0.8 ML). Focusing on the HR-XPS plots reported in figure 1 of the reprint reported at the end of this chapter, a modification of the Ti 2p peak shape takes place already after the first annealing at 410 K: the low BE component (455 eV, see also figure VIII.2), associated to the reduced Ti atoms that are surface-alloyed with the Pt substrate is somewhat reduced while the Ti^{4+} peak intensity (458.0 eV) increases and its position shifts to 458.6 eV, a BE value that is typical of the Ti^{4+}. This process

takes place up to 760 K, where the Ti-Pt contribution disappears while the Ti^{4+} one reaches its maximum intensity (peaks fitting in figure VIII.2). It is also important to note that the Fe 2p peak deconvolution in this temperature range (herein reported at 700 K, figure VIII.3) suggests that Fe remains in both a metallic (Fe^0) and an oxidised state (Fe^{2+} and Fe^{3+}), even if the overall peaks intensity decreases. Hence, in the 410-760 K temperature range a new counterintuitive phenomenon shows up: both the Ti and the Fe are in an oxidized state. The only way to conciliate such phenomenon, together with the Fe 2p peaks overall intensity decrease, is to take into account the assistance of thermal activated diffusion of Fe into the Pt substrate, with the consequent increase in the O/(Ti+Fe) ratio. In fact, during all the experiments, neither oxygen has been dosed nor the UHV chamber base pressure was higher than $5 \cdot 10^{-10}$ mbar. The migration of the Fe into the Pt substrate could lead to the formation of FeO_x/TiO_2 mixed oxide nanoislands, as a consequence of a new, thermal activated, competition between Fe and Ti for binding to the oxygen. This event can justify the increase in the 458.6 eV component in the Ti 2p signal and the presence of the corresponding Fe^{n+} components in the Fe 2p spectra.

The just mentioned thermal-induced electronic modifications correspond to a substantial structural change of the system, as clearly observed by STM for a Fe(0.5 ML)/*z'*-TiO_x/Pt(111) (figure VIII.6). The *zigzag-like* pattern showing the *stripes* and the *troughs* of the clean UT TiO_x film (figure VIII.6 a), completely disappears after the Fe deposition at RT (reported in figure VIII.7). The STM picture taken after annealing the system for 2' at 410 K (figure VIII.6 b) shows that around the NPs a partially ordered hexagonal arrangement of the UT TiO_x film is built (*h*-TiO_x), that becomes progressively more visible at higher temperatures (see figures VIII.6 c-d) and NPs pinned at the apex of the hexagons are present. In the same temperature range the TPD (figure VIII.4) put in evidence that almost all the metallic Fe sites (Fe^0) are no more accessible by the probe molecules (see also figure VIII.5 b, where the decrease in the Fe^0 peak area as a function of the temperature is reported), thus in line with a temperature driven Fe diffusion towards the Pt, also justified by a decrease in the overall Fe^{n+} peaks area (figure VIII.5 b). In fact, as a consequence of the Fe diffusion towards the Pt and the Ti oxidation, less Fe^{n+} active sites for the CO adsorption are available at the NPs edges.

To rationalize the photoemission evidences and establish a connection between them and the transition from the *z'*-TiO_x to the *h*-TiO_x UT film evidenced by STM, a

theoretical approach based on Density Functional Theory (DFT) was performed in Pisa. Actually, as reported in Chapter III, the structure of the *z'*-TiO_x/Pt(111) UT film is completely understood and also the *picoholes* described into details. In particular, the stoichiometry has been demonstrated to be *z'*-$TiO_{1.25}$.[9]

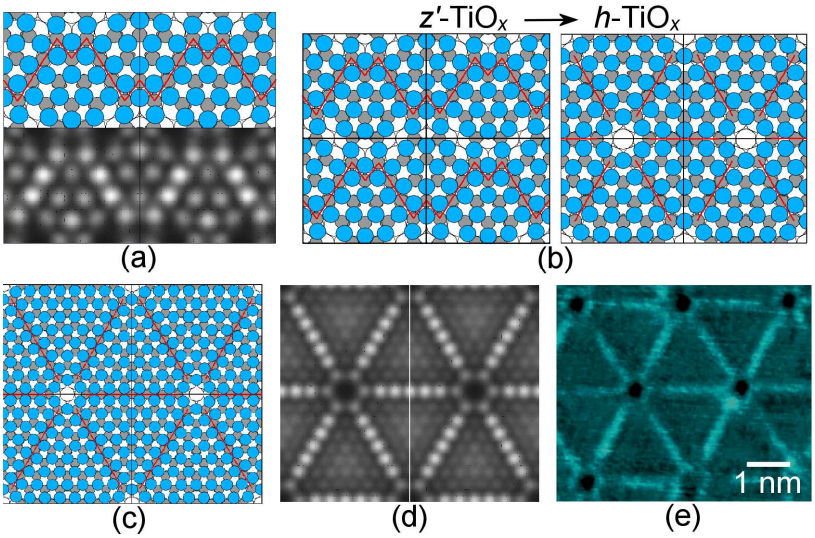

Figure VIII.9 (a) DFT structural model and STM simulated image (at a bias of +1.0 eV) of the z'-TiO_x film; (b) structural model of the transformation from the rectangular z'-TiO_x to the hexagonal h-TiO_x film (L=6); (c) structural model and (d) STM simulated image (at a bias of +1.0 eV) of h-TiO_x (L=9). Blue (larger) balls correspond to Oxygen atoms; grey (smaller) balls to Ti atoms. (e) STM image taken at RT of the h-TiO_x film.

Previous DFT studies have been also reported on the system composed by a few Fe atoms on the *z'*-$TiO_{1.25}$ film.[7,10] They have already demonstrated that Fe is already oxidized by simple adsorption on an almost not-restructured *z'*-$TiO_{1.25}$ film. This supports the evidences emerging from the XPS data shown before and regarding the system immediately after the Fe deposition and during the initial stages of the thermal processes. At higher temperatures, in the 410-760 range discussed above, complex diffusion and transformation mechanisms are activated. First of all there is a strong tendency to migration of the Fe atoms into the Pt bulk, which is mainly carried out through the *picoholes*. This phenomenon favours the restructuration of the *z'*-$TiO_{1.25}$ film, and leads to the formation of a new UT TiO_x film having an hexagonal arrangement, i.e. the *h*-TiO_x phase.

A thermodynamic analysis of the free energies is helpful to understand the factors at play and rationalize the observed behaviour. Assuming that the Fe deposition

determines the simultaneous formation of a mixed FeO_x/TiO_2 oxide with a supposed stoichiometry similar to that of $FeTiO_3$ (ilmenite) and the release of Ti atoms to the Pt support, a Gibbs free energy of –0.48 eV is calculated for the following process

$$z'\text{–}TiO_{1.25} / Pt + 0.15Fe \rightarrow 0.70 - h - TiO_{1.14} / Pt + 0.15FeTiO_3 + 0.15Ti$$

where the energy of an hypothetical $TiO_{1.14}$ phase was estimated from a linear extrapolation of known values of analogous TiO_x phases. The quantity of Fe involved in this reaction corresponds to a nominal coverage of 0.22 ML. The formation of a composite phase (*h*-$TiO_{1.14}$) made by a TiO_x film (further reduced with respect to z'-$TiO_{1.25}$) and FeO_x/TiO_2 nanoislands is thus thermodynamically favoured. As the number of oxygens is fixed under the present experimental conditions, this process entails a corresponding reduction of the TiO_x film from the 1:1.25 Ti/O ratio characteristic of the *z'*-TiO_x phase to a lower value.

The important point, now, is to theoretically support the formation of an hexagonal UT TiO_x film. To this end, making reference to the already published analysis of the building principles of reduced TiO_x/Pt(111) films is essential:[11] the reduced TiO_x/Pt(111) films are characterized by triangular pseudo-epitaxial regions of tri-coordinated Ti ions separated by dislocation lines of tetra-coordinated Ti (see Fig. VIII.9a for *z'*-TiO_x). A TiO_x stoichiometry with $x < 1.25$ can be achieved by enlarging the side length (L) of the triangles (which for *z'*-TiO_x is composed of 6 Ti atoms), thus increasing the ratio between tri-coordinated and tetra-coordinated Ti atoms. However, at this more reduced stoichiometry, a structural transformation is energetically favoured where the rectangular arrangements, typical of *z'*-TiO_x, gives way to hexagonal ones (*h*-TiO_x). Such a type of transformation has been already described:[12] it can be derived by a shift of ½ period of the rectangular unit cell together with a merging of the defective holes into a single larger one (as shown for *z'*-$TiO_{1.25}$ in Fig. VIII.9b). A complete set of DFT calculations allows us to predict that with a $TiO_{1.14}$ stoichiometry a very stable *h*-TiO_x configuration is formed (see Fig. VIII.9c), where the side length of the characteristic triangular pseudo-epitaxial regions is now composed by 7 Ti atoms. Even though the boundary between this *h*-TiO_x film and the mixed oxide islands have not been simulated, the merging of the defects into a single hole has been shown to be beneficial also for (and triggered by)

the presence of species adsorbed in the hole.[12] The simulated STM images of the *h*-TiO_x film are also shown in Fig. VIII.9d, and compare very well with the experimental STM images of Fig. VIII.9e.

It can be noted that at p = 10^{-13} atm and T = 673 K the formation of the *h*-TiO_x phase is not thermodynamically favoured, since the reduction process:

$$z'\text{–}TiO_{1.25} / Pt \rightarrow h - TiO_{1.14} / Pt + 0.05357O_2$$

has a ΔG of +0.25 eV. However, the *h*-$TiO_{1.14}$ phase, exhibiting Ti in a more reduced oxidation state, is expected to become more stable than *z'*-$TiO_{1.25}$ (at the same amount of deposited Ti) at higher temperatures (around 1500 K). Indeed, this phase has actually been obtained by annealing the *z'*-TiO_x at 1000 K for two hours and its STM image is also shown in Fig. VIII.9e.

In the highest explored temperature range (800–1000 K) the system undergo another deep modification that is immediately visible by STM. After thermal treatment at 810 K the NPs shape (in figure VIII.6 d clearly visible pinned at the centre of an hexagon) is modified into a more crystalline structure, as shown by the atomic contrast. At 900 K the STM image reported in figure VIII.6 d reveals the presence of both the *h*-TiO_x hexagonal features and the *troughs*, typical of the *z'*-TiO_x UT film.

At the same time the HR-XPS spectra reported in section VIII.1.1 show that the 458.5 eV shoulder in the Ti 2p peaks starts to decrease (at 910 K it is almost vanished and the peaks shape comes back to the one of the pristine TiO_x UT film), while the Fe 2p multipeak analysis (after thermal treatment at 900 K) put in light that a strong decrease both in the Fe^0 and Fe^{3+} components takes place, while the Fe^{2+} peaks intensity is just affected by a small decrease in its intensity. These evidences are in tune with a progressive temperature activated Fe diffusion from the NPs to the Pt substrate, and the consequent reduction of the FeO_x/TiO_2 mixed oxide. This means that at 810 K the NPs start to release oxygen to the *h*-TiO_x film (no oxygen loss was observed with TPD), whose stoichiometry (and then structure) comes back to the 1:1.25 value typical of the *z'*-TiO_x. The more crystalline structure observed on top of the islands by STM could be explained as a consequence of residual FeO layers (oxygen terminated) segregation, whose structure has already been reported in the literature.[13]

Focusing our attention on figure VIII.7 it is possible to observe the thermal evolution at 900 K of three different Fe coverages (0.3, 0.5 and 0.8 ML) Fe/*z*'-TiO_x/Pt(111) systems, and is quite clear that, as long as the Fe coverage is increased from 0.3 to 0.5 ML, also the island density at 900 K is increased. At the same time, almost no increase in the island density is observed after the Fe coverage is further increased from 0.5 to 0.8 ML. This probably happens because the highest is the amount of Fe, the highest is the *z*'-TiO_x UT film reduction reaction taking place; this leads to a more complete phase transformation to the *h*-TiO_x and to the formation of a larger quantity of FeO_x/TiO_2 mixed oxide NPs during the thermal evolution. Considering the apparent height histograms reported in figure VIII.7 b and referring to the analysis of the three coverages after the thermal treatment at 900 K, it is possible to realize that while at 0.3 ML Fe coverage only flat islands (0.18 nm thick) are present, when the Fe coverage is increased to 0.5 and 0.8 ML the NPs start to extend their size, forming a second layer (bimodal apparent height distribution, with a contribution from 0.36 nm high NPs). This means that an increase in the deposited amount of Fe leads first to an increase in the NPs density (passing from 0.3 to 0.5 ML), due to the higher *z*'-TiO_x → *h*-TiO_x conversion, and then to the formation of defects acting as NPs nucleation sites. At the same time, no increase in the NPs density is observed passing from 0.5 to 0.8 ML Fe coverage, but an increase in their size takes place (outlined by the histograms). This means that already at 0.5 ML Fe coverage a total conversion to the *h*-TiO_x has taken place, and the excess of deposited Fe can only contribute to increase the NPs size. Our TiO_x film acts as a sort of membrane, having a limited number of pores where the NPs can nucleate. When the temperature is increased on the higher coverage systems (0.5 and 0.8 ML of Fe), the FeO_x/TiO_2 reduction and thus the Fe diffusion processes are slower than in the case of 0.3 ML of deposited Fe, since the NPs size (and thus the amount of Fe) is larger. This leads to the presence of a larger number of islands that can be imaged at 900 K.

Finally, let us focus on the nanoislands observed in the highest investigated temperature range by STM (1000 K figure VIII.8). The large scale STM image shows that only a part of the residual islands is covered by the *z*'-TiO_x phase motif, while the rest show a typical metallic contrast, to be associated to the Pt substrate. At the same time, the TPD results reported in figure VIII.4 and relative to the 810-960 K temperature range, show the development of a peak centred at about 400 K,

corresponding to the CO desorption from the Pt metal, thus in agreement with the STM evidences. It is interesting to note that the peak shifts from 370 to 405 K when the annealing temperature is increased from 810 to 960 K. Comparing these values with some examples reported in the literature and regarding similar model systems,[14] it is possible to give an explanation for such a temperature shift. In fact when CO is adsorbed on Pt_xTi alloys, the desorption peaks temperature decrease to ca. 370 K, a value that is in line with the one observed in our experimental data collected at 810 and 860 K. On the contrary, the typical CO desorption temperature from a Pt(111) substrate is ca. 410 K, in tune with the values observed in our experiment at the highest explored temperature (960 K). Therefore, it is possible to conclude that when the temperature is raised over 810 K the great part of Fe diffuses from the NPs into the Pt substrate, together with a small part of the Ti atoms. This might result in the formation of partially alloyed Pt-Ti islands. When the temperature reaches 960 – 1000 K also the diffusion of the alloyed Ti into the Pt bulk is activated, so that metallic Pt islands could be "extracted" from the substrate. Also this process is "Fe amount dependent": a larger amount of Fe leads to the dissolution of a larger amount of Ti in the bulk (as it is possible to observe from the HR-XPS spectra reported in figure VIII.1 a by simply comparing the intensity of the Ti 2p peaks corresponding to the clean *z'*-TiO_x phase and the ones of the 900 K treated samples at the highest Fe coverages) and then to the formation of a larger amount of Pt islands.

VIII.2 The Fe(0.5 ML)/*w'*-TiO_x/Pt(111) system

Some experiments have also been carried on to explore another model system, obtained depositing 0.5 ML of Fe on the ultrathin polar *w'*-TiO_x phase. As already discussed in chapter III, the *z'* and the *w'*-TiO_x UT film are obtained depositing different amounts of Ti on the Pt(111) and post-annealing them at different temperatures. However, even if in presence of different temperature preparation and Ti coverages the two films have similar stoichiometry ($x \approx 1.2\text{-}1.25$)[11] and are both made by a Ti-O bilayer where Ti is at the interface with Pt and O forms the topmost layer, the former shows an ordered array of defects (*picoholes* inside the phase *troughs*) exposing the bare Pt, while the latter does not present long-range ordered defects. Our aim is to verify whether such morphological differences have an effect also on the electronic and structural properties of the Fe/TiO_x model systems. The data and their analysis is not as developed as the previous case, and the following considerations must be considered as preliminary.

VIII.2.1 The Fe(0.5 ML)/*w'*-TiO_x/Pt(111) system: XPS, TPD and STM

The XPS data shown below were acquired in the Surface Science Laboratory in Padova, using a conventional X ray source (Al K_α excitation photons) coupled with a single channeltron hemispherical electron analyzer (CLAM 2). The resolution is not comparable to that shown in figure VIII.1, hence further experiments are programmed at the Elettra synchrotron. The TPD and STM were acquired in Padova and Brescia, respectively, with the same procedures described previously.

The XPS spectra reported in figure VIII.10 show the thermal evolution of Fe(0.5 ML)/*w'*-TiO_x/Pt(111). In agreement with the data reported in figure VIII.1a, when Fe is deposited on the clean *w'*-TiO_x phase (figure VIII.10a) a shift to lower BE in the Ti 2p peaks is observed. Starting from the data acquired after the first thermal treatment (460 K) a shoulder in the main peak ($2p_{3/2}$), centred at about 458.5 eV and associated to Ti^{+4} is observed, whose intensity increases as long as the temperature reaches a value between 660 and 710 K. At the same time the peaks shifted to lower BE progressively disappear, and at 710 K it vanishes. After thermal treatment at 960 K, the original Ti 2p peaks shape is recovered even if the overall intensity is lower than the one corresponding to the clean phase. It is to be outlined that this final

intensity decrease is much higher than in the previous model catalyst based on the *z*'-TiO_x film.

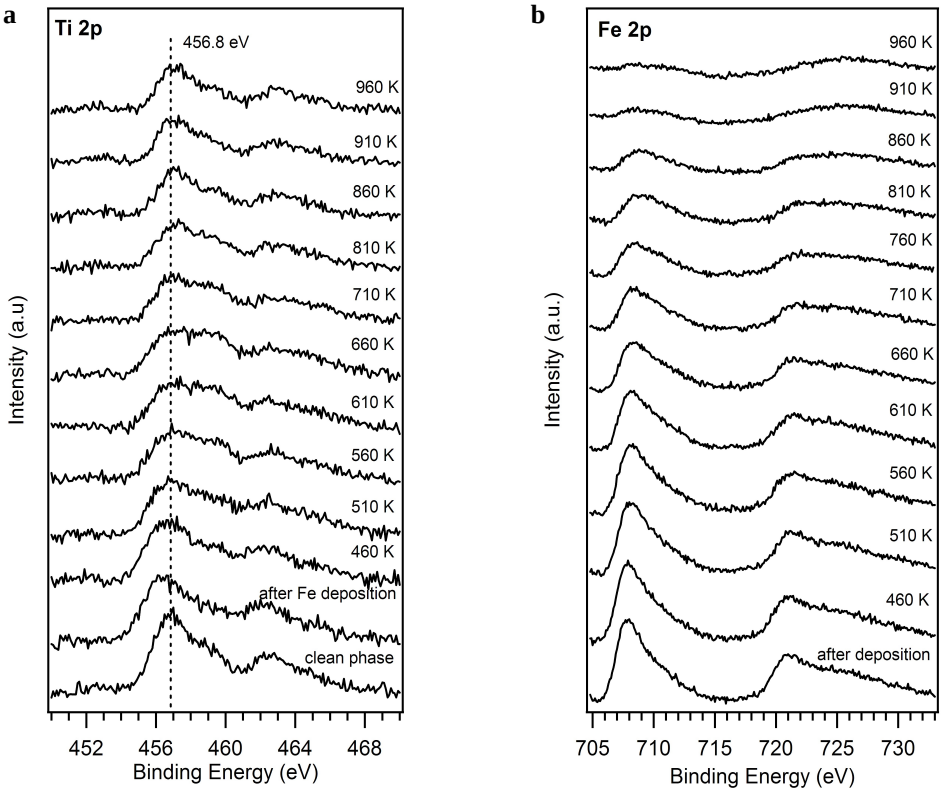

Figure VIII.10 Ti 2p (a) and Fe 2p (b) XPS spectra of the clean w'-TiO$_x$/Pt(111) phase and of the Fe(0.5 ML)/w'-TiO$_x$/Pt(111) system after thermal treatments at increasing temperature..

The Fe 2p peaks reported in figure VIII.10 b show the same broad feature already observed in the case of the Fe/*z*'-TiO_x system (figure VIII.1 b). This fact is in agreement with the presence of many components, corresponding to the Fe^0, Fe^{2+} and Fe^{3+} oxidation states as already observed before (figure VIII.3). What clearly emerges from these spectra is that, after the first annealing steps (in the RT-660 K range), the peaks intensity strongly decrease, and after thermal treatment at 960 K all the Fe is almost vanished.

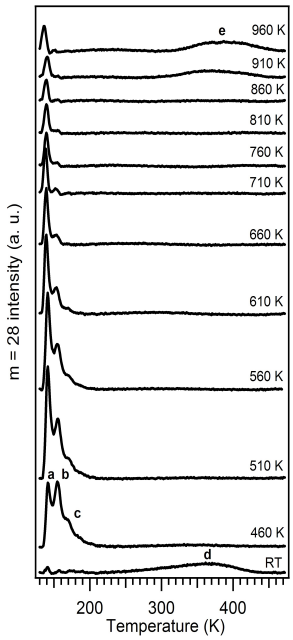

Figure VIII.11 TPD spectra for a Fe(0.5 ML)/w'-TiO$_x$/Pt(111) system collected from RT to 960 K.

Figure VIII.11 shows the CO TPD profiles, acquired with the same parameters specified in section VIII.1.2: after the Fe deposition (at RT) a major contribution to the CO desorption is observed and named d (in agreement with the peaks classification made in section VIII.1.2). This peak is centred at about 360 K and has been attributed to CO desorption from metallic Fe sites (Fe^0). Moreover, some broad and low intense features are present in the low temperatures range (140 – 200 K). Immediately after the first system annealing at 460 K for 2', the desorption profile changes dramatically: the broad peak **d** totally vanishes and three intense and well resolved peaks are present: **a** and **b**, centred at ca. 142 and 155 K respectively and typical of CO desorption from Fe^{2+} sites, and **c**, centred at about 175 K and referred to CO desorption from Fe^{3+} sites. After 510 K heating the peak **a** intensity still increases, while the other peaks remain almost unchanged. After the 560 K thermal treatment **a**, **b** and **c** peaks intensities progressively decrease and at the highest investigated temperature only one contribution is present, centred at about 140 K and corresponding to the feature **a**. After the last 2 annealing processes (910 and 960 K) a new broad peak centred at about 370 K and shifting to 390 K, starts to develop, whose characteristics are in line with peak **e** presented in section VIII.1.2 and attributed to CO desorption from metallic Pt on-top sites.

In figure VIII.12 the STM images corresponding to the clean *w'*-TiO$_x$ UT film and to the thermal treatment of a Fe(0.5 ML)/*w'*-TiO$_x$/Pt(111) are reported. The *wagon*

wheel motif of the UT film, which is clearly visible in figure VIII.12a, is no more observed after Fe deposition, in line with the previously reported results about the Fe/*z'*-TiO_x system (figure VIII.12b). It is also clear that in this case the Fe NPs nucleation is completely random, so that larger aggregates are visible both on the terraces and on the steps. After the first thermal treatment at 460 K (VIII.12c) the system seems to be heterogeneous and quite disordered.

A further thermal treatment at 610 K (VIII.12d) leads to more layered and faceted NPs, and also the substrate shows a more clear contrast, as emphasized also in the magnification (figure VIII.12e), where some kind of triangular and hexagonal motif (quite similar to the one observed for the Fe/*z'*-TiO_x system) of the titania layer appears. The next annealing step to 810 K (VIII,12f) shows no substantial modification from the 610 K observed morphology. The last investigated thermal treatment (to 910 K) put in light a partial substrate reconstruction towards the pristine UT film (the *w'*-TiO_x, figure VIII.12 g-h), while the NP structures show only 'granular' contrast.

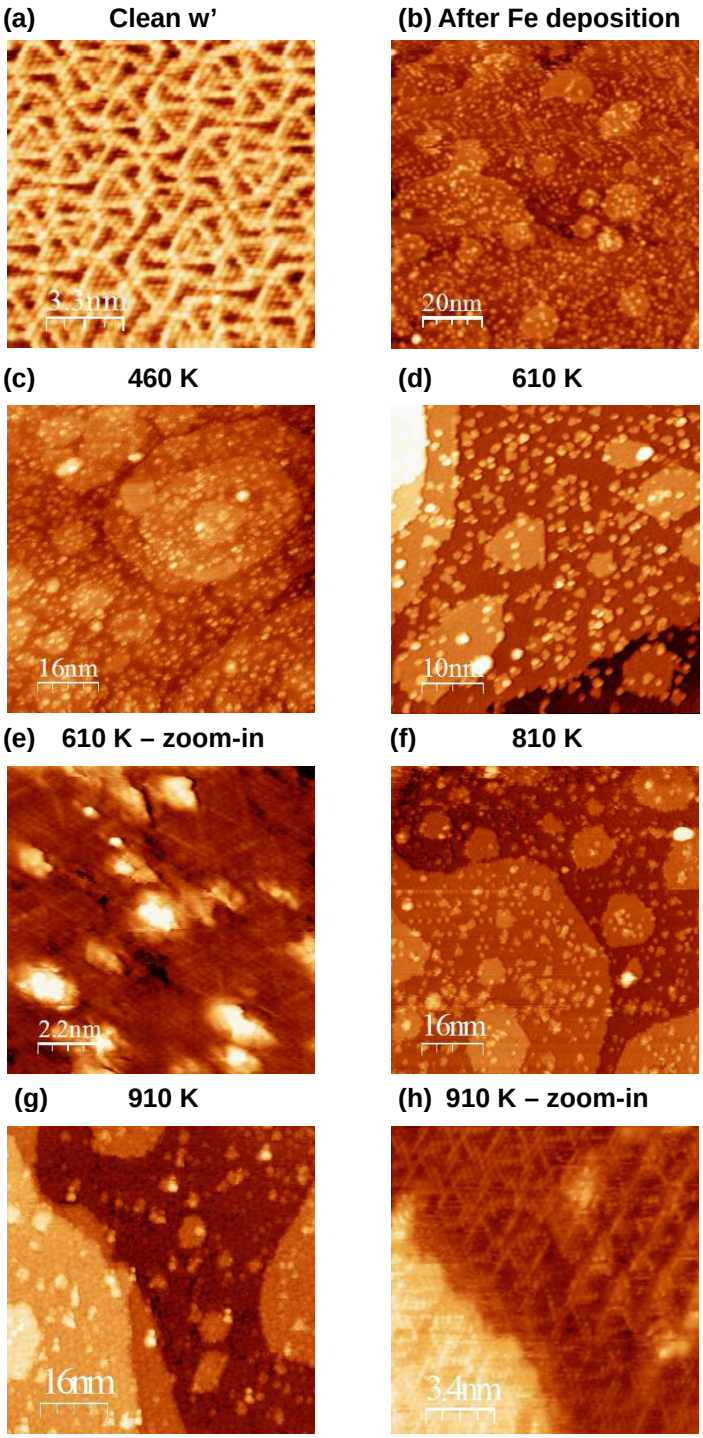

Figure VIII.12 STM images of the clean w'-TiO$_x$/Pt(111) UT film (a) and of the Fe(0.5 ML)/w'-TiO$_x$/Pt(111) system for different annealing temperatures (b-h).

VIII.2.2 Preliminary discussion on the Fe(0.5 ML)/*w'*-TiO_x/Pt(111) system

Let us start the discussion considering the XPS data collected after the Fe deposition. When Fe is deposited on the clean *w'*-TiO_x UT film, a shift by ca. 0.5 eV in the Ti 2p XPS peak (VIII.10a) is observed. Moreover the Fe 2p peak (VIII.10b) has a broad shape, in tune with the presence of more than one component as already observed in figure VIII.3. These evidences are in line with the results discussed in section VIII.1.4, and could be explained as a consequence of a TiO_x reduction taking place after the metal deposition. On the contrary, the CO desorption profile (figure VIII.11), collected immediately after Fe deposition, shows a predominant metallic component, and almost no other contribution is present. This is in contrast with the results collected on the Fe/*z'*-TiO_x (figure VIII.4), where CO desorption from both metallic (**d**) and oxidic sites (**a**, **b** and **c**) was observed. Hence, the XPS and TPD data suggest that when Fe is deposited on the *w'*-TiO_x phase an oxidation of the metal and the consequent reduction of the TiO_x substrate takes place, but only a few oxidic sites remain available for CO adsorption. An hypothesis that could explain this difference takes into consideration the different nucleation and growth modes of the Fe-related NPs on the two examined TiO_x substrates. In fact, the ordered arrays of defects (*picoholes* where Pt is left uncovered) of the *z'*-TiO_x act as preferential nucleation sites, allowing a direct contact between Fe and Pt, so establishing a preferential Fe diffusion paths into the Pt bulk. On the other side, when Fe is deposited on the *w'*-TiO_x, no preferential site is found, so that (as shown in figure VIII.12a) the NPs nucleation and growth is random. Since it can be supposed that the Fe has the same tendency to reduce both the TiO_x film (the stoichiometry is almost the same),[11] in the case of the Fe/*w'*-TiO_x system the path to diffuse into the Pt bulk implies a local disruption of the film, which requires an extra of energy. It can be then speculated that, while a similar interface reaction between the Fe and the TiO_x film is occurring, leading to the Fe oxidation and Ti reduction and thus to the formation of Fe^{n+} sites, in this case the result of such interaction is different because the Fe^{n+} sites are not accessible by CO molecules, and that the FeO_x NPs are most probably terminated by a Fe shell.

When the system is heated to 460 K, a new transformation takes place: the CO desorption profile shows no more metallic Fe sites contribution (the peak centred at 360 K almost vanishes) while three intense and well resolved peaks, corresponding to the presence of Fe^{n+} sites, develop at lower temperatures (ca. 140, 155 and 175 K).

At the same time, the Ti 2p peaks XPS shows an evident shoulder at ca. 458.5 eV, and STM images report an heterogeneous and quite disordered system, thus suggesting a NPs structure modification and leading to the formation of an heterogeneous system composed by FeO_x/TiO_2 mixed oxide NPs and the residual TiO_x UT film all around (whose motif is however not clearly discernible, probably because of an higher degree of disorder induced by the destructive redox reaction).

A further increase in the temperature cause a progressive re-ordering of the system, as it is possible to see in figure VIII.12 d, where more regularly shaped and faceted NPs are present. At the same time it is now possible to obtain the STM resolution of the surrounding UT TiO_x film (VIII.12 e), that gives us an output similar to the one observed in figure VIII.6 b,c and d. In fact some kind of triangular-hexagonal patches are observed, that could be in tune with the *h*-TiO_x phase structure discussed in section VIII.1.4. Since in the case of the Fe/*z'*-TiO_x system this Fe-mediated phase transition (*z'*-TiO_x → *h*-TiO_x) was observed at a lower temperature (410 K) it might be guessed that the ordered defects (*picoholes*) present in the *z'*-TiO_x phase are capable of promoting the Fe diffusion process into the Pt substrate, thus allowing the analogous reaction

$$z'\text{–}TiO_{1.25}/Pt + 0.15Fe \rightarrow 0.70 - hTiO_{1.14}/Pt + 0.15FeTiO_3 + 0.15Ti$$

to take place at lower temperatures. On the contrary, when Fe is deposited on a flat, oxygen terminated layer (the *w'*-TiO_x UT film) a higher activation energy is required to Fe to locally disrupt the TiO_x layer and then to diffuse through it to reach the Pt. Probably a sharp *w'*-TiO_x → *h*-TiO_x phase transformation is not observed because of the intrinsic higher disorder due to the disruption of the UT film.

After thermal treatment at 810 K (VIII.12 f), STM images do not show any substantial change. In the 660 – 810 K temperature range the XPS Ti 2p (VIII.10a) spectra show a progressive decrease in the intensity of the 458.5 eV component, the overall Fe 2p peaks intensity (VIII.10b) decrease and, at the same time, the desorption profiles (VIII.11) put in light a quenching of the **a**, **b** and **c** peaks. All these evidences are in tune with a gradual FeO_x reduction in the NPs and then the diffusion of metallic Fe into the bulk Pt. This process is almost terminated at the highest investigated temperature (910 K), where nearly all the Fe 2p XPS signal is quenched, the Ti 2p restores its original shape and the STM image (VIII.12 h) shows the pristine phase *wagon-wheel* motif. Hence I can conclude that, as long as FeO_x

reduces and Fe diffuses into the Pt, it is able to give its oxygen back to the TiO_x film. When the correct stoichiometry is achieved, then a *h*-TiO_x → *w'*-TiO_x phase transformation takes place, leading to the pristine UT film, in line with the evidences reported about the Fe/*z'*-TiO_x system.

It is important to precise that both the LEED pattern (figure VIII.13) and the STM images (not reported) obtained after the thermal treatment of the Fe(0.5 ML)/*w'*-TiO_x/Pt(111) system to higher temperature (960-1000 K) do not show only the *w'*-TiO_x phase presence.

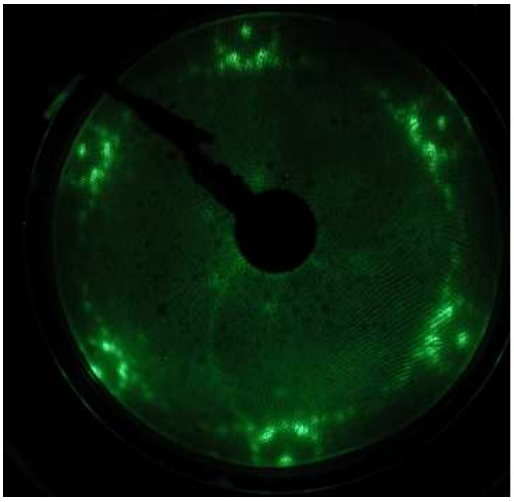

Figure VIII.13. LEED pattern of the Fe(0.5 ML)/w'-TiO_x/Pt(111) system after thermal treatment to 960 K

The LEED pattern reported in figure VIII.13 shows the superimposition of both the *w'* and the *z'*-TiO_x diffraction spots. This evidence has also been confirmed by STM and can be explained as a consequence of a partial, temperature mediated, Ti diffusion into the Pt substrate. As a consequence of this, some patches of a UT film that is usually grown at lower Ti coverages (the *z'*-TiO_x) are formed. Also the TPD is in tune with this last evidence, since the peak named **e**, which is already distinguishable at 910 K, shifts to higher temperature (from 370 to 390 K) after the system is heated at 960 K. A 370 K CO desorption temperature is somehow typical of a Pt-Ti alloy, while a positive increase in the temperature is in tune with a progressive diffusion of the Ti in the Pt bulk.

VIII.3 Conclusion

In this chapter I presented the results obtained on the Fe/TiO_x/Pt(111) model catalysts. Two TiO_x UT film grown on Pt(111) have been chosen as a support for the NPs growth: a templating substrate, the *z'*-TiO_x, whose defects are able to act as preferential nucleation sites, and the *w'*-TiO_x, whose stoichiometry and structure is similar to that of the *z'*-TiO_x but is free from defects.

The systems have shown a quite complex behaviour, both at RT (after the Fe deposition on the TiO_x UT films) and during a thermal evolution carried on from RT to 1000 K. Both the model catalysts have shown a TiO_x phase reduction occurring after the Fe deposition, that determine a re-organization of the UT film into an hexagonal motif (*h*-TiO_x). In the case of the *z'*-TiO_x phase, the reaction already starts at RT, while in the case of the *w'*-TiO_x a higher temperature is needed because an extra-amount of energy is required for the Fe to destroy the UT film and start to diffuse towards the Pt. This effect is most probably due to the presence of defects on the *z'*-TiO_x, where the NPs nucleates and grow in direct contact with the Pt and that can act as a preferential path for the Fe diffusion, so that already at RT the redox reaction between the Fe and the TiO_x can take place.

The thermal evolution of both the systems is similar, in the 460-810 K temperature range a clear evolution to a templating hexagonal phase, the *h*-TiO_x, is observed, and a progressive Fe diffusion through the TiO_x phase takes place to form FeO_x/TiO_2 mixed oxide NPs pinned at the apex of the hexagons. In the case of the Fe/*z'*-TiO_x system the phase transition is more clear, probably as a consequence of the higher degree of disorder induced by the disruption of the *w'*-TiO_x film. .

In the highest explored temperature range (810-1000 K) the Fe continues to diffuse through the UT film into the Pt substrate, thus giving back its oxygen to the TiO_x. In the end, the pristine UT films are almost recovered, although some Pt islands emerge from them, as a consequence of Ti diffusion into the single crystal bulk.

The most important and attractive issues coming out from these results are:

- the possibility to monitor in “real time” the transformations taking place on a model catalyst, at the interface between a metal and the oxide substrate
- the catalytic behaviour shown by the Fe, that is able to promote multiple solid state redox reactions

- the creation of a metastable *h*-TiO_x phase as a consequence of TiO_x reduction after the Fe deposition
- the role of phase defects, that are able to enhance the Fe catalytic activity towards the TiO_x UT films reduction and phase transformation.

VIII.4 Reprint of the paper: Probing Transformations of Relevance in Catalysis on a Single Oxide Layer: Fe on TiOx/Pt(111)

THE JOURNAL OF PHYSICAL CHEMISTRY Letters

pubs.acs.org/JPCL

Probing Transformations of Relevance in Catalysis on a Single Oxide Layer: Fe on TiO_x/Pt(111)

Luca Artiglia,[†] Emanuele Cavaliere,[‡,§] Gian Andrea Rizzi,[†] Luca Gavioli,[‡,§] and Gaetano Granozzi*[,†]

[†]Department of Chemical Sciences, via Marzolo 1, University of Padova, Italy, [‡]Department of Mathematics and Physics, Università Cattolica del Sacro Cuore, via dei Musei 41, I-25121 Brescia, Italy, and [§]Istituto Officina dei Materiali – CNR, Laboratorio TASC, Area Science Park – Basovizza, Strada Statale 14, Km.163.5 I-34149 Trieste, Italy

ABSTRACT The evolution of a Fe/z'-TiO_x/Pt(111) model catalyst in ultrahigh vacuum, studied by advanced surface science tools, reveals various phenomena occurring in different temperature ranges. In the room temperature (RT) < T < 460 K range, the deposited Fe atoms assemble as heterogeneous Fe and FeO_x nanoparticles (NPs), templated by the ordered array of defects (*troughs* and *picoholes*) of the oxide film. At 460 < T < 810 K, FeO_x NPs become predominant, and a metastable FeO_x/TiO_x mixed oxide is formed, assisted by the interdiffusion of Fe through the oxide into the Pt substrate, which triggers the z'-TiO_x structure transformation into a different TiO_x phase with a hexagonal pattern. At 810 < T < 1000 K, a Fe-mediated extraction of Pt produces Pt(111) islands, surrounded and partly encapsulated by the same z'-TiO_x phase, demonstrating the intrinsic high stability of the ultrathin oxide film. This represents one of the first examples of a phase transformation in a ultrathin oxide layer induced by an external metal deposit.

SECTION Surfaces, Interfaces, Catalysis

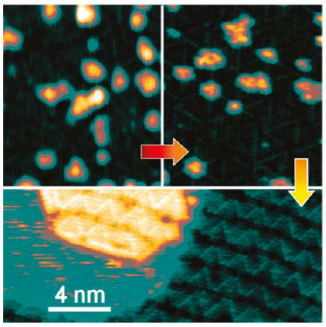

Iron and iron oxide (FeO_x) nanoparticles (NPs) play an important role in many chemical catalytic processes,[1,2] such as selective oxidations or the formation and cleavage of C–C bonds (e.g., Fischer–Tropsch process). In addition, FeO_x magnetic NPs have several applications in fields such as biomedicine, environmental sciences, information storage, micromechanics, and microfluidics.[3−6] It is now well established that the oxide support (OS), where the catalytic NPs are usually dispersed, can play a relevant role on the overall system catalytic activity.[7] In fact, several phenomena due to the NPs/OS interactions, either static (e.g., charge transfer, and interface states) or dynamical (e.g., encapsulation, spillover and reverse spillover, NP coalescence), have been well documented.[8] When the OS is reducible and some noble-like metal NPs (e.g., Pd and Pt) are involved, the observed effects have been attributed to a strong metal–support interaction, which has been described in detail.[9−11] For reactive transition metals of interest in catalysis, e.g., Fe and Co, the behavior is still a matter of debate, since the actual processes strongly depend on the balance between the surface energies and the metal work-function, and can lead both to oxidation or encapsulation of the metal NPs.[11,12]

A deep understanding of the relevant elementary steps in real catalytic processes can be obtained using transition metal/OS model systems based on ultrathin (UT) oxide films:[13] the effects due to morphology, defects, charge transfer, and interfacial states can be conveniently detailed. In addition, the UT films themselves are currently investigated as potential catalysts (monolayer catalysts) with improved performances.[13−15]

Here we investigate a Fe/TiO_x/Pt(111) model system, prepared by Fe deposition on a well-characterized UT TiO_x film epitaxially grown on Pt(111)[16] (hereafter indicated as z'-TiO_x). Adopting a series of advanced surface science tools, i.e., synchrotron (SR)-based high-resolution X-ray photoemission (HR-XPS), scanning tunneling microscopy (STM) and thermal programmed desorption (TPD), we follow the physical and chemical changes occurring after ultrahigh vacuum (UHV) annealing in a wide temperature range (from 300 K up to 1000 K).

The preparation of the z'-TiO_x film (x = 1.25) can be fine-tuned to obtain a *zigzag-like* wetting polar Ti–O bilayer, already described in great detail,[17,18] where the Ti ions are at the interface with the Pt substrate and the O ions form the topmost layer. The zigzag-like structure consists of an ordered array of rows (*troughs*), spaced by 1.44 nm and separating compact TiO_x *stripes*, where Ti ions present a different chemical and structural environment.[18] The troughs are characterized by Ti vacancies exposing the bare substrate surface, defined as *picoholes*, that have been demonstrated to be effective as nucleation sites for metal NPs growth.[19−21]

Received Date: April 21, 2010
Accepted Date: May 5, 2010

DOI: 10.1021/jz100511s | *J. Phys. Chem. Lett.* **2010**, *1*, 1660–1665

THE JOURNAL OF PHYSICAL CHEMISTRY Letters
pubs.acs.org/JPCL

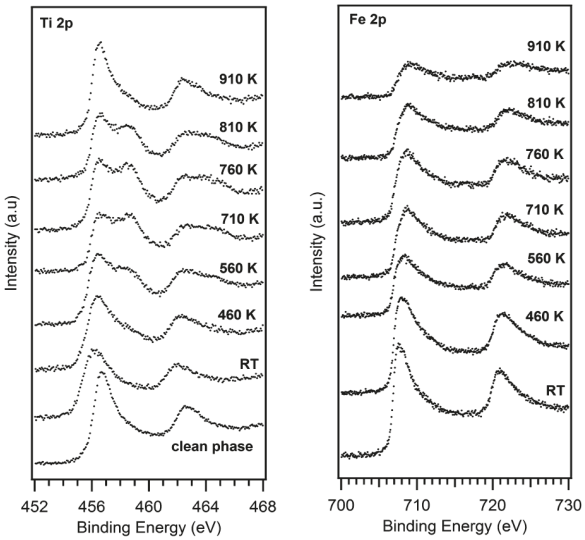

Figure 1. Ti 2p and Fe 2p HR-XPS spectra collected with a photon energy of 550 and 830 eV, respectively. The spectra were acquired after 2′ heat treatments at increasing temperatures.

Our model catalyst was prepared by depositing 0.5 monolayer (ML) of Fe on the clean z'-TiO_x phase. This system was then analyzed at room temperature (RT) and after short annealing (2′) in UHV at temperatures up to 1000 K.

Figure 1 shows the HR-XPS Ti 2p and Fe 2p core level data obtained on the Fe(0.5 ML)/z'-TiO_x system collected with a photon energy of 550 and 830 eV, respectively. The electron kinetic energy is on the order of 100 eV, ensuring a high surface sensitivity to the HR-XPS measurements. At RT, the Ti 2p spectrum (Figure 1) presents a predominant component centered at a binding energy (BE) of 456.5 eV, to be associated with Ti at the interface with the substrate.[17,22,23] The 0.4 eV energy shift toward lower BE with respect to the clean phase is due to the charge transfer and band bending resulting from the Fe deposition,[11] while the larger peak width is due to a second minor component at about 458.5 eV, which can be only appreciated after deconvolution of the peak profile. The Ti 2p component at higher BE has been associated with *oxidized* Ti ions sandwiched between two oxygen layers.[17] At RT, the Fe 2p spectrum (Figure 1) shows a predominant metallic component centered at about 707.5 eV, with a contribution from oxidized states (both Fe^{2+} and Fe^{3+}) visible after deconvolution of the peak profile.

Annealing the system up to 460 K results only in minor variation of the Ti 2p and Fe 2p spectra, i.e. a slightly increased intensity of the higher BE Ti 2p component and of the oxide-related Fe 2p peaks. However, starting from this temperature, some distinct changes in the XPS data are observed (Figure 1):

(a) The growth of a well-resolved component at higher BE in the Ti 2p spectra, centered at about 458.5 eV. Such peak reaches its maximum intensity at about 760 K and starts to decrease again above 810 K, completely disappearing at $T > 910$ K. At this temperature, the Ti 2p peak shape obtained at RT for the clean z'-TiO_x film is recovered, apart from the BE shift, that is still observed, probably due to the presence of residual FeO_x at the surface. However, the overall integral Ti 2p intensity remains almost unchanged in the investigated temperature range.

(b) A progressive broadening of the Fe 2p spectrum, due to the intensity increase of FeO_x components in the region where the corresponding shakeup satellites are expected and there is a decrease of the overall integral Fe 2p intensity, becoming relevant when the temperature goes beyond 800 K.

Such data suggest that there are two parallel phenomena, i.e., a progressive oxidation of Fe, already present at RT, but clearly increasing from 460 K, and a diffusion of Fe into the substrate, relevant beyond 800 K, while the amount of Ti is almost unchanged. Moreover, a quite peculiar phenomenon is observed: in the 460−810 K temperature range *both* Ti and Fe become apparently more oxidized. However, the process occurs at a constant oxygen amount since neither an oxygen load is given during the thermal treatments (done in UHV), nor an oxygen loss is observed using TPD. The important point to outline is the high stability of the Ti−O bond, since the preparation of the z'-TiO_x UT films is routinely carried out by annealing in UHV at high temperature (970 K). In our opinion, the only way to reconcile the experimental data is to consider a partial migration of Fe into the bulk substrate, and a concomitant restructuring of the z'-TiO_x film, leading to the formation of a mixed FeO_x/TiO_x oxide. In other words, kinetic phenomena, such as the interdiffusion of metals into the substrate bulk,[9,24] have to be considered to explain the rather unexpected oxidation process in UHV, as already suggested in a previous detailed investigation of the evolution of the z'-TiO_x film at high temperature in the same conditions.[25]

This hypothesis finds support from the STM and TPD data discussed below. In Figure 2 we show the evolution of the system morphology by STM examined at RT for the system prepared and treated exactly in the same conditions. At RT (Figure 2a) the Fe deposit forms NPs, predominantly aligned along the directions of the troughs.[21,26] Note, however, that the NPs are both nucleated on picoholes and on the TiO_x stripes, as a consequence of the low Fe mobility on TiO_x due to the Fe −O strong interaction and diffusion barriers.[26] Above 460 K, the STM data (Figure 2b) indicate that NPs stand in a slightly increased order, even if their density decreases by about 20% with respect to RT. Moreover, a different hexagonal arrangement of the UT film starts to appear amid the NPs (better observed at higher T, see Figure 2c,d). The important point to outline is that such modification of the TiO_x layer is definitely driven by the presence of Fe: in fact, the z'-TiO_x phase alone does not show any modification upon UHV annealing in a temperature range up to 970 K. A similar transformation from the rectangular z'-TiO_x phase to a hexagonal phase has been already described to occur at high temperature in the case of the Au/z'-TiO_x model system, where the NPs do not coalesce, but rearrange their shape and positions together with the adjacent regions of the oxide.[27] We recall that, at 460 K, we start to observe more clearly the higher BE component in the Ti 2p region, centered

DOI: 10.1021/jz100511s | J. Phys. Chem. Lett. 2010, 1, 1660–1665

THE JOURNAL OF PHYSICAL CHEMISTRY Letters
pubs.acs.org/JPCL

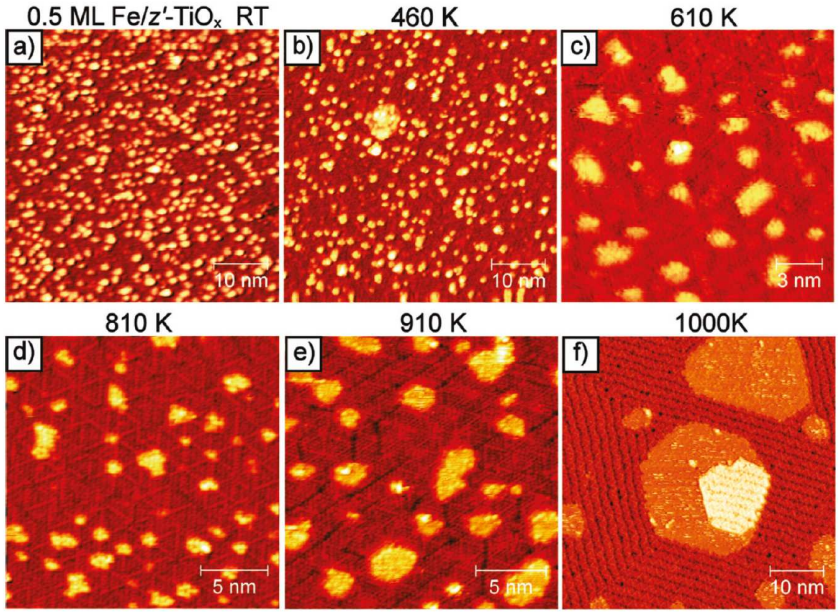

Figure 2. STM constant current images of the 0.5 ML Fe/z'-TiO$_x$ system taken at RT and after thermal treatments at increasing temperatures for 2′. Topography images have been shaded to enhance the substrate and on-top corrugation of the features. All images have been acquired at positive sample biases in the 0.3−2.0 V range, with tunneling currents between 0.1 and 1 nA.

at about 458.5 eV (Figure 1a), and the oxidation of Fe becomes relevant (Figure 1b). We can then speculate that because of the high tendency to alloy with Pt,[28] Fe atoms have a propensity to diffuse through the TiO$_x$ phase defects (troughs and picoholes), thus activating a restructuring process of the z'-TiO$_x$ bilayer itself. Moreover, the NPs shape changes from irregular and rounded to triangular and flat, showing on top a modulation that could be in tune with the one observed for a FeO(111) surface.[29,30] Considering the XPS spectrum at this temperature, we believe that the NP have transformed into FeO-like islands. Also, the NPs are located both at the center and at the vertices of the surrounding hexagons of the underlying UT film. The situation is even more evident if the temperature is raised up to 800 K (Figure 2d).

Figure 2e shows the STM data taken after a thermal treatment at 910 K. One can observe that the UT film pattern has mostly recovered the typical zigzag-like z'-TiO$_x$ arrangement, while only few spots with the hexagonal phase are still present. Also the islands are modified, with an apparent height (measured in the same tunneling conditions) reduced from 4 nm down to 1.2 nm, and a shape changing from triangular to hexagonal. At 1000 K (Figure 2f) the situation is largely modified: islands become larger with corrugation typical of a metallic surface and an apparent height of 0.1 nm, some of them being partially covered by a phase showing the typical z'-TiO$_x$ motif. Moreover, the islands are completely surrounded by the recovered zigzag-like pattern typical of the clean z'-TiO$_x$ phase. Consistently, the HR-XPS data after the annealing at 910 K show that the higher BE Ti 2p component at 458.5 eV is almost totally absent (Figure 1a), recovering the Ti 2p signature peculiar to the z'-TiO$_x$ reduced bilayer. At the same time the overall intensity of the Fe 2p spectra decreases, and a shift of the peak toward higher BE is observed as a consequence of an increase of the FeO$_x$/Fe^0 components ratio. Our interpretation of the presented data is that a major Fe dissolution into the Pt substrate is taking place above 910 K, which leaves only a minor residual amount of FeO$_x$ at the highest temperatures. The body of this experimental evidence suggests that the large islands observed by STM at 1000 K might well be uncovered portions of the Pt substrate, probably partially alloyed with Fe.

Such a hypothesis finds a strong support from the results of TPD experiments using CO as a probe (Figure 3). It is useful to recall that, while XPS gives chemical information for a finite depth slab, TPD probes the exposed chemisorption sites with respect to the probe molecule. In Figure 3 we report TPD data for the Fe(0.5 ML)/z'-TiO$_x$ sample, collected after exposure to 1.0 L of CO, prior to and after a thermal annealing made in the same conditions used for HR-XPS and STM.[31] Referring to literature data,[32−35] the desorption peaks shown can be related to CO desorption from Fe^{2+} (142 and 156 K), Fe^{3+} (190 K), and Fe^0 (broad peak centered around 340 K with many components) exposed sites. The TPD data of the as-grown sample (i.e., at RT) show that both metallic Fe and FeO$_x$ sites (both Fe^{2+} and Fe^{3+} with a large predominance of the former) are exposed, in agreement with the HR-XPS data presented in Figure 1. The most relevant result is that the broad metallic Fe^0 peak is almost vanished above 460 K, confirming the XPS indication that above this temperature most of the Fe NPs are oxidized. In the 460 < T < 800 K temperature range, TPD spectra show that the peak due to

DOI: 10.1021/jz100511s | J. Phys. Chem. Lett. 2010, 1, 1660–1665

THE JOURNAL OF PHYSICAL CHEMISTRY Letters
pubs.acs.org/JPCL

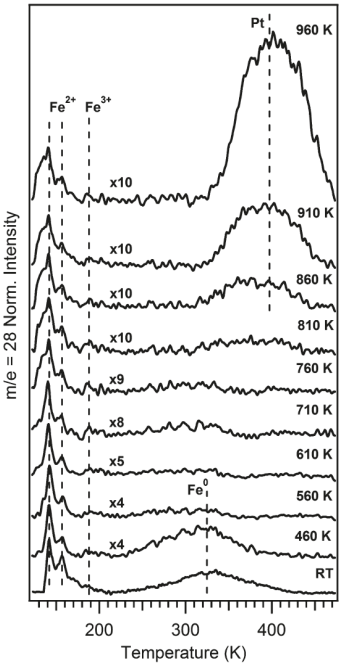

Figure 3. CO TPD spectra of 0.5 ML Fe/z'-TiO$_x$/Pt(111) after a 1.0 L exposure to CO and 2′ thermal treatments at increasing temperatures. In order to highlight the relative abundance of the different components, we renormalized the data with respect to the intensity of the peak seen at the lowest T. A comparison of their absolute intensities can be derived from the reported scale factors.

Fe^{3+} almost vanishes, while sites due to Fe^{2+} are still present up to the highest explored temperature. Such data are in agreement with the assignment of the protrusions observed in the STM data to FeO-like islands previously proposed (Figure 2c,d), where O ions are the topmost layer as a consequence of a *spillover* process. It is well-known that CO is not able to bind to this kind of oxygen terminated FeO films,[34,35] but a few active sites at the edges of the FeO islands remain exposed and can thus coordinate the small amount of CO that is visible with TPD. Above 810 K, the number of residual Fe^{2+} sites is very low, whereas a new broad peak centered at about 400 K becomes predominant. As already outlined, this peak corresponds to CO desorption from Pt(111), supporting the interpretation of the islands observed in the STM image of Figure 2f as uncovered Pt(111).

In conclusion, this work provides new detailed information on the thermal evolution of a Fe(0.5 ML)/z'-TiO$_x$/Pt(111) model catalyst prepared in UHV. Such a system has been used to monitor subtle transformations that might also be in operation in real catalysts and of relevance in the emerging field of monolayer catalysis. Our results suggest that the system evolution in the explored temperature range is largely driven by the facile interdiffusion of the Fe into the Pt substrate. According to our data, we can single out three temperature ranges where different phenomena occur:

(i) $RT < T < 460$ K: The Fe atoms adsorbed on the UT TiO$_x$ film at RT assemble as heterogeneous Fe and FeO$_x$ NPs both on the stripes and on the troughs of the UT film. In this temperature range, a progressive diffusion of Fe into the z'-TiO$_x$ phase defects (troughs and picoholes) and the creation of a first direct contact with the Pt substrate takes place. When Fe goes in direct contact with Pt through the picoholes, a preferential path for interdiffusion into the substrate is opened, and a mechanism for modifying the existing UT TiO$_x$ bilayer is started.

(ii) $460 < T < 800$ K: An oxidation of both Ti and Fe occurs, probably leading to the formation of a metastable FeO$_x$/TiO$_x$ mixed oxide. Such an oxidation is assisted by an interdiffusion of Fe into the Pt substrate, with the consequent increase in the O/M(Ti and Fe) ratio. During such a process, the z'-TiO$_x$ phase reorganizes into an *hexagonal*-TiO$_x$ pattern and FeO islands are prevalently pinned at the apex of the hexagons formed by the restructured UT TiO$_x$ film. However, based on the current data, we cannot exclude that the observed islands are formed by the mentioned metastable mixed oxide.

(iii) $800 < T < 1000$ K: While a residual amount of FeO islands is present, a Fe-mediated extraction of Pt, which creates Pt(111) nanoislands, progressively takes place. These islands are surrounded and partially covered by the z'-TiO$_x$, which is the most stable phase in these high temperature conditions.

EXPERIMENTAL METHODS

The data were collected in three different UHV equipments (for STM, TPD, and HR-XPS measurements, respectively), working with a base pressure of $< 5 \times 10^{-10}$ mbar, by reproducing exactly the same conditions for the Fe/z'-TiO$_x$/Pt(111) preparation and annealing. Further details regarding the procedures adopted to prepare the investigated TiO$_x$ film are reported in ref 21.

The STM data were acquired in constant current mode at RT, using an Omicron multiscan system, with tip to sample bias ranging from 0.3 to 1.0 V and tunneling current ranging from 0.1 to 1.0 nA.

The HR-XPS data were obtained at the Beamline for Advanced diCHroism (BACH, BL 8.2) at the Elettra Synchrotron Light Source in Trieste, Italy.[36] The photon/pass energies used to collect the Ti 2p and Fe 2p core levels were, respectively, 550 eV/20 eV and 830 eV/50 eV, allowing a total resolution of 0.229 and 0.374 eV. Measurements were taken at normal emission, and the energy calibration was made on the basis of the corresponding Fermi edge.

The TPD data were obtained using a Hyden Quadrupole Mass Spectrometer and monitoring the $m/e = 28$ corresponding to CO.

AUTHOR INFORMATION

Corresponding Author:
*To whom correspondence should be addressed. E-mail: gaetano.granozzi@unipd.it. Phone: +39-049-8275158.

ACKNOWLEDGMENT This work was supported by the University and Research (MIUR) through the program PRIN 2005 and 2006,

DOI: 10.1021/jz100511s | *J. Phys. Chem. Lett.* 2010, *1*, 1660–1665

THE JOURNAL OF PHYSICAL CHEMISTRY Letters

pubs.acs.org/JPCL

and by the University of Padova, through Grant CPDA071781. We thank Alessandro Fortunelli (Pisa) for clarifying discussions on the content of the manuscript. We thank the BACH Beamline staff (Elettra Synchrotron, Trieste) for their technical assistance during the measurements.

REFERENCES

(1) Schulz, H. Short History and Present Trends of Fischer–Tropsch Synthesis. *Appl. Catal., A* **1999,** *186*, 3–12.

(2) Riedel, T.; Claeys, M.; Schulz, H.; Schaub, G.; Nam, S. S.; Jun, K.-W.; Choi, M. J.; Kishan, G.; Lee, K. W. Comparative Study of Fischer–Tropsch Synthesis with H_2/CO and H_2/CO_2 Syngas Using Fe- and Co-Based Catalysts. *Appl. Catal., A* **1999,** *186*, 201–213.

(3) Laurent, S.; Forge, D.; Port, M.; Roch, A.; Robic, C.; Elst, L.-V.; Muller, R.-N Magnetic Iron Oxide Nanoparticles: Synthesis, Stabilization, Vectorization, Physicochemical Characterizations, and Biological Applications. *Chem. Rev.* **2008,** *108*, 2064–2110.

(4) Zeng, H.; Sun, S. H. Syntheses, Properties and Potential Applications of Multicomponent Magnetic Nanoparticles. *Adv. Funct. Mater* **2008,** *18*, 391–400.

(5) Lu, A.-H.; Salabas, E. L.; Schuth, F. Magnetic Nanoparticles: Synthesis, Protection, Functionalization, and Application. *Angew. Chem., Int. Ed.* **2007,** *46*, 1222–1245.

(6) Gao, J.; Gu, H.; Xu, B. Multifunctional Magnetic Nanoparticles: Design, Synthesis, and Biomedical Applications. *Acc. Chem. Res.* **2009,** *42*, 1097–1107.

(7) Kung, M. C.; Davis,and, R. J.; Kung, H. H. Understanding Au-Catalyzed Low-Temperature CO Oxidation. *J. Phys. Chem. C* **2007,** *111*, 11767–11775.

(8) Freund, H.-J.; Goodman, D.-W. In *Handbook of Heterogeneous Catalysis*, 2nd ed; Ertl, G., Knözinger, H., Schüth, F., Weitkamp, J., Eds.; Wiley-VCH Verlagsgesellschaft mbH: Weinheim, Germany, 2007; pp 1309–1338.

(9) Tauster, S.-J.; Fung, S.-C.; Garten, R.-L. Strong Metal–Support Interactions. Group 8 Noble Metals Supported on Titanium Dioxide. *J. Am. Chem. Soc.* **1978,** *100*, 170–175.

(10) Tauster, S.-J. Strong Metal–Support Interactions. *Acc. Chem. Res.* **1987,** *20*, 389–394.

(11) Fu, Q.; Wagner, T. Interaction of Nanostructured Metal Overlayers with Oxide Surfaces. *Surf. Sci. Rep.* **2007,** *62*, 431–498.

(12) Parteder, G.; Allegretti, F.; Surnev, S.; Netzer, F.-P. Growth of Cobalt on a VO(111) Surface: Template, Surfactant or Encapsulation Role of the Oxide Nanolayer? *Surf. Sci.* **2008**, *602*, 2666–2674.

(13) Freund, H.-J.; Pacchioni, G. Oxide Ultra-thin Films on Metals: New Materials for the Design of Supported Metal Catalysts. *Chem. Soc. Rev.* **2008,** *37*, 2224–2242.

(14) Sun, Y.-N.; Qin, Z.-H.; Lewandowski, M.; Carrasco, E.; Sterrer, M.; Shaikhutdinov, S.; Freund, H.-J. Monolayer Iron Oxide Film on Platinum Promotes Low Temperature CO Oxidation. *J. Catal.* **2009,** *266*, 359–368.

(15) Lewandowski, M.; Giordano, L.; Goniakowski, J.; Sun, Y.-N.; Qin, Z.-H.; Noguera, C.; Shaikhutdinov, S.; Pacchioni, G.; Freund, H.-J. Interplay Between Structure and CO Oxidation Catalysis on Metal Supported Ultrathin Oxide Films. *Angew. Chem., Int. Ed.*, in press.

(16) Wu, Q.-H.; Fortunelli, A.; Granozzi, G. Preparation, Characterisation and Structure of Ti and Al Ultrathin Oxide Films on Metals. *Int. Rev. Phys. Chem.* **2009,** *28*, 517–576.

(17) Sedona, F.; Rizzi, G.-A.; Agnoli, S.; Llabrés i Xamena, F.-X.; Papageorgiou, A.; Ostermann, D.; Sambi, M.; Finetti, P.; Schierbaum, K.; Granozzi, G. Ultrathin TiO_x Films on Pt(111): A LEED, XPS, and STM Investigation. *J. Phys. Chem. B* **2005,** *109*, 24411–24426.

(18) Sedona, F.; Granozzi, G.; Barcaro, G.; Fortunelli, A. Defect Evolution in Oxide Nanophases: The Case of a Zigzag-like TiO_x Phase on Pt(111). *Phys. Rev. B* **2008,** *77*, 115417/1–8.

(19) Sedona, F.; Agnoli, S.; Fanetti, M.; Kholmanov, I.; Cavaliere, E.; Gavioli, L.; Granozzi, G. Ordered Arrays of Au Nanoclusters by TiO_x Ultrathin Templates on Pt(111). *J. Phys. Chem. C* **2007,** *111*, 8024–8029.

(20) Rizzi, G.-A.; Sedona, F.; Artiglia, L.; Agnoli, S.; Barcaro, G.; Fortunelli, A.; Cavaliere, E.; Gavioli, L.; Granozzi, G. Au Nanoparticles on a Templating TiO_x/Pt(111) Ultrathin Polar Film: A Photoemission and Photoelectron Diffraction Study. *Phys. Chem. Chem. Phys.* **2009,** *11*, 2177–2185.

(21) Cavaliere, E.; Kholmanov, I.; Gavioli, L.; Sedona, F.; Agnoli, S.; Granozzi, G.; Barcaro, G.; Fortunelli, A. Directed Assembly of Au and Fe Nanoparticles on a TiO_x/Pt(111) Ultrathin Template: The Role of Oxygen Affinity. *Phys. Chem. Chem. Phys.* **2009,** *11*, 11305–11309.

(22) Finetti, P.; Sedona, F.; Rizzi, G.-A.; Mick, U.; Sutara, F.; Svec, M.; Matolin, V.; Schierbaum, K.; Granozzi, G. Core and Valence Band Photoemission Spectroscopy of Well-Ordered Ultrathin TiO_x Films on Pt(111). *J. Phys. Chem. C* **2007,** *111*, 869–876.

(23) Barcaro, G.; Agnoli, S.; Sedona, F.; Rizzi, G.-A.; Fortunelli, A.; Granozzi, G. Structure of Reduced Ultrathin TiO_x Polar Films on Pt(111). *J. Phys. Chem. C* **2009,** *113*, 5721–5729.

(24) The interdiffusion of metals into a Pt single crystal during UHV annealing is a well-known phenomenon (see ref 9). The preferential migration of Fe with respect to Ti might be explained by the higher affinity of the latter toward oxygen, which tends act as a more effective surfactant for Ti than for Fe.

(25) Agnoli, S.; Menteş, T.-O.; Niño, M.-A.; Locatelli, A.; Granozzi, G. A LEEM/μ-LEED Investigation of Phase Transformations in TiO_x/Pt(111) Ultrathin Films. *Phys. Chem. Chem. Phys.* **2009,** *11*, 3727–3732.

(26) Barcaro, G.; Fortunelli, A. Adsorption and Diffusion of Fe on a Titania Ultrathin Film. *J. Phys. Chem. A* **2009,** *113*, 14860–14866.

(27) Barcaro, G.; Fortunelli, A.; Granozzi, G.; Sedona, F. Cooperative Phase Transformation in Self-Assembled Metal-on-Oxide Arrays. *J. Phys. Chem. C.* **2009,** *113*, 1143–1146.

(28) Jerdev, D.-I.; Koel, B.-E. Fe Deposition on Pt(111): a Route to Fe-Containing Pt–Fe Alloy Surfaces. *Surf. Sci.* **2002,** *513*, L391–L396.

(29) Kim, Y.-J.; Westphal, C.; Ynzunza, R.-X.; Galloway, H.-C.; Salmeron, M.; VanHove, M.-A.; Fadley, C.-S. Interlayer Interactions in Epitaxial Oxide Growth: FeO on Pt(111). *Phys. Rev. B* **1997,** *55*, 13448–13451.

(30) Kim, Y.-J.; Westphal, C.; Ynzunza, R.-X.; Wang, Z.; Galloway, H.-C.; Salmeron, M.; Van Hove, M.-A.; Fadley, C.-S. The Growth of Iron Oxide Films on Pt(111): A Combined XPD, STM, and LEED Study. *Surf. Sci.* **1998,** *416*, 68–111.

(31) Preliminary experiments have demonstrated that such exposure is capable of saturating all the exposed chemisorption sites. All the TPD spectra reported in Figure 3 have been obtained by subtracting a background associated with the clean UT z'-TiO_x films. The clean UT film almost completely wets the Pt(111) substrate (96%), as judged from the evaluation of the CO desorbed from the corresponding exposed sites at about 400 K.

(32) Cameron, S.-D.; Dwyer, D.-J. A Study of π-Bonded CO on Fe(100). *Langmuir* **1988,** *4*, 282–288.

DOI: 10.1021/jz100511s | *J. Phys. Chem. Lett.* **2010,** *1*, 1660–1665

THE JOURNAL OF PHYSICAL CHEMISTRY Letters
pubs.acs.org/JPCL

(33) Lemire, C.; Meyer, R.; Henrich, V.-E.; Shaikhutdinov, S.; Freund, H. The Surface of Fe_3O_4(111) Films as Studied by CO Adsorption. *Surf. Sci.* **2004,** *572*, 103–114.
(34) Sun, Y.-N.; Qin, Z.-H.; Lewandowski, M.; Shaikhutdinov, S.; Freund, H.-J. CO Adsorption and Dissociation on Iron Oxide Supported Pt Particles. *Surf. Sci.* **2009,** *603*, 3099–3103.
(35) It is important to point out that, in literature, different metal Fe surfaces are reported to have three distinctive desorption peaks in the temperature range 300−370 K (named α, β, and γ). In our case, we only observe one broad feature, probably arising from the highly heterogeneous nature of Fe NPs.
(36) BACH - Beamline for Advanced diCHroism, 10, 2009; http://www.tasc.infm.it/research/bach/scheda.php

DOI: 10.1021/jz100511s | *J. Phys. Chem. Lett.* **2010,** *1*, 1660–1665

References

[1] F. Sedona, G. A. Rizzi, S. Agnoli, F.-X. Llabre's i Xamena, A Papageorgiou, D. Ostermann, M. Sambi, P. Finetti, K. Schierbaum and G. Granozzi, *J. Phys. Chem B* 2005, **109**, 24411.

[2] G. Bhargava, I. Gouzman, C.M. Chun, T.A. Ramanarayanan, S.L. Bernasek, *Appl. Surf. Sci.* 2007, **253**, 4322-4329.

[3] S. D. Cameron, D. J. Dwyer, *Langmuir* 1988, **4**, 282–288.

[4] C. Lemire, R. Meyer, V. E. Henrich, S. Shaikhutdinov, H. J. Freund, *Surf. Sci.* 2004, **572**, 103–114.

[5] Y. N. Sun, Z. H. Qin, M. Lewandowski, S. Shaikhutdinov, H. J. Freund, *Surf. Sci.* 2009, **603**, 3099–3103.

[6] L. Artiglia, E. Cavaliere, G. A. Rizzi, L. Gavioli, G. Granozzi, *J. Phys. Chem. Lett.* 2010, **1**, 1660-1665.

[7] E. Cavaliere, I. Kholmanov, L. Gavioli, F. Sedona, S. Agnoli, G. Granozzi, G. Barcaro, A. Fortunelli, *Phys. Chem. Chem. Phys.* 2009, **11**, 11305-11309.

[8] Cameron, S.-D.; Dwyer, D.-J., *Langmuir* 1988, **4**, 282–288.

[9] F. Sedona, G. Granozzi, G. Barcaro, A. Fortunelli, *Phys. Rev. B* 2008, **77**, 115417/1-8.

[10] G. Barcaro, A. Fortunelli, *J. Phys. Chem. A* 2009, **113**, 14860-14866.

[11] G. Barcaro, S. Agnoli, F. Sedona, G. A. Rizzi, A. Fortunelli, G. Granozzi, *J. Phys. Chem. C* 2009, **113**, 5721-5729.

[12] G. Barcaro, A. Fortunelli, G. Granozzi, F. Sedona, *J. Phys. Chem. C* 2009, **113**, 1143-1146.

[13] Y. J. Kim, C. Westphal, R. X. Ynzunza, Z. Wang, H. C. Galloway, M. Salmeron, M. A. Van Hove, C. S. Fadley, *Surf. Sci.* 1998, **416**, 68-111.

[14] S. Le Moal, M. Moors, J. M. Essen, C. Becker, K. Wandelt, *Surf. Sci.* 2010, **604**, 1637-1644.

Chapter IX
General conclusion and perspectives

During the three years of PhD I have focused my research efforts in the study of the model catalysts obtained by depositing a metal on TiO_x ultrathin (UT) films grown on Pt(111). The high degree of characterization of such supports, which had already been studied in my research group, has allowed a detailed study of both the electronic properties and the morphology of all the samples analyzed by means of the typical Surface Science techniques. Moreover, during my PhD experience, the strategies used to obtain and reproduce all the UT films were refined and the correct model for a stoichiometric phase, the *rect'*-TiO_2, was obtained by comparing new experimental results and theoretically Density Functional (DF) simulations. For the first time in the literature, an ultrathin film having the TiO_2 (B) structure has been deposited and characterized.

Concerning the model catalysts, I have been focusing on two different metals (Au and Fe). The Au was chosen considering its high reactivity at the nanoscale, especially towards the selective oxidation reactions (e.g. CO oxidation at low temperatures). In this thesis, the deposition of Au nanoparticles (NPs) has been monitored on both the reduced TiO_x and the oxidized TiO_2 UT films. The NPs have shown different growth modes, depending either on the TiO_x UT film oxidation state or the presence of preferential nucleation sites. In particular, one of the reduced UT films, the *z'*-TiO_x one, having an ordered array of defects (*picoholes* where the Pt support is left uncovered) has demonstrated to act as a templating substrate, allowing the Au NPs to grow along straight lines. Moreover, the NPs have shown different interactions with the TiO_x, mainly depending on the actual UT film stoichiometry: Au has a stronger interaction with the reduced substrates than with the stoichiometric ones, leading to the growth of flatter and smaller (1 to 4 nm diameter) NPs on the

former and three-dimensional and larger (6 to 8 nm diameter) NPs on the latter. Some interesting results have been also derived from the analysis of the properties of the model catalysts under realistic conditions, i.e. bridging the "pressure gap" (from the UHV 10^{-10} mbar pressures ranges to the quasi-atmospheric pressure of 10^{2} mbar). These experiments have been carried on thanks to an important collaboration with the Institute of Surface Chemistry and Catalysis of the University of Ulm, in the group of Prof. Dr. R. J. Behm. Through the use of a high pressure (HP) cell directly connected to a UHV chamber used for the *in-situ* preparation of the samples, it was possible to demonstrate the instability of the reduced model catalysts after 100 mbar $CO:O_2$ (1:1) dosing, , while the stoichiometric Au/*rect'*-TiO_2 model catalyst showed almost no modifications. In the case of the reduced Au/TiO_x model catalysts at HP, a Au/TiO_2 nano-composite was eventually obtained.

The other metal, Fe, has been chosen as an example of a much different metal with respect to Au, i.e. a reactive metal. I have studied the Fe deposition on two reduced TiO_x UT film, the templating *z'*-TiO_x and the *w'*-TiO_x, in order to understand the stability in UHV of the template itself when interacting with a reactive metal. Also the transformations of the Fe/TiO_x model catalysts after a thermal treatment at temperatures up to 1000 K have been thoroughly investigated. Thanks to the collaboration with the "Università del Sacro Cuore" of Brescia (Dr. L. Gavioli's research group), the "Istituto per i Processi Chimico-Fisici (IPCF)" of CNR, Pisa (Dr. A. Fortunelli's research group) and the use of synchrotron radiation at the BACH (Beamline for Advanced DiChroism) beamline of the Elettra synchrotron in Trieste, it was possible to find a consistent interpretation of the quite unusual thermally driven transformations. In particular, it has been shown that competitive solid-state redox processes and chemical/structural transformations of both the NPs and the oxide film can take place as a function of the temperature. This give rise to new distinctive phases: the system evolves from a NPs assembly on the pristine UT film at RT through an intermediate state, formed by a bi-component oxide material, i.e. mixed oxide FeO/TiO_2 nanoislands on a new reduced TiO_x UT film, to the thermodynamically stable phase at high temperature where Fe is dissolved into the substrate and the pristine UT film is rebuilt. To my best knowledge, this is the first example where atomic resolved STM images on the background UT oxide films are achieved in the presence of NPs, allowing a rather unique level of detail in the description of the observed chemical transformations that might be operating in real

nanostructured catalysts. The results have also evidenced the role of the defects of the templating *z'*-TiO_x UT film, which act as preferential diffusion paths for the Fe to reach the Pt support, thus leading to a higher reactivity of this phase towards the Fe with respect to the *w'*-TiO_x.

As a partial outline of the perspectives, I can mention the potentiality of the Au/TiO_2 nano-composite obtained exposing to "high pressures" environment the Au/reduced-TiO_x model catalysts. As a consequence of the finite Au/TiO_2 NPs sizes (outlined with STM to be in the 1-2 nm range) such a system could have interesting applications as a sensor or catalyst to use in real conditions.

Also the applications of the stoichiometric TiO_2 UT films grown on Pt(111) is an interesting research field where to invest, in particular the case of the nanoislands of Titania(B). The perspectives in such a case are associated to their potentially interesting photocatalytic properties, in particular, in the field of the photoassisted water-splitting reaction. H_2O adsorption on stoichiometric TiO_2/Pt(111) UT films of thicknesses up to 10 nm with different structure (lepidocrocite, Titania B and rutile) is currently under investigation..

Acknowledgement

This thesis is the outcome of a 4 years research in the Surface Science group of the University of Padova. The whole work would not have been possible without the help of many persons. Hence, I would like to thank Prof. Gaetano Granozzi, for the strong interplay during all the research work and his passion for my research topics. I also thank Prof. Gian Andrea Rizzi, for his assistance and helpfulness during the whole period. A special thank to all the group members, my friends and co-workers Stefano Agnoli, Francesco Sedona, Andrea Barolo, Giuseppe Giallongo and Enrico Reeder.

During the PhD I have spent a period of 5 months at the Institute of Surface Chemistry and Catalysis of the University of Ulm (Germany). This collaboration has been very important both from the scientific and "human" point of view and I would like to thank the group head, Prof. Rolf Juergen Behm, for having been interested in the $Au/TiO_x/Pt(111)$ subject. A grateful thank also to Joachim Bansmann for the scientific assistance during my visits in Ulm and to my friend Otavio Brandao-Alves.

Many thanks also to Dott. Luca Gavioli and Emanuele Cavaliere of the Nanoscience Laboratory of the University "Cattolica del Sacro Cuore" in Brescia, for the precious STM collaboration to the experiments and the long discussions carried on in Padova, Brescia and Trieste.

Finally, I would like to thank my family: my wife Veronica, my parents Cinzia and Andrea, my sister Francesca and my parents in-laws Cristina and Gabriele. Without a constant human support, especially in the most difficult moments, all the works done would not have been possible.